University of Glasgow | School of Chemistry

Design and advanced characterisation of lithium-rich complex oxides for all-solid-state lithium batteries

Marco Amores Segura, BSc, MSc

Submitted in fulfilment of the requirements for the
Degree of Doctor of Philosophy

School of Chemistry
College of Science and Engineering
Univeristy of Glasgow

Supervisors: Prof. Serena A. Corr and Dr. Edmund J. Cussen

October 2018

I am aware of and understand the University's policy on plagiarism and I certify that this assignment is my own work, except where indicated by referencing, and that I have followed the good academic practices noted by the University of Glasgow.

Signed:

Marco Amores Segura

Abstract

The aim of this thesis work has been focused on the development of Li-rich complex oxide materials and their advanced characterisation by a wide range of techniques for their application in Li batteries. To achieve this ultimate goal, it is necessary to consider the material design and discovery, the synthetic routes employed, and the characterisation of these materials to unpick the underpinning structure-property relations which govern functionality.

Chapter 1 introduces the basic aspects of current Li-ion battery technologies and their limitations. This is followed by a description of the all-solid-state battery concept and an examination of solid electrolyte candidate materials. Lithium-rich garnet materials are described in the following section with the conductivity-crystal structure relationship detailed. The role of lithium-excess in complex oxides for battery applications is explored followed by a section introducing the novel concept of lithium-rich double perovskites and the $Li_6Hf_2O_7$ system. Finally, a section reviewing the microwave and sol-gel synthetic pathways employed for battery materials will conclude this introductory chapter.

The chemicals and synthetic approaches employed in this thesis to develop the materials under study are detailed in Chapter 2. The basics behind the characterisation techniques employed in this thesis, including powder X-ray diffraction (PXRD) and neutron powder diffraction (NPD) techniques for structural characterisation, electrochemical impedance spectroscopy (EIS), cyclic voltammetry (CV) and galvanostatic cycling with potential limitation (GCPL) for electrochemical analyses, X-ray absorption spectroscopy (XAS) synchrotron-based techniques for local structure analyses and muon-spin relaxation (μ^+SR) for local Li^+ diffusion studies, among others, are also detailed.

The first results chapter, Chapter 3, details the studies performed on Zn-, Ga-, Al-doped $Li_6BaLa_2Ta_2O_{12}$ (LBLTO) garnet materials as solid-state electrolytes. The achievement of shorter reaction times and temperatures compared to conventional solid-state chemistry methods is detailed. The role of the dopant in the structure is analysed by PXRD and XAS studies and its influence on the ionic conductivity of the materials is examined. For the undoped material, local Li^+ diffusion analyses by μ^+SR are also evaluated and discussed.

Chapter 4 presents a novel microwave-assisted synthesis for Al- and Ga-doped $Li_7La_3Zr_2O_{12}$ (LLZO) garnets. The chapter discusses the stabilisation of the cubic phase of the LLZO garnet at lower temperatures and shorter reaction times. The structure of the

material and dopant positions are analysed by PXRD, XAS and PND studies. The macro and micro ionic transport properties of the materials are examined by EIS and μ^+SR and related to the macrostructure and dopant positions within the garnet structure.

The preparation of the homologous Al-doped LLZO cubic garnet by sol-gel chemistry is explored in Chapter 5. The stabilisation of the highly conducting cubic phase even at lower temperatures is analysed by conventional PXRD, advanced *in-situ* NPD and Raman spectroscopy. The reasons behind the ionic transport behaviour of this sol-gel prepared material are analysed by EIS and local Li^+ diffusion studied with μ^+SR.

Chapter 6 focuses on the synthesis and ionic conductivity studies of the novel Li-rich complex oxides In-and Y-doped $Li_6Hf_2O_7$ as solid-state electrolytes for lithium-ion batteries. The analysis of this new family of materials and their crystallographic structures are presented. The transport properties and the role of the dopant is discussed, with the ionic conductivity and activation energy for macroscopic ionic conduction presented.

In Chapter 7, a new family of Li-rich double perovskites as versatile novel materials for all-solid-state Li batteries is presented. The synthesis and structural characterisation of the $Li_{1.5}La_{1.5}WO_6$ (LLWO) and $Li_{1.5}La_{1.5}TeO_6$ (LLTeO) novel compounds by PXRD, NPD and XAS analyses is described. Investigation of $Li_{1.5}La_{1.5}WO_6$ as a candidate negative insertion electrode was analysed by CV and GCPL experiments, as well as the macro and microscopic study of their transport properties by EIS and μ^+SR techniques respectively. The chapter also includes the study and discussion of the redox stability and Li^+ conduction properties of $Li_{1.5}La_{1.5}TeO_6$ as a solid-state electrolyte and preliminary studies of a pseudo solid-state battery formed by these two novel Li-rich double perovskites.

In Chapter 8, the homologous Na-rich double perovskite $Na_{1.5}La_{1.5}TeO_6$ is presented. The crystal structure has been explored by PXRD, Raman spectroscopy and *in-situ* variable-temperature PXRD experiments. The transport properties have also been explored at the macroscopic and local level by EIS and μ^+SR and its compatibility with Na metal electrodes analysed in symmetrical cells.

To conclude, a summary of the main conclusions obtained from the work presented in this thesis, together with further lines of research to explore, are discussed in Chapter 9.

Acknowledgements

I want to thank a number of people which have contributed in one or another way to the realisation of this thesis.

First, I want to start thanking my supervisors, Dr. Serena Corr and Dr. Edmund Cussen, for giving me the opportunity to work in such a fascinating topic full of opportunities. Your determination, expertise and advice have made possible to get this thesis to its final shape and helped to get the best of me. Thank you for your hard work to secure funding which has allowed carrying this work and attending a number of invaluable conferences and training courses. It has been a great pleasure to be part of your research groups. Thank you to my second supervisor, Prof. Duncan Gregory, for his valuable feedback during annual progression examinations.

I want to thank all the past and present members of the Corr and Cussen groups for their continued support, friendship and many hours of good laughs, you've been great colleagues. In special, I want to thank Thomas for his friendship, enriching discussions and the good moments while on beamtime. Also thanks to Quique for his friendship and tireless endurance towards my energy peaks in the morning, I doubt anyone will be able to cope stoutly as you have! Thanks to Dr. Hany El-Shinawi for the many fruitful discussions and his willingness to extend a helping hand towards me anytime I needed it. Thanks to the members of the C5-12 tearoom, the Mediterranean team (Caroline and Julien) and Ying for her always comforting conversation over lunchtime at the Fraser building. Thanks to Irene, my also Glasgow Uni/Strathclyde hybrid colleague for our 5 minutes chats in the corridor which ended in one-hour long conversations. Michael Beglan, our incredible technician, thank you for being always available to organise plans and excursions and find solutions to any possible issue we could encounter. You all have a friend in me.

I would also like to thank the beamline scientists Dr. Peter Baker (EMU, ISIS), Dr. Ron Smith and Dr. Helen Playford (Polaris, ISIS) and Prof. Alan Chadwick (I18, Diamond) for their assistance on data collection and their kind guidance to the insights of their instruments. Also thanks to Yijin Liu (6-2b, SLAC) for his kind introduction to transmission X-ray microscopy. I also want to thank Dr. Pooja Panchmatia and Dr. Stephen Yeandel for their valuable DFT calculations on the Li-rich double perovskites work. Thanks to the technicians Peter Chang and Jim Gallagher for their assistance with microscopy imaging and to Alex Clunie for ICP-MS analyses.

During the second year of this PhD, I had the chance to visit the group of Dr. Marca

Doeff in the Lawrence Berkeley National Laboratory for which I would like to thank her kind welcoming and support during my stay. I would like to extend this thanks to her collaborator Dr. Guoying Chen and rest of the group (Tian, Jack, Hao) who made my stay a great experience.

I also want to express my gratitude to tax contributors for their financial contribution through EPSRC and the STFC for providing training and beamtime allocations. RSC is also acknowledged for their financial support to conference attendance. Thanks to the School of Chemistry in the University of Glasgow for PhD funding and use of facilities. Also thanks to The University of Strathclyde for access to their facilities and contribution to the Mac Robertson travel scholarship in conjunction with the University of Glasgow.

I don't want to forget to thank my high school science teachers, María José, Rafa, Rosario and Félix, for enlightening me towards the joy of science.

Gracias a Mariví y Patricia por estar ahí en los buenos y malos momentos durante estos últimos años cuando los experimentos funcionaban o se resistían.

A mis padres por su comprensión y su continuo esfuerzo para que avanzase en mis estudios y alcance mis metas, gracias.

Table of Contents

List of Acronyms and Abbreviations

a.u.	arbitrary units
AC	Alternative Current
CCR	Close Circuit Refrigerator
CV	Cyclic Voltammetry
DFT	Density Functional Theory
DMC	Dimethyl Carbonate
E_a	Activation Energy
EC	Ethylene Carbonate
EDX	Energy Disperse X-ray spectroscopy
EIS	Electrochemical Impedance Spectroscopy
EXAFS	Extended X-Ray Absorption Fine Structure
GCPL	Galvanostatic Cycling with Potential Limitation
HOMO	Highest Occupied Molecular Orbital
ICP-MS	Inductively Couple Plasma - Mass Spectrometry
ICSD	Inorganic Crystal Structure Database
LBLTO	$Li_6BaLa_2Ta_2O_{12}$
LISICON	Lithium Super Ionic Conductor
LHLZO	$Li_{7-x}H_xLa_{2.92}Zr_2O_{12}$
LLMO	$Li_{1.5}La_{1.5}MO_6$
LLTeO	$Li_{1.5}La_{1.5}TeO_6$
LLWO	$Li_{1.5}La_{1.5}WO_6$
LLZNbO	$Li_6La_3ZrNbO_{12}$
LLZO	$Li_7La_3Zr_2O_{12}$
LUMO	Lowest Unoccupied Molecular Orbital
μ^+SR	Muon-Spin Relaxation
NASICON	Sodium Super Ionic Conductor
NCA	$LiNi_xCo_yAl_zO_2$
NMC	$LiNi_xMn_yCo_zO_2$
NMR	Nuclear Magnetic Resonance
NPD	Neutron Powder Diffraction
Oh	Octahedral
ppb	part per billion
PTFE	Polytetrafluoroethylene
PXRD	Powder X-Ray Diffraction
Py_{14}TFSI	N-methyl-N-butylpyrrolidinium bis(trifluoromethylsulfonyl)imide
SEI	Solid-Electrolyte Interphase

SEM	Scanning Electron Microscopy
SQUID	Superconducting Quantum Interference Device
Td	Tetrahedral
U_{iso}	Isotropic atomic displacement parameter
XANES	X-ray Absorption Near Edge Spectroscopy
XAS	X-ray Absorption Spectroscopy

List of Tables

List of Figures

List of Publications and Presentations

Contributions to peer-reviewed journals

M. Amores, P. J. Baker, H. Plyford, S. A. Corr and E. J. Cussen. Li^+ diffusion and H^+/Li^+ exchange insights on low temperature cubic LLZO garnet. *In preparation.*

M. Amores, S. Yeandel, P.J. Baker, P. Panchmatia, E. J. Cussen and S. A. Corr. Li-rich double perovskites: A new family of materials for solid-state Li batteries. *In preparation.*

M. Amores, S. A. Corr and E. J. Cussen. Na^+ conduction in a novel Na-rich solid-state electrolyte. *Chem. Commun.*, 2018, 54, 10040.

M. Amores, S. A. Corr and E. J. Cussen. Synthesis and Ionic Conductivity Studies of In- and Y-Doped $Li_6Hf_2O_7$ as Solid-State Electrolyte for All-Solid State Li-Ion Batteries. *J. Electrochem. Soc.*, 2017, 164, A3695.

M. Amores, T. E. Ashton, P. J. Baker, E. J. Cussen and S. A. Corr. Fast microwave-assisted synthesis of Li-stuffed garnets and insights into Li diffusion from muon spin spectroscopy. *J. Mater. Chem. A.* 2016, 4, 1729.

Reviewer for the *Journal of The Electrochemical Society* and *Nanoscale*.

Participation in meetings and conferences

Gordon Research Conference in Batteries, Feb. 2018, Ventura (US), Poster contribution.
Gordon Research Seminar in Batteries, Feb. 2018, Ventura (US), Invited talk.
The 16th European Conference on Solid State Chemistry, July 2017, Glasgow (UK), Poster contribution
EPSRC council meeting, July 2017, Glasgow (UK), Poster contribution
The 14th International Conference on Muon Spin Rotation, Relaxation and Resonance, June 2017, Sapporo (Japan), Poster contribution
Butler Meeting, April 2017, Saint Andrews (UK), Poster contribution
ETP-SHFCA Energy Storage, April 2017, Edinburgh (UK), Poster contribution
RSC Solid State Group Meeting, December 2016, Loughborough (UK), Oral contribution
Challenges and Prospects for Solid State Chemistry, September 2016, Sevilla (Spain), Poster contribution
ISIS Neutron and Muons User Meeting, July 2016, Warwick (UK), Invited talk and

poster contribution

STFC Batteries annual meeting, July 2016, Abingdon (UK), Invited talk

International Meeting on Lithium Batteries, June 2016, Chicago (USA), Poster contribution

Butler Meeting. University of Glasgow, April 2016. Poster contribution

Thomas Graham Symposium. University of Strathclyde, April 2016. Poster contribution

Advances in Lithium-Battery Research: UK 2016. Bath, March 2016. Oral contribution

Conference on Analysis of Diffraction Data in Real Space. Grenoble. March 2016. Oral contribution

RSC Solid State Chemistry Group Christmas Meeting. University of Kent. December 2015. Poster contribution

STFC ISIS Neutron and Muon Student Meeting. Abingdon, October 2015. Oral contribution

The first 27 years of Reverse Monte Carlo Modelling. Budapest, September 2015. Poster contribution

Glasgow-Nankai Chemistry Symposium. University of Glasgow. April 17th, 2015

RSC Solid State Chemistry Group Christmas Meeting. Universities of Glasgow and Strathclyde. December 18-19th, 2014

Chapter 1: Introduction

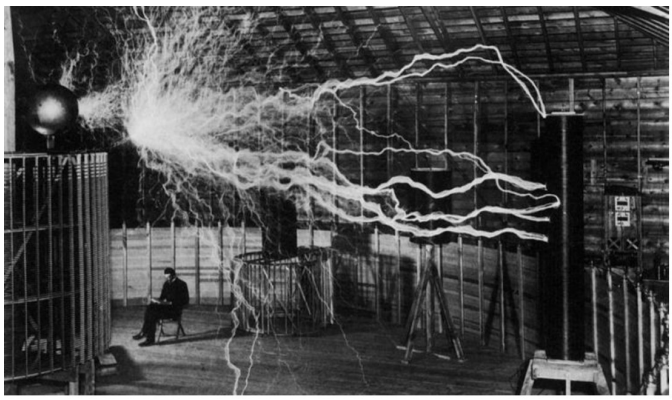

"The spread of civilisation may be likened to a fire; first, a feeble spark, next a flickering flame, then a mighty blaze, ever increasing in speed and power"
Nikola Tesla

Energía, pūngao, мощность, énergie, エネルギ, energy can be defined as the quantitative property that is transferred to an object in order to perform work on that object.[1,2] Energy may exist in potential, kinetic, thermal, electrical, chemical, nuclear, or other various forms.[3] Our society has become extremely dependant on energy sources with increasing demand to have it available anytime and anywhere. This, together with our need for less pollutant and more sustainable sources of energies such as intermittent-production renewables, has boosted the need for advances in energy storage technologies.[4,5]

The first commercial energy storage device was presented in 1799 by Alessandro Volta, the Volta pile, which was key in the development of telegraph technology.[6] Since then, other storage chemistries have evolved such as the Daniell cell in 1836 formed by Cu/Zn electrodes in sulfate solution,[7] the Leclanché cell in 1886,[8] the lead acid battery in 1859 by Planté[9] or the most recent nickel metal hydride rechargeable batteries.[10] It was in 1976 that Whittingham proposed the transformative Li-ion battery[11] which went to be commercialised by Sony in 1991.[12]

A Ragone plot assessing the energy and power densities of different energy storage technologies is presented in Figure 1.1.[4] From this, it is clear that Li battery technologies dominate in both metrics, almost doubling the energy density of the previous rechargeable Nickel-metal hydride technology. Lithium batteries not only provide higher energy densities but also provide an expanded cycling life as well as lower self-discharge rates.[12]

The high energy density of the lithium-ion battery has resulted in a ramp up of its production as a consequence of the large demand for portable electronics devices, which contribute 63% of worldwide sales with an estimated global market of $213.5 billion by 2020.[13,14] Lithium-ion batteries are ubiquitous, from the laptop this thesis is being written on to the new plug-in hybrid/all-electric cars. The development of electric vehicles and smart grid networks are further pushing research in improved lithium batteries to meet their power and capacity requirements. The energy density of lithium-ion batteries has increased by approximately 3-5% every year for the past several decades and it is currently just below 200 Wh kg^{-1}, which is still far from the target of 500 - 700 Wh kg^{-1} to

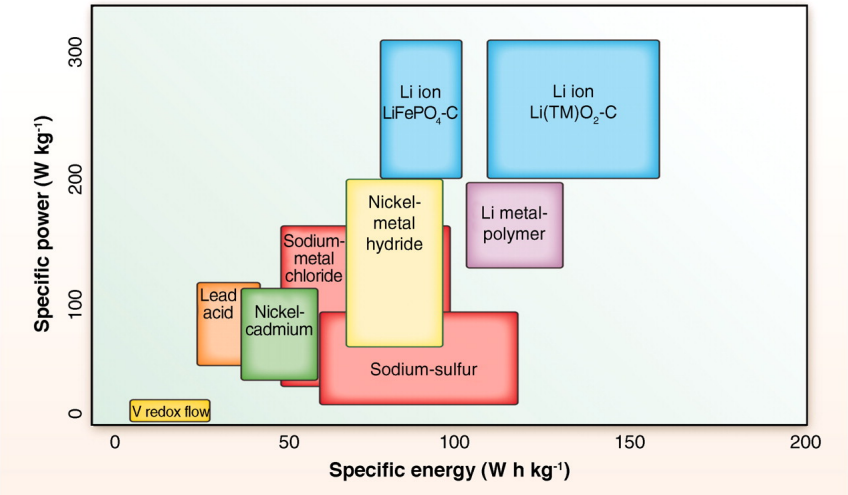

Figure 1.1: Ragone plot of different current energy storage technologies. Rectangles with same colour indicated variations within that energy storage system. Reprinted with permission from AAAS.[4]

meet the needs of vehicle electrification.[15]

1.1 The lithium battery

Traditional lithium batteries are galvanic electrochemical cells formed by two electrodes, an anode and a cathode, separated by a porous polymer membrane and immersed in an electrolyte solution. The working principle of the lithium battery is based on the movement of Li^+ between the anode and the cathode in parallel with electron movement through an external electrical circuit. Figure 1.2 shows a simplified diagram of this working principle for one of the state-of-the-art battery technologies, the NCA-graphite lithium-ion battery used in Tesla cars.[16]

During discharge, Li^+ flow from the graphite anode towards the layered $LiNi_{0.80}Co_{0.15}Al_{0.05}O_4$ (NCA) cathode material through the electrically insulating electrolyte solution, in this case $LiPF_6$ salt in a mixture of ethylene carbonate and dimethyl carbonate solvent. At the same time, electrons flow from the anode towards the cathode through the external electric circuit in the same direction. During charge, the reverse process occurs with Li^+ departing from the layers of the NCA cathode material towards the graphite anode layers, with the associated external current of electrons. These processes during battery (dis)charge are represented in Figure 1.2.

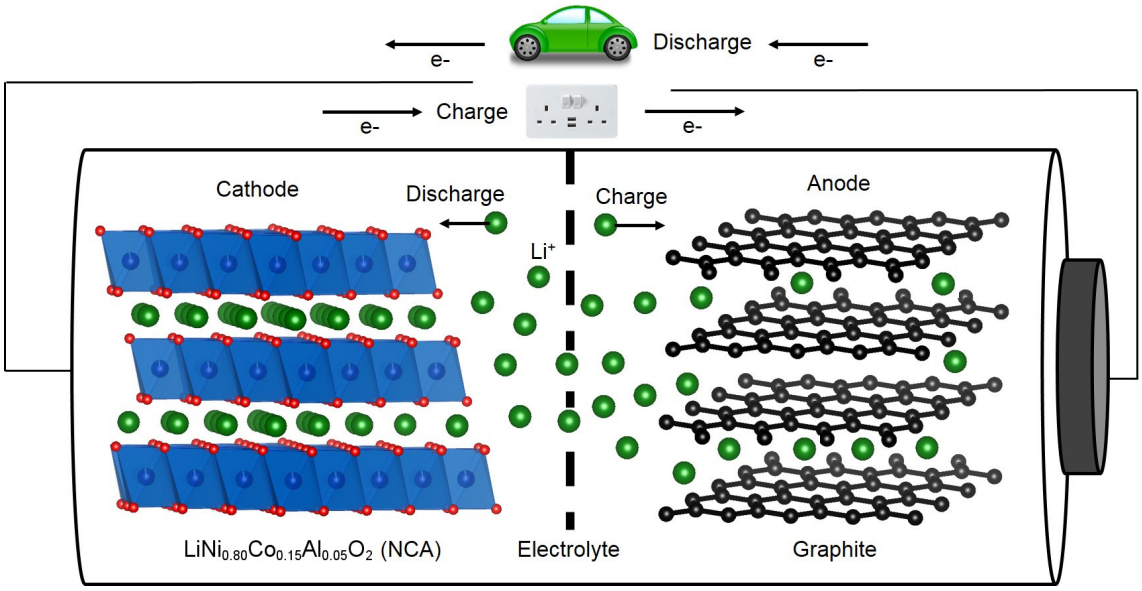

Figure 1.2: Schematic representation of a $LiNi_{0.80}Co_{0.15}Al_{0.05}O_4$–graphite lithium-ion battery. The cathode material is the layered $LiNi_{0.80}Co_{0.15}Al_{0.05}O_4$ material where Li^+ are represented in green, nickel cations octahedra in blue and oxygen anions in red. The anode material is graphitic carbon formed by layers of carbon atoms (black) where Li^+ can be reversibly inserted. The liquid electrolyte is simplified by the green Li^+ and both electrodes are separated by the porous membrane, indicated by the vertical discontinued line. Arrows indicate the direction of moving electrons and Li^+ during battery cycling.

The lithium battery can store electrical energy by converting it into chemical energy through (de)lithiation reactions at the electrodes which produce a potential difference across the cell. The relationship between the Gibbs free energy and the cell potential is shown in Equation 1.1, where n is the number of electrons which can be transferred during (dis)charge, F is the Faraday constant and E is the voltage of the cell:

$$\Delta G = -nFE \tag{1.1}$$

The Gibbs free energy also governs the direction of the electrochemical (de)lithiation reaction of the electrode materials. With a closed external circuit, to allow for electron current between electrodes and provided ΔG is negative, the redox reaction between the electrodes will occur spontaneously with the associated release of the stored energy and electric current flow. When ΔG reaches zero, then no reaction will occur spontaneously, as the cell has achieved equilibrium. If the cell is then connected to an external source which could reverse the direction of the current, then ΔG will become negative again as the voltage of the cell increments and the battery would start storing this energy.

The stored energy of the battery is proportional to the number of electrons/Li^+ that the electrode materials can host and to the operating voltage of the cell. The voltage of the cell is dictated by the difference in electrochemical potentials across the cell and can be calculated as shown in Equation 1.2, where μ_A and $\mu_C$are the electrochemical potentials

of the anode and cathode and *e* is the electrical charge of the electron:[17]

$$V_{oc} = \frac{\mu_A - \mu_C}{e} \tag{1.2}$$

A schematic representation of the Fermi and molecular energy levels for the main components of the cell and how they are related to the voltage of the battery is shown in Figure 1.3.

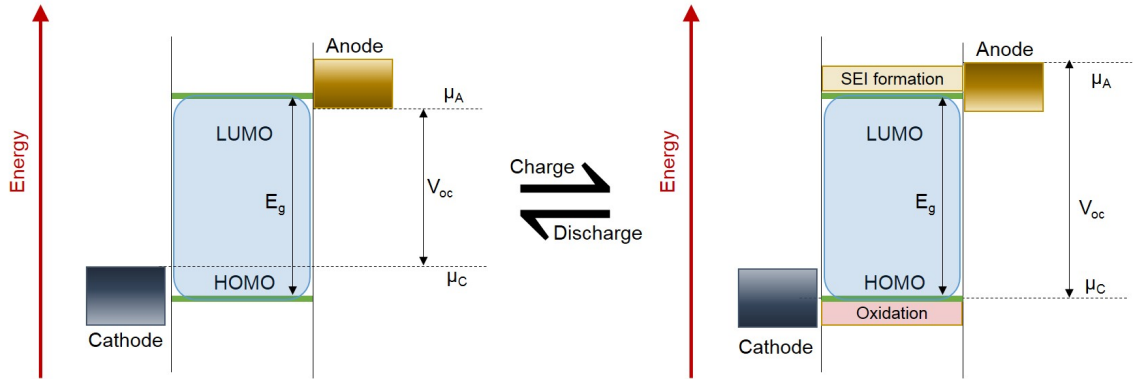

Figure 1.3: Schematic representation of the different energy levels involved during cycling of the battery. The open voltage circuit increase during charging and decrease during discharging while the electrolyte stability window remains constant.

The higher the difference in electrochemical potentials of both electrodes, the higher the voltage of the cell and hence the stored energy. However, the LUMO and HOMO energy levels of the liquid electrolyte also play a key role in this by determining the maximum voltage window safely allowable to the battery. The energy gap (E_g) between the LUMO and HOMO energy levels define the electrolyte stability window. This window must be observed due to the decomposition of the electrolyte if the electrochemical potentials of the electrodes fall outside the LUMO and HOMO gap. Specifically, if the electrochemical potential of the anode material is above the LUMO level of the electrolyte, the electrolyte will then be reduced by electron transfer from the anode. In the case of the HOMO energy level, if this falls below the cathode electrochemical potential, the electrolyte would then be oxidised by the cathode.

Changes in the electrochemical potentials during charging of the battery could result in surpassing the stability window of the electrolyte. These changes rely on the chemistry of the electrodes upon lithium intercalation. The Gibbs phase rule determines the degrees of freedom during the electrode reaction, *i.e.* the number of intensive thermodynamic parameters necessary to define the system. The Gibbs phase rule is shown in Equation 1.3, where *F* is the number of degrees of freedom, *C* the number of compounds involved in the reaction and *P* the number of phases involved during the electrode cycling.[18]

$$F = C - P + 2 \tag{1.3}$$

In battery cells, temperature and pressure are defined and have constant values. So if F = 2, the residual degrees of freedom would be zero and the chemical potential of the electrode won't change during cycling. If F $\geq$ 3, then there will be one degree of freedom remaining and the electrode potential needs to be defined and will change upon cycling. This difference may be observes when comparing $LiCoO_2$ and $LiFePO_4$ positive electrodes. In $LiCoO_2$ the number of components is 2 (Li^+ and $LiCoO_2$) and they form the Li_xCoO_2 solid-solution (P = 1) making F= 3 and the voltage of $LiCoO_2$ will vary during cycling (Fig. 1.4a). In the case of $LiFePO_4$, the number of components is also 2 but P = 2 as the intercalation mechanism in $LiFePO_4$ is based on phase segregation ($FePO_4$ and $LiFePO_4$) leaving F = 2 and in this case the voltage cannot be defined, remaining invariable during the charge/discharge processes (Fig. 1.4b).

Current liquid electrolytes for commercial applications, such as $LiPF_6$ in carbonate solutions, have a LUMO energy level below the electrochemical potential of lithium metal anode electrode, $\sim$ 1 V.[21,22] This, together with the dendrite formation that can occur in Li metal electrodes,[23] has hindered the use of lithium metal electrodes with the consequent loss in energy density. Alternative low voltage graphite electrodes are the most commonly employed anode material in commercial batteries, where partial decomposition of the solvent leads to the formation of a passivation layer, formally called the solid electrolyte interphase (SEI) during the first charge, as the potential of the graphite anode can vary during battery charging and surpass the LUMO level of the liquid electrolyte.[24–26] This SEI layer gets stabilised after the first cycle due to its electrically insulating nature that avoids further electron transfer between the graphite anode and the electrolyte. The formed SEI has some advantages as it allows Li^+ diffusion through and it can prevent graphite exfoliation. The SEI also present some disadvantages such as increasing the internal battery resistances and consumption of the liquid electrolyte which results in

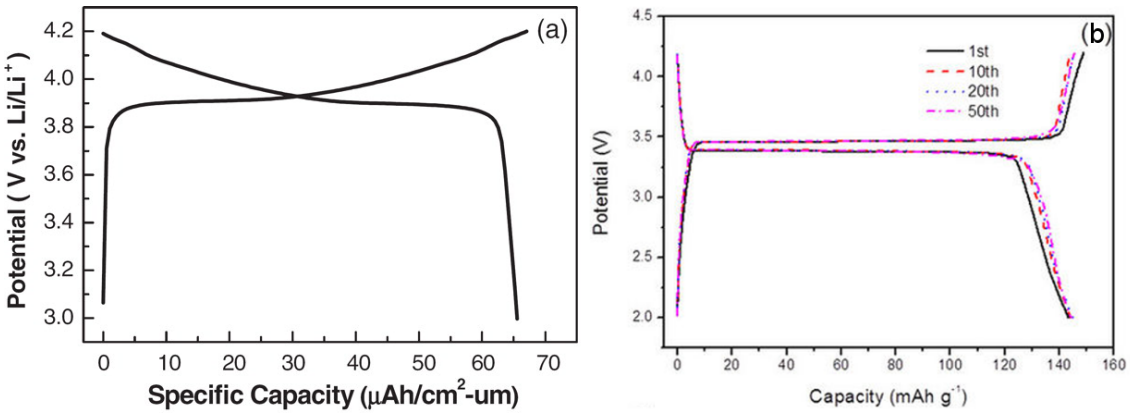

Figure 1.4: Cycling profiles of $LiCoO_2$ (a) and $LiFePO_4$ (b) in half-cells. For $LiCoO_2$ cathode a progressive change in voltage is observed during cycling while in the case of $LiFePO_4$ a flat plateau is observed with no voltage changes during the two phases coexistence region. (a) Adapted with permissions from The Electrochemical Society.[19] (b) Adapted with permission from Springer Nature.[20]

lower cycling efficiency.[27–30]

A more dangerous scenario appears when the chemical potential of the cathode material falls below the HOMO level of the electrolyte. In this case, the electrolyte p-band overlaps with transition metal valence band resulting in degradation of the electrode and O_2 generation together with decomposition of the electrolyte and release of CO_2. In addition, highly reactive PF_5 can be produced which could form intense chemical fires with the other components of the electrolyte under thermal runaway.[31–35]

Increasing the energy density of lithium batteries, which relies in the use of higher voltage cathode materials, is therefore limited by the electrochemical stability window of the liquid electrolyte. There are already several high voltage cathode candidates available, such as the $LiNi_{0.5}Mn_{1.5}O_4$ spinel or the $LiNiPO_4$ and $LiCoPO_4$ olivine phosphates among others. However, their application has been precluded by the lack of suitable high voltage stable liquid electrolytes.[36–42]

This indicates that in order to employ high voltage cathode materials to increase the cell potential and so the battery energy density, the electrolyte needs to be replaced by more stable and safer alternatives.

1.2 Solidifying lithium batteries: solid-state electrolytes and the all-solid-state battery

In order to overcome the safety issues related to the use of liquid electrolytes in lithium batteries, a number of alternatives have been explored such as the use of polymer electrolytes,[43–47] composite materials[48–52] or solid-state electrolytes,[53–63] which demonstrates a clear desire towards the solidification of the electrolyte.

The use of solid-state materials as electrolytes was first investigated by Michel Faraday back in 1839 and has been postulated as a promising alternative to liquid electrolytes in batteries to overcome most of the current safety concerns highlighted in recent decades.[61–63] Moreover, the replacement of the liquid electrolyte by a solid electrolyte would allow the use of lithium metal as an anode material by minimising the risk of short-circuit due to lithium dendrite growth resulting in a large increase in the energy density of the battery. In addition, the use of a solid electrolyte would also allow the use of high voltage Mn-containing cathodes, where typically Mn dissolution occurs in liquid electrolytes and is deposited on the negative electrode.[64] Furthermore, the use of solid electrolytes is not restricted to Li-ion and Li-metal chemistries. It can also benefit Li-S battery technology by suppressing the shuttle effect where the sulfur cathode dissolves and travels through the liquid electrolyte to the counter electrode.[65]

An ideal high energy solid-state lithium battery is represented in Figure 1.5 where the liquid electrolyte and separator have been replaced by a solid-state electrolyte, and a high voltage cathode has been paired with a lithium metal anode.

Unfortunately, the replacement of the liquid electrolyte by a solid electrolyte has some

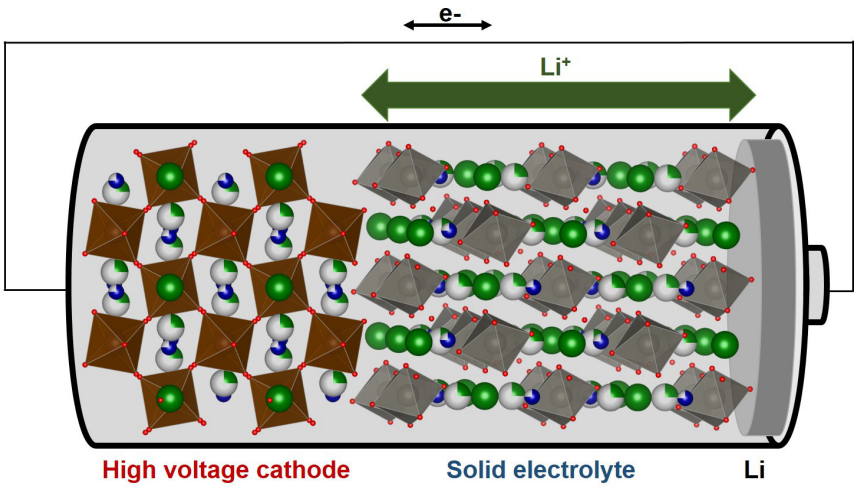

Figure 1.5: Schematic representation of an all-solid-state battery composed by a high voltage cathode and a lithium metal foil anode separated by a solid-state electrolyte which allows lithium diffusion and block electronic conduction through its crystal structure.

disadvantages. Sluggish Li^+ conduction through the solid electrolyte and interfacial resistances within the electrolyte grains and with the electrode materials are severely hampering their implementation in the battery field.[66–68] For this reason, further research to overcome these issues and the search for alternative systems are key in the realisation of the golden dream of high-performance solid-state batteries.

There are several inorganic solid electrolyte candidate systems currently under intensive research. These solid electrolytes can be classified by the type of anion present in their crystal framework as oxides, sulfides, halides, phosphates and nitrides or by the their crystal structure as in garnet, LISICON and NASICON-like, or perovskites, among others.[58,69] Figure 1.6 summarises the different ionic conductivities reported within different classes of solid electrolyte materials.

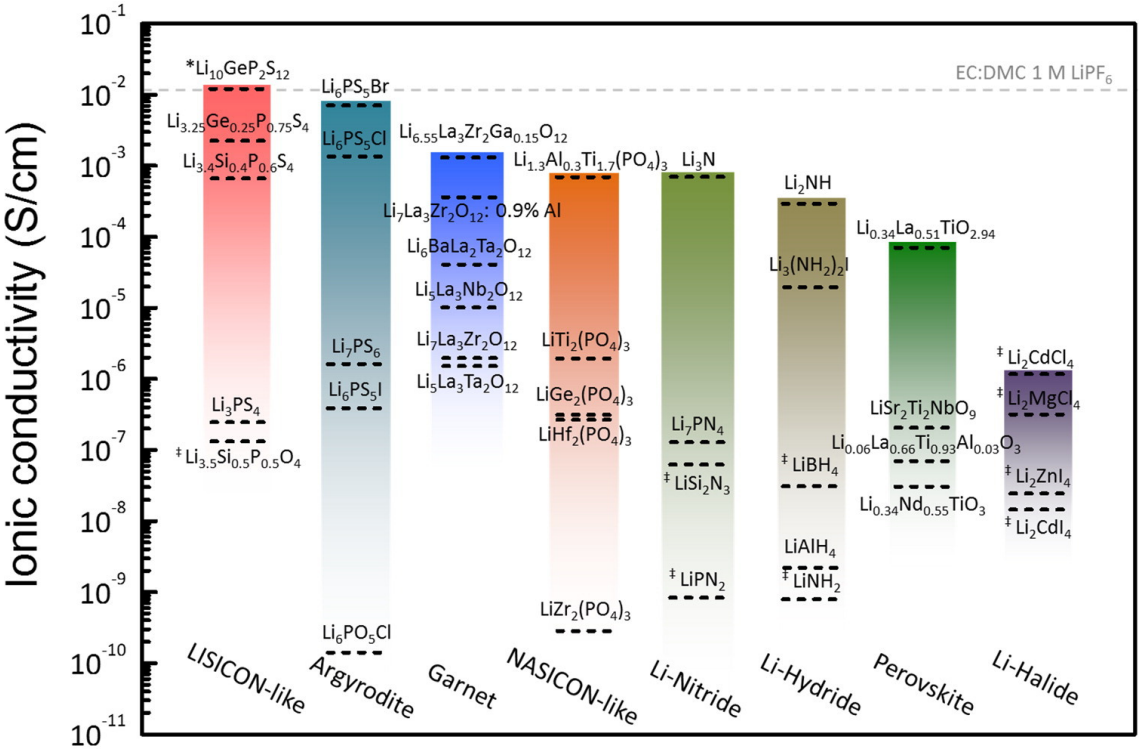

Figure 1.6: Reported total ionic conductivity at room temperature for the most studied solid electrolytes in the literature. Adapted with permission from the American Chemical Society. Copyright 2015.[58]

LISICON-like and Argyrodite structures possess exceptional ionic conductivities matching those of current liquid electrolytes.[70–72] With ionic conductivities near an order of magnitude lower appears the garnet family, followed very closely by the NASICON, Li_3N, Li-Hydrides and perovskite materials in the mS cm^{-1} range.[58,73] Sulfide materials appear poised to overtake liquid electrolytes in terms of ionic conductivity. However, these materials possess poor electrochemical stability against lithium metal and also can decompose at high voltages, precluding two of the main targets detailed above: the use of high voltage cathodes and a lithium metal anode.[74] Oxides, on the contrary, have good stability at high voltages and can also be compatible with lithium metal.[58,75] In this case, their lower ionic conduction properties and interfacial resistances have been the cause for their limited use for commercial applications. Figure 1.7 shows a radar chart grading the three most widely studied systems in terms of their properties as electrolytes for commercial solid-state batteries.[76–78]

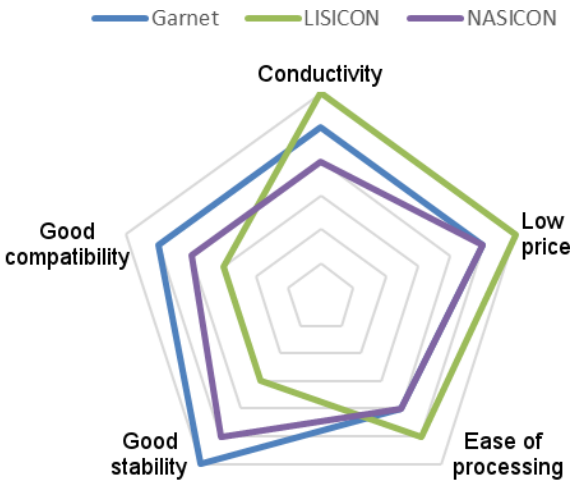

Figure 1.7: Radar chart showing the qualitative grading of different properties of three families of solid-state electrolytes owing the highest ionic conductivities. The grading has been selected as personally abstracted from the available literature. The closer of a data point to the outer pentagon the highest the grading of the property and viceversa.

In addition to the above mentioned conductivity and redox compatibility, the chart also includes processability and stability. Sulfide materials are relatively easy to integrate in devices due to their soft macro-structure while in the case of oxides and phosphates their processability is hampered by their hardness.[79] Regarding stability, oxides tend to be stable in air while sufide materials degrade in the presence of oxygen or moisture.[58] It seems clear that garnet materials possess well balanced properties, with sufficient ionic conductivity, good redox stability and scalable synthesis, and hence the choice of these materials for study in this thesis.

It should be noted that there are already examples of all-solid-state Li^+ batteries in the literature with garnet electrolytes, such as the work reported by Ohta *et al.* where $LiCoO_2$ was deposited on top of $Li_7La_3Zr_2O_{12}$ garnet material,[80] or the most recent work by Yan *et al.* on a $Li_7La_3Zr_2O_{12}$/$LiFePO_4$ cell.[81] However, in these works conventional cathodes and small areal electrical currents are employed, leaving the full potential of using a solid electrolyte untested.

1.2.1 Li-rich garnet electrolytes

Li-rich garnet materials have quickly climbed in the solid-electrolyte ranking in the last decade due to their excellent properties which include high Li^+ conductivities up to 10^{-3} S cm^{-1}, chemical stability with high voltage cathodes with a high electrochemical decomposition voltage above 6 V, lack of flammability, stability against lithium metal and their single-ion conductor behaviour.[58,73]

Lithium-containing garnets materials were first reported in 1969 by H. M. Kasper with the synthesis of the $Ln_3M_2Li_3O_{12}$ (M = Te, W; Ln = Y, Pr, La, Nd) series.[82] The lithium garnet crystal structure derives from that of the garnet mineral which can be described

by the formula $A_3B_3C_2O_{12}$, where *A* cations are located in an oxygen-tetrahedral environment, *B* cations are surrounded by 8 oxygen anions and *C* cations are accommodated in oxygen-octahedral sites. Specifically for lithium-containing garnets, Li^+ sit on the A sites with B sites occupied by a rare earth metal or a large alkaline earth metal and C sites can be occupied by a wide range of metal cations with oxidation states usually ranging from 4+ to 6+. Conventional $Li_3Ln_3M_2O_{12}$ lithium garnets crystallise in a body centred cubic structure with a $Ia\bar{3}d$ space group, where Li^+ occupy the tetrahedral 24d positions, Ln^{3+} are located in the 8-fold 24c positions and M^{6+} are located in the octahedral 16a positions with the O^{2-} sitting on the 96h positions making up the anionic framework (Fig. 1.8).[83,84]

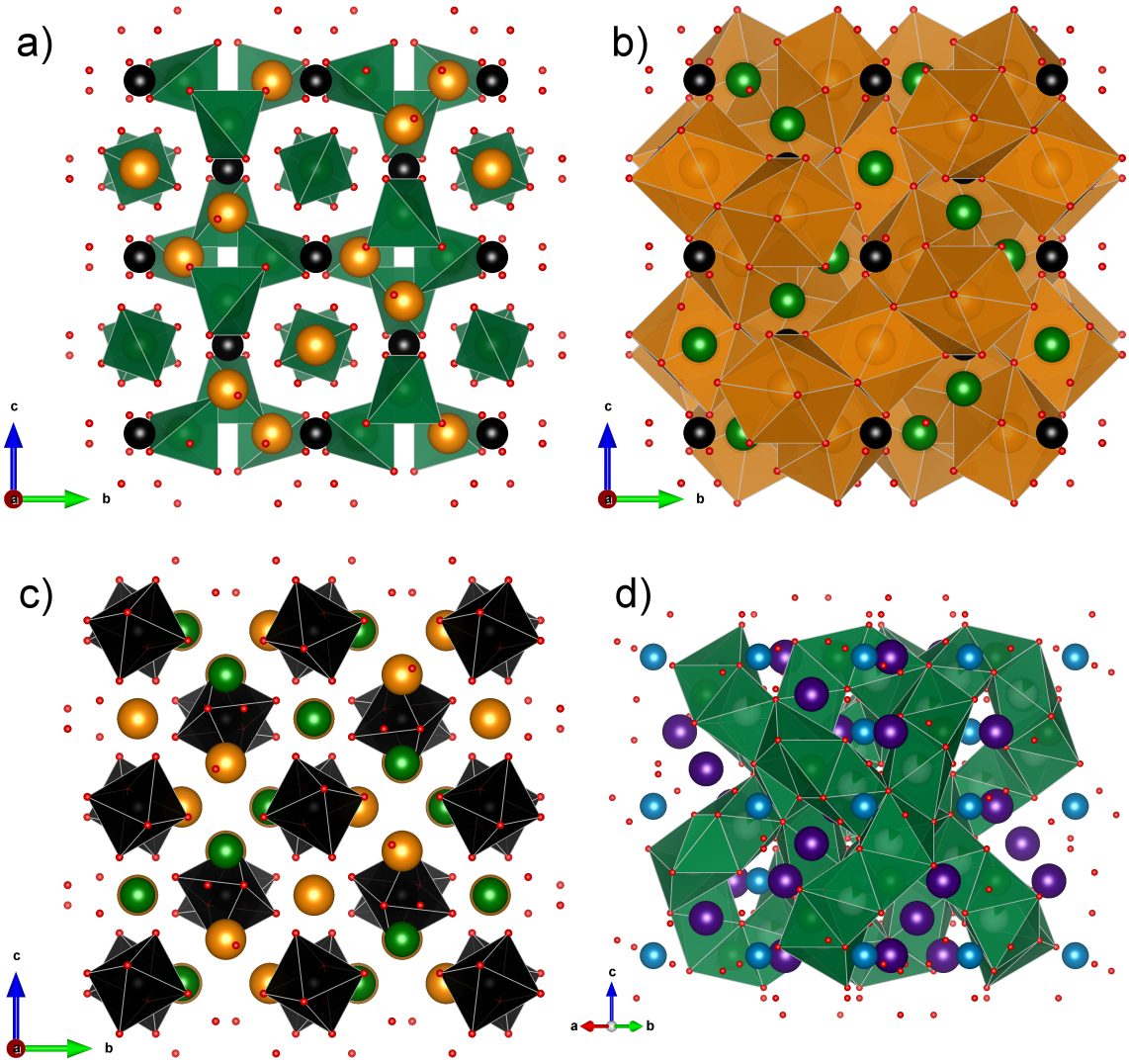

Figure 1.8: (a), (b) and (c) Crystallographic representation of the unit cell for the $Li_3Nd_3W_2O_{12}$ structure with $Ia\bar{3}d$ cubic symmetry where Nd^{3+} cations are represented in orange, W^{6+} in black, Li^+ ion in green and O^{2-} anions in red. Only the tetrahedral coordination polyhedra for the Li^+ are represented for clarity in (a), with the distorted cubic coordination polyhedra for the Nd^{3+} ions explicitly shown in (b) and the octahedral coordination polyhedra for W^{6+} ions represented in (c). (d) Crystal structure of a $Li_5MM'O_{12}$ garnet material where the network of face-sharing oxide octahedra and tetrahedra that are occupied by Li^+ in the Li-rich cubic garnets is shown.

The versatility of the garnet structure allows for a wide range of different cations in the framework.[73] By tailoring the oxidation state of the metal cations present in the B and C sites, additional Li^+ can be accommodated within the garnet structure in order to maintain the crystal electrical neutrality. This is illustrated by the $Li_5La_3M_2O_{12}$ (M = Ta^{5+}, Nb^{5+}) garnets reported in 1988 by Hyooma and Hayashi.[85] They found that the decrease of cationic charge as a consequence of the lower valence in the M metal allowed insertion of two additional mols of Li^+ per formula unit of garnet, producing the so-called Li-rich garnet materials. It was not until 2003 when the Thangadurai group revisited these materials and reported their conduction properties (10^{-6} S cm^{-1}) that interest in these materials began to ramp up as solid-state electrolytes.[86]

In these lithium-rich garnet phases, the additional lithium ions can be accommodated within interstitial distorted octahedral positions, in addition to the three fully occupied tetragonal sites on the conventional $Li_3B_3C_2O_{12}$ garnet.[83,87] These Li^+ in the distorted octahedral positions are statically disordered and can be found either close to the octahedron apexes (96h) or close to the octahedral centre (48h) positions. In addition, the increment of lithium concentration progressively displaces the Li^+ from the tetrahedral to the octahedral sites, creating vacancies on the tetrahedral sites. A schematic representation of this transition from a conventional to a Li-rich configuration is shown in Figure 1.9.

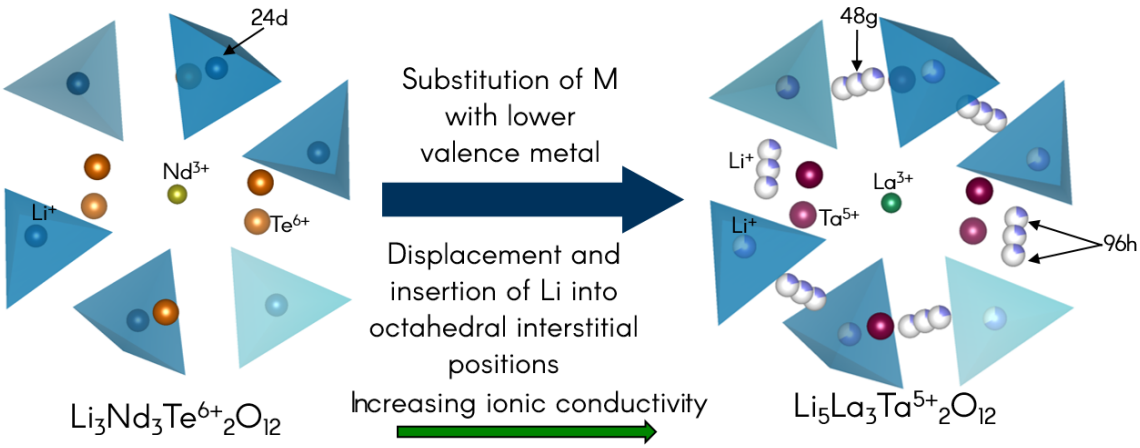

Figure 1.9: Schematic representation of the insertion of additional Li^+ within the garnet crystal structure due to replacement of Te^{6+} by Ta^{5+}. The simplified crystal structure represented is a portion of the unit cell perpendicular to the [111] direction.

It is now understood that the presence of these vacancies on the tetrahedral positions, together with the presence of Li^+ in the octahedral sites connecting two adjacent tetrahedral positions, is the main cause behind the observed increased ionic conductivities in the Li-rich compositions.[83,88–90] Cussen analysed and laid the foundations for understanding this Li^+ conduction in these Li-rich garnets in 2006.[87] In this work, he identified the octahedral sites which contain a minority Li^+ occupancy as responsible for Li^+ mobility *via* a clustering mechanism as shown in Figure 1.10 where the connectivity between these

octahedral sites gives rise to a 3-dimensionally connected Li^+ pathway.

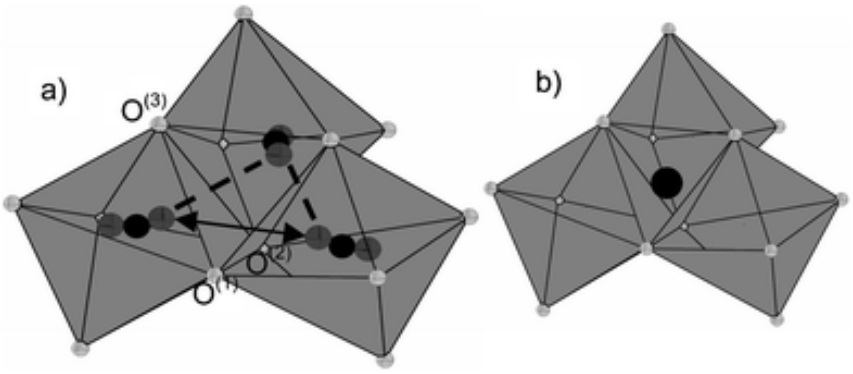

Figure 1.10: Li^+ coordination environments in $Li_5La_3Ta_2O_{12}$ show that (a) the short Li^+–Li^+ distances of 2.37(2) Å (dashed line) and 2.92(2) Å (arrow) between the displaced Li^+ cations (light grey spheres) occupying the octahedral interstices. (b) The Li^+ tetrahedral site is at the centre of four edge-shared octahedra. Reprinted with permission from The Royal Society of Chemistry.[87]

Following this trend of increasing lithium content to enhance the conduction properties, Thangadurai and Weppner reported the $Li_6ALa_2Ta_2O_{12}$ (A = Sr^{2+}, Ba^{2+}) Li-rich garnets in 2005 where an increase in the ionic conductivity of one order of magnitude, reaching the 10^{-5} S cm^{-1}, was observed.[91] Later in 2007 they also reported the $Li_7La_3Zr_2O_{12}$ garnet material with conductivities in the 10^{-4} S cm^{-1} scale, which led to this composition to become the most studied and investigated garnet in the following years to come.[92]

In theory, an upper limit of Li = 7.5 could be achieved when taking into account the high electrostatic repulsions occurring between Li^+ occupying the octahedral positions and the tetrahedral sites if the two adjacent tetrahedral positions are also occupied.[93] Experimentally, only compositions up to Li $\approx$ 7 have been achieved.[73,93] Furthermore, Li = 7 garnets are thermodynamically stable only in a tetragonal phase resulting from Li^+ ordering, as reported in 2009 by parallel studies of the Awaka and Slater groups for the $Li_7La_3Zr_2O_{12}$ and $Li_7La_3Sn_2O_{12}$ garnets respectively.[94,95] They found that Li = 7 garnets are more stable with Li^+ located in fully occupied tetragonal 8a, and octahedral 32g and 16f positions, crystallising in the tetragonal space group $I4_1/acd$ (Fig. 1.11). This Li^+ ordering, phase transformation and full occupancy of the Li^+ sites led to a dramatic decrease in the conduction properties of the garnet down to 10^{-6} S cm^{-1}.

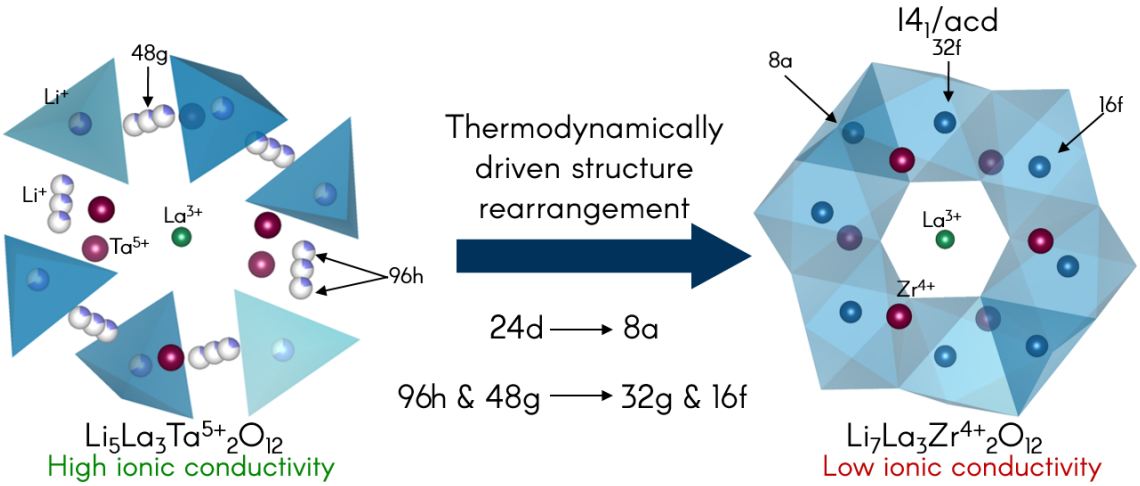

Figure 1.11: Simplified crystal structure view of the garnet structure transformation from cubic to tetragonal upon insertion of additional Li^+ due to replacement of Ta^{5+} by Zr^{4+}. The simplified crystal structure represented is a portion of the unit cell perpendicular to the [111] direction.

In 2012 it was found that Al contamination arising from the alumina crucible at high reaction temperatures led the stabilisation of the $Li_7La_3Zr_2O_{12}$ material in its cubic phase. The reason behind this was the partial replacement of Li^+ by Al^{3+} cations which then creates vacancies on the Li^+ positions, indicating the importance of the synthetic methodology employed.[96] This finding established the use of aliovalent doping in the $Li_7La_3Zr_2O_{12}$ material as a method to maximise the lithium concentration while retaining the highly-conducting cubic phase.[97–99] This doping strategy is represented in Figure 1.12:

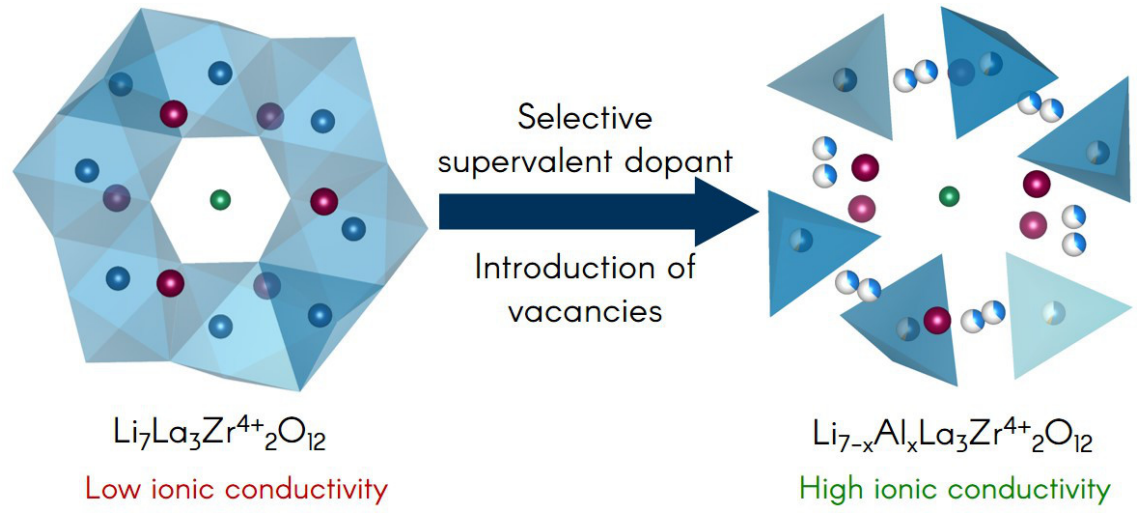

Figure 1.12: Simplified crystal structure view perpendicular to the [111] direction of the garnet structure transformation back from tetragonal to cubic phase due to the insertion of Al^{3+} into the structure which induces vacancies on the Li^+ positions.

A second strategy for aliovalent doping consists of doping the Zr^{4+} positions with another supervalent cation (M^{5+}, M^{6+}) in order to reduce the Li^+ concentration.[100–102] For example, Li *et al.* reported the $Li_{6.4}La_3Zr_{1.4}Ta_{0.6}O_{12}$ composition with an ionic conductivity

of mS cm^{-1} at room temperature.[103]

Stabilisation of the cubic phase is not the only benefit of aliovalent doping of the garnet structure on the Li^+ sites. Formation of additional Li^+ vacancies for facile diffusion of Li^+, formation of amorphous Li–$M^{2+/3+}$–O phases and enhanced grain sintering that can aid lithium diffusion between grains have also been reported.[96–98,104–106] Recent work in the group by El-Shinawi *et al.* have recently reported the synthesis of an Al-doped $Li_7La_3Zr_2O_{12}$ garnet material where the presence of Al_2O_3 nanosheets in the precursors allowed stabilisation of the cubic phase and enhanced sintering with low activation energy for ionic diffusion of 0.27 eV.[104]

To summarise this section, Figure 1.13 shows the relationship between the lithium content per formula unit of garnet and the ionic conductivity. It is clear that compositions from Li = 5.5 to Li = 6.5 possess the highest ionic conductivities and a dramatic decrease at Li = 7 is found as consequence of the phase transformation.[93]

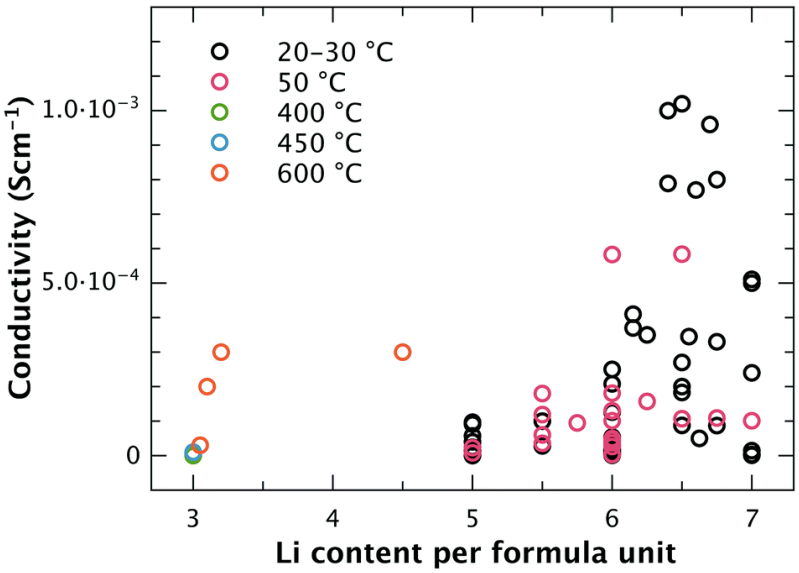

Figure 1.13: Ionic conductivities of lithium garnet materials as function of the Li^+ concentration per formula unit as reported in the literature. Reproduced with permission from The Royal Society of Chemistry.[93]

1.2.2 Novel Li-rich complex oxides

Lithium garnets materials are an excellent example of how the introduction of additional Li^+ in complex oxide structures over their conventional stoichiometry can enhance their ionic conduction properties. This is a recurrent methodology employed in the literature to overcome high energy barriers for ionic diffusion that hinder Li^+ conduction through the oxide crystal framework.[73,107–109]

The solid-state diffusion of ionic species in inorganic electrolytes is governed by the presence of interstitials and vacancies on the crystal lattice. The energy required for mobile ions to diffuse is the activation energy (E_a) and is determined by the balance

between the ion migration energy and the defect formation energy when the ion hops.[110]

Additional Li^+ in the crystal structure can be located in interstitial sites which can then enable new pathways for ionic diffusion, connecting Li^+ sites that otherwise would be at to great distance to be energetically favourable to hop at typical operating temperatures. In addition, the introduction of Li^+ can also introduce additional repulsive forces between adjacent Li^+ enhancing their mobility by increasing their initial energy which results in a lower energy barrier for their diffusion.

The ionic conductivity of a solid can be expressed by the Nernst-Einstein equation (Eq. 1.4), where n_i is the charge carrier concentration, Z_i is the charge of the mobile ion and μ_i is the mobility of the ionic charge carrier i:

$$\sigma = \sum_i n_i Z_i \mu_i \tag{1.4}$$

From Equation 1.4, it can be seen that increasing the number of mobile Li^+ would enhance the conduction properties of the solid electrolyte. However, the reader is advised that while this is generally the case for moderate increments of charge carrier concentrations, specific structural arrangements or a high increase of charge carriers must be taken into account as this could result in different ionic transport mechanisms and hence may differ from this generalisation.

A common strategy to introduce additional lithium is by atomic substitution of other metals present in the electrolyte crystal structure with lower valance cations which can be compensated by additional Li^+ in the framework, similar to the garnet materials.

In the case of the anode, the Li-rich vanadate $Li_{1+x}V_{1-x}O_2$ was reported by Islam and co-workers to experience an increase in the diffusion properties of Li^+ due to the insertion of additional Li^+ in the VO_6 layers which also enables the intercalation mechanism of the material at low voltages.[107,108] With respect to the cathode side, the group of Gerbrand Ceder reported in 2015 the improved capacity retention at high cycling rates of the $Li_xNi_{2-4x/3}Sb_{x/3}O_2$ (x = 1.00 – 1.15) cathode material by introducing a Li excess.[111] They found a complex nanostructure pattern of Li-Sb and Ni-Sb ordering where the interface between these domains form the correct local configuration for good lithium mobility. They also found that <1 nm Li-Sb stripe domains and their interfaces effectively act as nanohighways for lithium diffusion. In addition to lithium-rich garnets, lithium excess has also been explored in other solid electrolytes. Zhao and Daemen reported the Li-containing anti-perovskite (Li_3OX, where X = halide) as a new family of superionic solid electrolytes with ionic conductivities above the mS cm^{-1} range and low activation energies of 0.2 eV.[109] Later in 2015 Mouta *et al.* reported the insertion of interstitial Li^+ as effective charge carriers in lithium-rich antiperovskites ($Li_{3+x}O_{1+x}Cl_{1-x}$) to enhance the transport properties.[112] Another example of lithium excess in solid electrolytes was studied by the Ceder group for the $Li_{1+2x}Zn_{1-x}PS_4$ materials by DFT methods. They reported the introduction of extrinsic defects offers a lower energy barrier for cooperative

Li^+ migration and that an increase in the number of Li^+ allows lower energy percolation pathways.[113] These computationally predicted beneficial effects of lithium excess in the $LiZnPS_4$ material have been recently proved experimentally by the Nazar group, where an increase of more than 4 orders of magnitude in the ionic conductivity up to 10^{-4} S cm^{-1} were obtained compared to that of the parent $LiZnPS_4$ phase.[114] Tarascon and co-workers have also recently reported the improved ionic conductivity of the Mg-doped $Li_{2.2}SnMg_{0.1}O_3$ material compared to undoped Li_2SnO_3 where activation energies can be lowered from 0.90 to 0.70 eV due to the introduction of new activated Li^+ sites for ionic diffusion (Figure 1.14).[115]

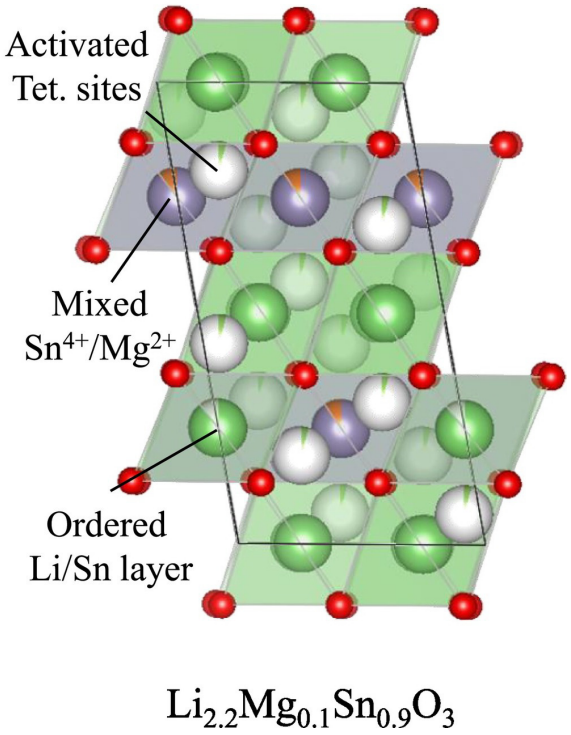

Figure 1.14: Structural model for the Mg^{2+} doped Li_2SnO_3 phase where the addition of Mg^{2+} ions produces the insertion of lithium excess on interstitial tetrahedral sites. Li^+ is displayed in green, Sn^{4+} in grey, Mg^{2+} in orange and O^{2-} in red. Adapted with permission from Elsevier.[115]

In light of the positive effects of lithium excess in battery materials, two new families of Li-rich complex oxides have been explored in the present thesis.

Li-rich $Li_6Hf_2O_7$

Lithium-rich garnet materials have excellent ionic conduction properties. However, the presence of three metals in their crystal structures, including heavy lanthanide cations, increase considerably the molecular weight of these garnets materials, usually above 800 g mol^{-1}. This may restrict their implementation in certain applications where weight is a primary design parameter.[116] Ideally, crystal structures with only one redox-stable metal cation to maintain the structure during Li^+ diffusion, would optimise the weight of the solid

electrolyte. In this regard, Ta^{5+}, Nb^{5+}, Sb^{5+} and Zr^{4+} d^0–redox stable containing ternary oxides have been widely studied in the past.[73,117,118] On the other hand, a search on the ICSD crystallographic database for ternary oxides with Li^+ and the redox-stable Hf^{4+} does not yield any results. A deep look in the literature, however, produces a few results of crystal structures of ternary oxides containing these two elements.

The Li_2HfO_3 with the monoclinic structure crystallising in the $C2/c$ space group was first reported in 1969[119] by Dittrich and Hoppe. In the same year, the Li_8HfO_6 was also reported by Hauck,[120] where in this case the material crystallises in a rhombohedral $R\bar{3}$ space group.

These materials were not investigated as solid-state electrolytes until the early 1980's. Brice and Ramdani studied Li_8HfO_6, reporting an ionic conductivity of 10^{-10} S cm^{-1} at room temperature with an activation energy of 0.67 eV.[121] The conductivity of the Li_2HfO_3 had also not been studied until recently when Buzlokov *et al.* reported in 2016 two different types of Li^+ motion in the material and an activation energy of 1.0 eV, as obtained from NMR measurements.[122]

The third known compound to complete the Li-Hf-O materials family is $Li_6Hf_2O_7$. The $Li_6M_2O_7$ (M = Zr^{4+}, Hf^{4+}) structure was reported for the first (and only time for M = Hf^{4+}) in 1993 in parallel by three independent research groups where no refined atomic param-

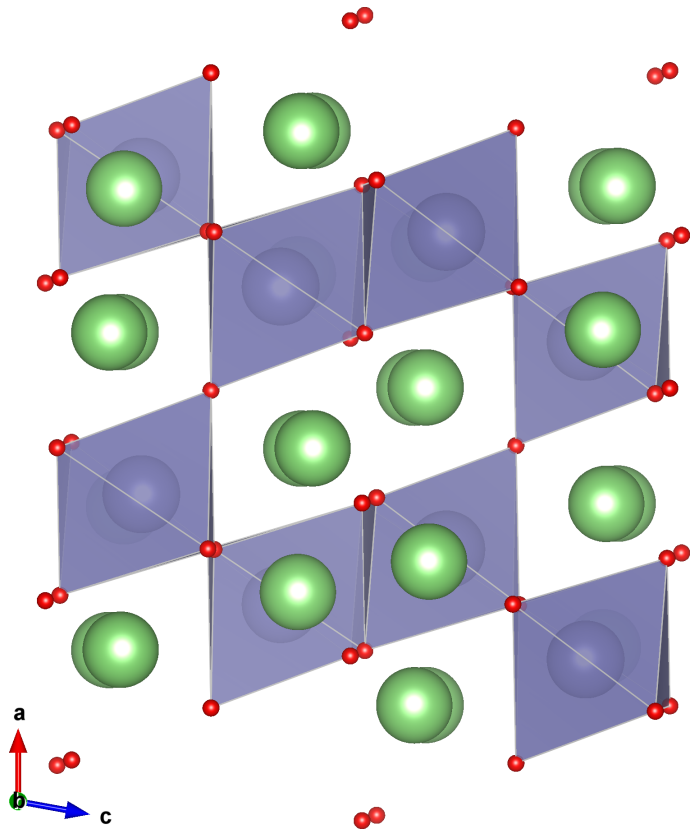

Figure 1.15: Crystal structure of the $Li_6Zr_2O_7$ material with $C2/c$ space group of symmetry. Li^+ are shown in green, O^{2-} anions are shown in red and Zr^{4+} are shown in blue with their octahedral coordination environment explicitly shown.

eters were provided for the $Li_6Hf_2O_7$ material.[123–125] While for the Li_2HfO_3 and Li_8HfO_6 materials there are complete studies of their ionic conduction properties, for the $Li_6Hf_2O_7$ material these were merely analysed by NMR at two different temperatures without any quantitative analysis.

The reported structure of the isostructural $Li_6Zr_2O_7$ material is shown in Figure 1.15. The material crystallises in a *C*2/*c* space group where Zr^{4+} are octahedrally coordinated and Li^+ occupy square-pyramidal sites forming pairs of one-dimensional chains. These chains of Li^+ along the *b*-axis could provide one-dimensional Li^+ conduction similar to the Li(Fe/Mn/Co/Ni)PO_4 olivine materials.[126]

The conduction properties of $Li_6Zr_2O_7$ have been reported in the literature and increases in the ionic conductivity have been achieved by Li^+ vacancy creation as demonstrated by Rao *et al.* in 2012.[127] They also analysed possible interstitial sites by a bond valence approach, where Li^+ could reside during diffusion (Fig. 1.16). One year after Rao's work, Liao *et al.* further optimised the conduction properties of this material by adding interstitial Li^+ to the crystal structure *via* aliovalent doping on the Zr^{4+} sites.[128] They found a decrease in the activation energy for ionic conduction from 0.84 to 0.67 eV and an increase in the ionic conductivity of two orders of magnitude from 10^{-4} to 10^{-6} S cm^{-1} at 300 °C.

More recently, this $Li_6Zr_2O_7$ material has been synthesised in nanofiber form by use of electrospinning techniques[129] and the adsorption properties has also been examined showing good performance for CO_2 gas capture[130–132] extending interest in this structure beyond its ability as an ionic conductor.

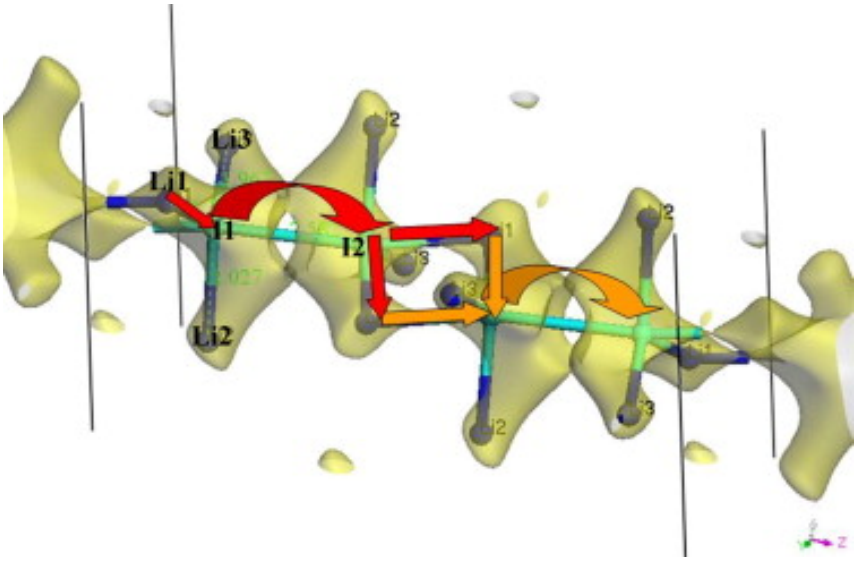

Figure 1.16: Li^+ transport pathway in $Li_6Zr_2O_7$ as calculated by Rao *et al.* where the thick lines with arrows are showing the direction of Li-ion transport. Reprinted with permission from Elsevier.[127]

Li-rich double perovskites

Oxide perovskite materials are versatile materials with an impressive range of applications due to their exotic physical properties including ferroelectric, dielectric, pyroelectric, and piezoelectric behaviours.[133] This versatility is due to the robust framework which also allows multiple combinations of different cations and anions present within the perovskite structure. The ideal cubic ABO_3 perovskite crystallises in the $Pm\bar{3}m$ space group, where metal cations A are 12-fold oxygen coordinated and the B cation is octahedrally coordinated by 6 oxygen atoms.[134] Lower-symmetry structures can be also produced by variations in the relative sizes of the A and B cations.[135] Despite the multiple applications of perovskite materials, their use in lithium-ion batteries has been very limited only with a few compounds for this purpose, namely the lithium lanthanum titanate, $Li_{3x}La_{0.67\text{-}x}TiO_3$, as a fast lithium conductor and the lithium niobiate, $LiNbO_3$, as an insertion electrode.[136,137]

The study of lithium conduction in perovskite materials goes back to 1984 when Latie *et al.* investigated the transport properties of the $Li_xLn_{0.33}Nb_{1-x}Ti_xO_3$ (Ln = La, Nd) solid-solution, with activation energies in the 0.42 - 0.55 eV range.[138] In 1993 Inaguma *et al.* studied the ionic conductivity in the $Li_{3x}La_{0.67\text{-}x}TiO_3$ series, where ionic conductivities in the mS cm^{-1} and activation energies below 0.4 eV were achieved.[139] The reason for this high ionic conductivity is based on the Li^+ sitting in the large 12-fold coordinated A-sites where they are far away from the closest oxygens and tend to displace toward the faces of the dodecahedral A-sites forming a square planar coordination. This unusual Li^+ coordination results in a high mobility of these Li^+ in the perovskite framework.[137]

It has been more than 25 years since the Inaguma work and many attempts to further increase the conductivity have been attempted, including stoichiometry tailoring, doping with other elements and producing layered structure perovskites. However, the mS cm^{-1} range reached by Inaguma has not been surpassed as yet.[118,140–142] Despite the high intra-grain conductivity of this perovskite being almost as good as current liquid electrolytes, the high inter-grain boundary resistances together with reduction of Ti^{4+} at low voltages *vs.* Li have precluded its utilisation as a solid electrolyte in Li-metal batteries.[137,143]

In this regard other perovskite compounds with different metals on the B-site have been explored in recent years. For example, Thangadurai and Weppner reported the successful synthesis of the $LiSr_{1.65}B_{1.3}B'_{1.7}O_9$ (B = Ti, Zr; B'= Nb, Ta) series where titanium was replaced by more redox-stable cations.[117] The downside of this strategy was the drop of at least two orders of magnitude in the ionic conductivity to 10^{-5} S cm^{-1}, compared to the original material.

An unexplored system until recently is the lithium-containing double perovskite family.[144] Introduction of a second cation on the B-site in the perovskite structure can produce complex structures. In the case of rock salt-type ordering between these two cations on the B-site along the perovskite framework, the lattice parameter doubles giving rise to the

so-called double perovskite structure. Double perovskite materials can crystallise in the cubic system but also may present distortions related to the different A/B relative atomic sizes ratio which forces the B-site octahedra to tilt in order to lower the energy of the structure.[145]

For double perovskites containing Li^{+} in the B-site and La^{3+} on the A-site, the other cations in B sites to complete the La_2LiMO_6 stoichiometry reported in the literature include Nb^{5+}, Mo^{5+}, Sb^{5+}, Ru^{5+}, Re^{5+} or Os^{5+}.[146–148] In all of these compounds, the relatively small size of the La^{3+} cations compared to the A-site void produced by the LiO_6 and MO_6 octahedra network results in the inclination and rotation of these octahedra towards the La^{3+}, producing a monoclinic symmetry of the crystal structure. A representation of this distortion from the cubic symmetry is shown in Figure 1.17, where the tilting of the B-site octahedra is clearly visible. Unlikely the $Li_{3x}La_{0.67-x}TiO_3$ materials, in these lithium-containing double perovskites the Li^{+} are located at the B-sites where they have a more stable coordination environment and thus no outstanding ionic conductivity has been reported for these materials.

Recently, and in parallel with the realisation of this thesis, a new Li-contain double perovskite, $Li_{1.5}La_{1.5}WO_6$, has been reported by Rosseinsky group.[144] In this novel

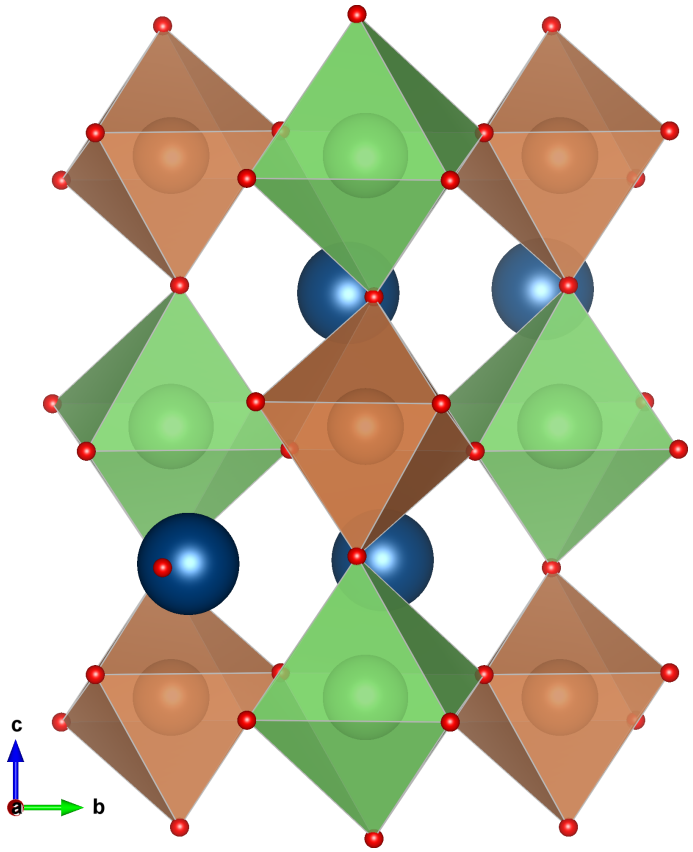

Figure 1.17: Crystallographic representation of the La_2LiMO_6 structure with monoclinic symmetry $P2_1/n$ where the M^{5+} cations are represented in brown, La^{3+} ions in dark blue, Li^{+} in green and finally O^{2-} anions are represented in red.

lithium-containing double perovskite, A-sites are not fully occupied by La^{3+} ions and Li^+ are located in both A- and B-sites. The presence of Li^+ back in the A-sites enables lithium conduction in the material, and Rosseinsky and co-workers have proposed this $Li_{1.5}La_{1.5}WO_6$ double perovskite as a solid electrolyte.

The studies carried out in this thesis show that the $Li_{1.5}La_{1.5}WO_6$ material undergoes reduction at low voltages *vs.* metallic lithium and that can reversibly intercalate Li^+, hence making it a good candidate as a negative electrode for Li-ion batteries. In order to find a the more redox-stable material, W^{6+} ions can be replaced by Te^{6+} ions leading to a solid electrolyte in this case.

This versatility for battery applications of this novel lithium-rich double perovskite structure suggests a promising future for this class of materials. For example, the use of electrode and solid electrolyte materials with similar crystal structures in the search for a lattice-matching system was proposed by Thackeray and Goodenough in the past, and it has been revisited recently by the Wilkening group, as a possible solution to alleviate interfacial resistances to Li diffusion between electrode and solid electrolyte (Fig. 1.18).[149,150]

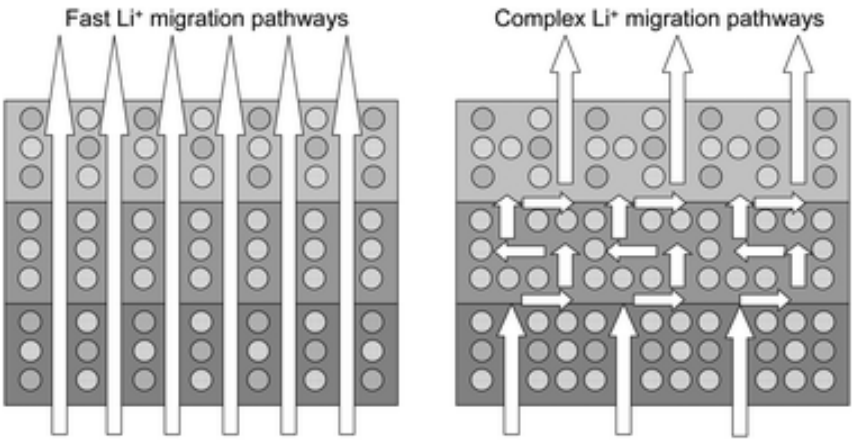

Figure 1.18: Schematic representation of a lattice-matching solid-state battery. Materials with the same crystal structure and similar lattice parameters (left) would display lower interfacial resistances and faster ionic transport through the device compared to a battery with complex electrode-electrolyte interfaces (right). Reproduced with permission from The Royal Society of Chemistry.[149]

1.2.3 Anode materials for all-solid-state batteries

The idea above of lattice-matching electrode and electrolyte materials highlights that the transitions towards all-solid-state batteries doesn't end by replacing the liquid electrolyte by a solid material. It is also important to take into account the volume changes experienced by the electrode materials during battery cycling as solid materials can't accommodate and cope with large volume expansions as well as liquid media. While most of the cathodes materials typically employed in lithium-ion batteries undergo small volume

changes during cycling, current graphitic anodes can expand by over 10% during lithiation.[151,152]

The ideal anode material, lithium metal, is still not fully compatible with most solid-electrolytes and thus the search for novel anode materials has gained great attention by the research community recently. Novel conversion metal oxides and alloys compounds as negative electrodes such as Si or Sn have been proposed as alternatives to lithium metal, promising large gravimetric capacities above 4000 mAh g^{-1}. However, these novel anode systems experience extreme capacity losses due to deleterious particle cracking and volume changes (Figure 1.19), in some cases over 400%.[153,154]

Alternative insertion electrodes are more limited, with the $Li_4Ti_5O_{12}$ spinel being the most widely studied material due to its virtually zero expansion upon lithiation. Unfortunately this material possesses a high intercalation voltage for an anode at around 1.5 V, which results in a decrease of energy density in a full cell.[155] There remains a need to find novel insertion negative electrodes which exhibit low volume expansion and low intercalation voltages, a space where the above mentioned $Li_{1.5}La_{1.5}WO_6$ could have its place.

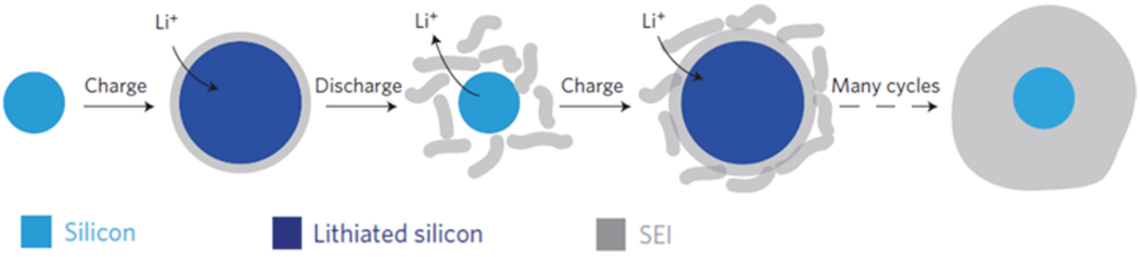

Figure 1.19: Schematic of SEI formation and cracking, and volume expansion on a silicon anode during cycling. Reproduced with permission from Nature Publishing Group. Copyright 2012.[154]

1.3 Synthetic methodologies to battery materials

The synthetic methodology employed for the preparation of battery materials is key in defining their resulting properties. Different methodologies are employed across the battery research community in order to obtain the desired materials depending on the specific requirements, including solid-state chemistry, sol-gel, solvothermal, mechanochemistry, spray pyrolysis, co-precipitation, and many others.[156,157]

Solid-state chemistry has been one of the preferred synthetic pathways for inorganic materials in the past due to its simplicity. The procedure usually requires intimate mixing of the starting materials and heating in a furnace for reaction to occur.[158] This simple methodology has some disadvantages such as the use of high temperatures and prolonged heating times to overcome mass transport limitations in the solid state. In the case of the synthesis of lithium-containing garnets by pure solid-state chemistry, it has led to the report of imprecise stoichiometries to obtain the highly conductive cubic $Li_7La_3Zr_2O_{12}$ garnet, which resulted from indirect Al contamination from reaction with the alumina cru-

cibles at high temperatures for prolonged times. In addition, for the synthesis of any lithium containing materials, special precaution needs to be taken into account in order to avoid lithium evaporation occurring at high temperatures.[73,92,96]

These issues have given rise to the search for improved solid-state methodologies for the synthesis of battery materials. One of these modifications to the solid-state method is the use of microwave irradiation to accelerate the reaction kinetics.

1.3.1 Microwave-assisted solid-state chemistry

Microwave-assisted solid-state chemistry, also denominated as microwave hybrid heating, involves the of microwave radiation to induce intrinsic heating in the precursor materials as well as heating by external conventional processes. Microwave radiation is a form of electromagnetic energy in the frequency range of 300 MHz to 300 GHz, *i.e.* wavelengths ranging from 1 mm to 1 m. The most commonly used frequencies for microwave heating purposes are 915 MHz and 2.45 GHz, which are derived from electrical energy with a transformation efficiency of about 85% and 50%, respectively.[159,160]

The efficient absorption of microwaves by the precursor materials is related to their dielectric interaction with microwaves. This dielectric interaction can be described primarily by the absorbed power function,[160,161] which is described in Equation 1.5:

$$P = \sigma |E|^2 = 2\pi f \varepsilon_0 \varepsilon''_{\text{eff}} |E|^2 = 2\pi f \varepsilon_0 \varepsilon'_r \tan\delta |E|^2 \tag{1.5}$$

where σ is the total effective conductivity, E is the magnitude of the internal electric field, f is the microwave frequency, ε_0 is the permittivity of free space, $\varepsilon"_{eff}$ is the relative effective dielectric loss factor, ε'_r is the relative dielectric constant and $\tan\delta$ is the loss tangent.

The loss tangent indicates the ability of the material to be polarised, and thus heated, by the microwave radiation and can be described as follows (Eq. 1.6):

$$\tan\delta = \frac{\varepsilon"}{\varepsilon'} \tag{1.6}$$

where ε' is the permittivity of the material and $\varepsilon"$ is the loss factor.

The major difference between microwave and conventional solid-state synthesis is the heating mechanism. In the case of conventional heating, heat is transferred *via* radiation, conduction and convection mechanisms from the heating elements, normally high resistances which convert electrical current to dissipated heat. In the case of microwave heating, the precursor materials absorb the microwave radiation themselves, transforming it into heat within their bodies. This, together with the higher penetration of microwave radiation, allows shortening of reaction times and intermediate mixing of the materials for homogeneity. Figure 1.20 shows the temperature gradient within a heated material by both mechanisms separately and by their combination.

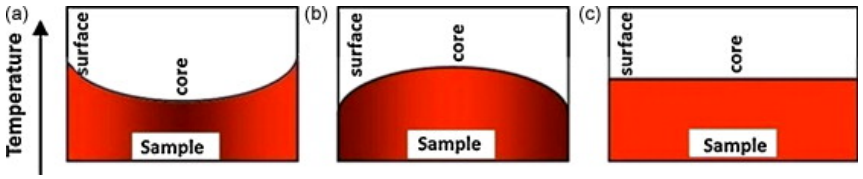

Figure 1.20: Temperature profile within a pelletised sample under conventional heating (a), microwave heating (b) and microwave hybrid heating (c). Reprinted with permission from Elsevier.[160]

When applying conventional heating alone, the surface of the material normally heats faster leaving the core isolated, specially in the case of oxide precursors with poor thermal conductivities. On the other hand, using pure microwave heating, the opposite situation occurs with an overheated core.[162] Ideally, a combination of both mechanisms could provide more homogeneous heating across the entire material aggregate. Furthermore, most microwave syntheses are based on the use of commercially available low-frequency (2.45 GHz) microwave magnetrons which don't couple efficiently with a wide range of materials at low temperatures.[163] The use of hybrid heating can provide the initial heating of the precursor materials by conventional heating to reach an optimum temperature where the materials can effectively couple with the microwave irradiation.

Most binary oxide materials exhibit high dielectric loss tangents at microwave frequencies, which facilitates the synthesis of ternary or quaternary oxides.[164] If the materials cannot couple effectively to the microwave radiation, the use of susceptors can also being employed. An ideal susceptor is a material that can couple strongly with microwave radiation and is unreactive towards the materials involved in the synthesis. The susceptor is intimately mixed with the precursor materials emitting and transferring heat produced from its coupling with the microwaves to the surrounding reactants. Commonly used susceptors includes silicon carbide, carbon or copper monoxide. Another route to optimise the coupling with the microwave radiation with the precursors is the use of single-mode cavities where the microwave radiation is concentrated at a point, in contrast with multimode cavities where microwave radiation is distributed randomly across the entire cavity, producing cold and hot spots.[164]

Examples of oxide materials for battery applications synthesised through microwave-assisted solid-state synthesis include the superionic lithium conductor $Li_{0.35}La_{0.55}TiO_3$ perovskite,[165] the high capacity LiV_3O_8 cathode material[166] or the $NaZr_2(PO_4)_3$ NASICON sodium ionic conductor.[164]

The milder conditions required for the synthesis of ceramic materials through the use of microwave radiation have led to the widespread use of this synthetic methodology in recent years and it is expected to play a key role in future synthetic avenues where energy efficiency is crucial.

1.3.2 Sol-gel synthesis

The search for even more energy efficient synthetic methods than solid-state based approaches has promoted the use of low temperature solution-based synthetic routes for the preparation of inorganic materials. One of the most successfully employed low temperature methodologies for the preparation of oxide battery materials has been the use of sol-gel chemistry. Sol-gel chemistry provides a high homogeneity of the precursor materials and allows for tailoring of the particle morphology. In addition, the high processability of the sols and gels into powders, fibres, ceramics and coatings has promoted its use.[167]

Sol-gel chemistry of inorganic materials consists in the hydrolysis of precursor materials to form a colloidal suspension (sol) which is then transformed into a non-fluid 3D network (gel). Additionally, a last step can also be included to convert the solvent-filled gel into a dry solid, depending on the desired final application of the prepared material.[168] A schematic representation of the sol-gel process and the different pathways to follow depending the final application is shown in Figure 1.21.

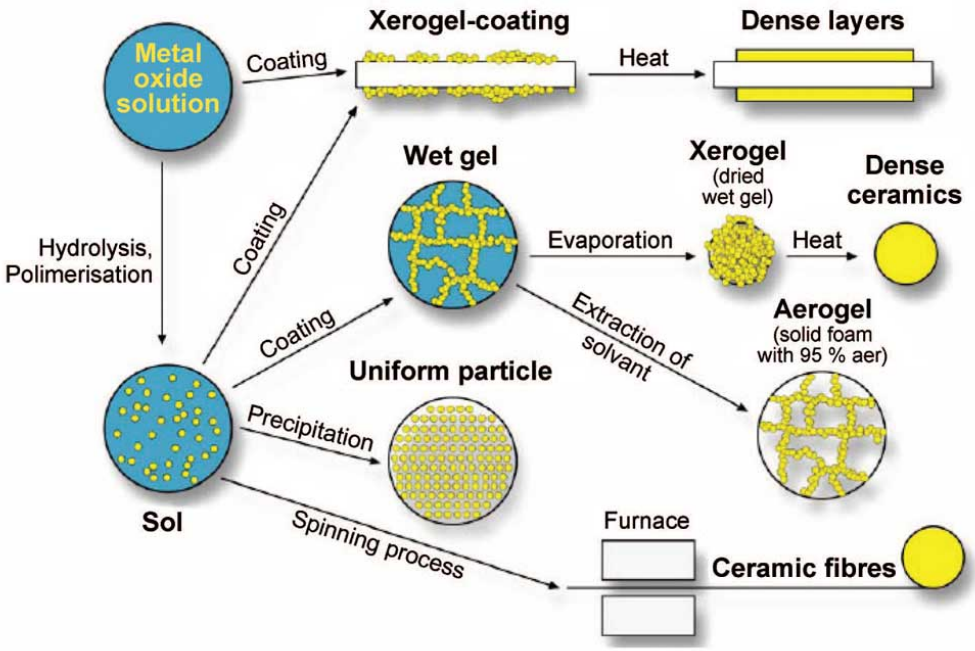

Figure 1.21: Schematic representation of the sol-gel methodology for oxide materials with the different steps during the process. The high processability of the sol allows for different applications and obtaining different types of gels. Figure credit: Universität Ulm, Anorganische Chemie.

Specifically for the preparation of oxide materials, the citrate sol-gel method has been particularly employed. The use of metal precursors can lead to quick precipitation of the metal complexes into binary metal oxides, precluding the formation of the sol.[169,170] Addition of a chelating agent to the precursor solution can avoid this oxide precipitation by chelating the metal ions/complexes in the sol. Citric acid is a weak triprotic organic acid with three carboxylic groups that can dissociate and then chelate metal ions. Com-

mon water-soluble metal precursors include hydroxides and nitrates. If metal nitrates are available, their use can also enable faster removal of the organic matter at the end of the process by self-propagating combustion where the nitrate acts as the oxidant and the citrate as the organic fuel.[171]

In the case of the garnet materials, the sol-gel methodology was successfully applied for the first time in 2010 when Gao *et al.* prepared the $Li_5La_3Ta_2O_{12}$ garnet material with a particle size of 100–200 nm at temperatures nearly 250 °C lower than conventional solid-state reactions.[172] The following year, Kokal *et al.* reported the synthesis of the cubic phase of the undoped $Li_7La_3Zr_2O_{12}$ garnet at temperature as low as 700 °C and 5 hours on the calcination step.[173] This represented a dramatic softening of the calcination conditions as the stabilisation of the high ionic conducting cubic phase for the LLZO family traditionally requires the use of high temperatures (above 1100 °C), prolonged ball milling and sintering times, and introduction of dopants by conventional solid-state chemistry.[73]

The use of this solution-based approach has led to the development of novel nanostructured lithium garnet materials, thin film depositions, electrospinning treatments and even core-shell structures.[174] However, the lack of reproducibility, poor stability at high temperatures, lower performance of the materials and an unclear understanding of the undoped cubic phase at low temperature have limited the widespread uptake of this synthetic methodology for high performance applications where good inter-grain conductivity is required. This opens a new avenue for research which is starting to be explored in the last few years to unveil the effect of different parameters, such as the synthetic atmosphere used, precursors employed or temperature evolution, on the properties of the sol-gel prepared cubic LLZO materials.[175–178]

1.4 Summary of main aims and objectives

The work carried out in this thesis aims to develop novel Li-rich complex oxides and to fully characterise these materials with a view to their applications in all-solid-state Li batteries.

The use of microwaves to assist the solid-state synthesis of lithium garnet materials was explored to provide an energy efficient, less aggressive and a more reliable synthetic route to complex oxides, as required for industrial commercialisation of battery materials. This work also aims to unveil the phenomena underpinning the functional properties in the LLZO garnet when synthesised by sol-gel chemistry and the effect and location of dopants within the LBLTO structure. By introducing Li-excess through aliovalent doping in $Li_6Hf_2O_7$ and designing novel Li-rich complex oxides, it was hoped that the material transport properties could be optimised as required for the use of materials for solid-state electrolytes.

The use of conventional diffraction, spectroscopic and electrochemical techniques in conjunction with the application of advanced synchrotron-based techniques to explore the

local ionic diffusion properties (μ^+SR), ascertain the local structure arrangements (XAS) and analyse phase formation *in-situ* (NPD) was expected to yield a broad picture of the material properties across multiple length scales.

The possibility of applying the synthetic strategies used for the discovery of these novel Li-rich complex oxides to obtain Na-rich versions also motivated part of this thesis work to provide new materials for Na batteries, extending the reach of the work in this thesis beyond lithium battery chemistry.

In summary, the successful realisation of this project was expected to provide an enhanced approach for the solid state synthesis of the Li-rich complex oxides, the understanding of their properties at the macro and local scale and producing novel materials with battery applications.

References

[1] A. Hobson, *Phys. Teach.*, 2004, **42**, 260–260.

[2] R. L. Lehrman, *Phys. Teach.*, 1973, **11**, 15–18.

[3] W. H. Wiser, *Energy Concepts, Forms, Laws*, Springer, New York, 2000, pp. 1–19.

[4] B. Dunn, H. Kamath and J. M. Tarascon, *Science*, 2011, **334**, 928–935.

[5] J. P. Barton and D. G. Infield, *IEEE Trans. Energy Conversion*, 2004, **19**, 441–448.

[6] A. Volta, *Ann. Chim.*, 1801, **40**, 225–256.

[7] J. F. Daniell, *Philos. Trans. R. Soc. Lond.*, 1836, **126**, 107–124.

[8] G. Leclanché, *Pile au peroxide de manganèse à seul liquide*, Les Mondes, 1866.

[9] G. Planté, *Nouvelle pile secondaire d'une grande puissance*, Mallet-Bachelier, Paris, 1860.

[10] K. Beccu, *Negative electrode of titanium-nickel alloy hydride phases*, 1972, https://patents.google.com/patent/US3824131.

[11] M. S. Whittingham, *Science*, 1976, **192**, 1126–1127.

[12] J. M. Tarascon and M. Armand, *Cah. Rev. The.*, 2001, **414**, 359–367.

[13] M. Kotobuki, *Open Electrochem. J.*, 2012, **4**, 28–35.

[14] X. B. Cheng, R. Zhang, C.-Z. Zhao and Q. Zhang, *Chem. Rev.*, 2017, **117**, 10403–10473.

[15] C. X. Zu and H. Li, *Energy Environ. Sci.*, 2011, **4**, 2614.

[16] L. Lu, X. Han, J. Li, J. Hua and M. Ouyang, *J. Power Sources*, 2013, **226**, 272–288.

[17] J. B. Goodenough and K.-S. Park, *J. Am. Chem. Soc.*, 2013, **135**, 1167–1176.

[18] R. Huggins, *Solid State Ionics*, 2000, **136-137**, 1321–1328.

[19] Y. Yoon, S. Lee, S. Cho and S. Nam, *J. Electrochem. Soc.*, 2011, **158**, A1313–A1319.

[20] J. Zhang, B. Sun, X. Huang, S. Chen and G. Wang, *Sci. Rep.*, 2014, **4**, 6007.

[21] Q. Li, J. Chen, L. Fan, X. Kong and Y. Lu, *Green Energy & Environment*, 2016, **1**, 18–42.

[22] X. Zhang, R. Kostecki, T. J. Richardson, J. K. Pugh and P. N. Ross, *J. Electrochem. Soc.*, 2001, **148**, A1341.

[23] J. G. Zhang, W. Xu and W. A. Henderson, *Lithium Metal Anodes and Rechargeable Lithium Metal Batteries*, Springer International Publishing, 2017.

[24] R. Fong, *J. Electrochem. Soc.*, 1990, **137**, 2009.

[25] P. Verma, P. Maire and P. Novák, *Electrochim. Acta*, 2010, **55**, 6332–6341.

[26] E. Peled, *J. Electrochem. Soc.*, 1979, **126**, 2047.

[27] D. Aurbach, *J. Electrochem. Soc.*, 1996, **143**, 3809.

[28] P. B. Balbuena and Y. Wang, *Lithium-Ion Batteries*, Imperial College Press, London, 2004.

[29] A. Chagnes and J. Swiatowsk, *Electrolyte and Solid-Electrolyte Interphase Layer in Lithium-Ion Batteries*, InTech, London, 2012.

[30] J. O. Besenhard, M. Winter, J. Yang and W. Biberacher, *J. Power Sources*, 1995, **54**, 228–231.

[31] D. Aurbach, B. Markovsky, G. Salitra, E. Markevich, Y. Talyossef, M. Koltypin, L. Nazar, B. Ellis and D. Kovacheva, *J. Power Sources*, 2007, **165**, 491–499.

[32] D. Aurbach, Y. Talyosef, B. Markovsky, E. Markevich, E. Zinigrad, L. Asraf, J. S. Gnanaraj and H.-J. Kim, *Electrochim. Acta*, 2004, **50**, 247–254.

[33] A. Wuersig, W. Scheifele and P. Novák, *J. Electrochem. Soc.*, 2007, **154**, A449.

[34] W. Kong, H. Li, X. Huang and L. Chen, *J. Power Sources*, 2005, **142**, 285–291.

[35] N. Kumar, K. Leung and D. J. Siegel, *J. Electrochem. Soc.*, 2014, **161**, E3059–E3065.

[36] Q. Zhong, A. Bonakdarpour, M. Zhang, Y. Gao and J. R. Dahn, *J. Electrochem. Soc.*, 1997, **144**, 205–213.

[37] S. Patoux, L. Daniel, C. Bourbon, H. Lignier, C. Pagano, F. L. Cras, S. Jouanneau and S. Martinet, *J. Power Sources*, 2009, **189**, 344–352.

[38] A. Iturrondobeitia, A. Goni, I. G. de Muro, L. Lezama, C. Kim, M. Doeff, J. Cabana and T. Rojo, *Inorg. Chem.*, 2015, **54**, 2671–2678.

[39] K. Amine, *ECS Solid State Lett.*, 1999, **3**, 178.

[40] M. B. Bechir, A. B. Rhaiem and K. Guidara, *B. Mater. Sci.*, 2014, **37**, 473–480.

[41] J. Wolfenstine and J. Allen, *J. Power Sources*, 2004, **136**, 150–153.

[42] J. Wolfenstine and J. Allen, *J. Power Sources*, 2005, **142**, 389–390.

[43] S. Popa, S. Iliescu, G. Ilia, N. Plesu, A. Popa, A. Visa and L. Macarie, *Eur. Polym. J.*, 2017, **94**, 286–298.

[44] B. Scrosati, *Lithium Polymer Electrolytes*, Springer, New York, 2002, pp. 251–266.

[45] B. Scrosati and C. A. Vincent, *Mrs Bull.*, 2000, **25**, 28–30.

[46] A. M. Stephan, *Eur. Polym. J.*, 2006, **42**, 21–42.

[47] A. M. Stephan and K. S. Nahm, *Polymer*, 2006, **47**, 5952–5964.

[48] A. M. Stephan, *Nanocomposite Polymer Electrolytes For Lithium Batteries*, Brill Academic Publishers, Leiden, pp. 455–482.

[49] L.-Z. Huang, Z.-Y. Wen, J. Jin and Y. Liu, *J. Inorg. Mater.*, 2012, **27**, 249–252.

[50] E. M. Masoud, *Polym. Test.*, 2016, **56**, 65–73.

[51] P. Pradeepa, S. Edwinraj, G. Sowmya, J. Kalaiselvimary, K. Selvakumar and M. R. Prabhu, *AIP Conf. Proc.*, 2016.

[52] L. Yang, Z. Wang, Y. Feng, R. Tan, Y. Zuo, R. Gao, Y. Zhao, L. Han, Z. Wang and F. Pan, *Adv. Energy Mater.*, 2017, **7**, 1701437.

[53] J. K. Ahn and S.-G. Yoon, *ECS Solid State Lett.*, 2005, **8**, A75.

[54] S. Boulineau, J. M. Tarascon, J. B. Leriche and V. Viallet, *Solid State Ionics*, 2013, **242**, 45–48.

[55] M. Chen and S. Adams, *J. Solid State Electr.*, 2015, **19**, 697–702.

[56] E. Kartini and M. Manawan, *AIP Conf. Proc.*, 2016.

[57] J. E. Trevey, J. R. Gilsdorf, S. W. Miller and S.-H. Lee, *Solid State Ionics*, 2012, **214**, 25–30.

[58] J. C. Bachman, S. Muy, A. Grimaud, H.-H. Chang, N. Pour, S. F. Lux, O. Paschos, F. Maglia, S. Lupart, P. Lamp *et al.*, *Chem. Rev.*, 2015, **116**, 140–162.

[59] X. Zhang and J. W. Fergus, *ECS Trans.*, 2016, **72**, 133–137.

[60] B. B. Owens, *J. Power Sources*, 2000, **90**, 2–8.

[61] C. Yu, S. Ganapathy, E. R. H. van Eck, H. Wang, S. Basak, Z. Li and M. Wagemaker, *Nat. Commun.*, 2017, **8**, 1086.

[62] A. R. Kulkarni, H. S. Maiti and A. Paul, *B. Mater. Sci.*, 1984, **6**, 201–221.

[63] J. B. Goodenough, *Solid State Ionics*, 1997, **94**, 17–25.

[64] Z. J. Zhang, S.-L. Chou, Q.-F. Gu, H.-K. Liu, H.-J. Li, K. Ozawa and J.-Z. Wang, *ACS Appl. Mater. Interfaces*, 2014, **6**, 22155–22165.

[65] F. Han, J. Yue, X. Fan, T. Gao, C. Luo, Z. Ma, L. Suo and C. Wang, *Nano Lett.*, 2016, **16**, 4521–4527.

[66] K. Takada, *Langmuir*, 2013, **29**, 7538–7541.

[67] K. Takahashi, H. Maekawa and H. Takamura, *Solid State Ionics*, 2014, **262**, 179–182.

[68] J. Li, C. Ma, M. Chi, C. Liang and N. J. Dudney, *Adv. Energy Mater.*, 2015, **5**, 1401408.

[69] C. Cao, Z. B. Li, X. L. Wang, X. B. Zhao and W. Q. Han, *Front. Energy Res.*, 2014, **2**, 25.

[70] Y. Deng, C. Eames, B. Fleutot, R. David, J.-N. Chotard, E. Suard, C. Masquelier and M. S. Islam, *ACS Appl. Mater. Interfaces*, 2017, **9**, 7050–7058.

[71] T. Inada, T. Kobayashi, N. Sonoyama, A. Yamada, S. Kondo, M. Nagao and R. Kanno, *J. Power Sources*, 2009, **194**, 1085–1088.

[72] M. Nagao, Y. Imade, H. Narisawa, T. Kobayashi, R. Watanabe, T. Yokoi, T. Tatsumi and R. Kanno, *J. Power Sources*, 2013, **222**, 237–242.

[73] V. Thangadurai, S. Narayanan and D. Pinzaru, *Chem. Soc. Rev.*, 2014, **43**, 4714–4727.

[74] Y. Zhu, X. He and Y. Mo, *ACS Appl. Mater. Interfaces*, 2015, **7**, 23685–23693.

[75] Y. Ren, K. Chen, R. Chen, T. Liu, Y. Zhang and C. W. Nan, *J. Am. Ceram. Soc.*, 2015, **98**, 3603–3623.

[76] M. Backhaus-Ricoult, *Solid State Ionics*, 2002, **150**, 143–156.

[77] R. H. Basappa, T. Ito and H. Yamada, *J. Electrochem. Soc.*, 2017, **164**, A666–A671.

[78] W. Luo, Y. Gong, Y. Zhu, Y. Li, Y. Yao, Y. Zhang, K. K. Fu, G. Pastel, C. F. Lin, Y. Mo, E. D. Wachsman and L. Hu, *Adv. Mater.*, 2017, **29**, 1606042.

[79] A. Sakuda, A. Hayashi and M. Tatsumisago, *Sci. Rep.*, 2013, **3**, 2261.

[80] S. Ohta, T. Kobayashi, J. Seki and T. Asaoka, *J. Power Sources*, 2012, **202**, 332–335.

[81] X. Yan, Z. Li, Z. Wen and W. Han, *J. Phys. Chem. C*, 2017, **121**, 1431–1435.

[82] H. M. Kasper, *Inor. Chem.*, 1969, **8**, 1000–1002.

[83] E. J. Cussen, *J. Mater. Chem.*, 2010, **20**, 5167.

[84] E. J. Cussen, T. W. S. Yip, G. O'Neill and M. P. O'Callaghan, *J. Solid State Chem.*, 2011, **184**, 470–475.

[85] H. Hyooma and K. Hayashi, *Mater. Res. Bull.*, 1988, **23**, 1399 – 1407.

[86] V. Thangadurai, H. Kaack and W. J. Weppner, *J. Am. Ceram. Soc.*, 2003, **86**, 437–440.

[87] E. J. Cussen, *Chem. Commun.*, 2006, **4**, 412–413.

[88] M. M. Ahmad, *Nanoscale Res. Lett.*, 2015, **10**, 58.

[89] R. Jalem, M. Nakayama, W. Manalastas, J. A. Kilner, R. W. Grimes, T. Kasuga and K. Kanamura, *J. Phys. Chem. C*, 2015, **119**, 20783–20791.

[90] C. R. Mariappan, K. I. Gnanasekar, V. Jayaraman and T. Gnanasekaran, *J. Electroceram.*, 2013, **30**, 258–265.

[91] V. Thangadurai and W. Weppner, *Adv. Funct. Mater.*, 2005, **15**, 107–112.

[92] R. Murugan, V. Thangadurai and W. Weppner, *Angew. Chem. Int. Ed.*, 2007, **46**, 7778–7781.

[93] W. G. Zeier, *Dalton Trans.*, 2014, **43**, 16133–16138.

[94] J. Awaka, N. Kijima, H. Hayakawa and J. Akimoto, *J. Solid State Chem.*, 2009, **182**, 2046–2052.

[95] J. Percival, E. Kendrick, R. Smith and P. Slater, *Dalton Trans.*, 2009, 5177–5181.

[96] E. Rangasamy, J. Wolfenstine and J. Sakamoto, *Solid State Ionics*, 2012, **206**, 28 – 32.

[97] C. Li, Y. Liu, J. He and K. S. Brinkman, *J. Alloy. Compd.*, 2017, **695**, 3744–3752.

[98] Y. Matsuda, A. Sakaida, K. Sugimoto, D. Mori, Y. Takeda, O. Yamamoto and N. Imanishi, *Solid State Ionics*, 2017, **311**, 69–74.

[99] R. Murugan, S. Ramakumar and N. Janani, *Electrochem. Commun.*, 2011, **13**, 1373–1375.

[100] L. J. Miara, S. P. Ong, Y. Mo, W. D. Richards, Y. Park, J.-M. Lee, H. S. Lee and G. Ceder, *Chem. Mater.*, 2013, **25**, 3048–3055.

[101] C. Deviannapoorani, L. Dhivya, S. Ramakumar and R. Murugan, *J. Power Sources*, 2013, **240**, 18–25.

[102] L. Dhivya, N. Janani, B. Palanivel and R. Murugan, *AIP Adv.*, 2013, **3**, 082115.

[103] Y. Li, J.-T. Han, C.-A. Wang, H. Xie and J. B. Goodenough, *J. Mater. Chem.*, 2012, **22**, 15357–15361.

[104] H. El-Shinawi, G. W. Paterson, D. A. MacLaren, E. J. Cussen and S. A. Corr, *J. Mater. Chem. A*, 2017, **5**, 319–329.

[105] H. El-Shinawi and J. Janek, *J. Power Sources*, 2013, **225**, 13–19.

[106] E. Hanc, W. Zajac, L. Lu, B. Yan, M. Kotobuki, M. Ziabka and J. Molenda, *J. Solid State Chem.*, 2017, **248**, 51–60.

[107] P. M. Panchmatia, A. R. Armstrong, P. G. Bruce and M. S. Islam, *Phys. Chem. Chem. Phys.*, 2014, **16**, 21114–21118.

[108] A. R. Armstrong, C. Lyness, P. M. Panchmatia, M. S. Islam and P. G. Bruce, *Nat. Mater.*, 2011, **10**, 223.

[109] Y. Zhao and L. L. Daemen, *J. Am. Chem. Soc.*, 2012, **134**, 15042–15047.

[110] R. J. Borg and G. Dienes, *Diffusion in Ionic Crystals*, Elsevier, London, 1988, pp. 111–133.

[111] N. Twu, X. Li, A. Urban, M. Balasubramanian, J. Lee, L. Liu and G. Ceder, *Nano Lett.*, 2015, **15**, 596–602.

[112] R. Mouta, E. M. Diniz and C. W. A. Paschoal, *J. Mater. Chem. A*, 2016, **4**, 1586–1590.

[113] W. D. Richards, Y. Wang, L. J. Miara, J. C. Kim and G. Ceder, *Energy Environ. Sci.*, 2016, **9**, 3272–3278.

[114] K. Kaup, F. Lalere, A. Huq, A. Shyamsunder, T. Adermann, P. Hartmann and L. F. Nazar, *Chem. Mater.*, 2018, **30**, 592–596.

[115] I. Blazquez-Alcover, G. Rousse, D. A. D. Corte, J. C. Badot, A. Grimaud, P. Rozier and J. M. Tarascon, *Solid State Ionics*, 2017, **308**, 16–21.

[116] M. Koniak and A. Czerepicki, *IOP Conf. Ser.: Mater. Sci. Eng.*, 2017, **211**, 012005.

[117] V. Thangadurai, A. K. Shukla and J. Gopalakrishnan, *Chem. Mater.*, 1999, **11**, 835–839.

[118] V. Thangadurai and W. Weppner, *J. Electrochem. Soc.*, 2004, **151**, H1.

[119] G. Dittrich and R. Hoppe, *Z. Anorg. Allg. Chem.*, 1969, **371**, 306–317.

[120] J. Hauck, *Z. Naturforsch., B: Chem. Sci.*, 1969, **24**, 1067.

[121] J.-F. Brice and A. Ramdani, *Mater. Res. Bull.*, 1981, **16**, 1487–1492.

[122] A. L. Buzlukov, I. Y. Arapova, Y. V. Baklanova, N. I. Medvedeva, T. A. Denisova and S. V. Verkhovskii, *J. Phys. Chem. C*, 2016, **120**, 23911–23921.

[123] R. Czekalla and W. Jeitschko, *Z. Anorg. Allg. Chem.*, 1993, **619**, 2038–2042.

[124] M. Zocchi, I. N. Sora, L. Depero and R. Roth, *J. Solid State Chem.*, 1993, **104**, 391–396.

[125] I. Abrahams, P. Lightfoot and P. Bruce, *J. Solid State Chem.*, 1993, **104**, 397–403.

[126] M. S. Islam, D. J. Driscoll, C. A. J. Fisher and P. R. Slater, *Chem. Mater.*, 2005, **17**, 5085–5092.

[127] R. P. Rao, M. V. Reddy, S. Adams and B. V. R. Chowdari, *Mater. Sci. Eng., B*, 2012, **177**, 100–105.

[128] Y. Liao, P. Singh, K.-S. Park, W. Li and J. B. Goodenough, *Electrochim. Acta*, 2013, **102**, 446–450.

[129] Y. Liu and X. Hua, *Int. J. Appl. Ceram. Tec.*, 2016, **13**, 579–583.

[130] S.-Z. Kang, T. Wu, X. Li and J. Mu, *Mater. Lett.*, 2010, **64**, 1404–1406.

[131] H. Pfeiffer and P. Bosch, *Chem. Mater.*, 2005, **17**, 1704–1710.

[132] X.-S. Yin, M. Song, Q.-H. Zhang and J.-G. Yu, *Ind. Eng. Chem. Res.*, 2010, **49**, 6593–6598.

[133] A. S. Bhalla, R. Guo and R. Roy, *Mater. Res. Innov.*, 2000, **4**, 3–26.

[134] M. A. Peña and J. L. G. Fierro, *Chem. Rev.*, 2001, **101**, 1981–2018.

[135] H. D. Megaw, *P. Phys. Soc.*, 1946, **58**, 340–340.

[136] M. Nakayama, K. Imaki, H. Ikuta, Y. Uchimoto and M. Wakihara, *J. Phys. Chem. B*, 2002, **106**, 6437–6441.

[137] S. Stramare, V. Thangadurai and W. Weppner, *Chem. Mater.*, 2003, **15**, 3974–3990.

[138] L. Latie, G. Villeneuve, D. Conte and G. Le Flem, *J. Solid State Chem.*, 1984, **51**, 293–299.

[139] Y. Inaguma, L. Che, M. Itoh and T. Nakamura, *Solid State Ionics*, 1994, **70-71**, 196–202.

[140] H. Kawai, *J. Electrochem. Soc.*, 1994, **141**, L78.

[141] Y. Inaguma, *Solid State Ionics*, 1995, **79**, 91–97.

[142] T. W. S. Yip and E. J. Cussen, *Inorg. Chem.*, 2013, **52**, 6985–6993.

[143] P. Knauth, *Solid State Ionics*, 2009, **180**, 911–916.

[144] A. B. Santibáñez-Mendieta, C. Didier, K. K. Inglis, A. J. Corkett, M. J. Pitcher, M. Zanella, J. F. Shin, L. M. Daniels, A. Rakhmatullin, M. Li, M. S. Dyer, J. B. Claridge, F. Blanc and M. J. Rosseinsky, *Chem. Mater.*, 2016, **28**, 7833–7851.

[145] S. Vasala and M. Karppinen, *Prog. Solid State Ch.*, 2015, **43**, 1–36.

[146] G. Demazeau, E. Oh-Kim, J. Choy and P. Hagenmuller, *Mater. Res. Bull.*, 1987, **22**, 735–740.

[147] K. Hayashi, H. Noguchi and M. Ishii, *Mater. Res. Bull.*, 1986, **21**, 401–406.

[148] M. López, M. Veiga, J. Rodríguez-Carvajal, F. Fernández, A. Jerez and C. Pico, *Mater. Res. Bull.*, 1992, **27**, 647–654.

[149] F. Rosciano, P. P. Pescarmona, K. Houthoofd, A. Persoons, P. Bottke and M. Wilkening, *Phys. Chem. Chem. Phys.*, 2013, **15**, 6107.

[150] M. M. Thackeray and J. B. Goodenough, *Solid state cell wherein an anode, solid electrolyte and cathode each comprise a cubic-close-packed framework structure*, 1985, https://patents.google.com/patent/US4507371A.

[151] T. Ohzuku, N. Matoba and K. Sawai, *J. Power Sources*, 2001, **97-98**, 73–77.

[152] T. Ohzuku, *J. Electrochem. Soc.*, 1993, **140**, 2490.

[153] S. Goriparti, E. Miele, F. D. Angelis, E. D. Fabrizio, R. P. Zaccaria and C. Capiglia, *J. Power Sources*, 2014, **257**, 421–443.

[154] H. Wu, G. Chan, J. W. Choi, I. Ryu, Y. Yao, M. T. McDowell, S. W. Lee, A. Jackson, Y. Yang, L. Hu and Y. Cui, *Nat. Nanotechnol.*, 2012, **7**, 310–315.

[155] T. Yuan, Z. Tan, C. Ma, J. Yang, Z. F. Ma and S. Zheng, *Adv. Energy Mater.*, 2017, **7**, 1601625.

[156] V. Palomares and T. Rojo, *Lithium Ion Batteries - New Developments*, InTech, London, 2012.

[157] M. S. Whittingham, *Lithium Batteries*, Springer, New York, 2009, pp. 85–109.

[158] A. R. West, *Solid state chemistry and its applications*, John Wiley & Sons, Chichester, 2014.

[159] K. E. Haque, *Int. J. Miner. Process.*, 1999, **57**, 1–24.

[160] M. Oghbaei and O. Mirzaee, *J. Alloy. Compd.*, 2010, **494**, 175–189.

[161] A. Metaxas, and R. J. Meredith, *Industrial microwave heating*, IET, London, 1983.

[162] A. Goldstein, N. Travitzky, A. Singurindy and M. Kravchik, *J. Eur. Ceram. Soc.*, 1999, **19**, 2067–2072.

[163] M. S. Spotz, D. J. Skamser and D. L. Johnson, *J. Am. Ceram. Soc.*, 1995, **78**, 1041–1048.

[164] H. J. Kitchen, S. R. Vallance, J. L. Kennedy, N. Tapia-Ruiz, L. Carassiti, A. Harrison, A. G. Whittaker, T. D. Drysdale, S. W. Kingman and D. H. Gregory, *Chem. Rev.*, 2013, **114**, 1170–1206.

[165] M. H. Bhat, A. Miura, P. Vinatier, A. Levasseur and K. J. Rao, *Solid State Commun.*, 2003, **125**, 557–562.

[166] G. Yang, G. Wang and W. Hou, *J. Phys. Chem. B*, 2005, **109**, 11186–11196.

[167] A. E. Danks, S. R. Hall and Z. Schnepp, *Mater. Horiz.*, 2016, **3**, 91–112.

[168] C. J. Brinker and G. W. Scherer, *Sol-gel science: the physics and chemistry of sol-gel processing*, Academic Press, Rijeka, 2013.

[169] P. Vaqueiro and M. Lopez-Quintela, *Chem. Mater.*, 1997, **9**, 2836–2841.

[170] B. Hwang, R. Santhanam and D. Liu, *J. Power Sources*, 2001, **101**, 86–89.

[171] W. Wen and J.-M. Wu, *RSC Adv.*, 2014, **4**, 58090–58100.

[172] Y. X. Gao, X. P. Wang, W. G. Wang and Q. F. Fang, *Solid State Ionics*, 2010, **181**, 33–36.

[173] I. Kokal, M. Somer, P. H. L. Notten and H. T. Hintzen, *Solid State Ionics*, 2011, **185**, 42–46.

[174] C. K. Chan, T. Yang and J. M. Weller, *Electrochim. Acta*, 2017.

[175] A. Orera, G. Larraz, J. A. Rodríguez-Velamazán, J. Campo and M. L. Sanjuán, *Inorg. Chem.*, 2016, **55**, 1324–1332.

[176] M. L. Sanjuán, A. Orera, I. Sobrados, A. F. Fuentes and J. Sanz, *J. Mater. Chem. A*, 2018, **6**, 2708–2720.

[177] N. Rosenkiewitz, J. Schuhmacher, M. Bockmeyer and J. Deubener, *J. Power Sources*, 2015, **278**, 104–108.

[178] K. B. Dermenci and S. Turan, *Ceram. Int.*, 2018.

Chapter 2: Experimental Methods

This chapter contains the detailed protocols employed during this thesis for the synthesis and characterisation of the materials under study together with the basic principles to understand the main characterisation techniques used to explore their properties.

2.1 Materials

All chemical employed were used as supplied without further purification unless otherwise indicated.

$LiOH \cdot H_2O$ (98%), $^7LiOH \cdot H_2O$ (98%), NaOH (98%), $LiNO_3$ (98%), La_2O_3 (99%), $ZrO(NO_3)_2 \cdot 6\,H_2O$ (99%), $C_6H_8O_7$ (citric acid) (99%), D_2O (99.9 atom % D) and 2-propanol (99.5%) were purchased from Sigma-Aldrich.

$Al(NO_3)_3 \cdot 9\,H_2O$ (98-102%), $Ga(NO_3)_3 \cdot 9\,H_2O$ (99.999%), $La(NO_3)_3 \cdot 6\,H_2O$ (99%), $Zn(NO_3)_2 \cdot 6\,H_2O$ (99%), ZrO_2 (99.978%), Ta_2O_5 (99.993%), $BaCO_3$ (99.997%), HfO_2 (99.99%), In_2O_3 (99.997%), Y_2O_3 (99.9%), WO_3 (99.95%) and TeO_2 (99.99%) were purchased from Alfa Aesar.

2.2 Synthetic procedures

The materials studied in this thesis have been developed by two main synthetic routes, by a microwave-assisted solid-state route and by sol-gel chemistry using the citrate protocol.

2.2.1 Microwave solid-state synthesis

Al-, Ga-, and Zn-doped $Li_6BaLa_2Ta_2O_{12}$

For the preparation of the $Li_{6-3x}(Al/Ga)_xBaLa_2Ta_2O_{12}$ and $Li_{6-2x}Zn_xBaLa_2Ta_2O_{12}$ garnet families, stoichiometric quantities of La_2O_3 (previously dried at 900 ^oC for 24h), Ta_2O_5, $BaCO_3$, $Al(NO_3)_3 \cdot 9\,H_2O$, $Ga(NO_3)_3 \cdot 9\,H_2O$, $Zn(NO_3)_2 \cdot 6\,H_2O$ and a 10 % excess of $LiOH \cdot H_2O$ were weighed and ball milled for 20 min at a vibrational frequency of 20 Hz in a stainless steel jar. Subsequently, the fine powder was pelletised at 3 tons under uniaxial pressure. The pelletised material was fired at 700 ^oC for 6 hours in order to decompose the starting materials. The main heat treatment was carried out in a 2.45 GHz CEM Phoenix hybrid microwave furnace composed of three silicon carbide walls which are heated by microwave irradiation surrounding the sample cavity. This main heat treatment was performed for 6 hours at 800 ^oC in an open atmosphere. In both cases, the bottom of the alumina crucibles were covered with mother powder in order to avoid any accidental Al contamination and the heating rate was 2 $^oC\ min^{-1}$.

Ga- and Al-doped $Li_7La_3Zr_2O_{12}$

For the microwave-assisted synthesis of the cubic $Li_{6.5}Al_{0.25}La_{2.92}Zr_2O_{12}$ and $Li_{6.25}Ga_{0.25}La_3Zr_2O_{12}$ garnet materials, stoichiometric quantities of La_2O_3 (previously dried at 900 °C for 24h), ZrO_2, $Al(NO_3)_3 \cdot 9\,H_2O$ and a 10 % excess of $LiOH \cdot H_2O$ were ball milled for 30 min at a vibrational frequency of 20 Hz in a stainless steel jar. Subsequently, the fine powder was pelleted at 3 tonnes under uniaxial pressure. The pelleted material was heated at 700 °C for 6 hours in the CEM Phoenix hybrid microwave furnace in order to decompose the starting materials. Subsequently, the material was reground and pelletised for a second heat treatment carried out in air at 950 °C for 6 hr in the same microwave furnace. For the Al-doped garnet, an additional annealing of 1 hour at 1000 °C in the same hybrid microwave furnace was required to obtain phase pure material. During each heat treatment, the bottom of the alumina crucibles were covered with mother powder in order to avoid any accidental Al contamination and the heating rate was held at 2 °C min^{-1} to reduce lithium evaporation.

In- and Y-doped $Li_6Hf_2O_7$ materials

For the microwave-assisted solid-state synthesis of the In- and Y-doped $Li_6Hf_2O_7$ materials, stoichiometric amounts of $LiOH \cdot H_2O$, In_2O_3, Y_2O_3 and HfO_2 were mixed and ball milled for 20 minutes at 20 Hz with stainless steel milling media. The resulting fine powder was pelleted at 3 tonnes under uniaxial pressure. The pelleted material was heated at 700 °C for 6 hours in a 2.45 GHz CEM Phoenix hybrid microwave furnace for the decomposition of the precursor materials. Subsequently, the material was reground and pelleted for a second heat-treatment carried out in air at 850 °C for 4 hours in the same microwave furnace with a low heating rate of 2 °C min^{-1} to reduce lithium evaporation. For higher doping levels of the dopant surpassing the 0.1 mols per formula unit, an additional heat-treatment of 850 °C for 4 hours was used to increase sample purity.

Na- and Li-rich double perovskites

For the microwave-assisted synthesis of the $Li_{1.5}La_{1.5}WO_6$, $Li_{1.5}La_{1.5}TeO_6$, $Li_{1.5}La_{1.5}W_{0.5}Te_{0.5}O_6$ and $Na_{1.5}La_{1.5}TeO_6$ double perovskites, stoichiometric amounts of La_2O_3 (previously dried at 900 °C for 24h), WO_3 and/or TeO_2, and, NaOH and/or a 10 % excess of $LiOH \cdot H_2O$ ($^7LiOH \cdot H_2O$ for NPD studies) were ball milled for 30 min at a vibrational frequency of 20 Hz in a stainless steel jar. Subsequently, the fine powder was pelleted at 3 tonnes under uniaxial pressure. The pelleted material was heated at 700 °C for 6 hours in a 2.45 GHz CEM Phoenix hybrid microwave furnace for the decomposition of the precursor materials. Subsequently, the material was reground and pelletised for a second heat treatment carried out in air at 900 °C for 6 hr in the same microwave furnace. The last treatment consisted in 1 hour at 1000 °C of the repelletised material in the same hybrid microwave furnace. In every calcination the heating rate was held at 2 °C min^{-1}

to reduce lithium evaporation.

2.2.2 Low temperature sol-gel synthesis of Al-doped $Li_7La_3Zr_2O_{12}$

The low temperature synthesis for the Al-doped $Li_{6.5}Al_{0.25}La_{2.92}Zr_2O_{12}$ cubic phase compound was performed *via* the Pechini modified sol-gel method. For the synthesis of 2 mmol of material, stoichiometric amounts of $ZrO(NO_3)_2 \cdot 6\,H_2O$, $Al(NO_3)_3 \cdot 9\,H_2O$, $La(NO_3)_3 \cdot 6\,H_2O$, 20% excess of $LiNO_3$, and 10.35 g of citric acid were dissolved in 600 mL of deionised water (D_2O for *in-situ* NPD studies) together with 100 mL of 2-propanol. The sol was heated in a hotplate at 150 °C under vigorous stirring in order to evaporate the solvent overnight. After the solvent was evaporated, a yellow gel was formed which was burned by elevating the hotplate temperature progressively up to 350 °C . The temperature was maintained for 2 hours until a brown foam formed. This brown foam was finally calcined at the desired temperature and time conditions for the phase formation studies, with the organic matter being decomposed above 500 °C in air.

2.3 Characterisation techniques

2.3.1 Crystal structure characterisation

Powder X-Ray Diffraction (PXRD)

PXRD is the main tool employed for the assessment of the purity and study of the crystal parameters for crystalline complex oxides compounds prepared in this thesis, due to the accessibility to instrumentation and speed of the data acquisition.

Crystal structure analyses by diffraction techniques are based on the coherent scattering of waves by an ordered atomic framework in the solid crystalline material. Diffraction can be analysed in terms of Von Laue and Bragg approaches, with the latter being the preferred method for PXRD of inorganic condensed matter.

In Bragg theory, a crystalline solid is interpreted as a three dimensional ordered arrangement of atoms forming the crystal. The ordered atoms form planes that can diffract incident radiation. When the diffracted radiation waves are in phase, a constructive interference is then produced (Fig. 2.1), while if they are out-of phase, a destructive interference would be produced with no measurable outcoming diffracted radiation. As observed in Figure 2.1, this constructive interference is produced when the wavelength of the incident radiation is proportional to the product of the inter-plane distance and the sine of the theta angle formed between the plane and radiation directions. This condition is defined by Bragg's law and enables the study of the crystal characteristics of condensed matter by PXRD. The benefit of X-ray radiation for diffraction is due to its wavelength range being on the same order of magnitude as the atomic distances in crystalline materials.

Figure 2.2a shows a conventional configuration for the PXRD analyses of powdered samples. This is the Bragg-Brentano where monochromatic X-ray radiation is emitted

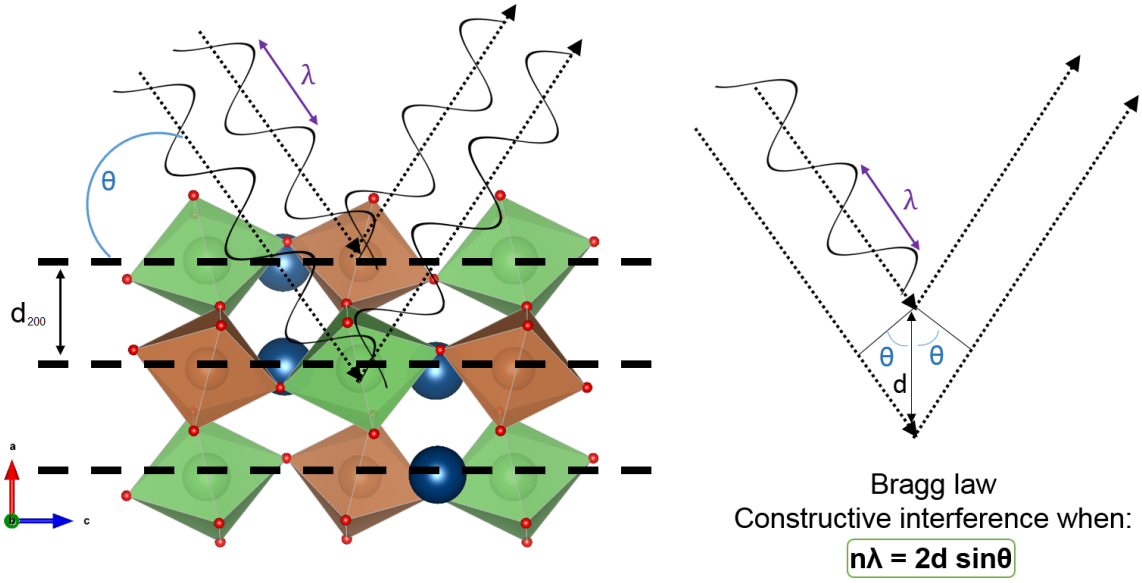

Figure 2.1: Schematic representation of the Bragg's law condition.

from a fixed source and directed to the packed powdered crystalline material in a flat sample holder. The sample stage and detector rotates allowing to vary the θ angle between the sample and the incoming radiation.

The powdered material contains crystallites with orientations distributed randomly within the sample body which results in the radiation emitted in cones from the sample for every crystalline plane. The detector in Bragg-Brentano configuration will detect only a portion of this cone, represented as a one dimensional data point as a function of the scanned 2θ angle. Since the radiation wavelength is fixed, by inserting the θ value when diffraction is detected into Bragg's law, inter-plane distances and other crystal structure parameters can be obtained.

For the PXRD analyses carried out in this thesis, a PANalytical X'Pert PRO Diffractometer was employed using Cu-Kα radiation in the 2θ with ranges between 10 – 130º with a step size of 0.016º and a nominal scan rate of 53.975 seconds per step for routine measurements and 800 seconds per step for long scan measurements in the case

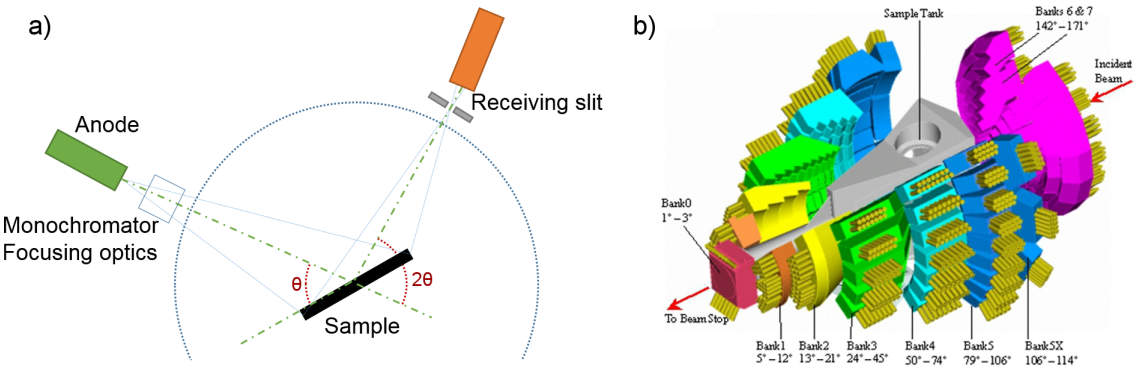

Figure 2.2: (a) Bragg-Brentano configuration for the PXRD set-up utilised in the PANalytical X'Pert PRO instrument. (b) Schematic representation of the GEM instrument for NPD at ISIS[1].

of the novel double perovskite materials. All measurements were carried out at room temperature unless otherwise indicated.

Neutron Powder Diffraction (NPD)

While X-ray photons are scattered by the atom's electron clouds, neutrons are scattered by the atomic nucleus. X-ray scattering intensity is then proportional to the atomic number which can make the analyses of diffraction arising from light atoms more difficult in presence of heavy atoms in the same compound. Neutrons scattering is not proportional to the atomic number, but is rather dictated by the coherent scattering length of each element which does not follow any rational trend. This allows one to study more precisely the crystal structure of materials containing light elements and pairs of isoelectronic elements.

Neutrons of the desired wavelength can be produced in nuclear reactors and the analyses of the diffraction can be carried out in a similar manner as for PXRD analysis. Neutrons can also be produced in spallation sources, where a tungsten target is hit by a high energy proton beam producing neutrons that are subsequently thermalised. In this case, the produced neutron beam is polychromatic and the experiment is performed as a time-of-flight measurement. To do this, an array of detectors are fixed surrounding the sample position from a fixed distance (L) as can be seen in Figure 2.2b. From the de Broglie equation, the wavelength of the diffracted neutrons can be obtained from their speed, which can be calculated from the time taken by the neutron to reach the detector (time-of-flight), modifying the Bragg's law as shown in Equation 2.1:

$$\lambda = ht / mL = 2d \sin\theta \tag{2.1}$$

where h is the Plank's constant, m is the neutron mass, t is the neutron's time-of-flight and θ is the angle formed between the incident beam and the fixed detectors positions.

NPD patterns in this thesis were acquired at the ISIS pulsed neutron and muon source at the Rutherford Appleton Laboratory in the UK using the HRPD instrument for the Al-doped LLZO garnet, and GEM and Polaris instruments for the Li-rich double perovskites. The samples, *ca.* 1 to 3 g, were placed in 6 and 11 mm diameter cylindrical vanadium cans and loaded into the beamline and the data were collected at room temperature. The broad incident pulsed neutron flux was narrowed in a 100 K methane moderator giving a peak flux at $\lambda \sim 2$ Å, prior to sample scattering. Data used for Rietveld refinements were collected in the backscattering detector, Bank 1 ($2\theta = 168.33^{o}$), and the 90^{o} detector, Bank 2 ($2\theta = 89.58^{o}$) for the garnet material measured in HRPD instrument. For the lithium-rich double perovskites, the data were collected in Bank 3 ($2\theta = 35.26^{o}$) and Bank 5 ($2\theta = 91.34^{o}$) at the GEM instrument, and Bank 3 ($2\theta = 51.99^{o}$) and Bank 5 ($2\theta = 146.94^{o}$) at the Polaris instrument. The data were collected over a time-of-flight region of 30–130 ms (HRPD) and were corrected for absorption, 0.25–23 ms (Polaris) and 0.9–

21.5 ms (GEM).

For the *in-situ* NPD measurements of the sol-gel prepared LLZO material on Polaris instrument, 1.55 g of pre-calcined sample at 600 °C were loaded into a quartz tube and evacuated under dynamic vacuum during the rest of the experiment. The sample was initially heated from room temperature to 600 °C and subsequently to 1000 °C at a ramp of 0.5 °C min^{-1} with 1 hour dwell steps every 50 °C to allow longer data collection and sample temperature stabilisation. The sample was then cooled down to room temperature naturally with data collection every 100 °C. Diffraction data were collected from 150 μA ($\sim$ 1 hour) beam exposure at each temperature dwell step.

Rietveld Refinements

In order to obtain the cell parameters, atomic positions, occupancy fractions and in some cases thermal parameters from the crystal structure of the synthesised materials, Rietveld refinements of the diffraction data were performed with the Generalised Structure Analysis System (GSAS),[2] along with the graphical user interface EXPGUI,[3] by means of a least squares approach.

The Rietveld method[4] uses a least squares approach to refine a theoretical crystallographic model until it matches the measured profile. During a Rietveld refinement, the intensity of each data point in the diffraction pattern is calculated using the expression in Equation 2.2:

$$Y_{ic} = Y_{ib} + \sum_{hkl} G_{ik} I_k \tag{2.2}$$

where Y_{ic} is the calculated intensity at point i in the diffraction pattern, Y_{ib} is the background intensity at point i, G_{ik} is the value of normalised peak profile function at point i for the reflection k, I_k is the Bragg intensity of reflection k with k being the hkl reflections contributing intensity to point i.

The basis of the Rietveld refinement is to minimise the function φ (Eq. 2.3) which analyses the difference between the calculated profile and the observed data.

$$\varphi = \sum_i W_i \left\{ y_i^{obs} - \frac{1}{c} y_i^{calc} \right\}^2 \tag{2.3}$$

where W_i is the statistical weight and c is an overall scale factor so y^{calc} and y^{obs} are comparable.

In order to analyse the goodness of the fit, different discrepancy parameters can be employed. The more commonly used in Rietveld refinements are the weighted R-factor $\left[R_{wp} = \sqrt{\varphi / \sum_i W_i (y_i^{obs})^2}\right]$ which derives from the square root of the minimised φ function and its scaled by the weighed intensities, the expected R-factor $\left[R_{exp} = \sqrt{N / \sum_i W_i (y_i^{obs})^2)}\right]$ which indicates the theoretical minimum R-factor that could be obtained taking into account the number of data points (N), and the goodness of fit χ^2

which is defined as $(R_{wp}/R_{exp})^2$, *i.e.* normalising the R_{wp} respect to the R_{exp} as the ideal model. The R-factors are reported as percentages with lower values indicating a better fit. In the case of the χ^2 parameter, the lower and closer the value to the unity the better the agreement between the experimental data and the theoretical model.

2.3.2 Raman spectroscopy

Raman spectroscopy allows the study of the vibrational modes of chemically bonded atoms. Raman spectroscopy is based on the inelastic scattering of light, usually in the visible, near infrared or near ultraviolet range, by the atoms forming the analysed compound. A monochromatic beam of light is focused toward the sample which absorbs part of the photons' energy. The absorbed photon energy is transferred to the vibrating atoms in the sample, producing a change in their vibrational energy to a virtual higher energy level for a short period of time. The atom pair energy then decays back to a lower energy level which can be different from the initial one before photon absorption. If the final energy state is higher than the initial state, then the Stokes scattering is produced with the scattered photons having less energy than the incident photons. On the other hand, if the final energy level is at lower energy than the initial one, then the scattered photons have higher energy than the incident ones, producing Anti-Stokes scattering. At room temperature the population state of a system is principally in its ground vibrational state so Stokes scattering is dominant.

Raman data in this thesis were acquired in a Horiba Jobin Yvon LabRAM HR system equipped with a Ventus 532 laser. Spectra were acquired in the 50 – 4000 cm^{-1} Raman shift range with a 532 nm wavelength laser with a 100 mW power . The light beam was masked to the appropriated level in order to obtain data intensity in a measurable range.

2.3.3 Scanning Electron Microscopy (SEM)

SEM allows to study the morphology and size of materials from few nanometers up to the millimetre scale. The technique produces images by scanning the sample surface with a focused beam of electrons. The electron beam hits the scanned sample surface producing the ejection secondary electrons with origin from the atom's core K-shell that are detected by scintillator-photomultipliers. The interaction of the beam with the sample can also produce elastic scattering resulting in back-scattered electrons that can also been detected and used to analyse the material topology.

In order to analyse the size and morphology of the particles for the materials synthesised in this thesis, SEM images were acquired with a Phillips XL30 ESEM microscope for all the lithium-rich garnet materials and the doped-$Li_6Hf_2O_7$ materials. In the case of the lithium- and sodium-rich double perovskites a Carl Zeiss Sigma microscope was employed. The electron beam was set up currents *ca.* 20 mA and a voltages of 20 and 25 kV. All samples were ground and a tiny amount of the fine powder was deposited over

a carbon-taped sample holder. Subsequently the samples were Au-coated to enhance their surface conductivity and avoid overcharging from irradiation by the electron beam.

2.3.4 Compositional analyses

Inductively Coupled Plasma-Mass Spectrometry (ICP-MS)

ICP-MS is an analytical technique that allows detection of metals at concentrations as low as ppb. The technique is based on the ionisation of the analysed sample by an inductively coupled plasma which then is coupled with a mass spectrometer able to separate and quantify the produced ions.

ICP-MS analyses were performed on an Agilent 7700 ICP-MS instrument. Approximately 6 mg of sample were dissolved in 50 mL of 2% HNO_3 solution in deionised water and immersed into an ultrasonic bath for 5 minute prior the measurements.

Energy Disperse X-ray spectroscopy (EDX)

The EDX technique allows the elemental analysis and chemical characterisation of a material. The technique is based on the detection of X-rays emitted by the sample when exposed to an electron beam. The subjection of a sample to a high energy electron beam produces the emission of core electrons with the subsequent migration of an electron from a higher energy orbital to fill the hole produced by the emitted core electron. This migration of an electron to a lower energy orbital results in the emission of radiation with energy equivalent to the difference in energy between both orbitals involved in the electron migration. This energy is element specific and detection of the energy of the outcoming radiation allows for element identification and quantification in the studied sample.

Energy-Dispersive X-Ray (EDX) spectra acquired during this thesis were recorded using an Oxford Instruments Energy 250 energy dispersive spectrometer system attached to an Phillips XL30 ESEM microscope. Copper tape was employed as a standard for calibration and the voltage of the incident electron beam was 25 KeV.

2.3.5 Electrochemical testing

Electrochemical Impedance Spectroscopy (EIS)

Lithium conductivity is a vital feature of a component expected to be used as an active material within a lithium-ion battery. In order to analyse the ionic conductivity through solid-state materials, EIS represents a fast, easy and standardised technique.

EIS technique allows for the measurement of the impedance (Z) that a material presents in response to an externally-applied sinusoidal AC potential (E). The impedance is a totally complex resistance encountered when a current flows through a circuit composed of resistors, capacitors, or inductors or any combination of these. The use of an AC method

is needed in order to investigate media where electronic conductivity is low, since DC methods generally require a relatively large perturbation which fail in these type of low conductivity media.

When a potential is applied in an electrochemical cell, a current originates due to the flow through the cell of ionic movements along the studied material. Since the potential applied is sinusoidal, $E = E_0 \sin(\omega t)$, the subsequent current will also be a sinusoidal response with a value of $I = I_0 \sin(\omega t + \varphi)$ which is phase-shifted with respect to the potential by the φ value, in linear systems. The impedance value is now accessible as a vector with a magnitude proportional to the relationship between the applied potential and the current flow ($\Delta E/\Delta I$). By applying Eulers relationship, it is possible to express this as a complex function as described in Equation 2.4:

$$Z(\omega) = Z_0(\cos\varphi + j\sin\varphi) \tag{2.4}$$

where Z_0 is the impedance magnitude and φ the phase shift between the applied potential and the produced current. In order to analyse the complex impedance function, the Nyquist plot is the most commonly employed representation (Fig. 2.3). In this type of plot, the imaginary part of the impedance (Z") is plotted against the real part of the impedance (Z'). The impedance vector can be represented as a vector of length |Z| with the angle between the vector and the x-axis being the φ phase shift.

Lithium and sodium solid-state electrolytes act as a pure electrical resistance leading to a magnitude of the impedance Z = R when the phase shift is zero. This can be appreciated in the Nyquist plot (Fig. 2.3), showing a semicircle in which the lower frequency extreme corresponds to the ionic resistance of the material.

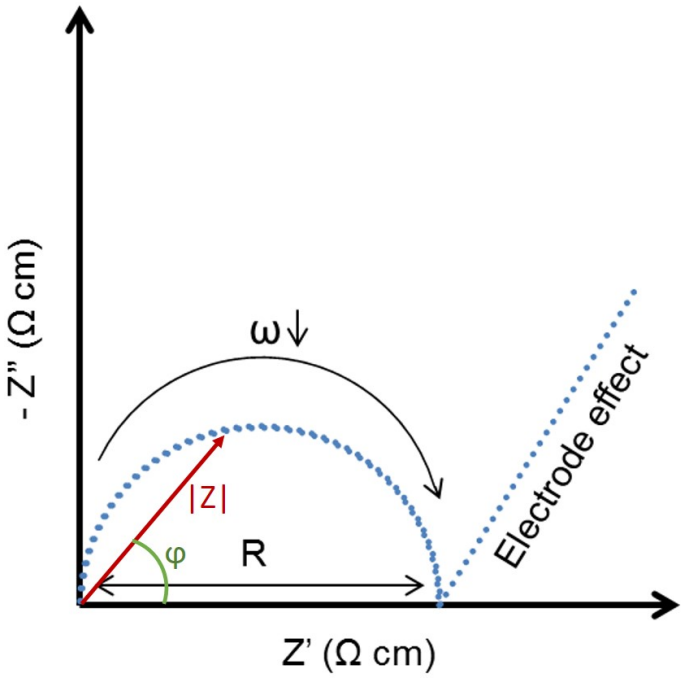

Figure 2.3: Nyquist plot example for a pure electrical resistance material with blocking electrodes.

The AC EIS measurements of the lithium-containing materials synthesised in this thesis have been carried out on a Solatron 1260 Impedance Analyser in the frequency range of 1-10^6 Hz with a 20 mV perturbation in the temperature range between RT and 400 ^{o}C in 30–50 ^{o}C intervals.

As-synthesised powdered materials were cold-pressed under uniaxial pressure at 10 tons and the resultant pellets fired during 1 to 2 hours at 900 - 1000 ^{o}C. In order to enhance the connection between the pellet and the electrodes, a suspension of 0.5-5 µm platinum particles in a highly volatile solvent (*n*-butyl acetate) was prepared and with help of a brush some drops of the suspension were extended along both surfaces of the pelletised material. The setup where the pellet is placed during the measurements is shown in Figure 2.4. The sample holder ensures pressure is held against the pellet and enhances contact with the electrodes. The electrodes consist of square pieces of 0.025 mm thickness platinum foil, connected through 0.127 mm diameter platinum wire to the impedance analyser.

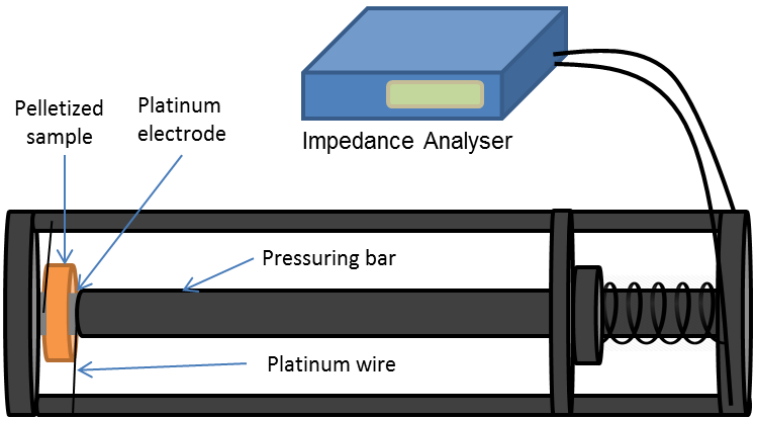

Figure 2.4: Experimental setup for EIS analyses carried out on the Solatron 1260 instrument.

Once the pelletised sample was safely in place with good contact with the electrodes, the sample holder is placed in a tube furnace to heat the sample at the required temperatures in air. Scheme 2.1 shows the heat program followed during the experiment. The impedance analyser is controlled externally by a PC with help of the SMaRT© software, thereby synchronising the measurements and the programmed temperatures in the tube furnace. Finally, once the data acquisition is finished, these were plotted and fitted with the ZView© software to the correspondent electric equivalent circuit to obtain the resistance values.

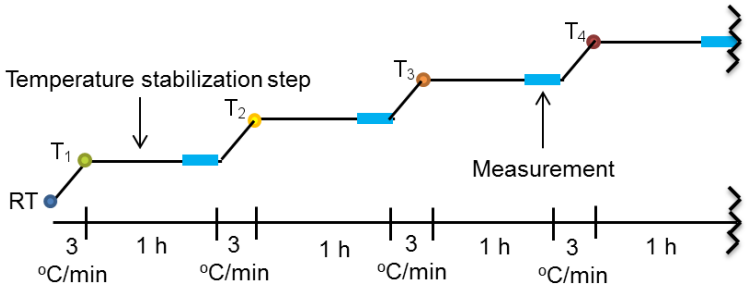

Scheme 2.1: Temperature scheme employed during the EIS experiments.

For the sodium-rich double perovskite material, impedance measurements were performed on a Biologic VSP-3 multichannel potentiostat in the frequency range of 1-10^6 Hz with a voltage perturbation of 500 mV and a temperature range between 20 and 70 °C. $Na_{1.5}La_{1.5}TeO_6$ powders were cold-pressed under uniaxial pressure at 5 tons and the resultant pellets were heated for 1 hour at 1000 °C. In order to enhance the connection between the pellet and the electrodes, a thin layer of gold was deposited on the pellet surface by physical vapour deposition. The prepared pelletised material were loaded into a stainless steel Swagelok cell.

In addition, for the lithium- and sodium-rich double perovskites solid-state electrolytes, symmetric cells in Swagelok cells with Li and Na metal electrodes, respectively, were prepared to analyse their stability against the metal anode.

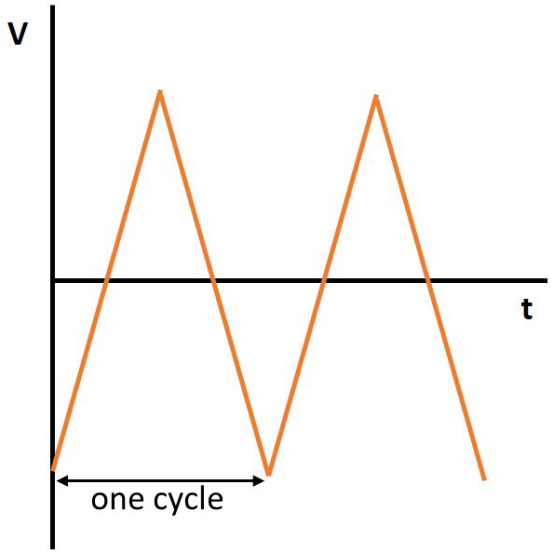

Figure 2.5: Schematic representation of the protocol carried out in a CV experiment where the voltage is scanned at a constant speed until certain voltage is reached. After the voltage limit is reached, the voltage scanning speed is reversed until a second voltage limit is then reached, completing a full cycle.

Cyclic Voltammetry (CV)

CV is an electrochemical technique that measures the current evolution developed in an electrochemical cell when voltage is cyclically scanned around the working electrode at a constant speed (Fig. 2.5). In the case of lithium half cells, the CV technique allows analysis of the redox events occurring in the working electrode upon reaction with Li^+. CV measurements allow assessment of the redox potentials of electrode materials to classify these as either positive or negative electrode materials for their battery application. In addition, in the case of electrolyte materials, the CV technique allows to assess its stability window, *i.e.* where no redox activity occurs, by scanning across a large potential range until a redox activity is found, delimiting the stability window of the electrolyte before decomposition occurs.

The CV analyses for the lithium-rich double perovskites were carried out on Swagelok cells as shown in Figure 2.6. The electrode material was formed by a mixture of the double perovskite material (90 %), electronically conductive carbon black Ketjenblack EC-600JD (AkzoNobel) (5%) and PTFE (5%) as binder to the electrode mixture. A Whatman glass microfibre filter was used as a separator with 1 M $LiPF_6$ in ethylene carbonate and dimethyl carbonate 1:1 v/v (Solvionic) as the electrolyte and Li metal of 0.75 mm thickness (Sigma Aldrich) as the reference and counter electrode.

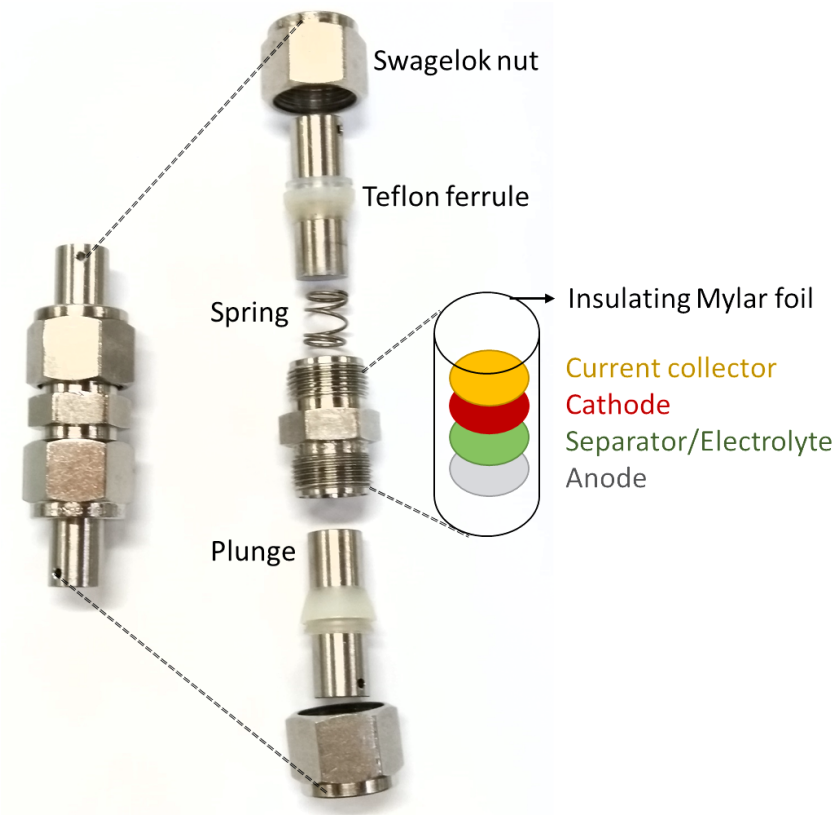

Figure 2.6: Swagelok cell set-up schematic where the different parts conforming the cell ready for testing are shown.

In addition for the $Li_{1.5}La_{1.5}TeO_6$ perovskite material, an asymmetrical cell composed of pelletised $Li_{1.5}La_{1.5}TeO_6$ material sandwiched between Li metal as reference electrode and sputtered gold as counter electrode was mounted on a Swagelok cell at 80 °C for CV analyses on the same VSP-3 instrument at a voltage scanning speed of 0.05 mV s^{-1}.

Galvanostatic Cycling with Potential Limitation (GCPL)

GCPL is an electrochemical technique that allows the analysis of the voltage evolution of an electrochemical cell when a constant current is applied across the cell until pre-established voltages limits are reached (Fig. 2.7).

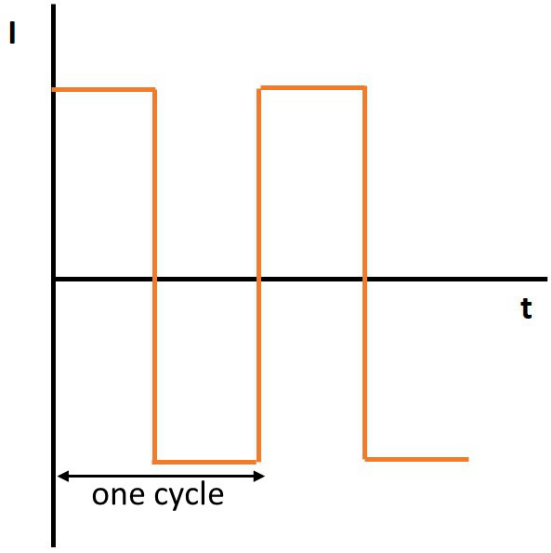

Figure 2.7: Schematic representation of the protocol carried out in a GCPL experiment where the applied current is constant until certain voltage is reached. After the voltage limit is reached, the current is then reversed until a second voltage limit is then reached, completing a full cycle.

In the case of lithium half-cells, the GCPL technique allows measurement of the specific capacity of an electrode material upon reaction and/or (de)insertion with/of lithium in an specific voltage range. The capacity of the electrode material can be calculated from Equation 2.5:

$$Q = \frac{nF}{M_w} \tag{2.5}$$

where Q is the electrode capacity in C kg^{-1}, n is the number of stored Li^+ in the electrode material upon cycling, F is the Faraday constant (*ca.* 96485 C mol^{-1}) and M_w is the molecular weight of the electrode active material. The number of stored Li^+ during the GPLC experiment can be calculated from Farady's Law as n = It / Fz, where I is the constant current applied, t is the duration of the charge/discharge cycling step and z is the ionic charge of the stored ion, one in the case of Li^+.

In order to analyse the crystal structure of the materials after cycling, the cycled cell was disassembled in an Ar-filled glovebox and the active electrode was washed with dry

THF to remove electrolyte residuals and dried before PXRD analysis.

2.3.6 X-ray Absorption Spectroscopy (XAS)

XAS is a powerful technique that can be applied to amorphous and crystalline materials providing information of the atom electronic structure and its local coordination environment. The technique is based in the excitation of core electrons of the atom when exposed to high energy X-ray radiation. When the X-ray photon energy is the same as the binding energy of a core electron, this core electron will be ejected from its core level to unoccupied higher energy orbitals or to the continuum. Each core electron has a defined binding energy which is element-specific. The technique relies on the analysis of the X-ray absorption (μ) by the analysed element with respect to the energy of the incident X-ray beam. $\mu(E)$ can be obtained in transmission experiments where $\mu(E)$ is calculated as the Napierian logarithm of the quotient between the incident X-ray radiation intensity on the sample and the transmitted intensity after the sample [$\mu(E) = \ln(I_0/I_t)$]. Other methods to obtain the $\mu(E)$ can be employed such as fluorescence or total electron yield measurements in the case of thick or diluted samples.

The abrupt X-ray absorption at a specific energy due to excitation from a core level is referred to as the "edge". The different edges for X-ray absorption at each different core level is denoted by capital letter and a Roman number subindex to differentiate between different type of orbitals in the same energy level. This edge notation begins with the

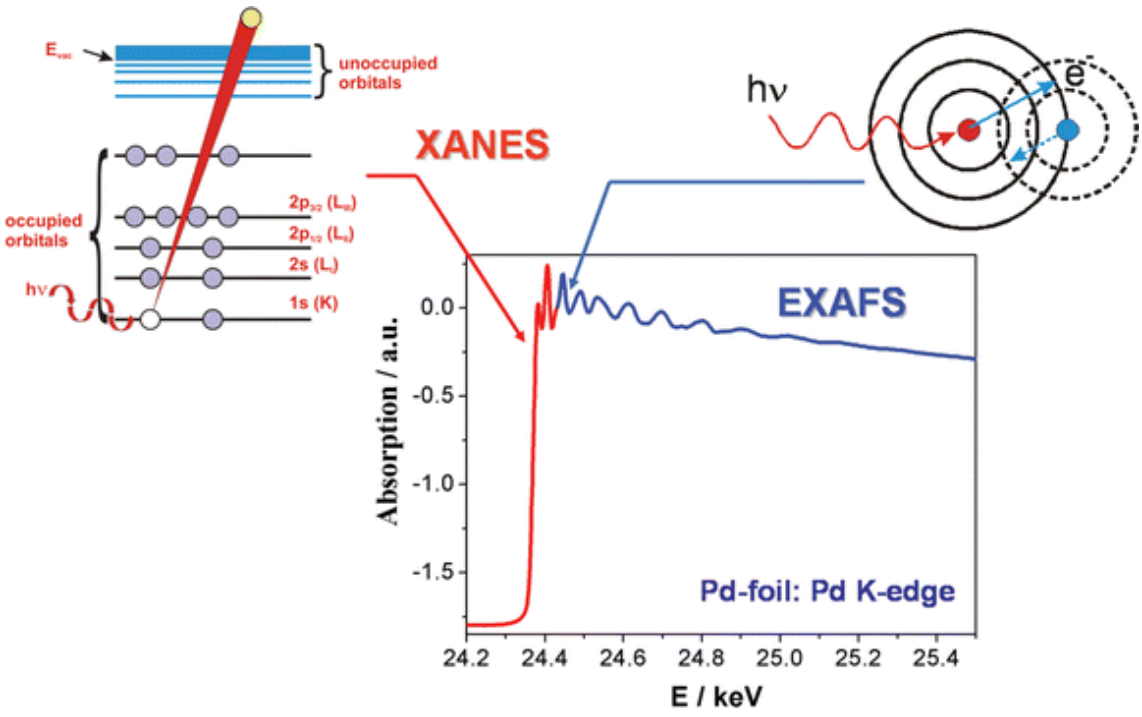

Figure 2.8: Schematic representation of the principle of XANES and EXAFS analyses and their regions within the XAS spectrum. Reprinted with permission from The Royal Society of Chemistry.[5]

letter K for the 1s orbital, L for the 2s and 2p orbitals (sub-classified as L_I, L_{II} and L_{III} for the different level sub-energies), M for the 3s,p,d orbitals and so on. In addition to the main edge, pre-edge features can also appear depending on the electronic structure and local symmetry of the element analysed.

Figure 2.8 shows the an example of the XAS spectrum for Pd metal where the two main zones of the spectra are indicated: the XANES region due to the emission of the photoelectron caused by the absorption of X-ray radiation by Pd atoms, and the EXAFS region due to interference between the emitted and backscattered photoelectrons.

X-ray Absorption Near Edge Structure (XANES)

The X-ray energy region of *ca.* 50–100 eV above the absorption edge is denoted as the XANES. The XANES region contains information of the oxidation state of the absorber and its local geometry. The position of the edge is related to the binding energy of the core electron, which can shift several eV depending on the oxidation state of the analysed atom. Increasing the oxidation state produces a higher positive charge on the excited atoms which results in electron states being more tightly bound and hence shifting the edge towards higher energy values. Comparison with standards of known oxidation states allows determination of the oxidation state the element under study by comparison of the edge position.

The local coordination geometry of the element can also be asserted by comparison of the main XANES features with standard materials of known coordination environments. In addition, the presence or lack of pre-edge features can also give insights into the electronic structure and local symmetry of the element. Transitions from s-orbitals to d-orbitals are forbidden by the dipole selection rule ($\Delta = 1$) for centrosymmetric coordination. The presence of pre-edge features can occur when transitions from the s orbital to the d orbitals are allowed by symmetry in non-centrosymmetric coordination geometries and if there are available free d-orbitals. In addition, hybridisation of the d-orbitals with p-orbitals of the ligands can also cause pre-edge features. As the name "pre-edge" indicates, these features appears at lower energies than the main edge, as the core electron is ejected to another orbital rather than to the continuum.

Extended X-ray Absorption Fine Structure (EXAFS)

The EXAFS is an oscillatory modulation in the X-ray absorption coefficient on the high-energy side of an absorption edge, *ca.* between 150 to 2000 eV after the absorption edge. This oscillatory modulation has its origin in the interaction of the emitted and backscattered photoelectrons by neighbouring atoms as represented in Figure 2.8. The EXAFS function (χ) can then be defined as in Equation 2.6, where μ represent the observed X-ray absorption value and μ_0 is the hypothetical smooth background absorption coefficient

due to the specific measured edge:

$$\chi = \frac{\mu - \mu_0}{\mu_0} \tag{2.6}$$

The backscattered photoelectron wave modifies the final-state wavefunction of the absorber, producing the variation between the expected linear smooth background and the observed oscillatory modulation. When the emitted and backscattered photoelectrons are in-phase, the wavefunction is increased producing a local maximum in the X-ray absorption. On the contrary, when these are out-of-phase the wavefunction is decreased producing a local minimum in the absorption coefficient.

The emitted photoelectrons have an associated wave vector, k, which then can be correlated to the EXAFS function and the local environment of the absorber atom (distance between the absorber and the scattering atoms and absorber coordination number) to meet the in- or out-of-phase conditions, as expressed on Equation 2.7:

$$\chi(k) = \sum_j \frac{N_j f_j(k) exp[-2k^2\sigma_j^2] exp[-2R_j\lambda]}{kR_j^2} sin[2kR_j + \delta_j(k)] \tag{2.7}$$

where N_j is the coordination number around the backscattered atom j, f_j represents the wave amplitude, δ_j(k) the phase shift between the photoelectron waves, λ is the mean free path of the photoelectron to travel and still participate in the EXAFS, σ_j is the Debye-Waller Factor which accounts for the decay with increasing energy as well as increasing disorder and R_j represents the distance between the emitting and the backscattering j atom.

In addition, the χ(k) can be multiplied by k^n (with n values between 1 and 3, usually) to amplify the low intensity oscillations at high k values.

The χ(k) data can be Fourier transformed and plotted as a function of the radial distance from the absorber which allows analysis of the radial distance between the absorber atom and its closest coordination shells.

The XAS data of all the samples analysed during this thesis were collected in the B18 beamline at Diamond Source of Light synchrotron. For the data acquisition, a few milligrams (between 10 – 100 mg) of the as-synthesised materials were mixed with cellulose fibre (*ca.* 100 mg) and compacted into a 10 mm diameter thin pellet. The thin pellet was mounted into a holder and exposed to the synchrotron X-ray radiation emitted by a bending magnet source which is monochromatised and focused by a vertically collimating Si mirror, a water-cooled Si(111) and Si(311) double crystal monochromator and a focusing double toroidal mirror. The data were collected in the transmission mode using three ionisation chambers mounted in series for simultaneous measurements on the sample and a tungsten foil as reference. Scans of *ca.* 3 to 5 minutes were collected over the desired energy range and merging of three consecutive scans was performed to obtain precise data sets. The data were processed and normalised using the Athena software

package using edge step normalisation. For fits of the EXAFS data, the Artemis software package was employed. The Artemis software allows one to perform FEFF calculations of the theoretical EXAFS from the crystal data obtained by diffraction methods to obtain the individual scattering pathways which then can be fit to the experimental EXAFS in order to compared atomic distances in the local and the average structures. Through the incorporated IFEFFIT algorithm, the data were fitted by a least-squares procedure until the best possible fit was achieved.

2.3.7 Microscopic Li^+ diffusion by muon-Spin Relaxation (μ^+SR)

In any alkali metal-ion battery material, the ionic diffusion is a key property which determines the performance of the battery, particularly the power delivery capability. There are different macroscopic methods for the study of the ionic conductivity in solid-state materials. However, these methods sometimes preclude the determination of the true material properties, since there are many external factors which may alter the obtained results. In the case of the most commonly employed AC impedance spectroscopy, several parameters such as the sintering temperature of the pelletised material, the contact electrodes employed, the pressing method or even the physical dimensions of the pelletised material can greatly affect the measured ionic conductivity.[6,7] This makes the direct comparison of ionic properties of a material with their counterparts in the literature a difficult task and even within the same research study the need for a precise control of all these parameters to avoid any misreading.

Microscopic techniques for ionic diffusion are also available such as quasi-elastic neutron scattering and NMR techniques. Unfortunately, the quasi-elastic neutron scattering time scale only allows the study of motional correlation events occurring in the 10^{-9} to 10^{-12} s range and depending on the diffusion rate of the ionic species, this can be outside of this range. In the case of NMR technique, this provides a wide time scale range, but the presence of magnetic ions in the material can interfere with the spin-lattice relaxation rate ($1/T_1$), complicating the analysis of the ionic diffusion. μ^+SR spectroscopy allows the study of ionic diffusion in solid state materials on a time scale between 10^{-5} to 10^{-8} s where most long-range and consecutive short-range jumps of ions between interstitial sites occur. In addition, μ^+SR also allows one to probe and model ionic diffusion in those materials which contains magnetic ions, since both electronic and nuclear contributions to the muon depolarisation can be separated, making μ^+SR an excellent technique for the microscopic study of the ionic motions in crystalline materials.[8] The μ^+SR technique was applied with success to study lithium diffusion in battery materials for the first time in 2009 by Sugiyama and co-workers on the layered cathode material Li_xCoO_2 and subsequently to other cathode materials such as the $LiMPO_4$ olivine family or the layered Li_2MnO_3.[9–12] Regarding solid-state electrolytes, there are only a few studies and specifically for garnet materials there is only one precedent on the $Li_7La_3ZrNbO_{12}$ family.[13] More recently the

technique has also been applied to study Na^+ diffusion in Na-battery materials, such as the $NaCoO_2$ layered cathode material.[8]

Spin polarised positive muons (μ^+) are subatomic particles with spin 1/2, a mass of 105.7 MeV c^{-2}, a charge of $+1e^-$ and a mean lifetime of 2.2 µs. μ^+ particles can be produced by hitting a carbon target with a high energy proton beam which produces pion particles. These pion particles decay within the nanoseconds to a neutrino and a muon. These muons, which are near 100 % spin polarised due to parity violation,[14] are guided and collimated through a complex system of bending magnets and quadrupoles until they reach the sample. Once the muons have been implanted into the sample, they form stable $\mu^+ - O^{-2}$ bonds of *ca.* 1.1 Å in oxide materials. Because of its net spin, muons are able to sense a field distribution width (Δ) due to the surrounding local magnetic fields of nuclear origin, and the motion of surrounding nuclei provokes the spin of the muon to fluctuate at a determined rate (ν). A simplified version of this process is represented in Figure 2.9.

After the muon has probed the properties of the material, it decays into a positron which leaves the material preferentially in the same direction of the muon spin at the moment of decay. This allows one to follow the muon spin dynamics by detecting the decay positron asymmetry (P_z) using two banks of detectors placed at the front and at the back of the sample stage. The asymmetry of the positron decay is defined by Eq. 2.8, where a_0 is the initial decay asymmetry, which mainly depends of the average energy of the muon beam, $N_{B,F}$ are the number of positrons detected by the backward and forward detectors and α is a calibration parameter to compensate for any displacement of the

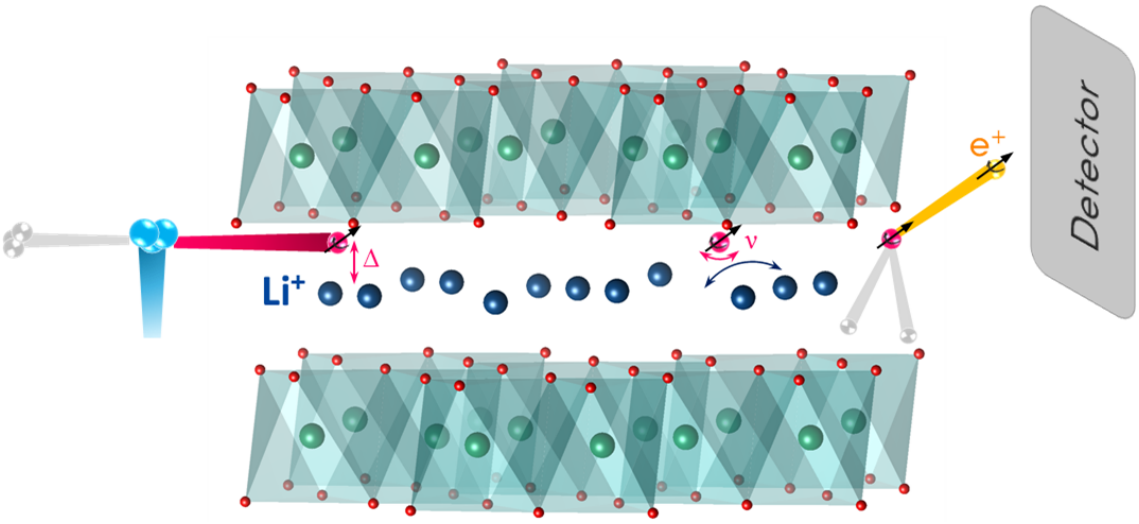

Figure 2.9: Simplified version of the muon implantation and interaction with the studied crystalline material. Blue balls represent the positive pions, grey balls are the expelled neutrinos and the pink balls are the positive µ.

sample from the centre of the detectors:

$$P_z(t) = a_0 \frac{N_F(t) - \alpha N_B(t)}{N_F(t) + \alpha N_B(t)} \tag{2.8}$$

The time evolution of the decay positron asymmetry can be modelled with the Keren function which represents an analytic generalisation of the Abragam function appropriate for the μ^+SR experiment (Eq. 2.9):[15]

$$P_z(t) = exp[-\Gamma(\Delta,\nu,\omega_L,t)t] \tag{2.9}$$

where in addition to the variation of Δ and ν parameters with time (t), this function also takes into account for the muon's Larmor precession frequency (ω_L). If there is any magnetic contribution due to the presence of unpaired electrons in the material, an additional temperature-independent relaxation rate [exp(λt)] can be added to the Keren function, to model the magnetic behaviour of the material.

The ν parameter can be then correlated to the ionic hopping rate and the ionic diffusion coefficient can be calculated taking into account the crystal structure parameters of the analysed materials, as specifically detailed in the corresponding results chapters.

μ^+SR studies were performed using the EMU instrument at the ISIS pulsed muon facility. The powdered sample, *c.a.* 1.5 g, was packed into a disk of 30 mm diameter and 1.5 mm thickness and sealed in a titanium sample holder where the front window was made of 25 μm thickness titanium foil. 3.2 MeV spin-polarised positive muons were implanted into the sample and the outcoming positrons were detected by 96 scintillator segments grouped in two circular arrays. The temperature was controlled from 100 K up to a maximum of 600 K by a hot stage attached to a closed cycle refrigerator and the measurements were acquired at three different applied longitudinal magnetic fields (0, 5 and 10 G). A 20 G transverse magnetic field was also applied for the initial asymmetry calibration. The data fits were carried out through the WiMDA data analysis program.[16]

References

[1] A. C. Hannon, *Nucl. Instrum. Methods Phys. Res., Sect. A*, 2005, **551**, 88–107.

[2] A. C. Larson and R. B. von Dreele, *Los Alamos Natl. Lab., [Rep.] LA (U. S.)*, 1994, 86–748.

[3] B. H. Toby, *J. Appl. Crystallogr.*, 2001, **34**, 210–213.

[4] H. Rietveld, *Acta Crystallogr.*, 1966, **20**, 508–513.

[5] J.-D. Grunwaldt and A. Baiker, *Phys. Chem. Chem. Phys.*, 2005, **7**, 3526–3539.

[6] J. Wolfenstine, J. Ratchford, E. Rangasamy, J. Sakamoto and J. L. Allen, *Mater. Chem. Phys.*, 2012, **134**, 571 – 575.

[7] H. El-Shinawi and J. Janek, *J. Power Sources*, 2013, **225**, 13 – 19.

[8] M. Månsson and J. Sugiyama, *Phys. Scr.*, 2013, **88**, 068509.

[9] J. Sugiyama, K. Mukai, Y. Ikedo, H. Nozaki, M. Månsson and I. Watanabe, *Phys. Rev. Lett.*, 2009, **103**, 147601.

[10] J. Sugiyama, *J. Phys. Soc. Jpn.*, 2013, **82**, SA023.

[11] T. E. Ashton, J. V. Laveda, D. A. MacLaren, P. J. Baker, A. Porch, M. O. Jones and S. A. Corr, *J. Mater. Chem. A*, 2014, **2**, 6238–6245.

[12] J. Sugiyama, H. Nozaki, K. Mukai, M. Harada, M. Månsson and A. Hillier, *Solid State Ionics*, 2014, **262**, 901 – 903.

[13] H. Nozaki, M. Harada, S. Ohta, I. Watanabe, Y. Miyake, Y. Ikedo, N. H. Jalarvo, E. Mamontov and J. Sugiyama, *Solid State Ionics*, 2014, **262**, 585 – 588.

[14] R. L. Garwin, L. M. Lederman and M. Weinrich, *Phys. Rev.*, 1957, **105**, 1415–1417.

[15] A. Keren, *Phys. Rev. B*, 1994, **50**, 10039–10042.

[16] F. Pratt, *Physica B*, 2000, **289**, 710–714.

Chapter 3: Aliovalent Zn-, Ga-, and Al-doped LBLTO garnet solid electrolytes

Lithium-containing garnets present a wide range of compositions due to the versatility of their crystal framework.[1] Li^+ content per formula unit in lithium garnet materials can vary from $Li^+ = 3$ for the conventional compound to a theoretical upper limit of $Li^+ = 7.5$ for the most lithium-rich compositions, depending on the combination of valencies for the other metals comprising the garnet crystal. Experimentally, only compositions up to 7 moles of lithium per formula unit have been practically achieved,[2] with garnets containing 5 to 7 Li^+ mols per formula unit achieving the highest ionic conductivities. Aliovalent doping on $Li^+ = 7$ compositions is required in order to avoid the phase transformation from the highly conducting $Ia\bar{3}d$ cubic phase to the low conducting $I4_1/acd$ tetragonal phase with increasing Li^+ content, *via* a vacancy-creation mechanism that stabilises the cubic phase.[3] It has been recently reported that lithium garnets with Li^+ integer compositions can present ordered ground-state crystal structures that can lower Li^+ mobility due to reductions in the Li-Li interactions on these ordered phases.[4] The introduction of a suitable dopant into the structure not only allows for the stabilisation of the cubic phase but can also increase the ionic transport of the garnet materials by increasing Li^+ dynamics through introduction of additional repulsive forces between dopants and Li^+ ions[5] or by reducing the grain boundary resistances with better particle sintering.[6–8] Thus, introduction of additional Li^+ vacancies in the garnet structure *via* aliovalent doping is expected to enhance the transport properties of these materials.

This chapter focuses on the solid state synthesis of the $Li_6BaLa_2Ta_2O_{12}$ garnet material (hereafter refereed to as LBLTO) and the subsequent aliovalent doping with Zn^{2+}, Ga^{3+} and Al^{3+} cations. Structural changes have been evaluated by PXRD and XAS measurements in order to identify the most likely atomic position for the dopant within the garnet framework. Variable temperature EIS studies of the synthesised materials have been employed to study the interrelation between the aliovalent substitutions of Li^+ and the ionic transport properties of the resultant materials. The local properties of the parent LBLTO garnet material have also been studied by means of μ^+SR spectroscopy to analyse the local dynamics of Li^+ ions in the microscopic range.

3.1 Synthesis, structural and morphological studies of aliovalently doped LBLTO

Zn-, Ga-, and Al-doped LBLTO garnet materials were synthesised by a microwave-assisted solid-state approach. By employing microwave-assisted solid-state methods, it was possible to take advantage of both types of heating: radiant and microwave heating. Radiant heating provides a controlled temperature along the sample cavity while microwave heat-

ing enhanced the kinetics of the reaction by providing faster, localised and homogeneous heating within the sample. Microwave heating is possible when any of the materials present in the reaction are relatively good dielectrics with high dielectric loss.[9] In this synthesis, $LiOH \cdot H_2O$ and Al, Ga and Zn nitrate precursors were employed which are reported to couple well with microwaves.[10,11] In addition, the use of microwave methods reduce the consumption of energy, due to the shorter reaction times and the more efficient use of the power supplied.

For the undoped LBLTO garnet material, the use of this microwave-assisted method led to reductions in the reaction times and temperatures required to obtain phase pure material compared with the original synthesis reported by Thangadurai and Weppner.[12] The reaction temperature was lowered by 100 °C and the time required to obtain phase pure material went from 24 hours to just 6 hours. Table 3.1 summarises the different compositions prepared in this chapter and the synthetic conditions employed for their preparation:

Table 3.1: Nomenclature employed for the prepared materials in this chapter and synthetic conditions employed for their microwave hybrid synthesis. Conventional synthesis reported in literature is also given for comparison.

Nominal composition	Microwave	Conventional
$Li_6BaLa_2Ta_2O_{12}$ (LBLTO)	800 °C, 6 hours	900 °C, 24 hours[12]
$Li_{5.70}Al_{0.10}BaLa_2Ta_2O_{12}$ ($Al_{0.10}$LBLTO)	800 °C, 6 hours	new composition
$Li_{5.25}Al_{0.25}BaLa_2Ta_2O_{12}$ ($Al_{0.25}$LBLTO)	800 °C, 6 hours	new composition
$Li_{5.70}Ga_{0.10}BaLa_2Ta_2O_{12}$ ($Ga_{0.10}$LBLTO)	800 °C, 6 hours	new composition
$Li_{5.25}Ga_{0.25}BaLa_2Ta_2O_{12}$ ($Ga_{0.25}$LBLTO)	800 °C, 6 hours	new composition
$Li_{5.70}Zn_{0.15}BaLa_2Ta_2O_{12}$ ($Zn_{0.15}$LBLTO)	800 °C, 6 hours	new composition
$Li_{5.25}Zn_{0.37}BaLa_2Ta_2O_{12}$ ($Zn_{0.37}$LBLTO)	800 °C, 6 hours	new composition

Sample purity was assessed by in-house PXRD. PXRD data of the parent compound LBLTO were indexed successfully to the $Ia\bar{3}d$ cubic space group with narrow Bragg peaks, indicating high crystallinity of the synthesised material (Fig. 3.1).

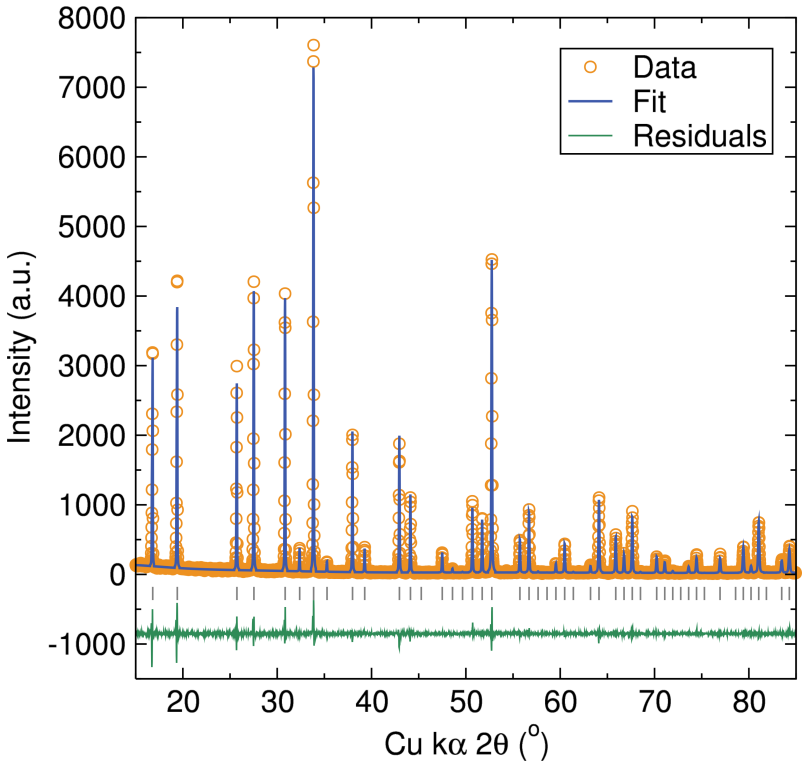

Figure 3.1: Rietveld refinements to PXRD data for the $Li_6BaLa_2Ta_2O_{12}$ material. Bragg peaks positions for the cubic $Li_6BaLa_2Ta_2O_{12}$ garnet structure are indicated by vertical grey tick marks. Fit was in good agreement to the cubic space group $Ia\bar{3}d$ with the following cell parameters: a = 13.0018(1) Å and V = 2197.89(3) Å^3. R_{wp} = 0.1381, R_p = 0.1002, R_{F^2} = 0.0344 and χ^2 = 2.055.

The atomic arrangement of the LBLTO garnet structure is represented in Figure 3.2. Ba^{2+} and La^{3+} cations are statically disordered, occupying the distorted cubic position indicated as 24c in Wyckoff notation. Ta^{5+} cations sit on the 16a Wyckoff position, occupying the centre of an octahedron. Finally, a Li^+ ionic network is formed on the 24d tetrahedral positions and the 48g octahedral positions.

Atom positions, fractional occupancies, thermal energies and cell parameters were calculated by Rietveld refinements of the garnet structure against the experimental data (Fig. 3.1). The refined parameters are summarised in Table 3.2. Atomic parameters for Li^+ ions were not refined as the Li^+ X-ray scattering form factor is too small compared to the heavy Ba^{2+}, La^{3+} and Ta^{5+} crystal neighbours, leaving Li^+ ions almost invisible to lab-quality PXRD. The refined unit cell parameter value was 13.0018(1) Å, in good agreement with the reported value of 13.00 Å for undoped LBLTO.[12,13]

Stoichiometries for the doped LBLTO garnets were tailored in a manner that the dopant cations would be inserted into the Li^+ ionic sublattice, replacing the Li^+ ions in the garnet structure. The election of the aliovalent dopant replacing the Li^+ was rationalised in terms of atomic size, charge compensation and site geometry. Li^+ ions have a cationic size of 59 pm in a tetrahedral environment and an increased size of 74 pm if the coordination environment is octahedral.[14] Al^{3+}, Ga^{3+} and Zn^{2+} have cationic sizes of 39, 47 and 60 pm respectively in a tetrahedral coordination, while their cationic sizes

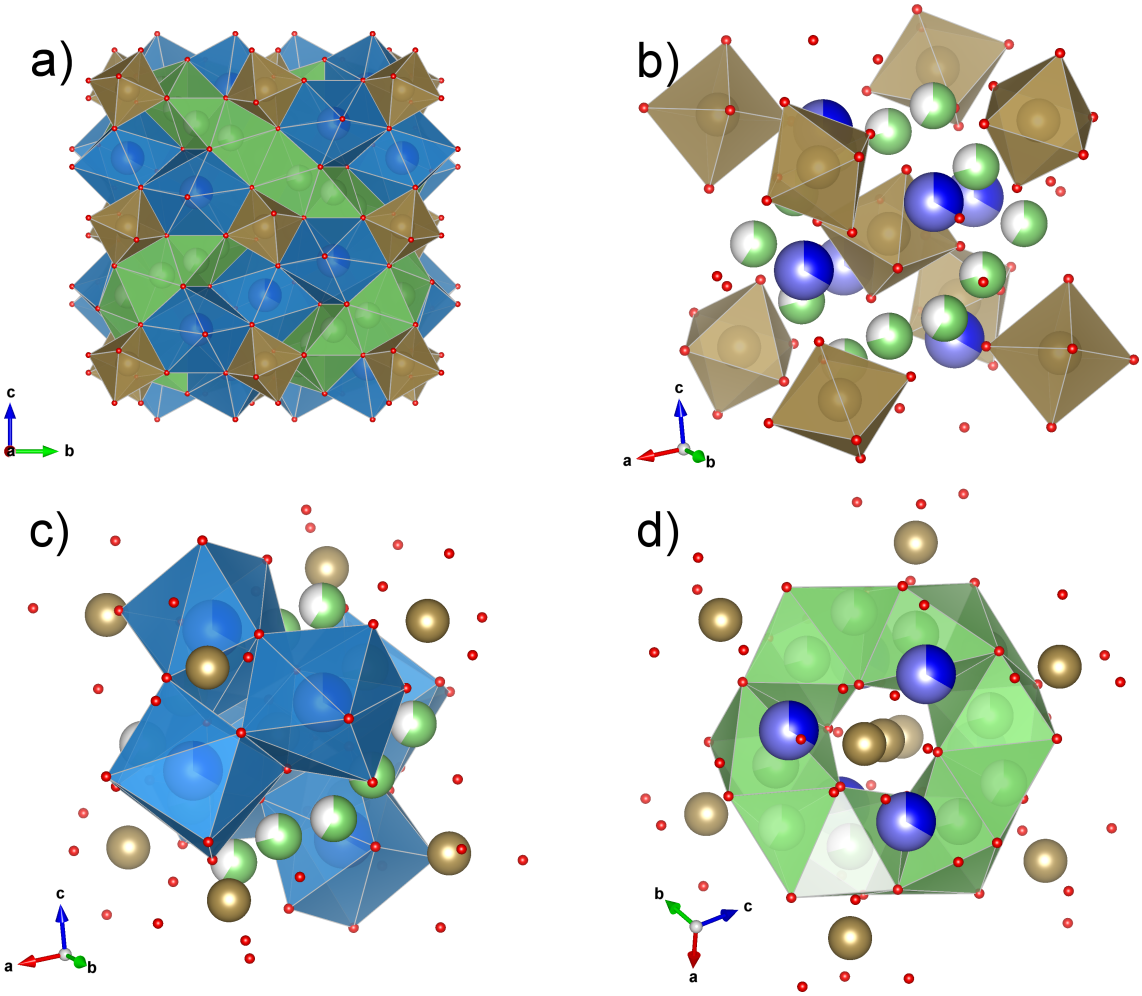

Figure 3.2: a) Crystallographic representation of the unit cell for the $Li_6BaLa_2Ta_2O_{12}$ structure with $Ia\bar{3}d$ cubic symmetry where Ba^{2+} and La^{3+} cations are enclosed in blue polyhedra, Ta^{5+} in brown polyhedra and Li^+ ion in the remaining green polyhedra. (b) small fraction of the crystal lattice for the $Li_6BaLa_2Ta_2O_{12}$ garnet structure with the octahedral coordination polyhedra for the Ta^{5+} ions explicitly shown. (c) small fraction of the crystal lattice for the $Li_6BaLa_2Ta_2O_{12}$ garnet structure where only the distorted cubic coordination polyhedra for the Ba^{2+}/La^{3+} ions are represented for clarity. (d) small fraction of the crystal lattice for the $Li_6BaLa_2Ta_2O_{12}$ garnet structure where the tetrahedral and octahedral coordination polyhedra for Li^+ ions are represented.

Table 3.2: Extracted atomic parameters from Rietveld refinement of the $Li_6BaLa_2Ta_2O_{12}$ PXRD. Refined a = 13.0018(1) Å.

Atom	x	y	z	Uiso (100/Å^2)	Site	Frac.
Li1	3/8	0	1/4	2.43	24d	0.300
Li2	0.1456	0.656485	0.56	2.41	96h	0.420
Ba1	1/8	0	1/4	2.34(4)	24c	0.330(3)
La1	1/8	0	1/4	2.34(4)	24c	0.666
Ta1	0	0	0	2.34(4)	16a	1.000
O1	-0.0355(4)	0.0473(5)	0.1456(4)	2.35(4)	96h	1.000

increase to 53, 62 and 75 pm on octahedral coordination, respectively.[14] In addition to this, La^{3+} and Ba^{2+} have far larger cation sizes (>100 pm on their 8-fold coordination)[14] and the relative low valence of Zn^{2+} compared to the Ta^{5+} cations makes unlikely for Zn^{2+} to replace Ta^{5+} in the garnet structure since this position is occupied predominantly by $M^{>4+}$ cations.[2] The relatively close ionic sizes and charges between the dopants and the Li^{+} ions indicates that doping into the Li^{+} positions is a plausible route for the insertion of the dopants into the LBLTO garnet structure. Recent computational analyses over a wide range of dopants for the garnet structure has shown that Al^{3+}, Ga^{3+} and Zn^{2+} display a preference for the Li^{+} positions.[15] Moreover, similar substitutions routes have been experimentally explored for the LLZO garnet family, also demonstrating the preference of Al^{3+}, Ga^{3+} and Zn^{2+} towards the Li^{+} positions.[5–7,16,17]

The dopant concentrations were chosen to allow for direct comparison between various doped materials in terms of the Li^{+} carrier concentrations on the ionic conductivity analyses. The Li^{+} concentration was set at two values to generate two comparable materials groups: one with a Li^{+} content of 5.25 moles per formula unit and the other at 5.7 moles per formula unit. Dopant levels were then chosen to ensure overall charge balance is maintained.

Figure 3.3 shows the in-house PXRD data at RT for the different doped LBLTO compositions synthesised. The profiles of the PXRDs displayed sharp peaks, indicative of the high crystallinity of the microwave synthesised materials with no other noticeable Bragg reflections from impurities detected. The dotted line corresponding to the (402) reflection is used as a eye guide to follow the small displacement of the peak towards higher diffraction angles due to cell contraction with doping.[18]

The low level of the dopants in the crystal structure of the synthesised materials, together with the relatively small X-ray form factors of these dopants compared to the other heavier metals present in the structure, presents a challenge in realistically refining their atomic parameters - at least with laboratory PXRD data. To try to evaluate the insertion of the dopant into the garnet structure, Le Bail analyses[19] of the PXRD data to the $Ia\bar{3}d$ space group were performed.

Figure 3.4 shows the variation of the unit cell parameter respect to the dopant concentration on the LBLTO material. Since all dopants had a smaller than or similar size to the substituted Li^{+} ions, the cell parameter experienced a linear decrease with increasing concentration of the dopant as expected. Attempts were made to prepare materials with higher dopant concentrations, for example $Li_{4.5}Al_{0.5}BaLa_2Ta_2O_{12}$. However, as the solubility limits of the dopant were surpassed, these attempts resulted in high impurity content materials. The cell parameter variation is in good agreement with Vegard's law, indicating the effective formation of a solid-solution.[20]

Zn^{2+} ions have a similar ionic radius as Li^{+}, thus displaying the lowest gradient in the Vegard fit. The larger cationic charge on Zn^{2+} ions results in stronger bonding to the surrounding oxygen anions leading to a smaller cell parameter to compensate for the

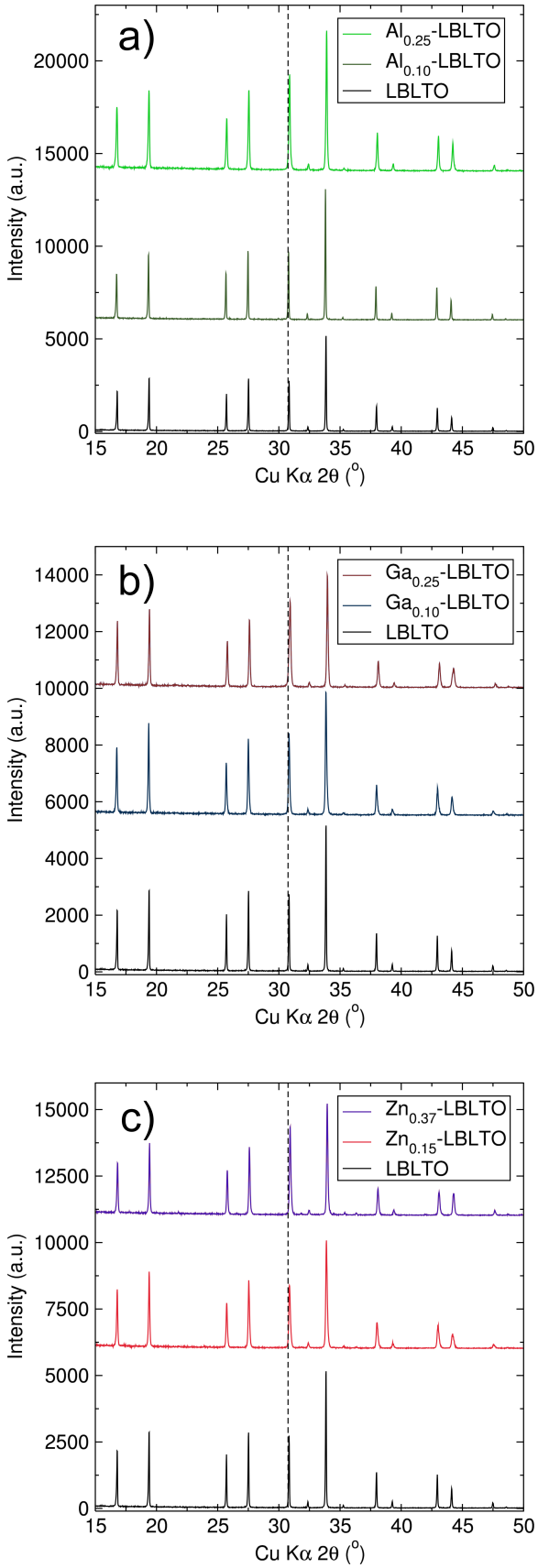

Figure 3.3: PXRD patterns collected from the (a) Al-doped $Li_{6-3x}Al_xBaLa_2Ta_2O_{12}$ (Al_x-LBLTO), (b) Ga-doped $Li_{6-3x}Ga_xBaLa_2Ta_2O_{12}$ (Ga_x-LBLTO) and (c) Zn-doped $Li_{6-2x}Zn_xBaLa_2Ta_2O_{12}$ (Zn_x-LBLTO) materials.

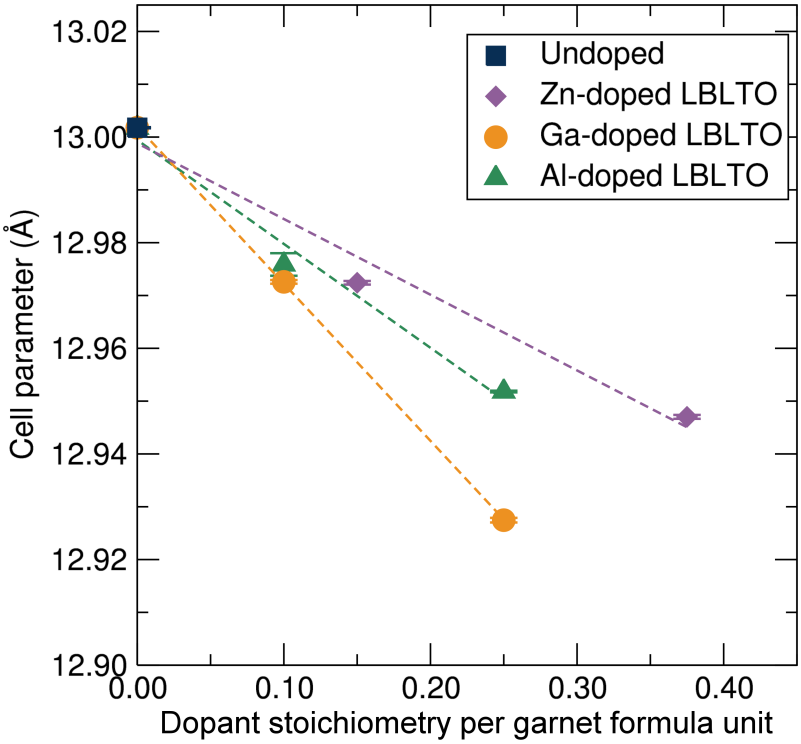

Figure 3.4: Unit cell parameter evolution for the cubic $Ia\bar{3}d$ garnet crystal structure with increasing dopant concentration.

higher valence of the Zn^{2+} cation. In the case of Al^{3+}, despite possessing the largest difference in atomic size compared with Li^{+}, the slope of the Vegard fit for the Al^{3+} doped samples is smaller than that for the Ga^{3+} dopant. with a smaller ionic size difference with Li^{+}. A plausible explanation could be that some of the Ga^{3+} cations also occupy the larger 48h octahedral positions, where Ga^{3+} can be accommodated, allowing the crystal cell to further contract.

XAS experiments were carried out to analyse the local coordination environment of the dopants in the garnet structure. Hard-XAS measurements on the Ga and Zn K-edges (10.37 and 9.66 keV respectively) were performed at B18 beamline at the Diamond Light Source synchrotron. Unfortunately, measurement on the Al K-edge (1.56 eV) was not possible as this edge falls outside the energy range available at the B18 beamline (2.05 – 35 eV). The presence of strong absorption edges from the Ta L_{II} (11.14 keV) and L_{III} (9.89 keV) edges precluded a detailed EXAFS analysis of the local coordination shells of the dopant, limiting to qualitative assessments of the XANES region of the dopant against standards with known coordination environments.

For the Zn K-edge analyses, ZnO and $Zn(NO_3)_2 \cdot 6\,H_2O$ were chosen as standards. ZnO crystallises in the wurtzite structure under ambient conditions with a $P6_3mc$ group space symmetry.[21] In this crystal structure, Zn^{2+} cations are tetrahedrally coordinated to four O^{2-} anions. In the case of $Zn(NO_3)_2 \cdot H_2O_6$, the compound crystallises in the orthorhombic space group *Pnma*, where the Zn^{2+} cations are coordinated to six O^{2-} anions forming an octahedron.[22]

Figure 3.5 shows the Zn K-edge XANES data of the Zn-doped $Li_{5.25}Zn_{0.37}BaLa_2Ta_2O_{12}$ garnet material together with the ZnO and $Zn(NO_3)_2 \cdot 6\,H_2O$ standards. The profile of the $Li_{5.25}Zn_{0.37}BaLa_2Ta_2O_{12}$ garnet spectrum shares almost identical features with the ZnO standards, where Zn^{2+} form oxygen-coordinated tetrahedra. The main features are highlighted by shadowing rectangular boxes. The absorption intensity of the Zn K-edge is related to electronic transitions from Zn 1s orbital to the empty Zn 4p orbital. The absence of empty 3d orbitals in Zn^{2+} cations precludes the easy differentiation between tetrahedral and octahedral coordination due to the lack of a pre-edge feature in the Zn K-edge spectra. In the former, a pre-edge feature could appear from s to d transitions while in the latter the centrosymmetry of the octahedral environment would forbid this transition. In the case of Zn^{2+} in an octahedral environment, a single strong peak is observed. When the local environment is changed to a tetrahedral coordination, a split on the main peak is produced with a shoulder noted. A similar profile is noted for the $Li_{5.25}Zn_{0.37}BaLa_2Ta_2O_{12}$ material. This gave a rough indication that the Zn^{2+} cations in the garnet structure tend to occupy the tetrahedral Li^+ 24d positions.

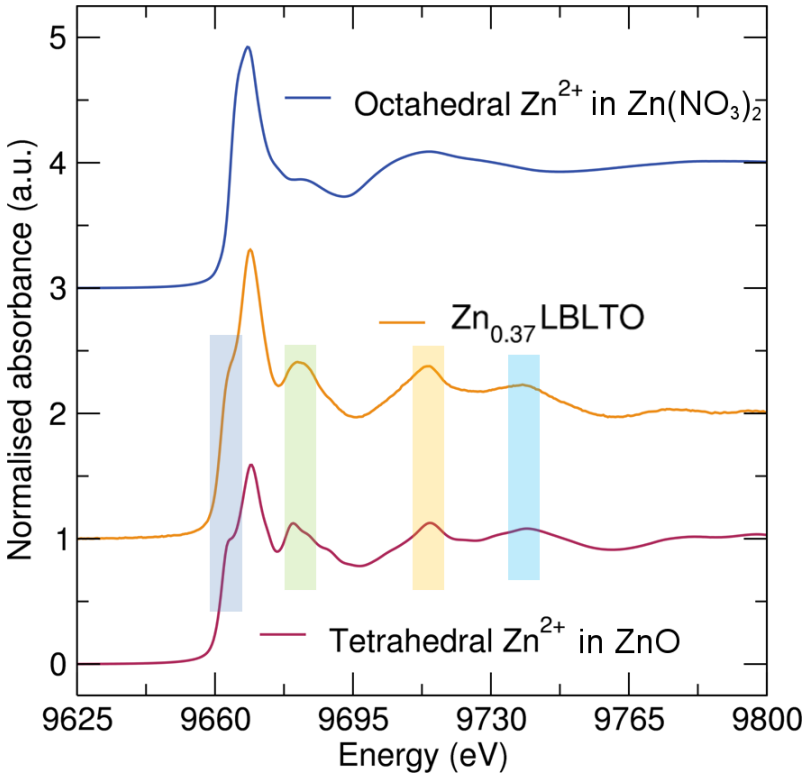

Figure 3.5: XANES region of the XAS data measured on the Zn K-edge for $Li_{5.25}Zn_{0.37}BaLa_2Ta_2O_{12}$, and $Zn(NO_3)_2 \cdot 6\,H_2O$ and ZnO standards.

Analogous analyses were carried out for the $Li_{5.25}Ga_{0.25}BaLa_2Ta_2O_{12}$ garnet material. Figure 3.6 shows the XANES region of the XAS data on the Ga K-edge for the $Li_{5.25}Ga_{0.25}BaLa_2Ta_2O_{12}$ material and the β-Ga_2O_3 and $Ga(NO_3)_3 \cdot 9\,H_2O$ standards. $Ga(NO_3)_3 \cdot 9\,H_2O$ crystallises in a monoclinic structure with space group $P21/c$ where the Ga^{3+} cations occupy the centre of an octahedron.[23] The β-Ga_2O_3 standard crystallises in

a monoclinic structure with point symmetry *C*2/*m*, where Ga^{3+} cations are distributed in both octahedral and tetrahedral oxide coordination sites.[24] Again, as Ga^{3+} is isoelectronic with Zn^{2+} and possesses full 3d orbitals, simple confirmation of tetrahedral or octahedral coordination from the presence/absence of pre-edge features is not possible.

In the $Li_{5.25}Ga_{0.25}BaLa_2Ta_2O_{12}$ XANES data, the peak splitting observed on the main edge indicates the lack of exclusive octahedral coordination around the Ga^{3+} cations, indicating that the Ga^{3+} ions are also occupying tetrahedral Li^+ 24d positions in the garnet structure, similar to the Zn doped analogue. However, this does not exclude the possibility of some Ga^{3+} ions being located on octahedral coordination sites. In fact, a similar feature between the $Li_{5.25}Ga_{0.25}BaLa_2Ta_2O_{12}$ garnet material and the $Ga(NO_3)_3 \cdot 9\,H_2O$ standard, highlighted with a blue rectangular box, could indicate the possibility of Ga^{3+} ions occupying octahedral as well as tetrahedral Li^+ positions in the garnet structure. This observation is in agreement with studies by Rettenwander *et al.* where Ga^{3+} has been found to be located on both Li^+ 24d and 48g positions by NMR studies.[25] There is, however, an active debate within the literature as to the different dopant positions within the garnet structure, specially for Al^{3+} and Ga^{3+} in the LLZO system, where doping is required to stabilise the cubic phase.

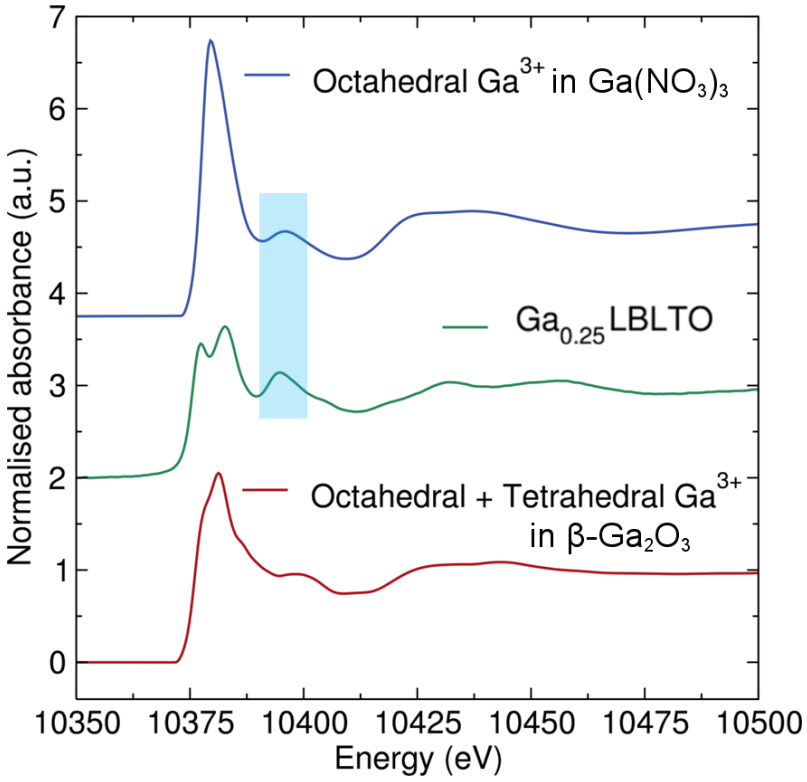

Figure 3.6: XANES region of the XAS data measured on the Ga K-edge for $Li_{5.25}Ga_{0.25}BaLa_2Ta_2O_{12}$ and $Ga(NO_3)_3 \cdot 9\,H_2O$ and Ga_2O_3 standards.

SEM images of the synthesised material were obtained in order to assess the particle size and morphology (Fig. 3.7). The micrographs revealed inhomogeneous particles with non-regular shapes with sizes ranging from ≈ 1 to 10 micrometers. The particle sizes and

morphologies had no apparent changes with the insertion of the dopant into the garnet structure. EDX analyses were also performed for the highest doped LBLTO garnets to analyse the stoichiometry of the compositions studied (Table 3.3). Atomic concentrations from EDX measurements were all, within the standard deviations, in agreement with the nominal stoichiometries of the synthesised materials. The atomic concentrations were normalised to the Ta^{5+} concentration, as this element is fully occupying its site within the garnet structure and has negligible volatility compared to other elements present in the materials. All pelletised samples had a similar relative geometric density of $\sim$ 80%, with no variation within the uncertainty of the density measurements.

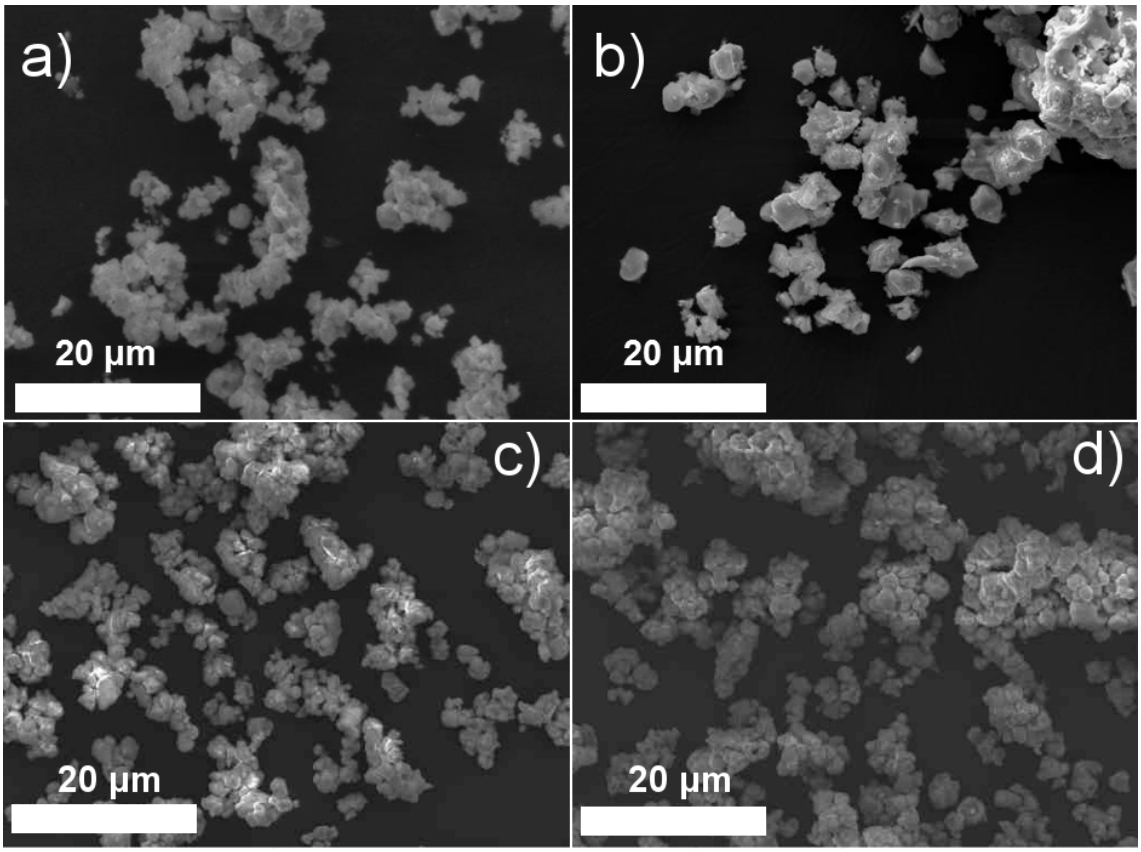

Figure 3.7: SEM images of the (a) undoped $Li_6BaLa_2Ta_2O_{12}$, (b) $Li_{5.25}Al_{0.25}BaLa_2Ta_2O_{12}$, $Li_{5.25}Ga_{0.25}BaLa_2Ta_2O_{12}$ and (c) $Li_{5.25}Zn_{0.37}BaLa_2Ta_2O_{12}$ garnet materials.

Table 3.3: Atomic concentration of the different metals present in the $Li_6BaLa_2Ta_2O_{12}$, $Li_{5.25}Al_{0.25}BaLa_2Ta_2O_{12}$, $Li_{5.25}Ga_{0.25}BaLa_2Ta_2O_{12}$ and $Li_{5.25}Zn_{0.37}BaLa_2Ta_2O_{12}$ materials as obtained from EDX measurements.

Metal	LBLTO	$Al_{0.25}$LBLTO	$Ga_{0.25}$LBLTO	$Zn_{0.37}$LBLTO
Al	-	0.3(3)	-	-
Ga	-	-	0.2(2)	-
Zn	-	-	-	0.2(3)
Ba	1.1(6)	1.3(3)	1.0(2)	0.9(3)
La	2.2(8)	2.8(9)	1.7(5)	2.0(6)
Ta	2.0(3)	2.0(3)	2.0(2)	2.0(3)

3.2 Ionic transport properties

The LBLTO garnet material is reported to be one of the best performing garnet composition in terms of transport properties. The LBLTO intra-grain ionic conductivity is on the order of 10^{-5} S cm^{-1}, with reported activation energies as low as 0.4 eV.[12] Most studies have focussed in modifying the transport properties of the LBLTO material by tweaking the Ba^{2+}/La^{3+} ratios or by Ta^{5+} substitutions[26,27] with other elements. Microstructure engineering has also been explored to reduce inter-grain resistances.[28,29] Doping on the Li^+ positions, however, has remained unexplored for this garnet composition where no studies have been performed to date.

In order to evaluate the impact of doping into the Li^+ positions on the macroscopic transport properties, EIS measurements were carried out. Figure 3.8 shows the room temperature Nyquist plots of the EIS measurement for the undoped LBLTO material and the Al-, Ga- and Zn-doped Li = 5.7 garnet compositions. The Nyquist plots show the resistance of the materials towards the applied ac current. The presence of a tail at low frequencies due to the Pt blocking electrodes indicates the ionic character of this resistance due to Pt blocking electrodes.[30] Unlike other ionic conductors where intra-grain and inter-grain contributions to the total ionic resistance can normally be separated, this is not always a trivial task in the case of the garnets, where the total resistance (sum of intra- and inter-grain resistance) is often reported since separation of the two contributions cannot always be resolved at higher temperatures.[31,32] There are some exceptions to this, as in the case of hot pressed garnet materials where both contributions to the total resistance can be resolved.[33]

The total resistance for the LBLTO materials was modelled according to an external electrical circuit composed of a resistance with a parallel constant phase element. As previously introduced, lithium solid-state electrolytes act as pure electrical resistances which allows to calculate their ionic conductivity from the measured resistance in the EIS experiments. The constant phase element models double layer capacitance behaviour

between the electrode and the garnet material. A constant phase element was used instead of a capacitor in order to account for any nonideal behaviour and dispersion in the time constant.[34]

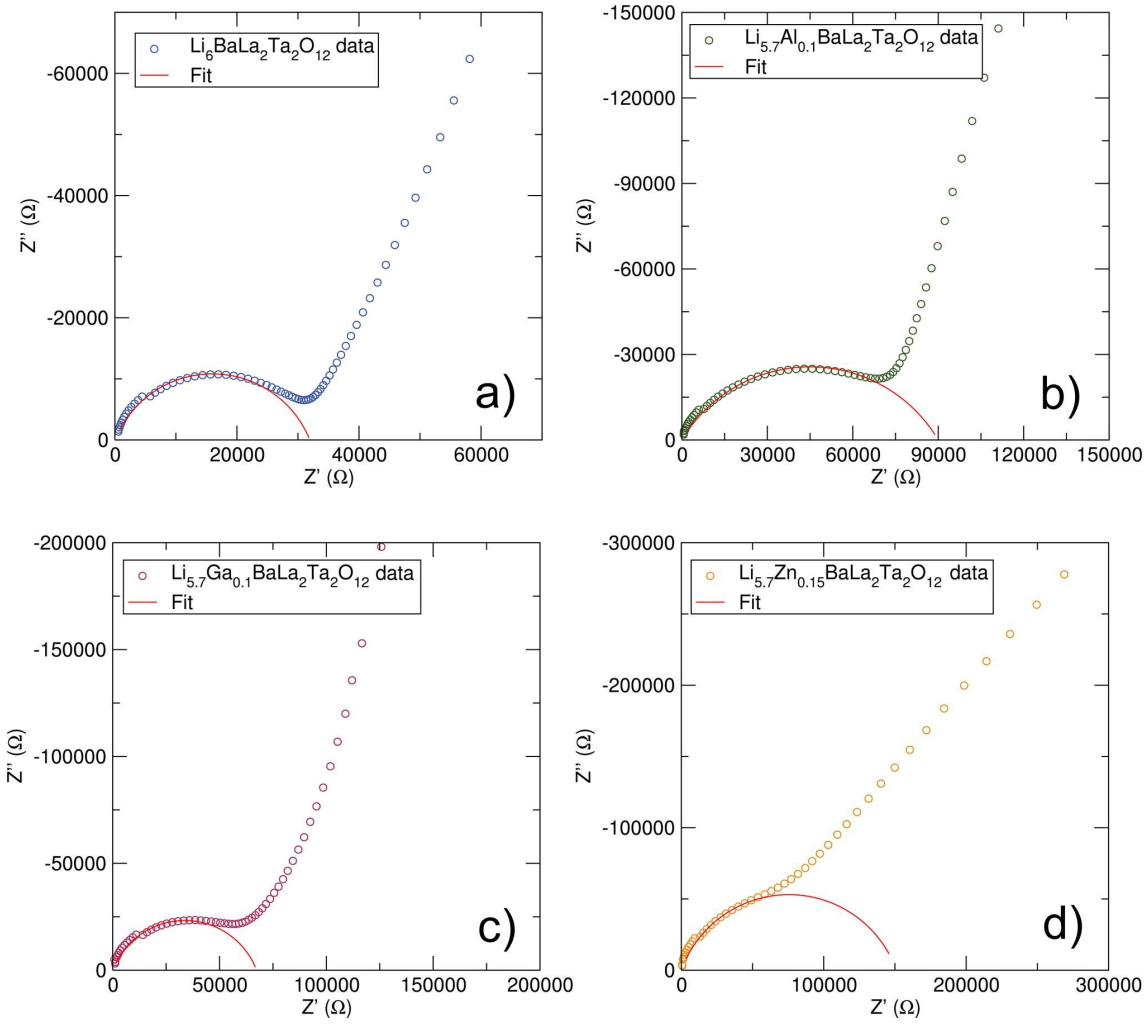

Figure 3.8: Nyquist plots of the EIS experimental data at room temperature (open circles) and their fit (solid line) to a resistance with a parallel constant phase element.

The ionic conductivity of the material can be calculated from the resistance obtained in the fitted models. This can be done by applying Pouillet's law (Eq. 3.1), where, in the case of cylindrically pelletised materials, σ represents the ionic conductivity, t accounts for the thickness of the analysed pellet, A is the area of the electrode in contact with the pelletised material, and R is the resistance calculated from fits to the Nyquist plots.

$$\sigma = \frac{t}{A \cdot R} \tag{3.1}$$

The calculated room temperature ionic conductivities for all the synthesised materials are given in Table 3.4 and represented in Figure 3.9. The room temperature ionic conductivity of the undoped LBLTO material is 3.7×10^{-6} S cm^{-1}. This value is one order of magnitude lower compared to the original report for this material.[12] This difference may

be due to the lower temperature and shorter times employed during the synthesis which may result in poorer grain sintering leading to a higher inter-grain resistance of the material. Since the authors did not report their pellet density, it was not possible to draw a clear conclusion on this. A review of the literature reveals that a wide range of ionic conductivity values are reported for the same type of garnet material depending on different factors.[2] EIS measurements are sensitive to changes in the set up and different synthetic and sintering conditions can interfere with the analyses, often hampering a direct comparison of conductivity values in the literature. By contrast, in this study it is possible to accomplish a direct comparison between the transport properties of the materials studied since the experimental conditions are controlled and reasonably homogeneous across the different samples (same instrument, same experimenter, amount of materials, pellet densities and electrodes employed).

Table 3.4: Room temperature ionic conductivity of the undoped and Al-, Ga-, Zn-doped $Li_6BaLa_2Ta_2O_{12}$ materials calculated from EIS measurements.

Material	σ (S cm^{-1})
$Li_6BaLa_2Ta_2O_{12}$	3.7×10^{-6}
$Li_{5.70}Al_{0.10}BaLa_2Ta_2O_{12}$	7.9×10^{-7}
$Li_{5.25}Al_{0.25}BaLa_2Ta_2O_{12}$	2.8×10^{-9}
$Li_{5.70}Ga_{0.10}BaLa_2Ta_2O_{12}$	3.2×10^{-6}
$Li_{5.25}Ga_{0.25}BaLa_2Ta_2O_{12}$	2.6×10^{-6}
$Li_{5.70}Zn_{0.15}BaLa_2Ta_2O_{12}$	1.2×10^{-6}
$Li_{5.25}Zn_{0.37}BaLa_2Ta_2O_{12}$	6.6×10^{-7}

From the room temperature conductivity measurements, it is clear that Al-doping had a detrimental impact on the ionic conductivity of the materials, decreasing progressively to 7.9×10^{-7} S cm^{-1} for the $Li_{5.70}Zn_{0.15}BaLa_2Ta_2O_{12}$ material and a further decrease of two orders of magnitude lower for the $Li_{5.25}Al_{0.25}BaLa_2Ta_2O_{12}$ garnet to a value of 2.8×10^{-9} S cm^{-1}. A similar effect, albeit less pronounced, was observed upon introduction of the Zn dopant to the garnet framework. The room temperature ionic conductivity decreased to a value of 1.2×10^{-6} S cm^{-1} for the $Li_{5.70}Zn_{0.15}BaLa_2Ta_2O_{12}$ material with a further decrease to 6.6×10^{-7} S cm^{-1} noted for the higher $Li_{5.25}Zn_{0.37}BaLa_2Ta_2O_{12}$. In the case of Ga-doped LBLTO materials, the room temperature ionic conductivity remained within the same order of magnitude, only experiencing a small decrease of the conductivity to 3.2×10^{-6} S cm^{-1} and 2.6×10^{-6} S cm^{-1} for the $Li_{5.70}Ga_{0.10}BaLa_2Ta_2O_{12}$ and $Li_{5.25}Ga_{0.25}BaLa_2Ta_2O_{12}$ garnet materials respectively. This difference in behaviour between Ga^{3+} and, Al^{3+} and Zn^{2+} dopants again points to the possibility of Ga^{3+} occupying the octahedral Li^+ 48g positions in the garnet structure in agreement with XANES observations. The presence of dopant ions on the Li^+ 24d positions has been reported to

have a detrimental effect on the conductivity of the materials, while displacing the dopant towards 48g positions can alleviate this effect.[35] This is essentially due to the 24d sites dominating the ionic conductivity, as they act as nodes between the transport pathways of four Li^+ located on the neighbouring 48g sites, while the 48g positions act as connection points only between the transport of two Li^+ located on the 24d positions.[36,37]

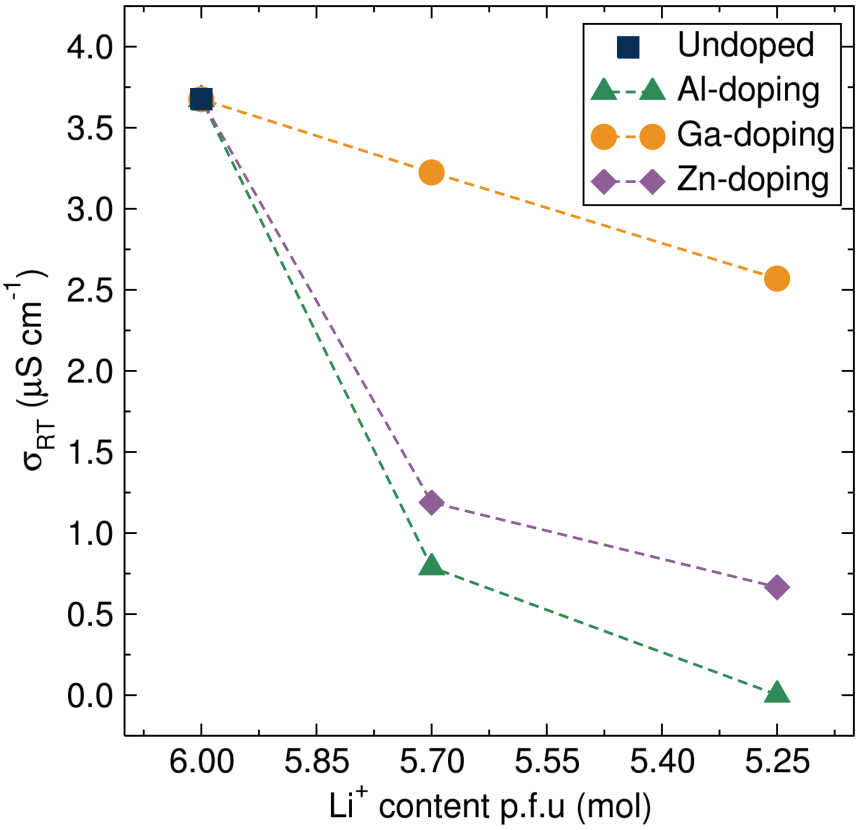

Figure 3.9: Graphic representation of the EIS calculated room temperature total ionic conductivity of the undoped and Al-, Ga-, Zn-doped $Li_6BaLa_2Ta_2O_{12}$ materials evolution with decreasing Li^+ content.

In order to further understand the effects of the dopant on the macroscopic transport properties of these garnet materials, temperature variable EIS measurements were also carried out. This allowed analysis of the Arrhenius behaviour of the ionic conductivity and calculation of activation energies for the total ionic diffusion. Figure 3.10 shows the different Arrhenius plots for all the compositions synthesised and the specific values of the activation energies calculated from these plots.

The activation energy for the undoped LBLTO garnet materials had a calculated value of 0.41(4) eV which is within the 0.40 - 0.44 eV range of values reported by other authors.[12,26,38] For the Al^{3+} doping, the low concentration of the dopant had a positive effect on the activation energy for total conductivity, lowering this from 0.41(4) eV for the undoped material to a value of 0.35(4) for the Li = 5.7 material. This indicates the potentially beneficial effect, in agreement with previous studies where an Li-Al-O amorphous layer is reportedly formed between the grains, where a 0.10 mol of Al^{3+} per formula unit of garnet

reduced the porosity of the pelletised material from an 11% to a value close to 1%.[39] This amorphous Li-Al-O layer has been reported to enhance the particle contact in garnet materials, lowering the energy requirement for Li^+ to cross grain boundaries. However, when surpassing the $Li_{5.70}Al_{0.10}BaLa_2Ta_2O_{12}$ doping to the higher $Li_{5.25}Al_{0.25}BaLa_2Ta_2O_{12}$ values, the activation energy then increases to 0.48(3) eV, indicating that the beneficial effect of a possible Li-Al-O layer was then overshadowed by detrimental effects on the intra-grain conductivity as a consequence of lower carrier concentration and blockage of the 24d sites.[40]

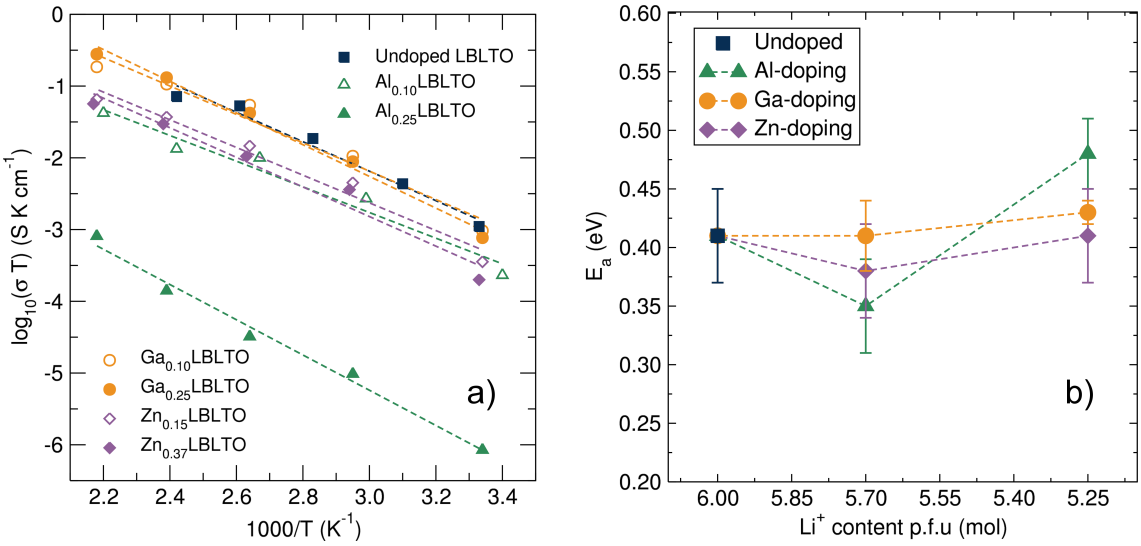

Figure 3.10: Activation energy evolution for the total ionic conduction of the undoped and Al^{3+}, Ga^{3+}, Zn^{2+} doped $Li_6BaLa_2Ta_2O_{12}$ materials from EIS measurements.

Table 3.5: Activation energy for the total ionic conductivity and the correspondent R^2 from the Arrhenius fits for the undoped and Al^{3+}, Ga^{3+}, Zn^{2+} doped $Li_6BaLa_2Ta_2O_{12}$ materials calculated from EIS measurements.

Material	E_a (eV)	R^2 of fit
LBLTO	0.41(4)	0.98
$Li_{5.70}Al_{0.10}BaLa_2Ta_2O_{12}$	0.35(4)	0.96
$Li_{5.25}Al_{0.25}BaLa_2Ta_2O_{12}$	0.48(3)	0.99
$Li_{5.70}Ga_{0.10}BaLa_2Ta_2O_{12}$	0.41(3)	0.98
$Li_{5.25}Ga_{0.25}BaLa_2Ta_2O_{12}$	0.43(1)	0.99
$Li_{5.70}Zn_{0.15}BaLa_2Ta_2O_{12}$	0.38(4)	0.97
$Li_{5.25}Zn_{0.37}BaLa_2Ta_2O_{12}$	0.41(4)	0.97

3.3 Local lithium diffusion studies by μ^+SR

In order to unveil the local Li^+ diffusion properties of the undoped LBLTO garnet material, μ^+SR studies were performed on the EMU instrument at the ISIS Neutron and

Muon Source. Powdered samples were studied using a low background Ti sample holder and the temperature was controlled by a CCR. The temporal evolution of the implanted positron decay asymmetry collected at zero field and two different longitudinal applied magnetic fields is shown in Figure 3.11. By applying different longitudinal applied magnetic fields, interactions between the muons and any local nuclear magnetic field distribution can be decoupled, separating theses from the stronger electronic contributions which can arise from paramagnetic ions in the material, if any.[41] In addition, the use of different longitudinal magnetic fields resulted in additional data sets that could be co-fitted, increasing the number of constraints resulting in more reliable fits. The evolution of the asymmetry of the positron decay with increasing applied longitudinal magnetic field showed a slower decrease of the positron decay asymmetry as a result of the forced realignment of the muon spins with the parallel longitudinal magnetic field.

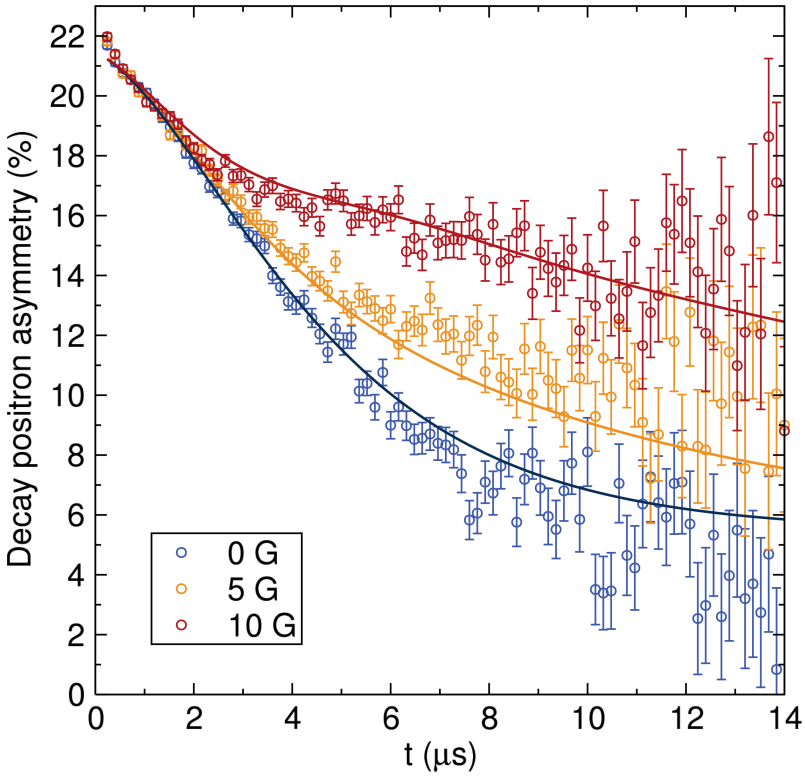

Figure 3.11: μ^+SR raw data collected at room temperature at zero field (blue) and applied fields of 5 G (yellow) and 10 G (red) and fit to the data using the Keren function (solid line) for the undoped $Li_6BaLa_2Ta_2O_{12}$ garnet material.

The decay in the positron asymmetry experiences a moderate relaxation at short times, indicating the absence of any fast depolarisation of the muon spin due to any magnetic field in the sample which would have resulted in a much acute decay of the positron asymmetry.[41] This was expected for the undoped LBLTO garnet, where all the elements forming the material are diamagnetic in their present valence. The positron asymmetry decay at longer times follows a slower relaxation due to muon interactions with nuclear magnetic fields of elements in the samples with positive spins that can interact

with the muon's spin. These active nuclei interacting with the muons are both of ^{6}Li and ^{7}Li with spins = 1 and 3/2 respectively, ^{139}La and ^{181}Ta with spins = 7/2 and ^{135}Ba with spin = 3/2.

The acquired data were fitted to the Keren analytical expression for the Abragam function which describes the temporal evolution of the positron asymmetry decay in terms of the fluctuation of the muon, the nuclear field width distribution and any additional relaxation due to electronic magnetic field contributions.[42] The Keren function is shown in Equation 3.2 where ν is the fluctuation rate of the muon spin due to Li^+ diffusion, Δ is the field width distribution around the muon stopping site, ω is the Larmor precession frequency in the applied magnetic field and λ accounts for temperature-independent fluctuations associated with electronic magnetic fields. From the fits, ν and Δ parameters related to Li^+ diffusion were extracted. As for the garnet materials, the λ contribution is negligible, simplifying the analyses.

$$P_z(t) = exp[-\Gamma(\Delta,\nu,\omega_L,t)t]exp(-\lambda t) \tag{3.2}$$

Temperature variable measurements were carried out in order to study the temperature dependence of the Li^+ diffusion on the undoped LBLTO material. The temperature evolution of ν and Δ is represented in Figure 3.12. The fluctuation rate presents a flat region at low temperatures, followed by a thermally activated region above 225 K, where ν experiences an exponential increase with temperature due to lithium diffusion. The field width parameter Δ remains constant across the range of temperatures measured with a value close to 0.25 MHz, indicative of the static behaviour of the implanted muon within the garnet framework. This Δ value is in line with other oxide materials, where the muon stopping site is at *ca.* 1 Å distance from the oxygen anions.[41] Specifically for garnet materials, similar values in the range of 0.2 to 0.3 MHz have been previously reported.[43,44]

Li^+ diffusion coefficients were obtained by applying Equation 3.3, which relates the diffusion coefficient with the fluctuation rate and the crystal structure of the material in the solid state.[45] The term N_i refers to the number of accessible Li^+ sites in the i-th path, $Z_{v,i}$ is the vacancy fraction of the destination sites, s_i is the jump distance between Li^+ sites, and ν the calculated fluctuation rate from the μ^+SR measurements at each temperature. By considering the crystal structure shown in Fig. 3.13, it is commonly agreed that for Li-rich garnet materials there are two main accessible pathways for Li^+ diffusion to occur, as noted previously. These two hopping pathways involve the Li^+ hopping from the tetrahedral 24d site to one of the four 48g neighbouring octahedral sites or from one octahedral 48g site to either of the two surrounding 24d neighbouring tetrahedral sites,[36,37] with a hopping distance between 24d and 48g sites of 1.99 Å for the LBLTO garnet.[38]

$$D_{Li^+} = \sum_{i=1}^{n} \frac{1}{N_i} Z_{v,i} s_i^2 \nu \tag{3.3}$$

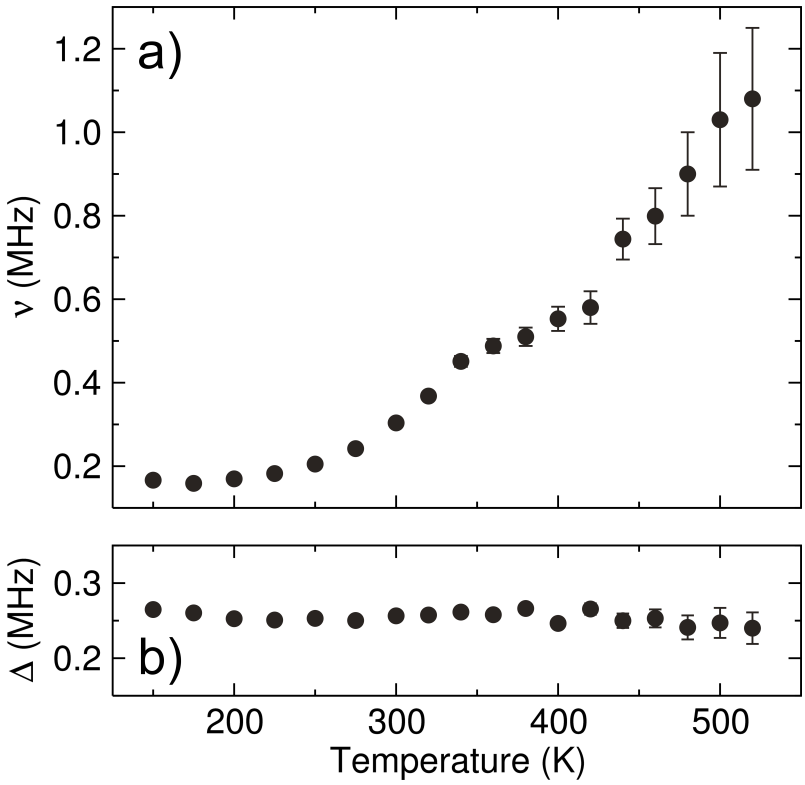

Figure 3.12: Temperature dependence of (a) ν and (b) Δ values obtained for fits to the Keren function for the undoped $Li_6BaLa_2Ta_2O_{12}$ garnet measured from 150 K to 525 K.

The calculated room temperature Li^+ diffusion coefficient was 3.35 $\times$ 10^{-11} cm^2 s^{-1}. This value is very close to the one reported for the $Li_6La_3ZrNbO_{12}$ related garnet material[44] and slightly lower than the value reported for the Al-doped LLZO garnet material of 4.9 $\times$ 10^{-11} cm^2 s^{-1} obtained by the same technique.[43] These Li^+ diffusion coefficients are all on the same order of magnitude and the decrease of the value in the Li = 6 material compared to the Li = 6.5 Al-doped LLZO garnet could be related to the lower carrier concentration and higher occupancy of the less mobile 24d sites, which limit Li^+ diffusion in the garnet crystal structure.[36]

An Arrhenius plot of the diffusion coefficients obtained at different temperatures is presented in Figure 3.14. The data fits to Arrhenius behaviour and an activation energy for local Li^+ diffusion of 0.16(1) was obtained from a linear fit. This value is similar to other activation energies reported by μ^+SR in garnets material of *ca.* 0.2 eV.[43,44] The value for the undoped LBLTO material studied here is slighly lower compared to the reported value for the Al-doped LLZO material.[43] This difference is likely due to the presence of Al ions on the 24d in the Al-doped LLZO material, which could force to some of the Li^+ located in the 48g/96h positions to jump to neighbouring 48g/96h positions, with the consequent increase in the energy required for that. Nevertheless, the activation energies are reasonably close when taking into account their standard deviations ($\sim$ 10%) to conclude that the energy required for lithium diffusion in both related materials is almost identical, with Li^+ carrier concentration and the balance between the 24d and 48g positions which reg-

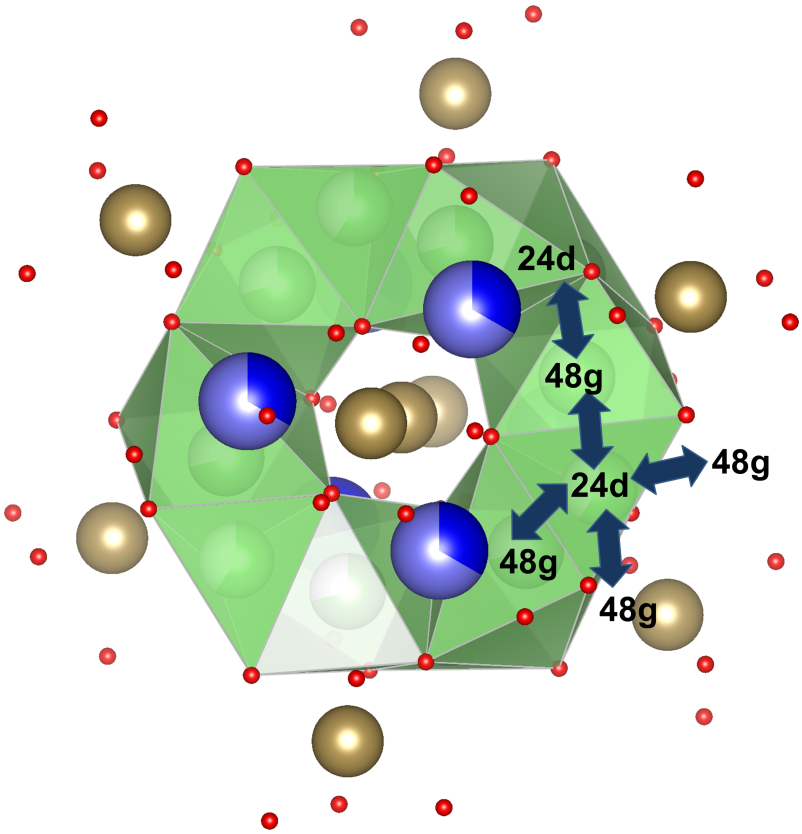

Figure 3.13: Simplified crystal structure representation of the cubic $LiBaLa_2Ta_2O_{12}$ undoped material, where the diffusion pathways between 24d and 48g sites for Li^+ has been indicated by the blue arrows. Ba^{2+} and La^{3+} cations are shown in blue and purple respectively, Ta^{5+} in brown, O^{2-} anions in red and Li^+ ion in green enclosed in their coordination polyhedra.

ulates the diffusion coefficient and conductivity of the material, in line with macroscopic measurements.

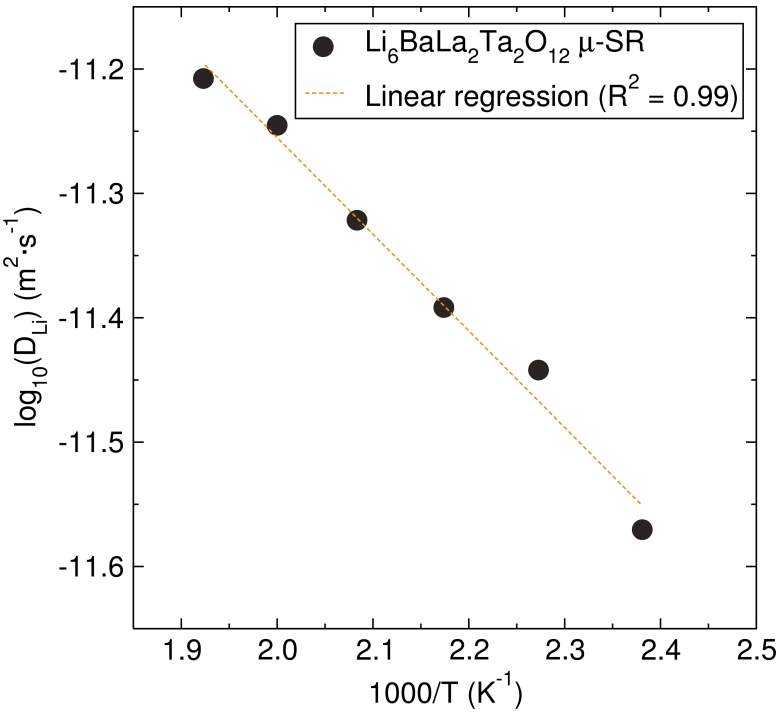

Figure 3.14: Arrhenius plot of the diffusion coefficient calculated from μ^+SR for the undoped $Li_6BaLa_2Ta_2O_{12}$ garnet. The calculated activation energy from it is 0.16(1) eV.

The Li^+ coefficient value reported here is also similar to current cathode materials used such as the $LiFePO_4$ [46] or the high energy density NMC family,[47] indicating that if the grain boundary resistance in these materials could be engineered to be reduced to a minimum, the solid-electrolyte would not be a limiting factor on the specific power output of the battery.

3.4 Conclusions

In this chapter, the synthesis, structural characterisation and study of the transport properties of Al-, Ga- and Zn-doped LBLTO garnet materials has been carried out. The use of microwave radiation during the synthesis allowed a reduction in the reaction times and temperatures to 6 hours and 800 °C . The introduction of a dopant within the garnet structure was analysed by PXRD, showing a decrease in the unit cell parameter as a consequence of the different cationic charge/size. XAS analyses on the Zn and Ga K-edge indicated that the Zn^{2+} is most likely to be located on the tetrahedral 24d sites, whereas the Ga^{3+} cations could be located in both tetrahedral 24d and octahedral 48g sites. The macroscopic ionic conductivity of the materials was analysed by EIS, demonstrating that low concentrations of Al^{3+} doping have a positive effect on conductivity, decreasing the activation energy for total ionic diffusion in this garnet material from 0.41(4) to 0.38(4) eV.

In all the cases, a decrease on the room temperature conductivity was found. μ^+SR measurements were carried out on the undoped LBLTO material in order to analyse the local Li diffusion properties of the material. A low activation energy for lithium diffusion at the local scale of 0.16(1) eV was calculated from temperature variable measurements and a lithium diffusion coefficient of 3.35 $\times$ 10^{-11} cm^2 s^{-1} was obtained at room temperature, indicating the good intra-grain transport properties of this LBLTO material.

References

[1] S. Ramakumar, C. Deviannapoorani, L. Dhivya, L. S. Shankar and R. Murugan, *Prog. Mater. Sci.*, 2017, **88**, 325 – 411.

[2] V. Thangadurai, S. Narayanan and D. Pinzaru, *Chem. Soc. Rev.*, 2014, **43**, 4714–4727.

[3] E. J. Cussen, *J. Mater. Chem.*, 2010, **20**, 5167–5173.

[4] B. Kozinsky, S. A. Akhade, P. Hirel, A. Hashibon, C. Elsässer, P. Mehta, A. Logeat and U. Eisele, *Phys. Rev. Lett.*, 2016, **116**, 055901.

[5] R. Jalem, M. Rushton, W. Manalastas, M. Nakayama, T. Kasuga, J. A. Kilner and R. W. Grimes, *Chem. Mater.*, 2015, **27**, 2821–2831.

[6] H. El-Shinawi and J. Janek, *J. Power Sources*, 2013, **225**, 13 – 19.

[7] E. Hanc, W. Zajac, L. Lu, B. Yan, M. Kotobuki, M. Ziabka and J. Molenda, *J. Solid State Chem.*, 2017, **248**, 51 – 60.

[8] S. Ohta, J. Seki, Y. Yagi, Y. Kihira, T. Tani and T. Asaoka, *J. Power Sources*, 2014, **265**, 40 – 44.

[9] H. J. Kitchen, S. R. Vallance, J. L. Kennedy, N. Tapia-Ruiz, L. Carassiti, A. Harrison, A. G. Whittaker, T. D. Drysdale, S. W. Kingman and D. H. Gregory, *Chem. Rev.*, 2014, **114**, 1170–1206.

[10] W. Hennig, W. Voss, J. Dubowik, J. Piche, R. Griffiths, R. Kovar and H. Kua, *Novel microwave susceptor composition and method for making same*, 1991, http://www.google.com/patents/WO1991015094A1?cl=en, WO Patent App. PCT/US1991/001,782.

[11] K. E. Gibbons, M. O. Jones, S. J. Blundell, A. I. Mihut, I. Gameson, P. P. Edwards, Y. Miyazaki, N. C. Hyatt and A. Porch, *Chem. Commun.*, 2000, 159–160.

[12] V. Thangadurai and W. Weppner, *Adv. Funct. Mater.*, 2005, **15**, 107–112.

[13] M. P. O'Callaghan and E. J. Cussen, *Chem. Commun.*, 2007, 2048–2050.

[14] R. D. Shannon, *Acta Crystallogr. A*, 1976, **32**, 751–767.

[15] L. J. Miara, W. D. Richards, Y. E. Wang and G. Ceder, *Chem. Mater.*, 2015, **27**, 4040–4047.

[16] D. Rettenwander, G. Redhammer, F. Preishuber-Pflügl, L. Cheng, L. Miara, R. Wagner, A. Welzl, E. Suard, M. M. Doeff, M. Wilkening, J. Fleig and G. Amthauer, *Chem. Mater.*, 2016, **28**, 2384–2392.

[17] W. Gu, M. Ezbiri, R. P. Rao, M. Avdeev and S. Adams, *Solid State Ionics*, 2015, **274**, 100 – 105.

[18] W. Bragg, *P. Camb. Philos. Soc.*, 1913, **17**, 43–57.

[19] A. Le Bail, *Powder Diffr.*, 2005, **20**, 316–326.

[20] L. Vegard, *Z. Phys.*, 1921, **5**, 17–26.

[21] S. C. Abrahams and J. L. Bernstein, *Acta Crystallogr. B*, 1969, **25**, 1233–1236.

[22] A. Ferrari, A. Braibanti, A. M. M. Lanfredi and A. Tiripicchio, *Acta Crystallogr.*, 1967, **22**, 240–246.

[23] A. D. Hendsbee, C. C. Pye and J. D. Masuda, *Acta Crystallogr. E*, 2009, **65**, i65.

[24] S. Geller, *J. Chem. Phys.*, 1960, **33**, 676–684.

[25] D. Rettenwander, J. Langer, W. Schmidt, C. Arrer, K. J. Harris, V. Terskikh, G. R. Goward, M. Wilkening and G. Amthauer, *Chem. Mater.*, 2015, **27**, 3135–3142.

[26] R. Murugan, V. Thangadurai and W. Weppner, *J. Electrochem. Soc.*, 2008, **155**, A90–A101.

[27] Y. Zhong, Q. Zhou, Y. Guo, Z. Li and Y. Qiang, *Ionics*, 2013, **19**, 697–700.

[28] I. Kokal, K. Ramanujachary, P. Notten and H. Hintzen, *Mater. Res. Bull.*, 2012, **47**, 1932 – 1935.

[29] J. Reinacher, S. Berendts and J. Janek, *Solid State Ionics*, 2014, **258**, 1 – 7.

[30] Y. Li, C.-A. Wang, H. Xie, J. Cheng and J. B. Goodenough, *Electrochem. Commun.*, 2011, **13**, 1289 – 1292.

[31] E. J. Cussen, T. W. Yip, G. O'Neill and M. P. O'Callaghan, *J. Solid State Chem.*, 2011, **184**, 470 – 475.

[32] V. Thangadurai, H. Kaack and W. J. F. Weppner, *J. Am. Ceram. Soc.*, 2003, **86**, 437–440.

[33] W. E. Tenhaeff, E. Rangasamy, Y. Wang, A. P. Sokolov, J. Wolfenstine, J. Sakamoto and N. J. Dudney, *ChemElectroChem*, 2014, **1**, 375–378.

[34] R. A. Huggins, *Ionics*, 2002, **8**, 300–313.

[35] J.-F. Wu, E.-Y. Chen, Y. Yu, L. Liu, Y. Wu, W. K. Pang, V. K. Peterson and X. Guo, *ACS Appl. Mater. Interfaces*, 2017, **9**, 1542–1552.

[36] M. Xu, M. S. Park, J. M. Lee, T. Y. Kim, Y. S. Park and E. Ma, *Phys. Rev. B*, 2012, **85**, 052301.

[37] D. Wang, G. Zhong, W. K. Pang, Z. Guo, Y. Li, M. J. McDonald, R. Fu, J.-X. Mi and Y. Yang, *Chem. Mater.*, 2015, **27**, 6650–6659.

[38] J. Awaka, N. Kijima, Y. Takahashi, H. Hayakawa and J. Akimoto, *Solid State Ionics*, 2009, **180**, 602 – 606.

[39] Y. Wang, P. Yan, J. Xiao, X. Lu, J.-G. Zhang and V. L. Sprenkle, *Solid State Ionics*, 2016, **294**, 108 – 115.

[40] D. O. Shin, K. Oh, K. M. Kim, K.-Y. Park, B. Lee, Y.-G. Lee and K. Kang, *Sci. Rep.* , 2015, **5**, 18053.

[41] M. Mansson and J. Sugiyama, *Phys. Scripta*, 2013, **88**, 068509.

[42] A. Keren, *Phys. Rev. B*, 1994, **50**, 10039–10042.

[43] M. Amores, T. E. Ashton, P. J. Baker, E. J. Cussen and S. A. Corr, *J. Mater. Chem. A*, 2016, **4**, 1729–1736.

[44] H. Nozaki, M. Harada, S. Ohta, I. Watanabe, Y. Miyake, Y. Ikedo, N. H. Jalarvo, E. Mamontov and J. Sugiyama, *Solid State Ionics*, 2014, **262**, 585 – 588.

[45] R. J. Borg and G. Dienes, *An Introduction to Solid State Diffusion*, Academic Press, San Diego, 1988, pp. 161 – 172.

[46] T. E. Ashton, J. V. Laveda, D. A. MacLaren, P. J. Baker, A. Porch, M. O. Jones and S. A. Corr, *J. Mater. Chem. A*, 2014, **2**, 6238–6245.

[47] M. Mänsson, H. Nozaki, J. M. Wikberg, K. Prša, Y. Sassa, M. Dahbi, K. Kamazawa, K. Sedlak, I. Watanabe and J. Sugiyama, *J. Phys: Conf. Ser.*, 2014, **551**, 012037.

Chapter 4: Fast microwave-assisted synthesis of Al- and Ga-doped LLZO garnets

The doping of LLZO garnet materials is vital in order to stabilise the highly conducting $Ia\bar{3}d$ cubic phase. In the past, this cubic phase stabilisation have been produced by Al contamination from the alumina crucibles used during synthesis and sintering processes at high temperatures for prolonged times, as was the case in the original 2007 report.[1] This has resulted in reproducibility issues and difficulties to obtain precise stoichiometries. To avoid these, new synthetic methodologies with increased reliability and reproducibility together with faster reaction times and lower temperatures are needed.

As previously introduced, stabilisation of the $Ia\bar{3}d$ cubic phase in lithium-rich garnets is not the only benefit of Al insertion within the garnet structure. Formation of additional lithium vacancies due to Al^{3+} incorporation (Fig. 4.1) facilitates diffusion of lithium and the potential formation of an amorphous Li-Al-O phase could aid lithium diffusion between grains.[2] Recent reports have also shown that insertion of Ga^{3+} into the LLZO garnet structure has a similar effect.[3,4] The positions of these dopants within the garnet framework is still unclear and further studies are needed to clarify it and to understand

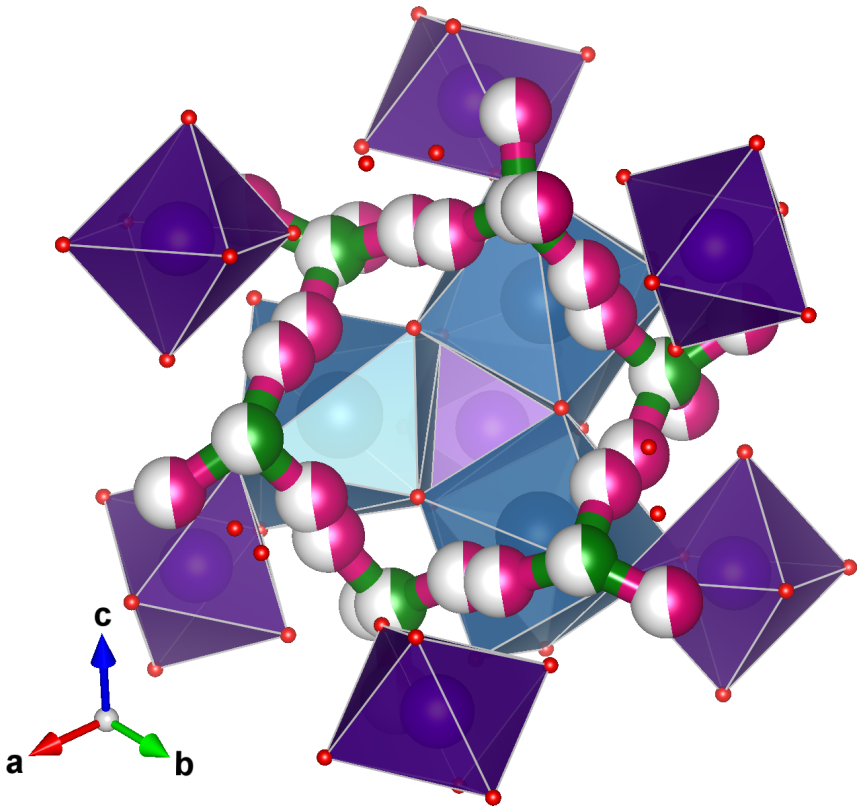

Figure 4.1: Simplified representation of the crystal structure for the cubic $Li_7La_3Zr_2O_{12}$ garnet. Zr^{4+} ions are represented in purple and enclosed in their octahedral 16a positions, La^{3+} (blue) are fully occupying the 8-coordinated 24c positions and Li^+ ions partially occupy the tetrahedral 24d (green) and off-centred octahedral 96h (pink) Wyckoff positions.

their role in the Li^+ conduction properties. In this cubic Al-doped LLZO garnet structure, the Zr^{4+} cations occupy the 16a Wyckoff positions, La^{3+} sit on the 24c sites and Li^+ are distributed between the tetrahedral 24d and the octahedral 96h positions.

Based on these facts, in this chapter a fast, reliable microwave-assisted approach for the syntheses at of Al- and Ga-doped LLZO garnet with nominal compositions of $Li_{6.5}Al_{0.25}La_{2.92}Zr_2O_{12}$ and $Li_{6.25}Ga_{0.25}La_3Zr_2O_{12}$ respectively, is presented. The average crystal structure was studied by PXRD and NPD analyses and the local coordination environments of Ga^{3+} and Zr^{4+} cations were analysed by XAS measurements. The Li^+ diffusion behaviour was examined by both EIS and μ^+SR. Analogous to the previous chapter, μ^+SR studies enabled the examination of the local dynamics of lithium ions with no interferences extrinsic to the doped LLZO material itself, as occurs in traditional EIS analyses.

4.1 Synthesis, crystal structure and chemical composition analyses

The Al- and Ga-doped LLZO cubic garnets with nominal compositions $Li_{6.5}Al_{0.25}La_{2.92}Zr_2O_{12}$ and $Li_{6.25}Ga_{0.25}La_3Zr_2O_{12}$ were prepared by the same microwave-assisted solid-state method as for the LBLTO materials. The absorption of microwave irradiation in this approach was facilitated in this case by the presence of $LiOH \cdot H_2O$ and ZrO_2 precursors in the reaction that can effectively absorb microwave radiation, efficiently converting this into heat.[5] A dramatically enhanced absorption of microwave radiation for ZrO_2 has also been reported at temperatures above 800 °C .[6] Specifically, the microwave irradiation was absorbed by the SiC walls of the microwave-assisted furnace releasing thermoradiation as a blackbody, heating the precursor materials initially. In a second heating stage, ZrO_2 can couple effectively to the microwave radiation as the furnace temperature increases, driving the reaction towards completion.

To demonstrate the robustness of this method, the Al-doped LLZO garnet was also prepared using a conventional furnace. For the same times and temperatures employed, it is clear that with a conventional solid-state approach the cubic garnet is not fully formed, while with the microwave-synthetic approach, highly crystalline cubic garnet is obtained as evidenced by PXRD (Fig. 4.2). The splitting of the (440) and (521) Bragg reflections (Fig. 4.1 b and c) on the conventionally prepared Al-doped LLZO material suggests a phase coexistence between the high conducting cubic phase and the low ionic conducting tetragonal phase. These extra peaks arise from the (004) and (440) and, (512) and (521) family of planes that are present in the lower symmetry tetragonal phase, which merge when transforming to the higher symmetric cubic LLZO phase.

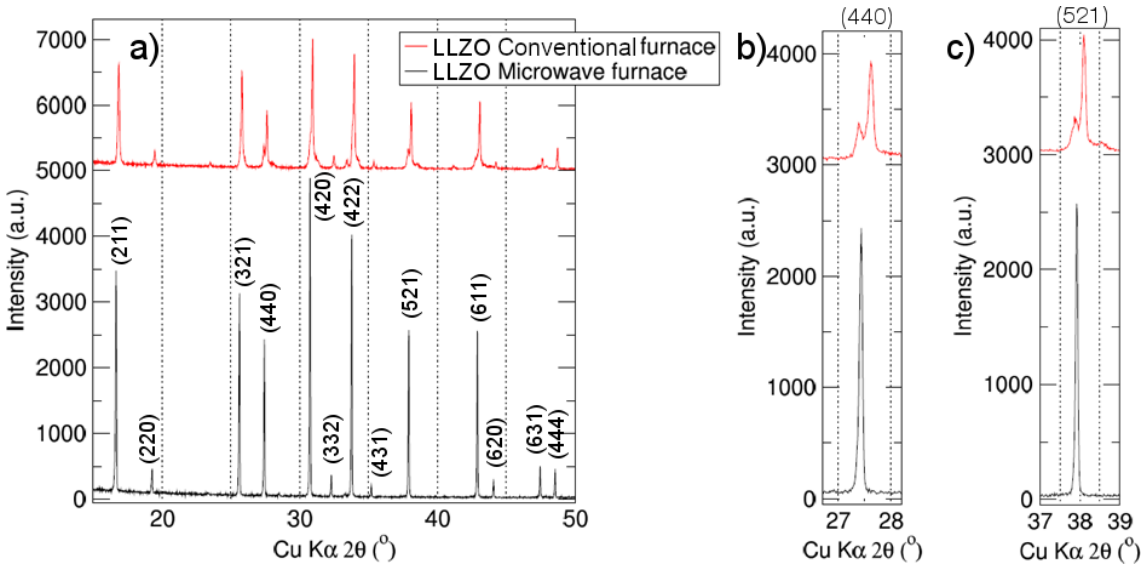

Figure 4.2: PXRD pattern of the as-synthesised $Li_{6.5}Al_{0.25}La_{2.92}Zr_2O_{12}$ garnet by microwave-assisted vs conventional solid-state approach (a). Amplifications of the (440) and (521) Bragg reflections have been included (b) and (c), respectively, where the differences in crystallinity and phase purity can be clearly observed.

A Rietveld refinement of the PXRD data collected for the as-synthesised Al-doped LLZO garnet, shown in Figure 4.3, revealed a highly crystalline single phase garnet, corresponding to the cubic form of the LLZO garnet with *Ia*$\bar{3}$*d* space group. The lattice parameter obtained from PXRD Rietveld refinements was found to be 12.9744(1) Å, which is in good agreement with the reported cubic LLZO garnet.[7]

The intentional Al^{3+} doping allowed stabilisation of the high conductive cubic LLZO phase. Different Al^{3+} concentrations ranging from 0.1 up to 0.5 mol per formula unit were tested to asses the minimum Al^{3+} concentration required to completely stabilise the cubic phase and the solubility limit of Al^{3+} on the garnet phase. It was found that at least 0.25 mol of Al^{3+} per formula unit of garnet was required to readily form a single cubic phase, while concentrations above this resulted in the formation of $LaAlO_3$ or $La_2Zr_2O_7$ by-products (Fig. 4.4).

The chemical composition of the Al-doped garnet was investigated by ICP-MS analyses which indicated that the Al^{3+} content of the sample had been accurately controlled by the synthetic approach. The analysis gave a stoichiometry of $Li_{6.3(2)}Al_{0.237(7)}La_{3.06(6)}Zr_{2.00(1)}O_{12}$, in good agreement with the target stoichiometry. No other major metal impurities were detected as possible contaminants (for example Fe contamination from the ball milling procedure).

NPD studies of the Al-doped garnet after the muon experiment (Fig. 4.5) revealed a good fit to the cubic phase, with a small (∼2%) impurity phase, identified as LiOH.[8] The stoichiometry extracted from Rietveld refinement of NPD data for the Al-doped LLZO garnet phase was $Li_{6.3(2)}Al_{0.23}La_{2.91}Zr_{2.02(2)}O_{12}$ which is very close to the nominal stoichiometry targeted. In addition, EDX analyses indicated a stoichiometry for Al, La and Zr

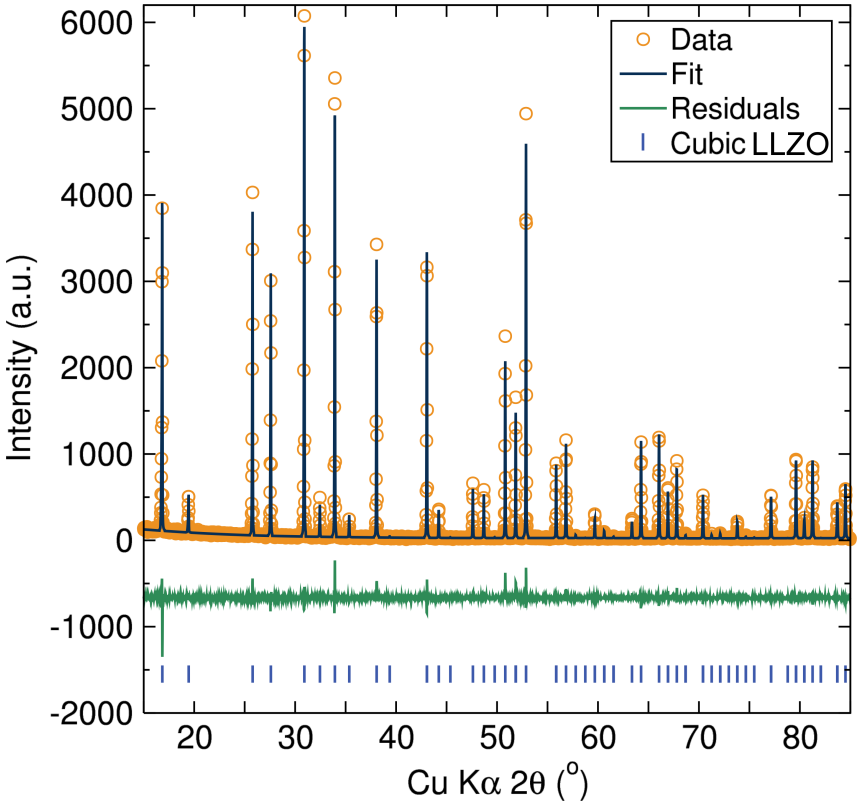

Figure 4.3: Rietveld refinement for the Al-doped $Li_{6.5}Al_{0.25}La_3Zr_2O_{12}$ PXRD data fit to the cubic ($Ia\bar{3}d$) space group. R_{wp} = 0.1346, R_p = 0.0976, χ^2 = 1.674 and R_{F^2} = 0.0515. Data are shown as orange circles, the fit to these data as a dark blue line and the difference curve in green. Blue tick marks denote expected reflections for this phase.

of $Al_{0.17(4)}La_{2.9(2)}Zr_{2.0(2)}$. The presence of the small LiOH secondary phase could have two origins: it could be a residue from the Li precursor excess invisible to laboratory PXRD or it may be produce as consequence of small Li^+/H^+ exchange from exposure to atmospheric air during transportation and measurements (see discussion below).

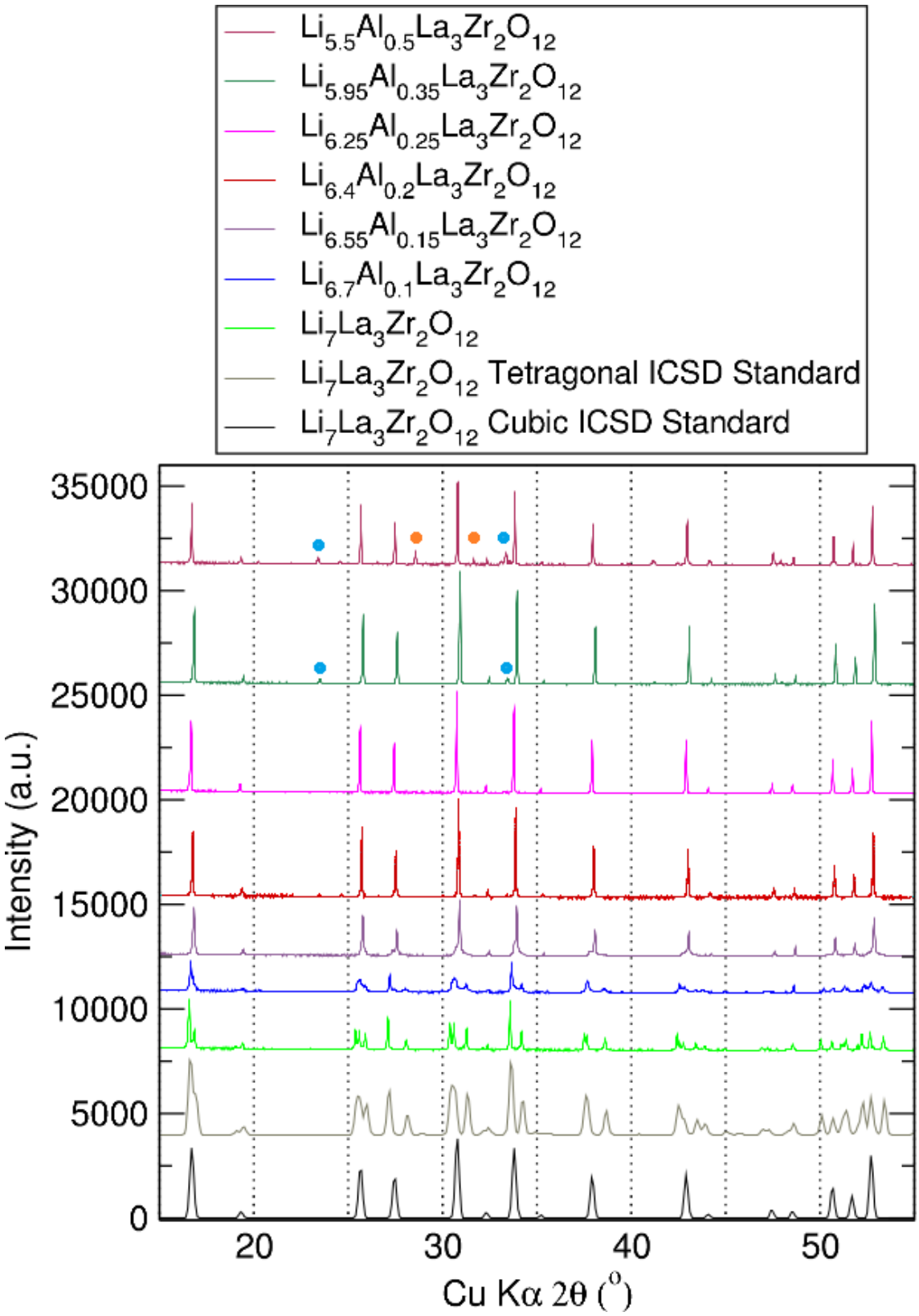

Figure 4.4: PXRD patterns of the different $Li_{7-3x}Al_xLa_3Zr_2O_{12}$ compositions tested. Bragg reflections arising from the $LaAlO_3$ perovskite and $La_2Zr_2O_7$ pyrochlore are indicated by blue and orange dots respectively.

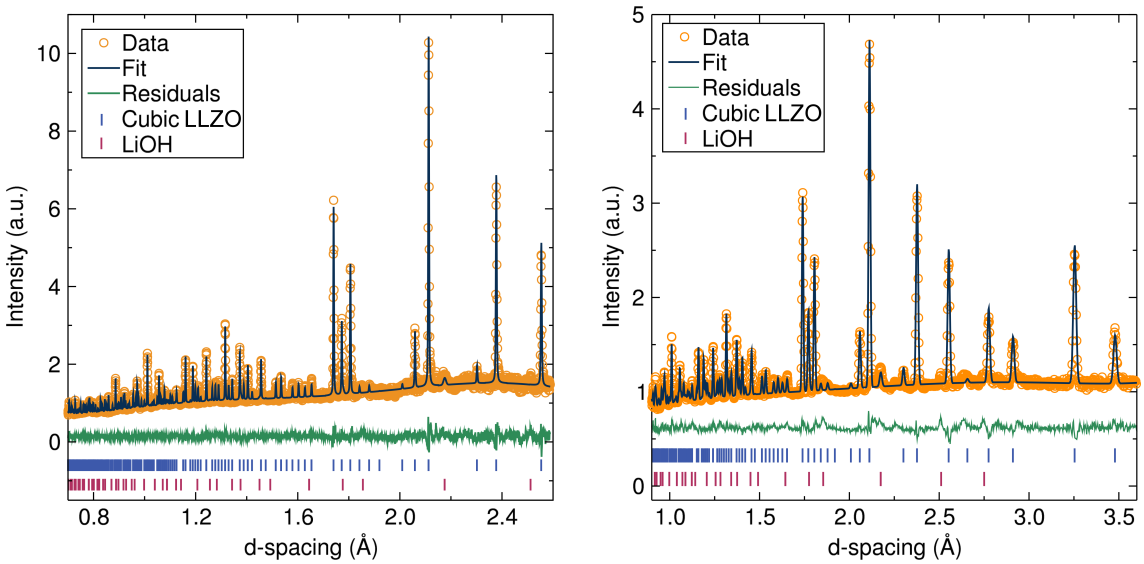

Figure 4.5: Rietveld refinements and extracted parameters for NPD data for the $Li_{6.5}Al_{0.25}La_{2.92}Zr_2O_{12}$ garnet fit to the cubic ($Ia\bar{3}d$) space group and LiOH with $P4/nmm$ symmetry. Backscattering detector (top left): R_{wp} = 0.0377, R_p = 0.0377 and R_{F^2} = 0.1120. Orthogonal detector (top right) R_{wp} = 0.0254, R_p = 0.0222 and R_{F^2} = 0.1604. Reduced χ^2 = 3.119.

The NPD data were fitted using the above introduced model for Li-stuffed garnets, with a disordered occupancy of Li across tetrahedral, 24d sites and off-centred octahedral 96h sites. Due to the small quantity of Al^{3+} present, it was not possible to unambiguously identify the site for this cation within the structure. From consideration of the cation radii and from previous reports, it was elected to place the Al^{3+} on the 24d site with the stoichiometry derived from the ICP analysis.[9] The Li^+ occupancies across the two sites were allowed to refine freely, *i.e.* with no compositional restraint on the Li content. The Zr^{4+} site fraction was also allowed to freely refine (Table 4.1). For the La^{3+} content, it was fixed at the target composition, an assignment supported by the ICP and EDX analyses and in agreement with the literature where a small amount of La^{3+} vacancies have been reported.[10] Taken in conjunction with ICP and EDX, the $Li_{6.5}Al_{0.25}La_{2.92}Zr_2O_{12}$ targeted stoichiometry of falls within the estimated standard deviation of each measurement.

Vacancy formation on the La^{3+} site (Table 4.1) at concentrations greater than 0.15 mol Al was also detected, leading to formation of a $LaAlO_3$ perovskite impurity. This has also been observed recently where doping of Al^{3+} cations led to lanthanum off-stoichiometry by introduction of a small percentage of vacancies on the La^{3+} site.[10] This observation of vacancies was confirmed by NPD studies. Therefore, the nominal stoichiometry employed was $Li_{6.5}Al_{0.25}La_{2.92}Zr_2O_{12}$ in order to prevent any $LaAlO_3$ perovskite side-product formation. In addition, this stoichiometry possessed the lithium content at which maximum conductivity was observed in the literature for a wide range of lithium-rich garnet systems studied.[11]

Table 4.1: Extracted parameters for NPD data for the $Li_{6.5}Al_{0.25}La_{2.92}Zr_2O_{12}$ fit to the cubic ($Ia\bar{3}d$) space group.

Atom	Site	Frac.	x	y	z	Uiso (100/Å^2)
Li1	24d	0.30(3)	-0.125000	0.000000	0.250000	2.3(1)
Li2	96h	0.45(1)	0.100100	0.671100	0634100	2.3(1)
Al	24d	0.077	-0.125000	0.000000	0.250000	3.2(1)
La	24c	0.973	0.000000	0.250000	0.125000	0.35(4)
Zr	16a	1.01(1)	0.000000	0.000000	0.000000	1.14(5)
O	96h	1.000	-0.03186(9)	0.0561(1)	0.1481(1)	0.80(3)

To avoid any potential moisture uptake by the Al-doped LLZO garnet, the sample was stored in a glovebox under argon and transported for measurement in glass vials under argon. Issues with moisture uptake have been reported for Li-rich garnets previously,[12] where Li^+ can be exchanged with H^+ from reaction with water molecules, a phenomenon which will be explored in greater detail in Chapter 5. When this occurs to a significant extent, there are changes in the cell parameters and a reduction in space group symmetry.[13] In this case, a relatively small change in cell parameter was observed (<0.5%), exhibited in the lattice parameter from the fitted neutron diffraction [13.02051(5) Å] data compared to original PXRD data collected immediately post syntheisis [12.9744(1) Å]. The possibility of the Li^+/H^+ exchange must be considered since NPD experiments were performed on a sample which had been examined by μ^+SR and hence was exposed to the atmosphere for a short time. The NPD data indicated the sample has the target stoichiometry, within the precision of the high resolution diffraction measurement at the HRPD instrument at ISIS. It was believed that this <0.5% change in the unit cell parameter is due to the slight uptake of water by the sample. This may have occurred inadvertently during sample cool-down after muon measurements were taken. In order to be consistent, the same sample was used for neutron diffraction studies. This absorption of water can occur either by direct insertion of water molecules into the garnet structure or through a H^+/Li^+ exchange mechanism as previously reported.[13,14] Since the refined Li^+ content from neutron data is in agreement with both the nominal stoichiometry and ICP analysis, any potential H^+/Li^+ exchange must be limited suggesting that in this case it may be some minor uptake of water which causes the observed small lattice expansion.

The use of this microwave-assisted synthetic approach presented here along with the intentional Al-doping resulted in faster reactions (up to 36 times) and a 230 °C reaction temperature decrease compared with the original synthesis reported by Muragan *et al.* for the LLZO material (36 hours at 1230 °C).[1] Compared to the faster solid-state syntheses of Al-doped LLZO reported in the literature, this approach is still up to four times faster in the final annealing step without the formation of any $La_2Zr_2O_7$ or $LaAlO_3$ impurities.[2]

SEM images of the Al-doped LLZO materials synthesised by the microwave-assisted

method and by a conventional solid-state approach were acquired in order to evaluate any microstructural changes as a result of synthetic methodology (Fig. 4.6). The approximated average particle size (from a sampling of 20 particles) for the microwave-assisted prepared sample is 1.5(4) µm, while the sample prepared *via* conventional ceramic methods displays slightly larger average particle size of 2.3(9) µm. The small size of the particles prepared by the microwave-assisted method may be related to the shorter reaction times and lower temperatures employed which could result in lower sintering and particle growth.

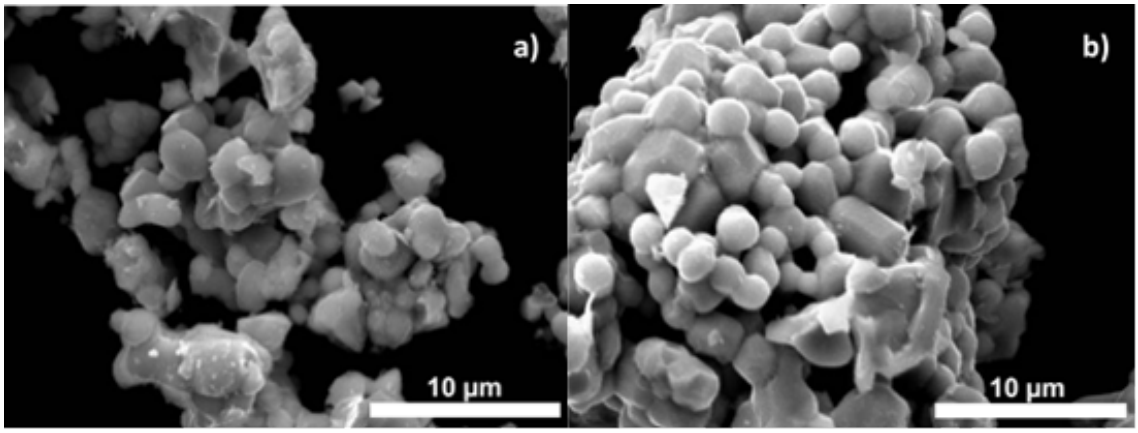

Figure 4.6: SEM images of the $Li_{6.5}Al_{0.25}La_{2.92}Zr_2O_{12}$ sample prepared *via* microwave-assisted (a) and conventional (b) solid-state approaches.

In the case of the Ga-doped LLZO material, the composition $Li_{6.25}Ga_{0.25}La_3Zr_2O_{12}$ led to phase pure cubic garnet. The cubic phase Ga-doped LLZO material was achieved at 950 °C for 6 hours without the need of a final high temperature heating step at higher temperature or prolonged times (Fig. 4.7). This temperature is 280 °C lower compared to the original cubic LLZO synthesis,[1] and between 100 to 150 °C lower compared to recent reports of Ga-doped LLZO synthesis by solid-state chemistry.[4,15] Rietveld refinements of the PXRD data resulted in a cell parameter of 12.9703(4) Å almost identical to the Al-doped LLZO material and in good agreement with the cell parameter reported by Wolfenstine *et al.* of 12.97 Å.[16] EDX analyses revealed a stoichiometry of $Ga_{0.3(2)}La_{3.1(3)}Zr_{2.0(4)}$, in good agreement with the target stoichiometry.

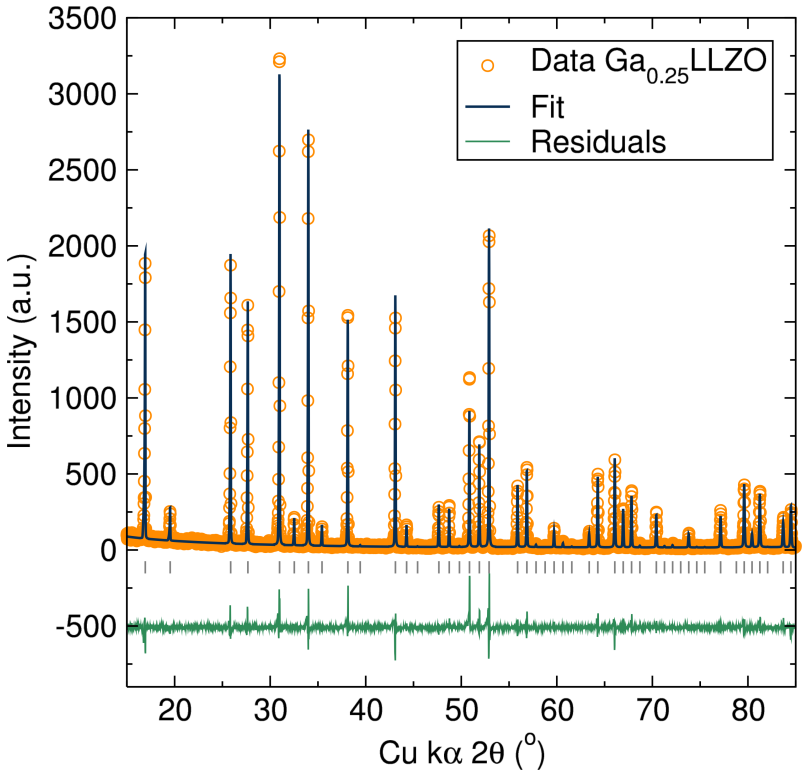

Figure 4.7: Rietveld refinement for the $Li_{6.25}Ga_{0.25}La_3Zr_2O_{12}$ PXRD data fit to the cubic ($Ia\bar{3}d$) space group. R_{wp} = 0.1946, R_p = 0.1421 and χ^2 = 2.417. Data are shown as orange circles, the fit to these data as a dark blue line and the difference curve in green. Grey tick marks denote expected reflections for this phase.

Figure 4.8 shows a SEM images of the Ga-doped LLZO material, where particles with sizes below 10 µm with irregular shapes are observed.

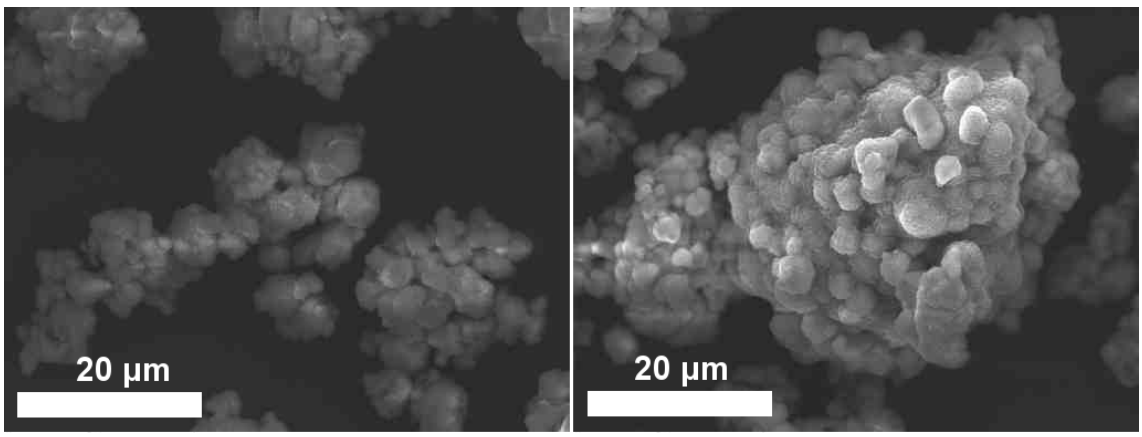

Figure 4.8: SEM images of the $Li_{6.25}Ga_{0.25}La_3Zr_2O_{12}$ sample prepared *via* microwave-assisted solid-state chemistry.

In order to confirm the presence and position of Ga^{3+} within the garnet LLZO framework, XANES studies were performed for the Ga-doped LLZO material. Figure 4.9 shows the XANES region of the XAS data for the Ga K-edge measurements on the Ga-doped LLZO material and the two standard materials, β-Ga_2O_3 and $Ga(NO_3)_3 \cdot 9\,H_2O$. As pre-

viously explained in Chapter 3, Ga^{3+} ions are exclusively octahedrally coordinated in the $Ga(NO_3)_3 \cdot 9\,H_2O$, while in the β-Ga_2O_3 standard Ga^{3+} cations are both octahedrally and tetrahedrally coordinated.

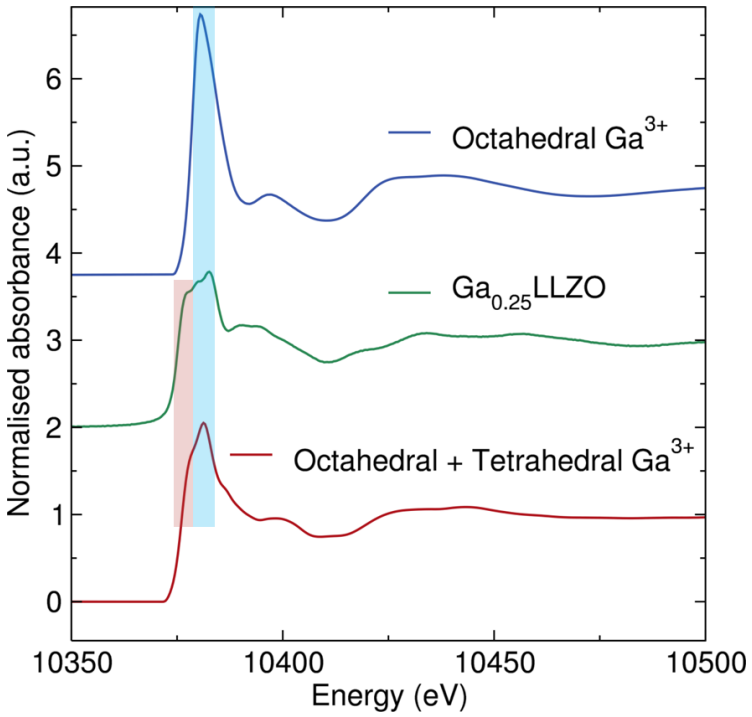

Figure 4.9: XANES region of for the XAS data measured on the Ga K-edge for the β-Ga_2O_3 standard (red) $Li_{6.25}Ga_{0.25}La_3Zr_2O_{12}$ garnet (green) and, $Ga(NO_3)_3 \cdot 9\,H_2O$ standard (blue).

The XANES profile for the Ga-doped LLZO displayed a rising edge followed by a plateau region. The features in this plateau region for the Ga-doped LLZO sample appear to overlap with features of both standard material. This suggest that the Ga^{3+} cations in the Ga-doped LLZO garnet could be located on both tetrahedral and octahedral Li^+ sites, similarly to the Ga-doped LBLTO material studied in this thesis and in agreement with reports of Ga-doped LLZO material.[4,10] In these reports, it has been found that in Ga-doped LLZO materials, Ga^{3+} cations can be located in both 24d and 48g positions, by experimental and computational methods.

It has been recently reported that Ga-introduction in the LLZO garnet structure can also induce a lowering in the garnet symmetry from the $Ia\bar{3}d$ to the $I\bar{4}3d$ space group. This transformation implies a distortion on the Zr^{4+} octahedron. The PXRD pattern of the Ga-doped garnet did not show any clear evidence of this transformation in the average structure, indicating that if this transformation has happened it occurred to a minor extend or at the local level. In order to assess the presence of this symmetry change on the local scale, the coordination environment of Zr^{4+} within the Ga-doped garnet framework was studied by XAS measurements. Figure 4.10 shows the XANES data of the Zr K-edge for the Ga-doped LLZO garnet and the monoclinic ZrO_2 standard material, where the absorption edge results from 1s to 5p electronic transitions. The Zr K-edge for the

Ga-doped LLZO material was aligned with the monoclinic ZrO_2 standard, confirming the oxidation state of Zr cations in the Ga-doped LLZO material was 4+. The shape of the edge in the case of the ZrO_2 standard revealed a single peak with a shoulder on the higher energy side, in good agreement with previous reports, where Zr^{4+} is in a 7-fold coordination environment. The data for the Ga-LLZO doped showed a doublet, indicative of an octahedral coordination for the Zr^{4+} cations as it occurs on the $ZrBaO_3$ perovskite and the $La_2Zr_2O_7$ pyrochlore materials. A detailed look on the edge reveals the presence of a small shoulder in the middle of the edge marked by a dotted box in Figure 4.10. This shoulder suggests the occurrence of electronic transitions from the 1s to the empty 4d orbitals. This may imply a degree of loss in centrosymmetry around the Zr^{4+} due to the distortion on the Zr^{4+} octahedron, which may result from the presence of a small population of garnet with $I\bar{4}3d$ space group, as suggested above.

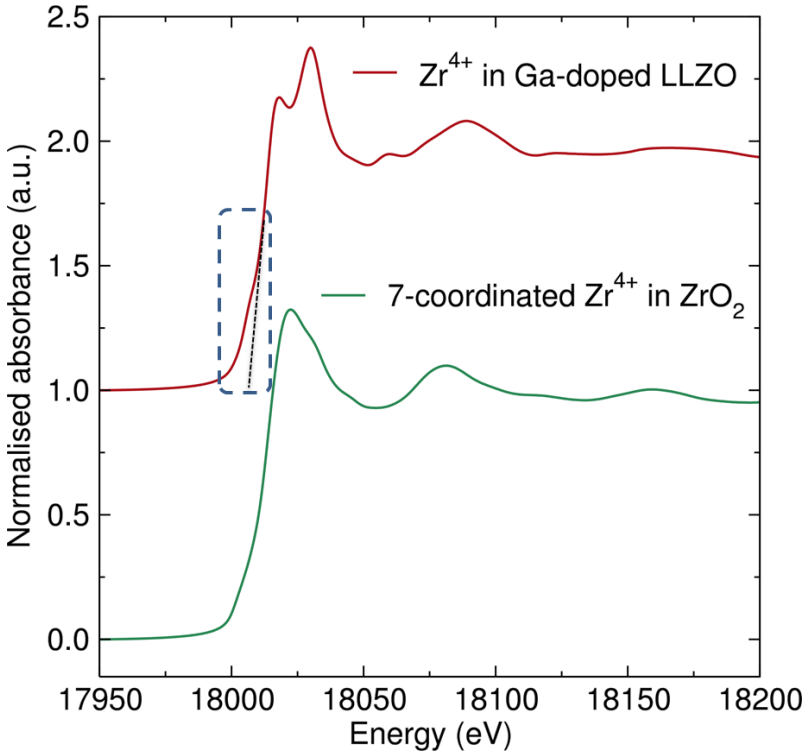

Figure 4.10: XANES region of for the XAS data measured on the Zr K-edge for the $Li_{6.25}Ga_{0.25}La_3Zr_2O_{12}$ (red) and ZrO_2 standard (green). The dotted straight line emphasises the pre-edge feature.

To study in more detail the local coordination of the Zr^{4+} cations on the Ga-doped LLZO material, the EXAFS region of the Zr K-edge was also analysed. The data were fit to the cubic $Ia\bar{3}d$ space group for the LLZO garnet between 1.5 and 4 Å. The fit revealed a mean Zr-O distance of 2.096(9) Å and a Zr-La distance of 3.59(1) Å, both in good agreement with the average crystal structure of the Ga-doped LLZO of 2.109(4) and 3.6293(2) Å.[10] Unfortunately, due to the thermal broadening (these data were acquired at 300 K), any small changes in distances on the ZrO_6 octahedra were buried within the

broadening of the corresponding peak as this effect is larger than the shift in distance.

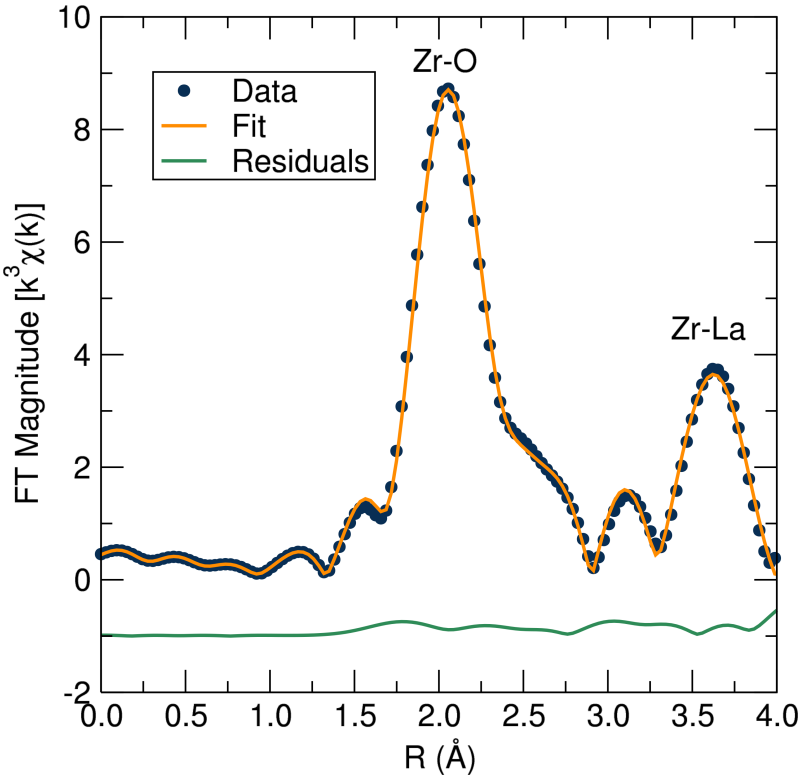

Figure 4.11: Real part of the Fourier transform for the experimental data at room temperature of the $Li_{6.25}Ga_{0.25}La_3Zr_2O_{12}$ garnet (blue circles). The fit (orange solid line) has been performed over the 1.5 to 4 Å region. The residuals of the fit are represented by the green solid line, with a R_{wp} value of 0.01.

4.2 Li^+ ionic conductivity probed by standard EIS technique

Macroscopic Li^+ ionic conductivity studies on the Al- and Ga-doped LLZO materials were carried out by EIS measurements. Analogous to the LBLTO material studied in the previous chapter, the LLZO garnet possesses almost negligible electronic conductivity;[17] therefore the resistance value extracted from EIS analyses is derived from the ionic resistance of the material. Figure 4.12 shows a Nyquist plot at 298 K, 338 K and 378 K, where up to three different components were noted at 338 K for this sample. At 298 K a small semicircle (Fig. 4.12 inset) due to the intra-grain resistance to Li^+ diffusion and a large incomplete semicircle (Fig. 4.12 main) due to the resistance at the inter-grain boundaries can be observed. As the measurement temperature is increased to 338 K, the large semicircle due to resistance at the inter-grain boundaries is reduced significantly and can be clearly appreciated. The third component observed at 338 K is the straight line after the inter-grain boundary resistance at low frequencies which corresponds to the Warburg impedance arising from the interface with the Pt blocking electrodes, indicating the predominantly ionic-conduction behaviour. Further increase of the temperature to 378 K results in the merging of the two semicircles due to intra- and inter-grain resistances,

at which point it is only possible to refer to the total ionic resistance and so separate activation energies for inter- and intra-grain conductivities cannot be determined. In order to obtain a value of the Li-ion conductivity, each semicircle present on the Nyquist plots was fitted to a resistance with a parallel constant phase element. At lower temperatures, where more than one semicircle was observed, the resistances were summed to give a value for the total resistance. The total conductivity of the sample was calculated by means of Pouillet's law (Equation 3.1) from the resistances calculated from the Nyquist plots (Table 4.2). The intra-grain ionic conductivity at room temperature was 3.7×10^{-6} S cm^{-1}, which decreases to a value of 4.4×10^{-9} S cm^{-1} when the inter-grain resistance is taken into account. These values are lower compared to the benchmark conductivity for this material of $\sim 10^{-4}$ S cm^{-1}, which again, may be due to the less aggressive sintering treatments or additional processing techniques employed in this fast microwave-assisted synthesis. For example, Xia *et al.* reported the solid-state synthesis of Al-doped LLZO cubic garnet at 1000 ºC for 9 hours with conductivity values in the 10^{-6} S cm^{-1} scale an activation energies in the range of 0.45 – 0.55 eV.[18] The authors reported an increase of one order of magnitude in the conductivity when increasing 100 º the sintering temperature, indicating the great effect of the sintering temperature on the conduction properties measured by EIS.

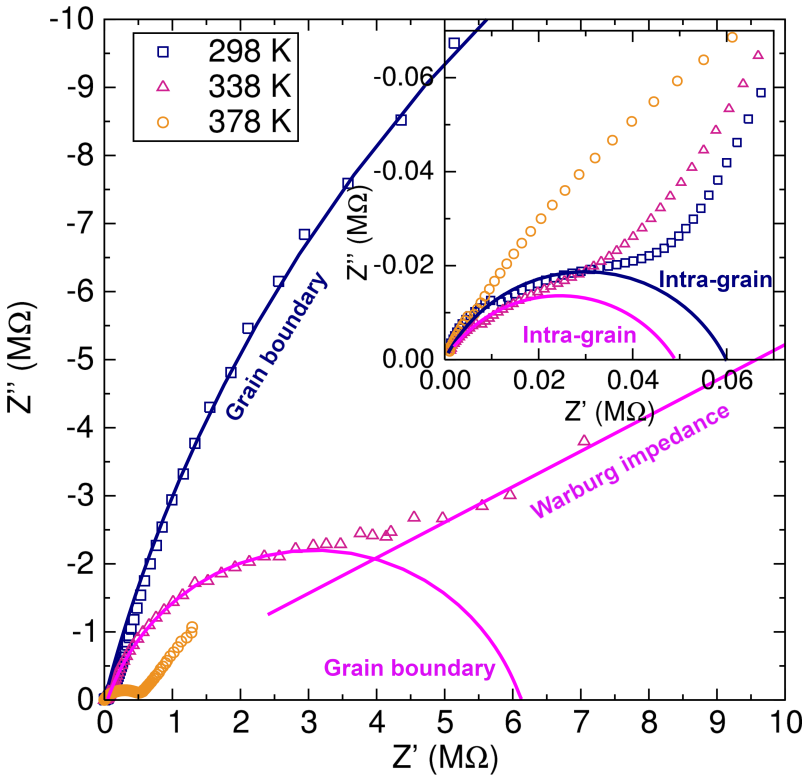

Figure 4.12: Nyquist plot of the impedance for the $Li_{6.5}Al_{0.25}La_{2.92}Zr_2O_{12}$ garnet at 298 K (blue squares), 338 K (pink triangles) and 378 K (orange circles). Inset highlights the first semicircle at high frequency due to intra-grain resistance to lithium diffusion. Solid lines indicate fits to the individual resistances.

Table 4.2: Ionic conductivity values obtained from EIS at different temperatures for the Intra-Grain (I-G) and Grain Boundary (GB) components and total ionic conductivity for the $Li_{6.5}Al_{0.25}La_{2.92}Zr_2O_{12}$ garnet.

T (K)	I-G Ionic Cond. (S cm^{-1})	GB Ionic Cond. (S cm^{-1})	Total Cond. (S cm^{-1})
298	3.74×10^{-6}	4.41×10^{-9}	4.40×10^{-9}
338	4.33×10^{-6}	3.21×10^{-8}	3.19×10^{-8}
378	-	-	2.53×10^{-7}
418	-	-	9.09×10^{-7}
458	-	-	6.23×10^{-6}

The activation energy was then extracted from the linear fit to an Arrhenius plot which is shown in Figure 4.13 and was found to be 0.55(3) eV. This value is higher than that reported for related cubic phase LLZO garnets of similar composition ($\sim$ 0.3 - 0.5 eV).[1,7] For this microwave-assisted synthesised material, which has a relative density of 81.5%, the observed increase in activation energy may be due to the lower sintering temperature and shorter time, resulted in higher resistance to ionic diffusion through grain boundaries, in agreement with suggestions in the literature.[19,20] For example, Xue *et al.* has reported recently a decrease in the activation energy in Al-doped LLZO garnet materials from 0.41 to 0.28 eV by increasing the sintering temperature from 1150 to 1210 ºC.[21]

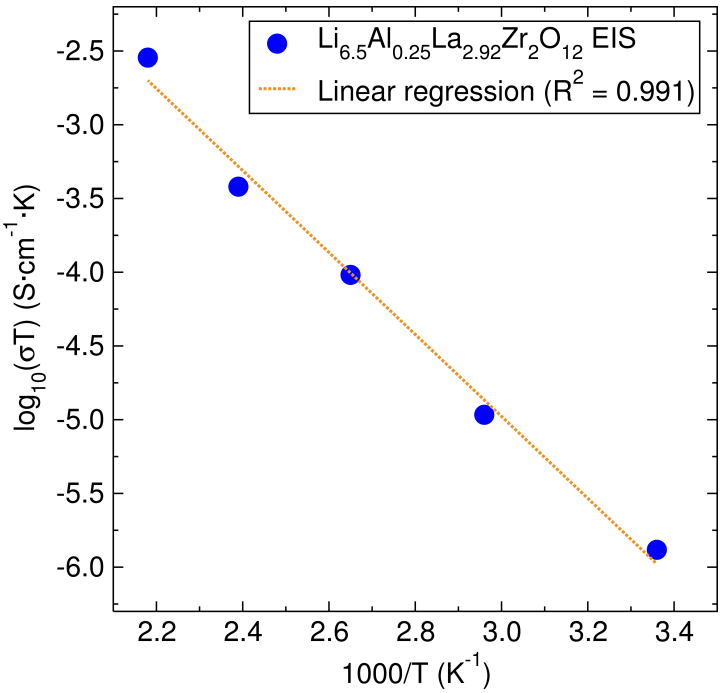

Figure 4.13: Arrhenius plot of the conductivity coefficients for the $Li_{6.5}Al_{0.25}La_{2.92}Zr_2O_{12}$ garnet. The calculated activation energy is 0.55(3) eV.

For the Ga-doped LLZO material, the Nyquist plot for the sample measured at RT is shown in Figure 4.14. As previously observed for the Al-doped material, the intra- and

inter-grain resistance contributions merge when heating the pellet above 100 °C . The calculated ionic conductivity values are given in Table 4.3. The intra-grain ionic conductivity at room temperature was 2.6 $\times$ 10^{-5} S cm^{-1}, which in this case is closer to the to 10^{-4} S cm^{-1} benchmark value.[7] The total ionic conductivity decreases to 2.2 $\times$ 10^{-7} S cm^{-1} when accounting for the inter-grain resistance, which is two orders of magnitude higher compared to the analogous Al-doped LLZO material, as the focus of this work was to study the materials in their as-synthesised form without further heat sintering steps. This difference could be related to the longer final heat treatment for the Ga-doped LLZO synthesis of 6 hours at 950 °C vs the 1 hour at 1000 °C for the Al-doped LLZO. As previously mentioned, it has been reported that for Al- and Ga-doped LLZO materials, the introduction of Ga^{3+} cations is most favourable for ionic conductivity of the material as the Ga^{3+} could be also to occupying the Li^{+} 48g positions instead of exclusively occupy the Li^{+} 24d node positions which block the transit between Li^{+} hoping between their 4 neighbouring 48g sites.

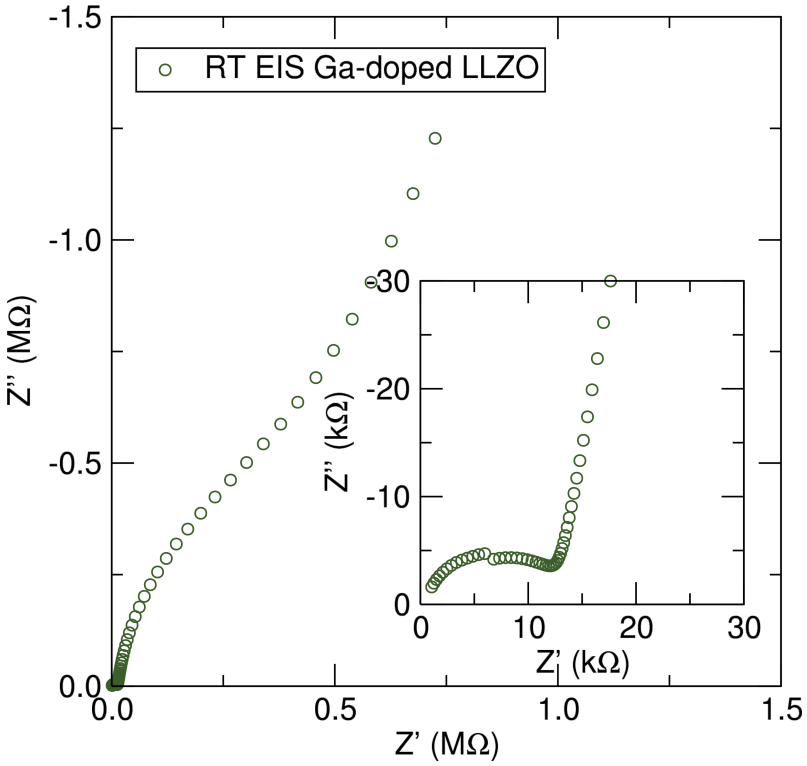

Figure 4.14: Nyquist plot of the impedance for the $Li_{6.25}Ga_{0.25}La_3Zr_2O_{12}$ garnet at room temperature. Inset highlights the first semicircle at high frequency due to intra-grain resistance to lithium diffusion.

Table 4.3: Ionic conductivity values obtained from EIS at different temperatures for the Intra-Grain (I-G) and Grain Boundary (GB) components and total ionic conductivity for the $Li_{6.25}Ga_{0.25}La_3Zr_2O_{12}$ garnet material.

T (K)	I-G Ionic Cond. (S cm^{-1})	GB Ionic Cond. (S cm^{-1})	Total Cond. (S cm^{-1})
295	2.62×10^{-5}	2.18×10^{-7}	2.16×10^{-7}
333	1.32×10^{-4}	1.93×10^{-6}	1.90×10^{-6}
383	3.65×10^{-4}	3.48×10^{-6}	3.45×10^{-6}
403		3.09×10^{-5}	3.09×10^{-5}
433		1.39×10^{-4}	1.39×10^{-4}
453		2.33×10^{-4}	2.33×10^{-4}
483		9.04×10^{-4}	9.04×10^{-4}
533		$4.55E\times10^{-3}$	4.55×10^{-3}

The ionic conductivity for the Ga-doped LLZO material fits well to an Arrhenius type behaviour (Fig. 4.15) The activation energy calculated for the Ga-doped LLZO materials was 0.60(5) eV, which is approximately the same as in the Al-doped LLZO case, and higher than the benchmark values for the Ga-doped LLZO material of 0.25 eV on a >96% dense pellet.[4]

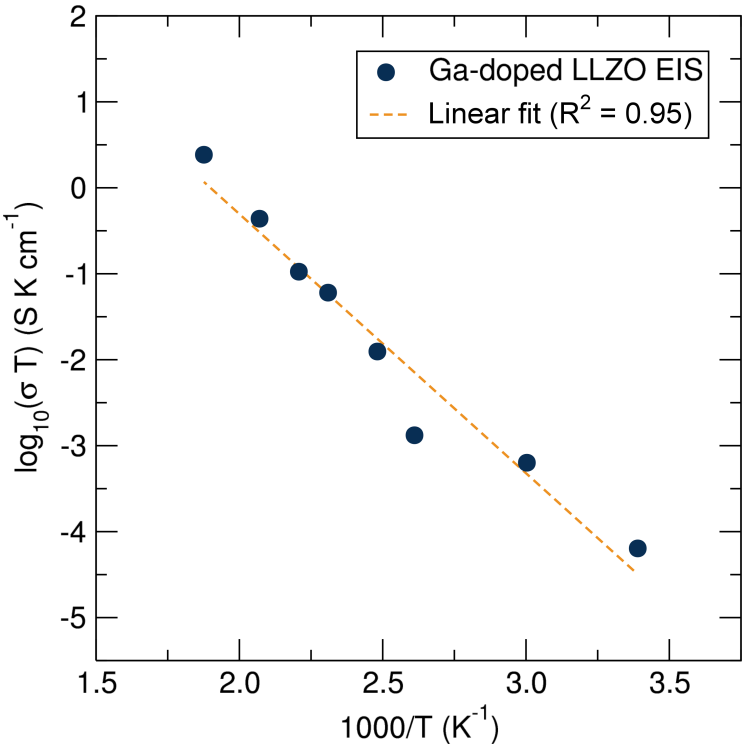

Figure 4.15: Arrhenius plot of the conductivity coefficient for the $Li_{6.25}Ga_{0.25}La_3Zr_2O_{12}$ garnet. The calculated activation energy is 0.60(5) eV.

As introduced in the previous chapter, the EIS technique is widely employed for evaluating the lithium ion conductivity in lithium-stuffed garnets.[7] However, variations in sin-

tering temperatures,[19] density of the pellet,[20] the electrodes employed (from platinum deposited particles to sputtered and melted gold) or the use of hot-pressing techniques[2] can greatly influence the experimental values, leading to the wide range of values reported for the LLZO garnet material. Specifically, for a similar range of Al-doped cubic LLZO garnets, the values of the activation energy for the Li^+ ionic conduction can vary from 0.26 eV, where the material was hot-pressed and sputtered with gold electrodes,[2] to 0.56 eV for a pellet of a lower relative density.[22] These discrepancies are related to the measurement experimental set up and the microstructure of the sample, rather than to the intrinsic nature of the material itself. To examine the microwave-assisted synthesised garnet material in greater detail but with a local probe instead of a bulk technique, μ^+SR analyses have been also performed for the Al-doped LLZO garnet.

4.3 Probing local Li^+ diffusion by μ^+SR studies

In order to study the lithium ion diffusion behaviour in greater detail for the Al-doped LLZO garnet, μ^+SR was employed as a local probe. Due to the limited chance of obtaining the beamtime necessary for these measurements, the Al-doped LLZO garnet was chosen for μ^+SR analysis. Also, this phase represents one of the most widely studied LLZO material and μ^+SR had not previously been applied. Al-doping has also been the dopant of choice to date, where other strategies such as the Ga-doping itself or substitutions on the Zr^{4+} positions are only recently gaining attention.

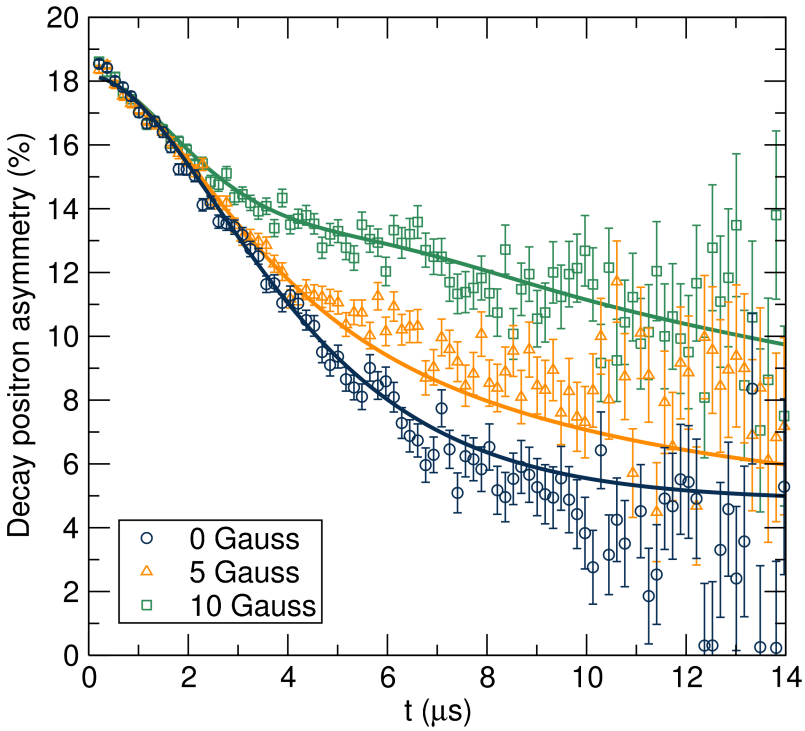

Figure 4.16: μ^+SR raw data collected at room temperature at zero field (circles) and applied fields of 5 G (triangles) and 10 G (squares). Fits are shown as solid lines using the Keren function for the $Li_{6.5}Al_{0.25}La_{2.92}Zr_2O_{12}$ garnet.

The temporal evolution of the decay positron asymmetry for the Al-doped LLZO material is shown in Figure 4.16. At short times, the decay positron asymmetry followed a moderate decay, while at longer times the asymmetry decrease followed a slower trend. This is consistent with the absence of paramagnetic ions within the structure and the presence of active nuclear spins (^{27}Al, ^{139}La and ^{91}Zr) that can interact with the muon spin.

To obtain the fluctuation rate of the muons due to lithium ion diffusion, the muon decay asymmetry data were fit using Keren's analytic generalisation of the Abragam function appropriate for μ^+SR [$P_z(t) = exp[-\Gamma(\Delta,\nu,\omega_L,t)t]$],[23] without the need of any temperature-independent relaxation rate.

The data for the Al-doped LLZO materials were also fit to the Keren function for each temperature at three longitudinal applied magnetic fields (0, 5 and 10 G) parallel to the initial muon spin polarisation and the raw data fits are shown in Figure 4.16. The calculated ν and Δ values are plotted in Figure 4.17 as a function of temperature.

Here, a plateau region is observed followed by an exponential increase in the fluctuation rate, due to the thermally activated lithium ion diffusion above 290 K. The plot of the field width distribution parameter Δ shows a progressively small decrease as the static lithium ions become mobile, reducing their contribution to the static width for the local field distribution.[24]

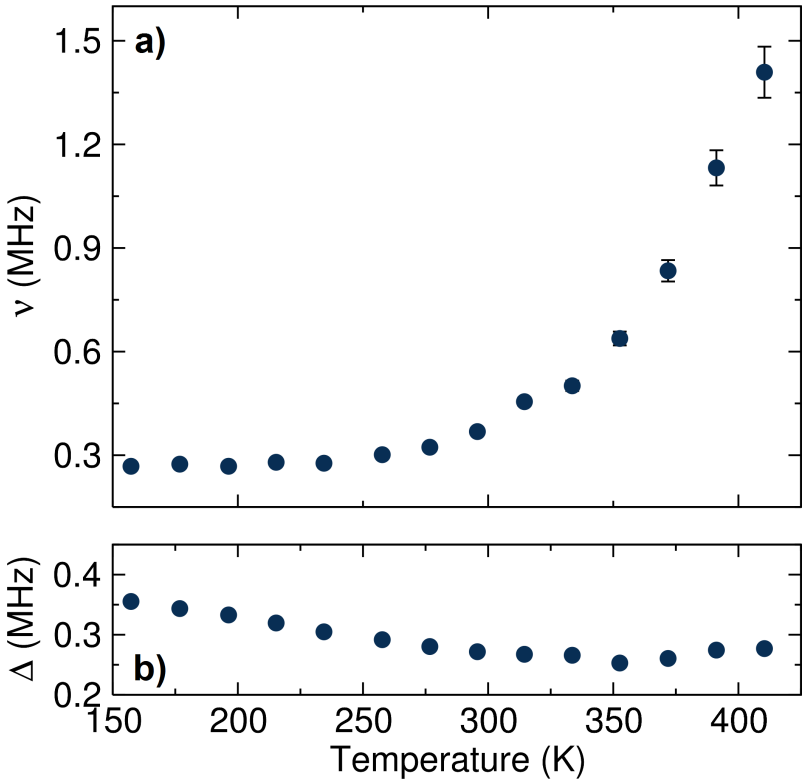

Figure 4.17: Temperature dependence of (a) ν and (b) Δ values obtained for the fits to the Keren function for the $Li_{6.5}Al_{0.25}La_{2.92}Zr_2O_{12}$ garnet measured from 150 K to 420 K.

In order to calculate the Li^+ diffusion coefficient from the fluctuation rate, correspond-

ing to the lithium ion jump rate between neighbouring sites, equation 4.1 was applied:[25]

$$D_{Li^+} = \sum_{i=1}^{n} \frac{1}{N_i} Z_{v,i} s_i^2 \nu \tag{4.1}$$

where N_i is the number of accessible Li sites in the i-th path, $Z_{n,i}$ is the vacancy fraction of the destination sites, s_i the jump distance between Li sites, and ν the calculated fluctuation rate at each temperature. In Figure 4.18, an electronic density map for the cubic LLZO material at high temperature[26] has been overlaid onto a representative portion of the LLZO crystal structure, highlighting the main two hopping pathways for Li^+ diffusion in the Al-doped LLZO material. These pathways involve the jump from the tetrahedral 24d site to the four 96h neighbouring octahedral sites and from the octahedral 96h sites to their two surrounding 24d neighbouring tetrahedral sites.

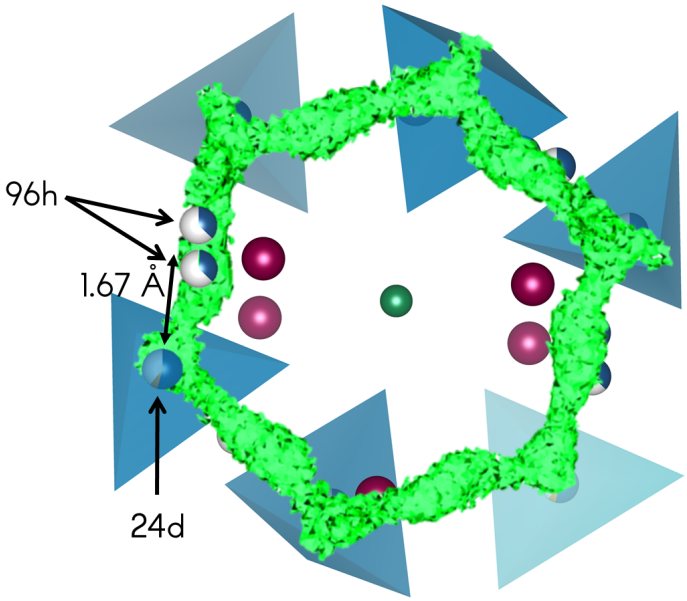

Figure 4.18: Simplified crystal structure of an Al-doped LLZO garnet showing both possible Li^+ positions. The lithium ions are drawn in blue, showing tetrahedral environment for the 24d site explicitly. Zr(V) ions in green and La(III) ions given in magenta. Al-dopant ions are shown as an orange fraction in 24d sites. The green mark denotes a molecular dynamic calculated pathway for Li^+ diffusion on cubic LLZO garnet which has been adapted into the crystal structure plot with permission from The Royal Society of Chemistry.[26]

From these pathways, the calculated lithium diffusion coefficient at room temperature was 4.62×10^{-11} cm^2 s^{-1}, which is greater than that reported for a non-doped tetragonal LLZO garnet (10^{-14} cm^2 s^{-1}) obtained through NMR studies, as expected.[27] This value is on the same order of magnitude, but slightly higher, compared to the LBLTO material

studied here and similar to the value reported for a Nb substituted LLZNbO material.[28] As explained in Chapter 4, the higher diffusion coefficient on the LLZO material compared to the LBLTO material could be due to the higher Li^+ concentration on the more mobile 96h position in the former.

The activation energy required for Li^+ diffusion was then calculated from an Arrhenius plot of the Li^+ diffusion coefficients (Figure 4.19) and was found to be 0.19(1) eV. This value is in good agreement with that reported by Nozaki *et al.* of *ca.* 0.20 eV for the related LLZNbO family,[28] and slightly higher than that obtained in this thesis for the LBLTO material of 0.16(1) eV. The difference may be due, as mentioned in the previous chapter, to the presence of Al^{3+} ions on the Li^+ 24d positions, blocking four 96h-24-96h routes and redirecting Li^+ traffic to 96h-96h higher energy demanding alternative route.

The difference in the activation energy between μ^+SR and EIS values [0.19(1) vs 0.55(4) eV for the Al-doped LLZO] arises from the different resistance contributions to the measurements. In EIS, resistance to Li^+ diffusion through grain-boundaries contributes to the total resistance of the sample, increasing the activation energy required for lithium ion conduction. On the other hand, μ^+SR acts as a local probe sensing mostly intra-grain diffusion for lithium ions, not being altered by other extrinsic interferences. These results encourage the necessity of a better understanding of the sintering processes employed for these materials in order to find an optimal reduction in grain boundaries, without the use of high temperatures and long times.[29]

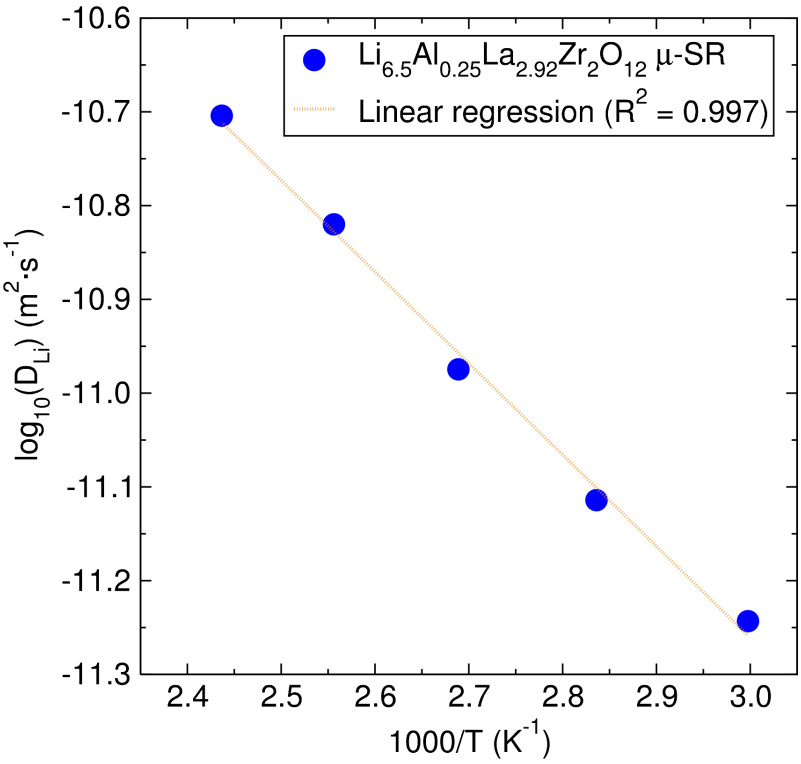

Figure 4.19: Arrhenius plot of the diffusion coefficient calculated from μ^+SR for the $Li_{6.5}Al_{0.25}La_{2.92}Zr_2O_{12}$ garnet. The calculated activation energy is 0.19(1) eV.

4.4 Conclusions

Al- and Ga-doped LLZO cubic garnets were synthesised by a fast microwave-assisted solid-state approach. Highly crystalline cubic phase material was obtained for both materials at lower heating temperatures and shorter reaction times compared with any conventional solid-state methods previously reported. ICP-MS analyses and NPD studies confirm the stoichiometry of the Al-doped LLZO garnet, where La^{3+} vacancies were required to obtain phase pure material. Ga^{3+} and Zr^{4+} local environments where studied by XAS analyses, indicating the possibility of Ga^{3+} cations occupying the Li^{+} 48h position and inducing distortions on the Zr^{4+} octahedra. The Li^{+} transport properties were studied using EIS and μ^{+}SR, with ionic conductivities at room temperature on the order of magnitude of 10^{-6} and 10^{-5} S cm^{-1} for the Al^{3+} and Ga^{3+} samples respectively, with low intra-grain activation energy of 0.19(1) eV for the Al-doped LLZO material. This demonstrated the potential of these materials as solid-state electrolytes for lithium-ion batteries. The work in this chapter also marks a new approach to accessing high quality garnets in a fast, clean manner and also illustrates the use of μ^{+}SR as an excellent local probe for the elucidation of Li^{+} diffusion in these materials.

References

[1] R. Murugan, V. Thangadurai and W. Weppner, *Angew. Chem., Int. Ed.*, 2007, **46**, 7778–7781.

[2] E. Rangasamy, J. Wolfenstine and J. Sakamoto, *Solid State Ionics*, 2012, **206**, 28 – 32.

[3] H. El-Shinawi and J. Janek, *J. Power Sources*, 2013, **225**, 13 – 19.

[4] J.-F. Wu, E.-Y. Chen, Y. Yu, L. Liu, Y. Wu, W. K. Pang, V. K. Peterson and X. Guo, *ACS Appl. Mater. Interfaces*, 2017, **9**, 1542–1552.

[5] H. J. Kitchen, S. R. Vallance, J. L. Kennedy, N. Tapia-Ruiz, L. Carassiti, A. Harrison, A. G. Whittaker, T. D. Drysdale, S. W. Kingman and D. H. Gregory, *Chem. Rev.*, 2014, **114**, 1170–1206.

[6] J. Lasri, P. D. Ramesh and L. Schächter, *J. Am. Ceram. Soc.*, 2000, **83**, 1465–1468.

[7] V. Thangadurai, S. Narayanan and D. Pinzaru, *Chem. Soc. Rev.*, 2014, **43**, 4714–4727.

[8] S. L. Mair, *Acta Crystallogr. A*, 1978, **34**, 542–547.

[9] H. Buschmann, J. Dolle, S. Berendts, A. Kuhn, P. Bottke, M. Wilkening, P. Heitjans, A. Senyshyn, H. Ehrenberg, A. Lotnyk, V. Duppel, L. Kienle and J. Janek, *Phys. Chem. Chem. Phys.*, 2011, **13**, 19378–19392.

[10] D. Rettenwander, G. Redhammer, F. Preishuber-Pflügl, L. Cheng, L. Miara, R. Wagner, A. Welzl, E. Suard, M. M. Doeff, M. Wilkening, J. Fleig and G. Amthauer, *Chem. Mater.*, 2016, **28**, 2384–2392.

[11] T. Thompson, A. Sharafi, M. D. Johannes, A. Huq, J. L. Allen, J. Wolfenstine and J. Sakamoto, *Adv. Energy Mater.*, 2015, **5**, 1500096.

[12] Y. Wang and W. Lai, *J. Power Sources*, 2015, **275**, 612 – 620.

[13] G. Larraz, A. Orera and M. L. Sanjuan, *J. Mater. Chem. A*, 2013, **1**, 11419–11428.

[14] G. Larraz, A. Orera, J. Sanz, I. Sobrados, V. Diez-Gomez and M. L. Sanjuan, *J. Mater. Chem. A*, 2015, **3**, 5683–5691.

[15] D. Rettenwander, C. A. Geiger, M. Tribus, P. Tropper and G. Amthauer, *Inorg. Chem.*, 2014, **53**, 6264–6269.

[16] J. Wolfenstine, J. Ratchford, E. Rangasamy, J. Sakamoto and J. L. Allen, *Mater. Chem. Phys.*, 2012, **134**, 571 – 575.

[17] V. Thangadurai and W. Weppner, *J. Power Sources*, 2005, **142**, 339 – 344.

[18] Y. Xia, L. Ma, H. Lu, X.-P. Wang, Y.-X. Gao, W. Liu, Z. Zhuang, L.-J. Guo and Q.-F. Fang, *Front. Mater.*, 2015, **9**, 366–372.

[19] R. Murugan, V. Thangadurai and W. Weppner, *J. Electrochem. Soc.*, 2008, **155**, A90–A101.

[20] C. Yang, L. Yi-Qiu and G. Xiang-Xin, *Chin. Phys. B*, 2013, **22**, 078201.

[21] W. Xue, Y. Yang, Q. Yang, Y. Liu, L. Wang, C. Chen and R. Cheng, *RSC Advances*, 2018, **8**, 13083–13088.

[22] R. Djenadic, M. Botros, C. Benel, O. Clemens, S. Indris, A. Choudhary, T. Bergfeldt and H. Hahn, *Solid State Ionics*, 2014, **263**, 49 – 56.

[23] A. Keren, *Phys. Rev. B*, 1994, **50**, 10039–10042.

[24] M. Månsson and J. Sugiyama, *Phys. Scr.*, 2013, **88**, 068509.

[25] *An Introduction to Solid State Diffusion*, ed. R. J. B. G. Dienes, Academic Press, San Diego, 1988.

[26] M. Klenk and W. Lai, *Phys. Chem. Chem. Phys.*, 2015, **17**, 8758–8768.

[27] A. Kuhn, S. Narayanan, L. Spencer, G. Goward, V. Thangadurai and M. Wilkening, *Phys. Rev. B*, 2011, **83**, 094302.

[28] H. Nozaki, M. Harada, S. Ohta, I. Watanabe, Y. Miyake, Y. Ikedo, N. H. Jalarvo, E. Mamontov and J. Sugiyama, *Solid State Ionics*, 2014, **262**, 585 – 588.

[29] N. Janani, C. Deviannapoorani, L. Dhivya and R. Murugan, *RSC Adv.*, 2014, **4**, 51228–51238.

Chapter 5: Studies of the sol-gel synthesis of the Al-doped LLZO garnet

Synthesis of LLZO garnet materials usually requires calcination steps at high temperatures (>1000 ^{o}C) to obtain the desirable highly ionic conducting $Ia\bar{3}d$ cubic phase. The use of high temperatures during the synthesis can lead to contamination from the alumina crucible containers and difficulties in obtaining precise compositions due to lithium evaporation at those temperatures.[1,2] In the last decade, sol-gel methodologies have been developed for the synthesis lithium garnet materials, designed for stabilising the cubic phase at temperatures as low as 700 ^{o}C.[3] Sol-gel routes also allow for the preparation of smaller particle sizes compared to conventional solid-state methods, a requirement for the preparation of homogeneous electrode-solid electrolyte composite materials.[4] The low temperature stabilisation of the cubic phase remains unclear, with the absorption of water and CO_2 molecules, together with possible Li^+ deficiency, proposed as possible causes of this.[5–8] The transport properties of materials synthesised by sol-gel chemistry, however, experience a detrimental drop in the ionic conductivity of up to three orders of magnitude and solving this is an outstanding challenge.[6,9] Energy efficient lower, temperature routes represent a big step necessary for the commercialisation of battery materials. Despite this, the sol-gel synthesis of LLZO materials has not experienced such great development due to the observed decline in transport properties. The reasons underpinning this declining behaviour remains under study and further investigation is required in order to tailor the synthetic approach to overcome this effect.

For these reasons, in this chapter, sol-gel chemistry techniques have been successfully employed to prepare the cubic phase Al-doped LLZO garnet material at low temperatures. In order to explore this LLZO low temperature cubic phase and the possible causes underlying the worsening transport properties, in-depth characterisation has been performed. The crystal structure of the material synthesised by this route has been examined by PXRD and variable temperature in-situ NPD. Raman spectroscopy analyses have been employed to study the presence of secondary Li-containing phases on the garnet surface, as well as the presence of H^+ inside the garnet crystal structure due to a possible Li^+/H^+ exchange. The macroscopic Li^+ transport properties have been studied by conventional EIS analyses. For the microscopic lithium diffusion behaviour, μ^+SR spectroscopy has also been employed.

5.1 Synthesis, structural characterisation and Li^+/H^+ exchange

In order to carefully study the properties of the material synthesised *via* sol-gel chemistry, a nominal stoichiometry of the material, $Li_{6.5}Al_{0.25}La_{2.92}Zr_2O_{12}$, was chosen in line with high temperature solid-state synthesis.

The Al-doped LLZO low temperature cubic phase was prepared by a modified sol-gel Pechini method, similar to that originally reported by Kokal *et al.* in 2011.[3] Nitrate precursors employed for the synthesis were selected due to their reasonable solubility in the aqueous media in order to obtain the initial sol. Citric acid was employed as chelating agent to stabilise the metal cations, avoiding any oxide precipitation, and isopropanol was added as an organic surface active agent. The evaporation of the solvent led to the formation of the gel, containing a polymeric mixture of the metal cations and citrate ion.[10]

Figure 5.1 shows the PXRDs of the products resulting from calcination of this gel at different temperatures. At moderate temperatures (<600 ºC), the gel collapses to form a brown foam containing a mixture of amorphous materials, Li_2CO_3 and nanocrystalline $La_2Zr_2O_7$ pyrochlore, as indicated by the broad Bragg reflections. Increasing the calcination temperature above 650 ºC, leads to emergence of the garnet cubic phase with a single phase present at 700 ºC after two hours. Surprisingly, the material started to decompose above 800 ºC; the corresponding solid-state synthesised LLZO material is stable. This decomposition at high temperatures for the sol-gel synthesised material has also been previously reported.[3,9,11] At temperatures higher than 800 ºC, secondary phases phases such as the $La_2Zr_2O_7$ pyrochlore and $LaAlO_3$ perovskite form due to lithium evaporation, despite the use of a 20% lithium precursor excess. The first synthetic attempts with lower Li precursor excess failed to yield phase pure materials at any temperature. This fact could be attributed to a possible Li^+/H^+ exchange occurring during the sol-gel synthesis as this is performed in an aqueous protic media, which would lead to a protonated lithium-deficient garnet. Li^+/H^+ exchange is known to occur at room temperature in high-temperature synthesised garnet materials, when exposed to humid air or immersed in acid solutions for prolonged times.[8,12,13] In the case of the sol-gel synthesis, this Li^+/H^+ exchange could be occurring during the early stage of the synthesis, promoted by the high proton concentration in the synthetic media.

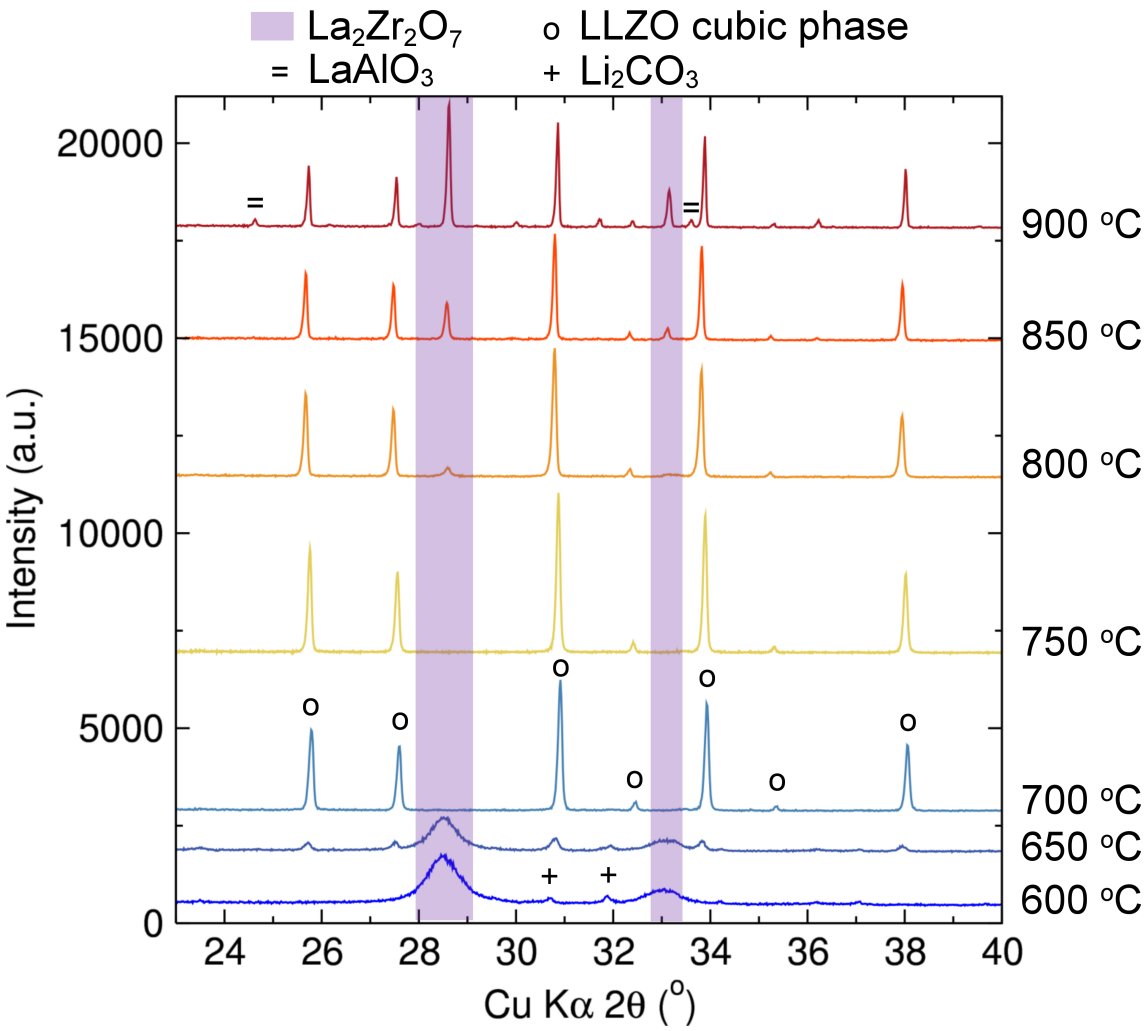

Figure 5.1: PXRD data collected *ex-situ* from $Li_{6.5}Al_{0.25}La_{2.92}Zr_2O_{12}$ garnet synthesised *via* sol-gel chemistry and calcined at different temperatures. Main Bragg reflections for the $LaAlO_3$ (24° and 33° 2θ) and $La_2Zr_2O_7$ (28° 2θ) secondary phases are indicated; Bragg peaks arising from the cubic garnet target phase are indicated by the open circles.

Rietveld refinements of the PXRD data for the gel calcined at 700 °C for 2 hours revealed phase pure LLZO cubic garnet with a good agreement between the experimental data and the cubic $Ia\bar{3}d$ garnet space group (Fig. 5.2). The unit cell parameter calculated from these Rietveld refinements had a value of 12.9965(1) Å, which was expanded compared to value for the high temperature solid-state synthesised material (∼12.96 Å) and in line with the reported values for sol-gel synthesis.[3,14]

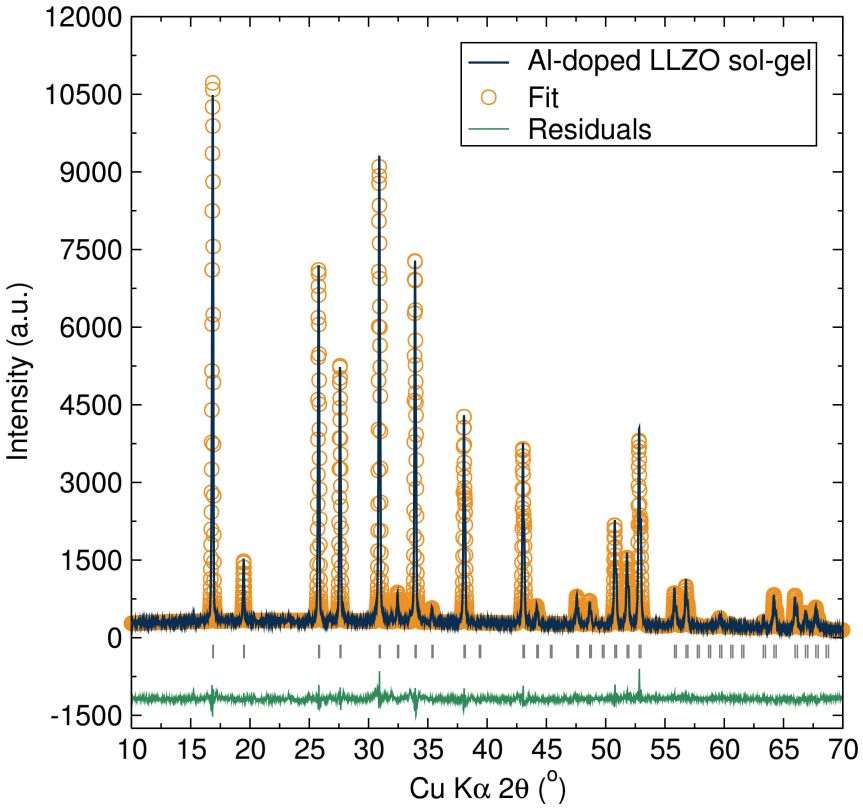

Figure 5.2: Rietveld refinement for the $Li_{6.5}Al_{0.25}La_{2.92}Zr_2O_{12}$ garnet sol-gel synthesised at 700 °C for 2 hours PXRD data fit to the cubic ($Ia\bar{3}d$) space group. R_{wp} = 0.0774, R_p = 0.0578 and χ^2 = 2.661.

This small cell expansion has also been observed in Li^+/H^+ exchanged high temperature prepared lithium garnets and perovskite materials in previous reports, which has been attributed to the replacement of strong Li–O bonds by weak hydrogen H–O· · ·H bonds associated with the Li^+/H^+ exchange.[8,15–19] Similar protonation phenomena have been also reported in other systems, such as Li-containing perovskites, experiencing a similar expansion in the unit cell.[17,20] Larraz studied this unit cell parameter expansion as a consequence of Li^+/H^+ exchange in the high temperature synthesised LLZO garnet by exposing the material to continuous water vapour.[21] He demonstrated a linear relationship between the progressive protonation of the LLZO garnet materials and the expansion of the unit cell, from 12.96 Å for the unprotonated material up to 13.09 Å for the pentaprotonated LLZO material (Fig. 5.3).[21] Interpolating the value obtained from the sol-gel synthesised material studied here ($\sim$ 13 Å), a Li^+/H^+ exchange of 1.5 mols could be estimated.

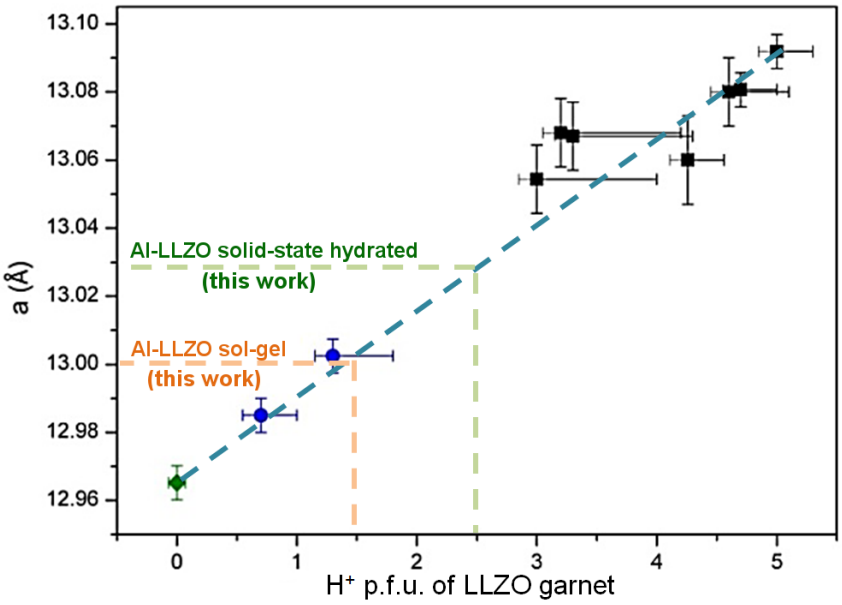

Figure 5.3: Relationship between the protonation level of the cubic $Li_{7-x}H_xLa_3Zr_2O_{12}$ garnet and the crystal unit cell parameter for aged samples under water vapour at *ca.* 325 ºC. This figure has been adapted from reference[21]. The dotted lines have been added manually as a eye guide. Adapted from Reference[21]. Copyright (2016) University of Zaragoza.

This expanded cell parameter observed by PXRD and the premature decomposition at high temperatures suggest a possible Li^+/H^+ exchange in the low temperature cubic Al-doped LLZO garnet material synthesised *via* this sol-gel chemistry procedure. In order to further study this possible Li^+/H^+ exchange, a protonated solid-state cubic LLZO garnet was prepared for comparison to this sol-gel sample. An as-synthesised solid-state cubic Al-doped LLZO garnet was exposed to water vapour for 12 and 24 hours in order to produce protonated garnet material. Figure 5.4 shows the PXRDs of the as-synthesised Al-doped LLZO sample produced by solid-state reaction and the sample after exposure to water vapour for 12 and 24 hours. There is a clear progressive displacement of the Bragg reflections towards larger d-spaces as the sample was exposed to the water vapour.

The sample exposed for 24 hours was then chosen for further characterisation together with the as-synthesised Al-doped LLZO samples prepared *via* sol-gel and high temperature solid-state approaches. The cell parameter of the 24 hours hydrated Al-doped LLZO synthesised by solid-state chemistry expanded from ≈12.96 Å on the as-synthesised material to 13.0296(8) Å, as obtained from Le Bail analyses. This cell expansion indicated the effective protonation of the garnet material. In this case, by the cell parameter figure, a protonation of *ca.* 2.5 H^+ could be estimated.

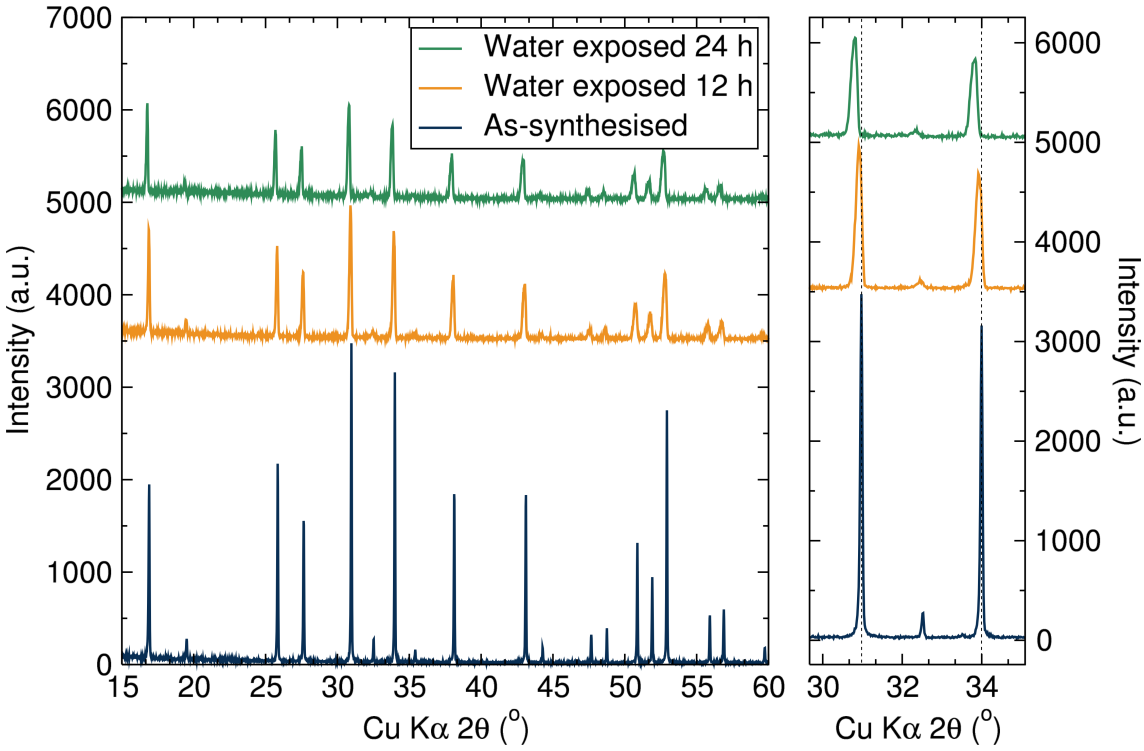

Figure 5.4: PXRD of the as-synthesised solid-state $Li_{6.5}Al_{0.25}La_{2.92}Zr_2O_{12}$ material before (blue) and after 12 (orange) and 24 hours (green) of water vapour exposure. The displacement of some garnet Bragg reflections are highlighted on the right [(420) (332) and (422) from left to right].

Li-containing side-products, such as LiOH and Li_2CO_3, have been reported to appear on the surface of lithium garnet as a consequence of Li^+/H^+ exchange and subsequent reaction with CO_2 (see Figure 5.5).[7,8,22] While these light weight (and poor X-ray scattering) compounds in small quantities on the garnet surface are usually "invisible" to laboratory PXRD, Raman spectroscopy can be used to detect them.

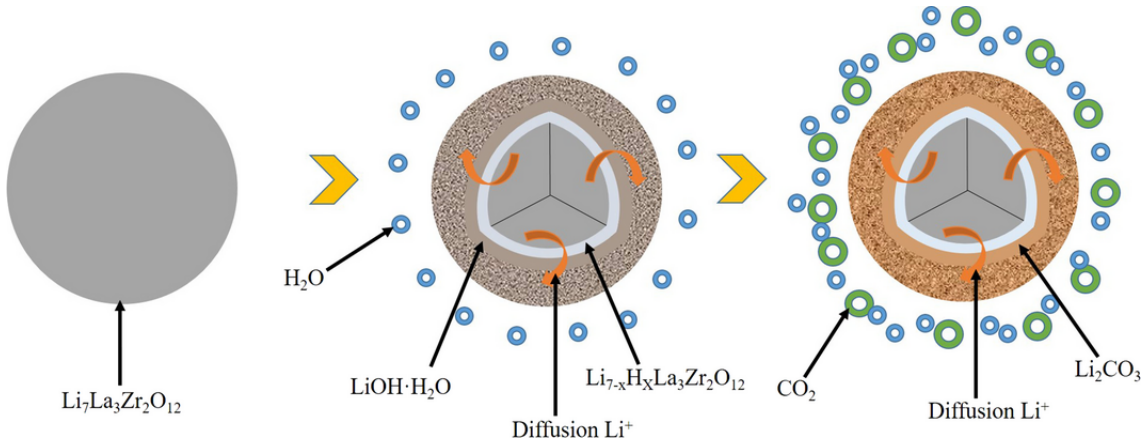

Figure 5.5: Schematic model illustrating the lithium hydroxide and carbonate formation process on the surface of lithium garnets. Reproduced with permission from Wiley.[22]

Raman spectroscopy can also provide clear information regarding the existence of protons within the garnet structure as well as any change produced in the local sym-

metry of the material. Galven *et al.* reported the co-existence of a secondary non-centrosimmetric cubic phase with space group $I\bar{4}3d$ when the garnet material is subjected to Li^+/H^+ exchange.[18] Ocera *et al.* confirmed later this space group symmetry change in detail in the cubic LLZO system synthesised by solid-state chemistry and treated with water vapour.[23] This symmetry distortion induces changes in the Li-O vibration region, as well as a split in the Zr-O vibration peak as consequence of Zr^{4+} cation displacement from the ZrO_6 octahedral centre (Fig. 5.6). In addition, they also calculated and corroborated experimentally an additional vibration band produced by the H^+ bounded to oxygen anions within the garnet framework. This band is formed by a convolution of several O-H vibrational modes in the high frequency region of the Raman spectrum, above 3400 cm^{-1}.

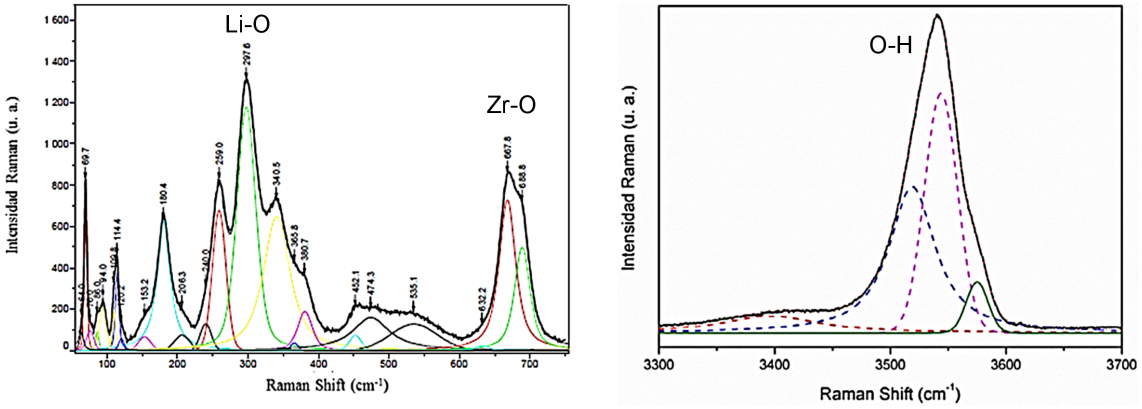

Figure 5.6: Experimental data and calculated Raman spectrum for the $I\bar{4}3d$ garnet space groups produced by Li^+/H^+ exchanged in solid-state synthesised LLZO cubic garnet material by exposure to water vapour. Adapted from Reference[21]. Copyright (2016) University of Zaragoza.

The Raman spectra from the LLZO garnet materials are plotted in Figure 5.7. From the Raman profiles, it is clear that the high temperature solid-state freshly prepared material retained the features of the high temperature cubic LLZO phase,[8] with additional peaks arising from the contribution of LiOH (3675 cm^{-1}) and an almost negligible presence of Li_2CO_3 (1088 cm^{-1}). The LiOH side-product can have its origin in the excess employed in the reaction synthesis while Li_2CO_3 could be due to air exposure during sample handling and subsequent reaction with atmospheric CO_2.[24] In the case of the sol-gel and hydrated solid-state samples, there was a clear change in the Raman spectra. The shape of the Raman bands in the Li-O region changed, displaying a stronger peak at 300 cm^{-1} with a splitting of the Zr-O band due to the loss in symmetry on the ZrO_6 octahedra. These changes mimic the predicted Raman spectra for the Li^+/H^+ exchanged LLZO material by Larraz.[21] In addition, for these two protonated materials, contributions from Li_2CO_3 and $LiOH{\cdot}H_2O$ were also detected. As previously noted (Fif. 5.5), these two side-products can appear as a consequence of the reaction between the expelled lithium from the garnet structure after the Li^+/H^+ exchange and atmospheric CO_2.

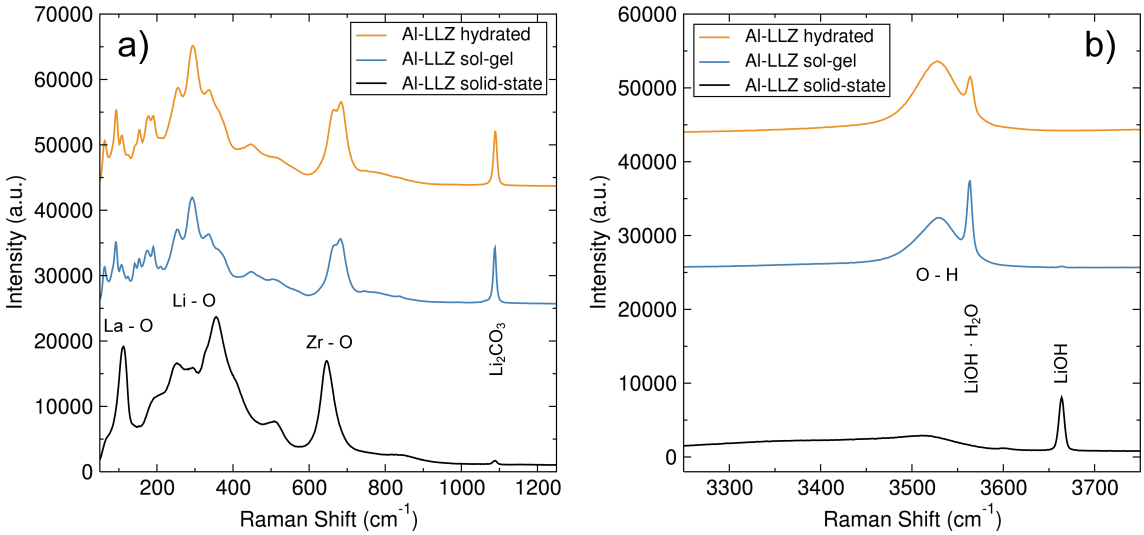

Figure 5.7: Low (a) and high (b) frequency Raman spectra for the as-synthesised sol-gel and solid-state LLZO materials and the hydrated solid-state synthesised $Li_{6.5}Al_{0.25}La_{2.92}Zr_2O_{12}$ cubic garnet.

The truly revealing confirmation of Li^+/H^+ exchange was confirmed by the presence of a broad peak centred at 3530 cm^{-1} for the two protonated garnets (Fig. 5.7b), typical of hydroxyl moieties. Specifically, this broad band arises from the presence of non-equivalent oxygen positions in the garnet crystal framework and/or from different configurations of proton bonding.[25,26] The lack of stretching bands around 3400 cm^{-1} where the ν_1 and ν_3 modes of water typically appear, indicates the absence of water molecules adsorbed on the garnet surface.

While the reasons for Li^+/H^+ exchange are relatively well understood for the water vapour exposed samples, this exchange for the sol-gel prepared LLZO takes place during the gel formation, as this was the only time when the sample was readily exposed to water. Raman analyses clearly showed the large presence of the $I\bar{4}3d$ non-centrosymmetric space group in the protonated garnets. This observation was not possible to confirm by diffraction techniques, due to the minimal difference between diffractograms of the $Ia\bar{3}d$ and the $I\bar{4}3d$ space groups. Also, this difference manifests a small extra peak at 2.3 Å in d-space,[17] which is unobservable using laboratory PXRD. It is likely that the Li^+/H^+ exchange occurs on the surface of the garnet particles where Raman spectroscopy displays higher sensitivity, thus being mostly "invisible" to conventional PXRD. In addition to this, it was proposed that at least 4 H^+ per formula unit of garnet are needed for a net bulk transformation into the $I\bar{4}3d$ group.[23] Therefore it is likely the materials studied in this chapter are below this threshold.

5.2 Phase formation insights by *in-situ* NPD diffraction studies

It is clear that the sol-gel synthesised LLZO cubic phase garnet experiences Li^+/H^+ exchange, most likely during the gel formation. In order to gain further information on the phase formation of the Al-doped cubic LLZO garnet synthesised by sol-gel, *in-situ* NPD measurements were carried out at ISIS Polaris instrument. The use of neutrons, allows to study the presence of poorly X-ray scattering phases, such as the light molecular weight lithium hydroxides or carbonates. These NPD measurements also provide a more precise garnet stoichiometry, including lithium site distribution, which are not possible by PXRD.

The Al-doped LLZO gel precursor was pre-calcined at 600 ^oC *ex-situ* to remove all organic matter before being loaded in the beamline for further heat treatment. In addition, the *in-situ* experiment was performed under continuous dynamic vacuum to avoid any possible pressure increase due to release of gases during subsequent heating.

Figure 5.8 shows the neutron diffraction patterns of the sample at different temperatures as collected from the backscattering detector bank, which possesses the highest d-space resolution. The main Bragg peaks for the major phases detected have been highlighted by shadowing boxes for clarity. The diffraction patterns presented a high background due to the contribution from the silica glass container, as previously observed in other experiments on the same instrument with a similar setup.[27] This background due to the amorphous quartz cell was fitted from linear interpolation between manually selected points, chosen to ensure they did not interact with the Bragg peaks of the phases under study.

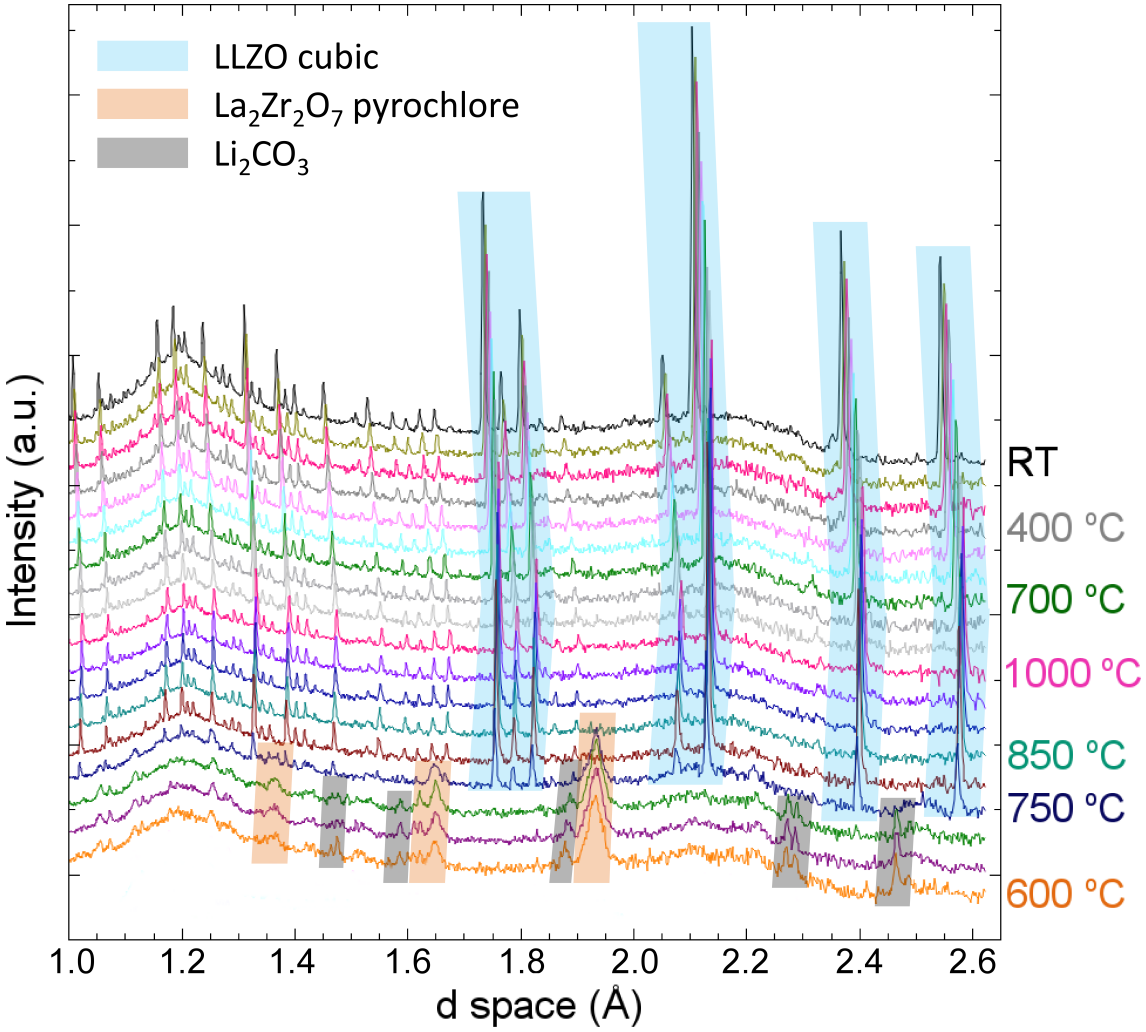

Figure 5.8: NPD patterns for the *in-situ* calcination of the $Li_{6.5}Al_{0.25}La_{2.92}Zr_2O_{12}$ gel at different temperatures. The temperature steps between 600 and 1000 °C are 50 at °C increments. The temperature steps are increased to 100 °C then when cooling down from 1000 to 200 °C. The main peak for the different phases present are shadowed by different colours as indicated in the legend.

The pre-calcined material was initially heated from room temperature to 600 °C where the main crystalline phases could be ascribed to a mixture of Li_2CO_3 and $La_2Zr_2O_7$ pyrochlore, dominated by the presence of the latter with a small crystallite size as indicated by the peak broadening. The sample was then heated up to 1000 °C at a ramp of 0.5 °C min^{-1} with 1 hour dwell steps every 50 °C to allow longer data collection and sample temperature stabilisation. The Bragg peaks from the lithium carbonate disappeared at temperatures above 700 °C, while the pyrochlore material was stable up to 750 °C. It is at this temperature that the first Bragg reflections from the LLZO garnet material arise. There was no appreciable peak splitting, indicating the formation of the cubic phase with no tetragonal phase contribution. This temperature for the formation of the LLZO garnet cubic phase is slightly higher than the temperature found in the case of *ex-situ* calcinations. This slightly higher calcination temperature needed to obtain the garnet phase in

the *in-situ* experiment may be due to the shorter time at which the sample was held at 700 °C, half the time compared with the *ex-situ* calcination. At 800 °C, only the LLZO cubic phase was present with no secondary phases detected. The cubic LLZO phase was stable up to 1000 °C without decomposition to other Li-deficient secondary phases, which is typically observed for samples calcinated in air for *ex-situ* PXRD measurements. This difference in calcination behaviour can be related to the absence of air during the *in-situ* experiment. The lack of air prevents reaction of the garnet material with CO_2 and oxygen. This avoids garnet decomposition since lithium is not removed from the garnet surface. After reaching 1000 °C, the material was then cooled down to room temperature, with 1 hour dwell steps every 100 °C until a temperature of 200 °C is reached. After that, the material was cooled down to room temperature where a longer scan for Rietveld refinement was carried out.

Rietveld refinements of the *in-situ* formed LLZO cubic garnet at (a) 1000 °C and (b) cooled to room temperature are shown in Figure 5.9. The Rietveld refinement of the garnet material at 1000 °C showed a good agreement between the diffraction data and the cubic $Ia\bar{3}d$ LLZO crystallographic model. The sample presented high phase purity with no other secondary phases present. The high temperature of the measurement precluded unambiguous refinement of the atomic parameters, other than the cell parameter (a = 13.1821(5) Å) and so these were fixed to the standard model. Rietveld refinements of the room temperature diffraction data allowed refinement of some of these atomic parameters (Table 5.1).

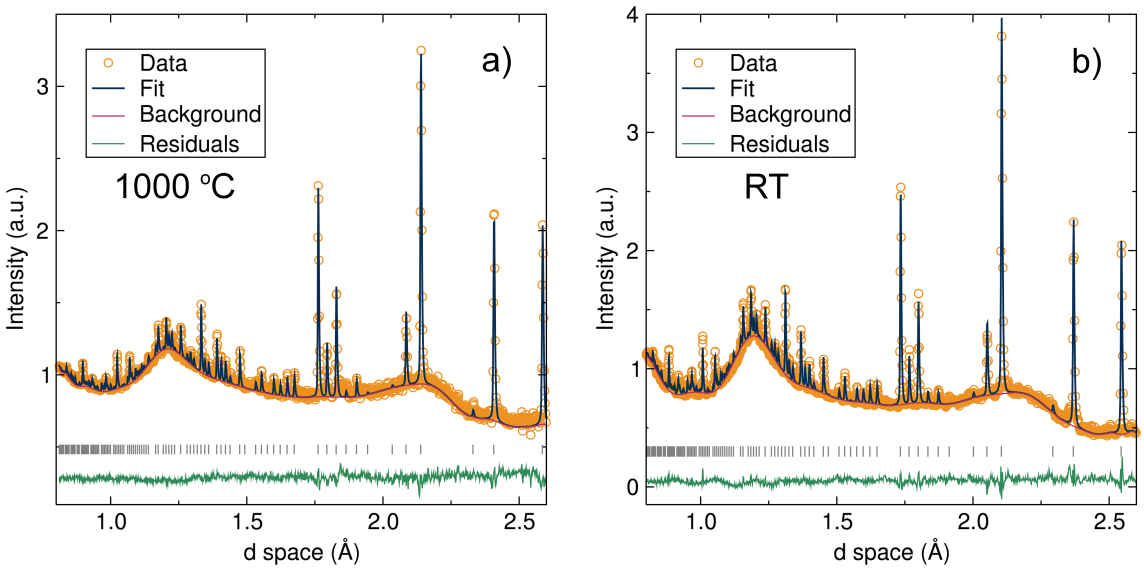

Figure 5.9: Rietveld refinements for NPD data for the sol-gel synthesised $Li_{6.5}Al_{0.25}La_{2.92}Zr_2O_{12}$ garnet fit to the cubic ($Ia\bar{3}d$) space group at 1000 °C (a) and room temperature (b) collected from the backscattering detector bank. For the 1000 °C refinement, R_{wp} = 0.0153, R_p = 0.0214 and reduced χ^2 = 1.880. For the room temperature refinement, R_{wp} = 0.0135, R_p = 0.0175 and educed χ^2 = 3.791.

Table 5.1: Extracted parameters for NPD data at room temperature for the sol-gel synthesised $Li_{6.5}Al_{0.25}La_{2.92}Zr_2O_{12}$ fit to the cubic ($Ia\bar{3}d$) space group.

Atom	Site	Frac.	x	y	z	Uiso (100/Å^2)
Li1	24d	0.4(2)	-0.125000	0.000000	0.250000	6(4)
Li2	96h	0.36(5)	0.100400	0.685300	0.576900	3(1)
Al	24d	0.08	-0.125000	0.000000	0.250000	0.5
La	24c	0.94(3)	0.000000	0.250000	0.125000	1.6(1)
Zr	16a	1	0.000000	0.000000	0.000000	1.3(1)
O	96h	1.04(3)	-0.0323(3)	0.0528(3)	0.1495(3)	2.5(1)

The stoichiometry obtained from the Rietveld refinements at room temperature was $Li_{5.5(9)}Al_{0.25}La_{2.82(9)}Zr_2O_{12.5(4)}$. As suspected, the Li^+ concentration per formula unit in the sol-gel synthesised material is lower than that obtained for the solid-state prepared analogue[28] ($\sim$ 1 Li^+ lower). Addition of protons to the garnet structure in the refinements was not possible, as this led to inconsistent refinements. There are numerous potential reasons for this, such as the low concentration of protons together with their segregation/disorder within the structure. In addition, measurements at room temperature are still high temperature for refinement of these light atoms, where normally lower temperature measurements are employed to investigate these atoms.

In order to estimate the proton concentration within the sol-gel synthesised LLZO material, the garnet crystal electrical neutrality was considered. Supposing full occupancy of oxygen, the crystal electrical neutrality of the sol-gel synthesised Al-doped LLZO garnet material would be unbalanced by a defect of *ca.* 1.3 positive charges, mainly due to Li^+ deficiency. This number could therefore be attributed as the number of protons introduced in the garnet framework as a consequence of Li^+/H^+ exchange, leaving an estimated stoichiometry of $Li_{5.5(9)}H_{1.3}Al_{0.25}La_{2.82(9)}Zr_2O_{12.5(4)}$ which, within the standard deviations, is electrically balanced. This number of protons inserted into the garnet framework was within the range of protonation already reported for solid-state synthesised LLZO material, where up to 5 protons can be inserted per formula unit by Li^+/H^+ exchange.

Reaction between the quartz tube container and the *in-situ* formed garnet material at high temperatures cannot be ruled out as this could have resulted in dissolution of Li^+ from the garnet framework and hence the decreased Li^+ stoichiometry in the garnet. In addition, the refined cell parameter of 12.9721(6) Å for the *in-situ* formed sol-gel sample is slightly smaller compared to the sample calcined in air at lower temperature which may indicate a lower level (if any) of garnet protonation. This could be expected as the maximum temperature achieved during the *in-situ* experiment of 1000 ^{o}C makes unlikely for any proton in the garnet framework to be retained. It is also possible that accidental exposure to air after the heat treatment would have resulted in water uptake by the garnet material. Furthermore, hindering the formation of lithium carbonates due to a dynamic

vacuum environment during the *in-situ* experiment could also preclude lithium hydroxide formation from Li^+/H^+ exchange, limiting the protonation of the garnet. Some of the protons could have also left the sample as water molecules during heating at elevated temperatures with Li^+ being partially reinserted to the garnet structure from surface lithium carbonate or hydroxide entities, and hence the smaller cell parameter.[23] The presence of small amorphous lithium hydroxide or carbonate surface phases could not being discarded, since the high background in the diffraction data may preclude their observation. Considering the relatively high standard deviations of the Li^+ occupancy fractions from the Rietveld refinements, it may be also possible that no Li^+ has left the garnet framework if the upper limit of Li^+ stoichiometry, 6.4 Li^+ per garnet formula unit, is taken into account.

Another effect observed from the Li^+/H^+ exchange was a Li^+ redistribution across the garnet structure. In the solid-state prepared material, the molar ration between the tetrahedral 24d and octahedral 96h Li^+ from NPD was 0.17 (0.9 mol Td Li^+ and 5.4 mol Oh Li^+). In the sol-gel prepared material, this ratio is found to be 0.28 (1.2 mol Td Li^+ and 4.3 mol Oh Li^+), indicating that the 96h positions are the most likely to be replaced by protons during the Li^+/H^+ exchange. This is also in agreement with previous reports, where similar trends were found, with Li^+ on the 96h position more readily replaced by protons, while the 24d positions were not taken up by protons.[18,29] This Li^+ redistribution can also produce a migration of the highly mobile Li^+ in octahedral positions towards the less mobile tetragonal sites with symmetry transformation to the $I\bar{4}3d$ non-centrosymmetric space group.[23,30] Furthermore, Galven *et al.* reported the full replacement of the Li^+ located in the 96h sites by H^+ for the $Li_5La_3Nb_5O_{12}$ cubic garnet treated with benzoic acid in hot ethanol.[16]

The above differences in the behaviour in the calcination of the sol-gel precursor to obtain the LLZO cubic phase garnet under air and vacuum, and the different protonation mechanisms employed in this chapter are summarised in Figure 5.10.

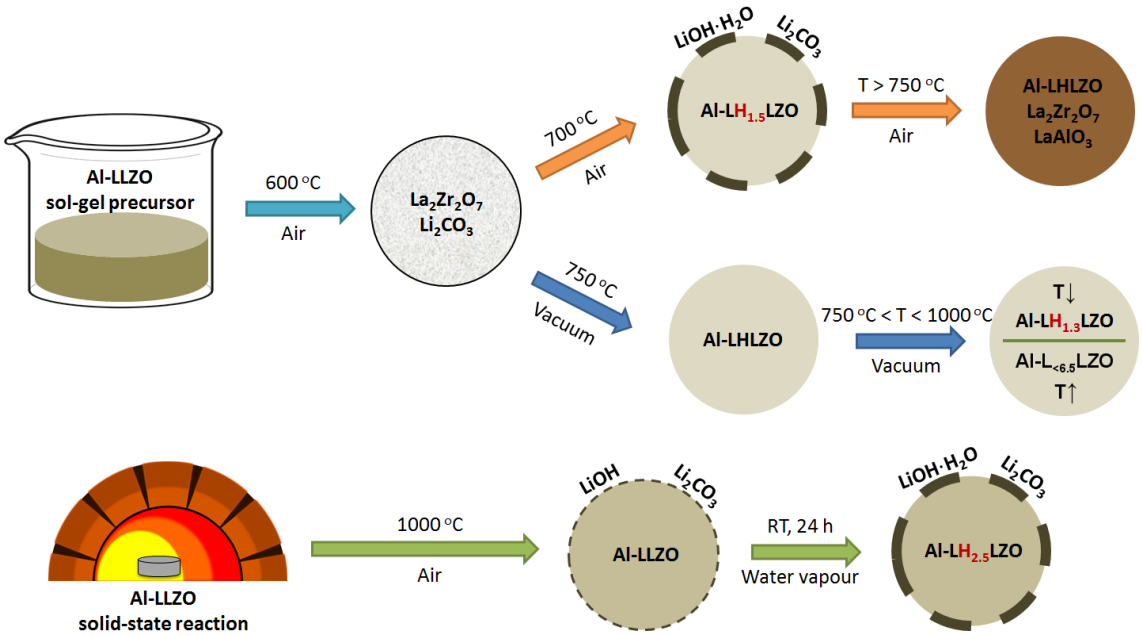

Figure 5.10: Schematic illustration of the sol-gel garnet cubic phase formation under the different atmospheres studied in this chapter. Al-LLZO refers to $Li_{6.5}Al_{0.25}La_{2.92}Zr_2O_{12}$ and Al-LH$_x$LZO to $Li_{6.5-x}H_xAl_{0.25}La_{2.92}Zr_2O_{12}$.

The microstructure of the sol-gel material calcinated in air was studied by SEM. The obtained SEM micrographs revealed LLZO particles with sizes near the sub-micron region. As expected, the sol-gel prepared material presented a smaller particle size compared to the high temperature solid-state synthesised LLZO material.

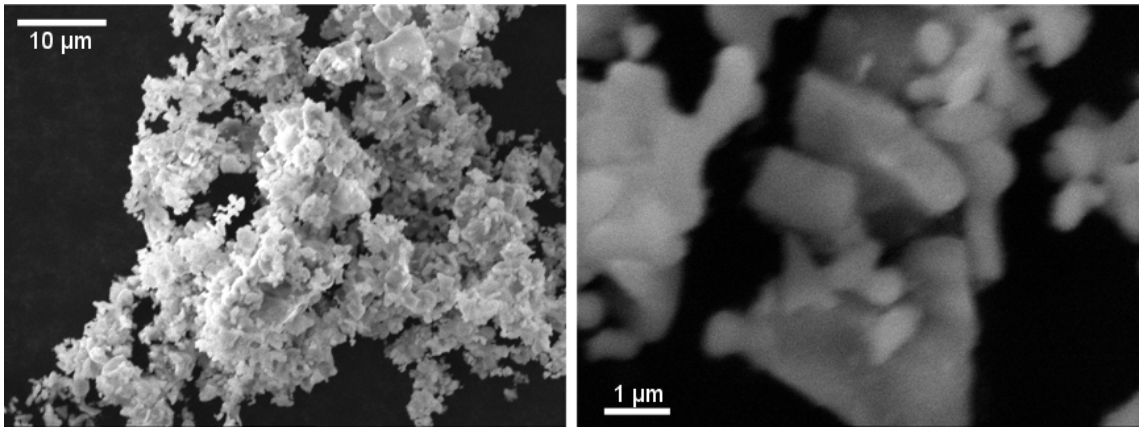

Figure 5.11: SEM images of the $Li_{6.5}Al_{0.25}La_{2.92}Zr_2O_{12}$ sample prepared *via* sol-gel chemistry and calcined in air.

5.3 Lithium-ion diffusion studies

5.3.1 Macroscopic ionic diffusion analyses by EIS

In a first approach to study the transport properties of the sol-gel synthesised cubic LLZO garnet material, AC EIS measurements were carried out. Figure 5.12a shows the Nyquist

plots of the EIS data collected at room temperature for the Al-doped LLZO cubic garnet materials synthesised by high temperature solid-state approach and sol-gel chemistry. As expected, the Nyquist plot of the LLZO synthesised by sol-gel displayed a semicircular shape, due to its resistance towards ionic conduction. The sol-gel prepared LLZO garnet material displayed a higher impedance, with higher normalised resistance toward intra-grain ionic conduction compared to the solid-state prepared sample. The intra- and inter-grain resistances merged when heating up the pellet, so the total ionic conductivity values were reported for temperatures above 60 °C.

The resistance towards ionic transport was calculated from the Nyquist plots fits to each impedance contribution to an electrical equivalent circuit formed by a resistance with a parallel constant phase element. The ionic conductivity values (Table 5.2) were then calculated by Pouillet's law (Equation 3.1).

These EIS measurements showed a decrease in the intra-grain ionic conductivity by more than one order of magnitude from 3.74 $\times$ 10^{-6} to 3.87 $\times$ 10^{-7} S cm^{-1}, from the solid-state to the sol-gel synthesised LLZO materials respectively. An activation energy of 0.83(4) eV for the total ionic conductivity was calculated from the Arrhenius plot of the total conductivity values (Fig. 5.12b), which represented an increase of nearly 0.3 eV additional energy required for the total ionic conduction for the sol-gel prepared material.

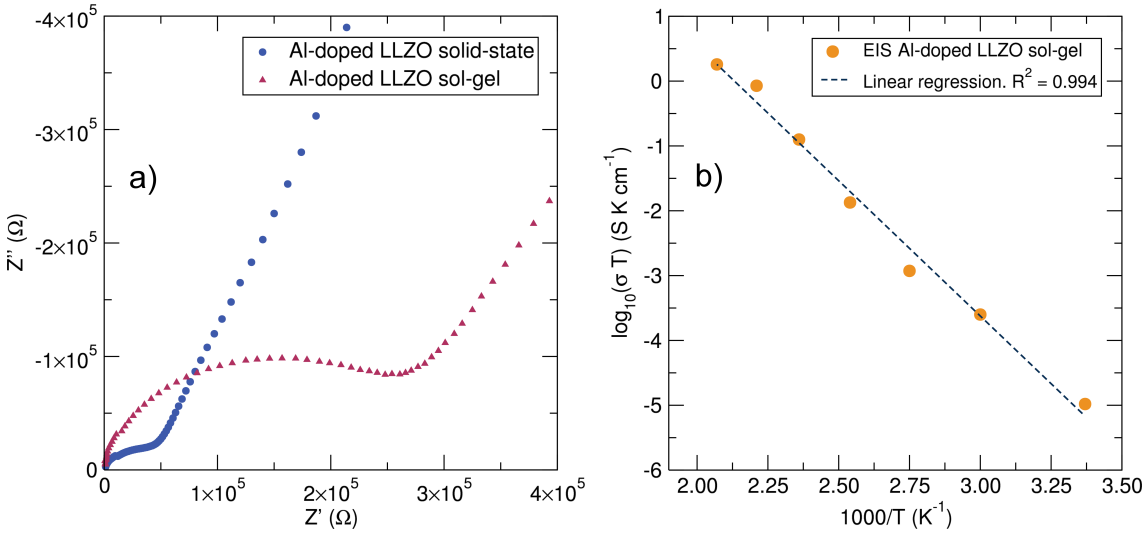

Figure 5.12: (a) Nyquist plot of the EIS data for the $Li_{6.5}Al_{0.25}La_{2.92}Zr_2O_{12}$ garnet at room temperature synthesised by solid-state (circles) and sol-gel (triangles) chemistries. A larger resistance to ionic diffusion is observed in the case of the sol-gel synthesised material. (b) Arrhenius plot of the conductivity coefficients for the sol-gel synthesised $Li_{6.5}Al_{0.25}La_{2.92}Zr_2O_{12}$ garnet. The calculated activation energy from it is 0.83(4) eV.

Table 5.2: Ionic conductivity values obtained from EIS at different temperatures for the Intra-Grain (I-G) and Grain Boundary (GB) components and total ionic conductivity for the sol-gel synthesised Al-doped LLZO garnet.

Temp. (K)	I-G (S cm^{-1})	GB (S cm^{-1})	Total Cond. (S cm^{-1})
297	3.9×10^{-7}	3.9×10^{-8}	3.5×10^{-8}
333	1.9×10^{-6}	1.3×10^{-6}	7.5×10^{-7}
363	-	-	3.3×10^{-6}
393	-	-	3.4×10^{-5}
423	-	-	3.0×10^{-4}
453	-	-	1.9×10^{-3}
483	-	-	3.7×10^{-3}

These results were in agreement with similar studies in the literature, where the low temperature prepared LLZO materials showed worsened transport properties.[3,6,9] For example, Goodenough and co-workers reported the synthesis of Al-free cubic LLZO by sol-gel chemistry, obtaining conductivity values on the order of 10^{-6} S cm^{-1}.[9] A similar activation energy increase has also been found recently by Yow *et al.* for the LLZO material after protonation (from 0.32 eV up to 0.85 eV for the highly protonated version).[31] These poorer ionic transport properties could be due to a combination of several factors such as the lower lithium concentration,[32] the use of a lower sintering temperature leading to lower density,[33] the smaller particle size which increases the GB resistance, or even the greater presence of Li_2CO_3 on surface[24,34]. μ^+SR studies were also performed in order to shed some light into the microscopic lithium diffusion properties of the sol-gel synthesis LLZO material.

5.3.2 μ^+SR local lithium diffusion studies

In order to unveil the influence of the synthetic method on the local lithium-ion dynamics, analogous μ^+SR studies to those performed on the high temperature solid-state synthesised LLZO material were performed.[28] The decay positron asymmetry at room temperature is showed in Figure 5.13a.

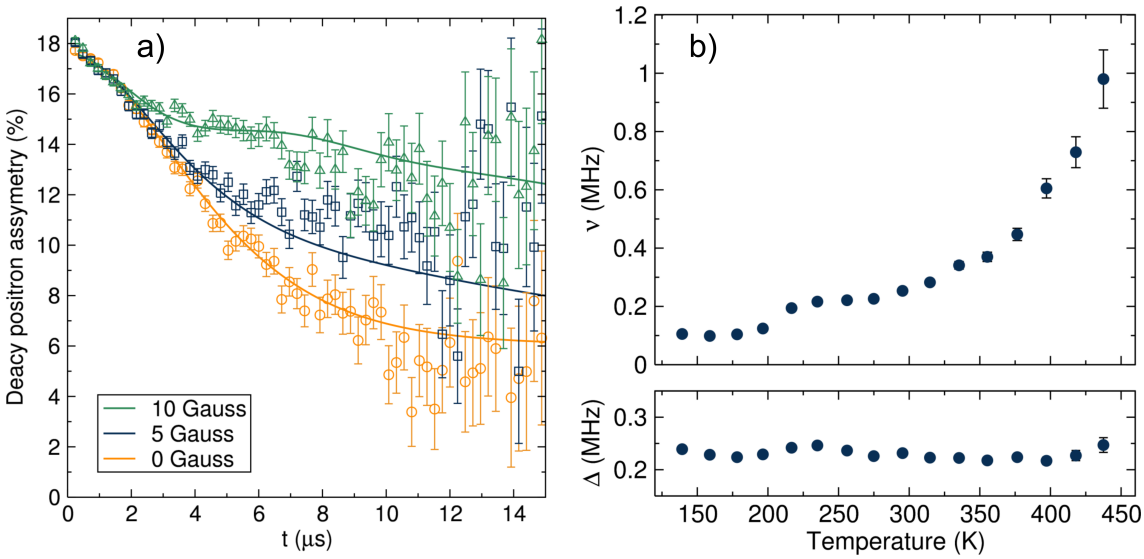

Figure 5.13: (a) μ^+SR raw data collected at room temperature at zero field (circles) and applied fields of 5 G (squares) and 10 G (triangles), fit using the Keren function for the sol-gel synthesised $Li_{6.5}Al_{0.25}La_{2.92}Zr_2O_{12}$ garnet. (b) Temperature dependence of ν and Δ parameters obtained from fits to the Keren function from 140 K to 440 K.

As expected, the decay positron asymmetry experiences a moderate relaxation at short times. This indicated the absence of any fast depolarisation of the muon spin due to electronic magnetic fields in the sample which would have resulted in a more acute decay of the positron asymmetry.[35,36] The decay positron asymmetry at longer times followed then a slower relaxation due to muon interactions with nuclear magnetic fields of elements in the samples with positive spins (^{27}Al, ^{139}La and ^{91}Zr) that can interact with the muon's spin, in a similar manner as in the analogous high temperature LLZO. The decay positron asymmetry also experienced a lower relaxation with increasing applied longitudinal magnetic field, as the muon spin followed the parallel magnetic field.

The decay positron asymmetry over time at different temperatures was fitted (Fig. 5.13a) using the Keren function (Equation 2.9). The temperature dependence of the ν and Δ parameters (Fig. 5.13b) followed a similar trend as observed in the other Li-rich garnet systems studied in Chapters 4 and 5, with a thermally activated lithium diffusion above 300 K as the ν parameter experienced an exponential increase. The Δ parameter remained stable indicating that the muon was not itself diffusing due to the increasing thermal energy.[35,36]

In order to calculate the Li^+ diffusion coefficient from Equation 3.3 in the sol-gel prepared LLZO material, the structural data from the NPD experiment were employed with the same Li^+ diffusion model used in the previous chapters, *i.e.* Li^+ hopping from the 24d sites to the four surrounding 96h sites and from the 96h sites to the two neighbouring 24d sites. The lithium diffusion coefficient at room temperature was calculated to be 3.2×10^{-11} cm^2 s^{-1}.

This Li^+ diffusion coefficient for the sol-gel LLZO garnet is nearly 30% lower compared

to the high temperature analogue material (4.62×10^{-11} cm^2 s^{-1}).[28] The activation energy for the local lithium-ion diffusion had a calculated value from Arrhenius analyses of 0.19(1) eV, coinciding with the value obtained for the high temperature material (Fig. 5.14).

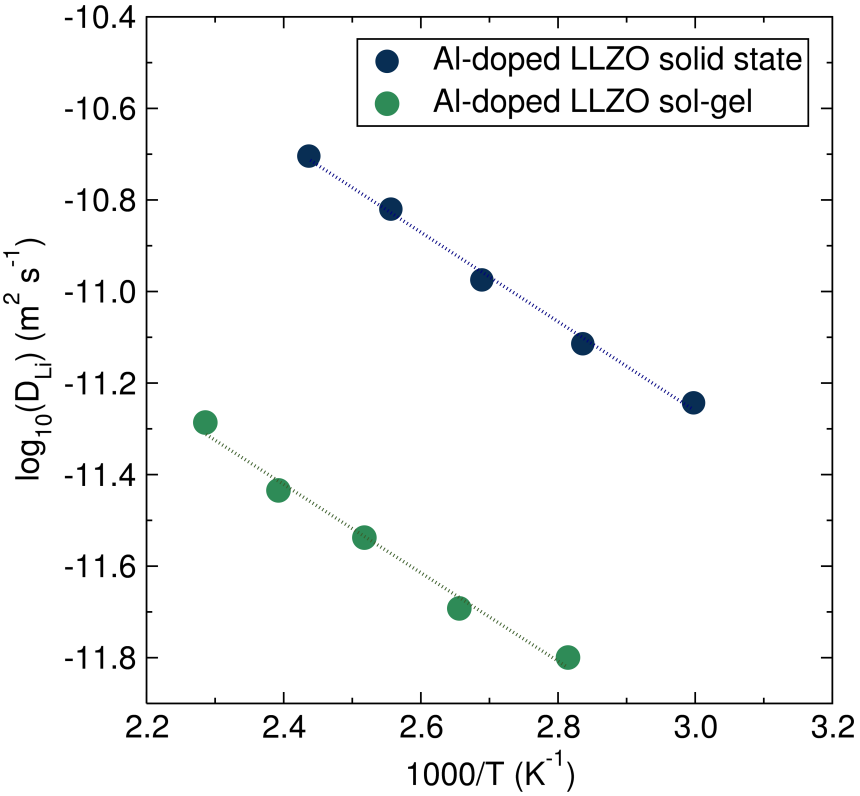

Figure 5.14: Arrhenius plot of the diffusion coefficient calculated from μ^+SR for the $Li_{6.5}Al_{0.25}La_{2.92}Zr_2O_{12}$ garnet synthesised *via* solid-state and sol-gel chemistries. The calculated activation energy from it is 0.19(1) eV for both materials.

These findings suggested that lithium-ions are able to diffuse with the same energetic requirement in both materials, but the flux of mobile lithium-ions diffusing is decreased in the sol-gel synthesised material. While the activation energy for the Li-ions to hop depends mainly on the distance between the starting and final hopping positions, and the structural atomic arrangement around the diffusion pathway, the Li diffusion coefficient relies also on the number of mobile Li-ions.[30,32,37,38] As mentioned in the previous section, the sol-gel synthesised LLZO experienced a lithium redistribution from the highly mobile 96h sites to the less mobile 24d. This redistribution together with the lower concentration of Li^+ could led to a lower overall microscopic diffusion coefficient of the sol-gel prepared LLZO material. In addition, Sanjuan *et al.* have reported recently this year how the protonation of the $Li_5La_3Nb_2O_{12}$ garnet by Li^+/H^+ exchange affects the Li^+ diffusion properties of the material.[26] Specifically, they have found that the presence of H^+ in the 96h octahedral cavities hinders the Li^+ diffusion, lowering the net flux of Li^+ circulating around the garnet framework. This effect can be extrapolated to the LLZO material synthesised by sol-gel in this chapter, reinforcing the hypothesis that the presence of H^+ ions in the

material could be responsible for the lower microscopic Li^+ diffusion coefficient compared to the unprotonated solid-state prepared LLZO material.

5.4 Conclusions

In this chapter, the sol-gel synthesis of cubic LLZO garnet materials has been successfully carried out. The synthesised material presented an expanded cell parameter and lower thermal stability compared to the analogous material synthesised by solid-state chemistry. Raman spectroscopy analyses revealed that the surface of the sol-gel synthesised LLZO material presented a distortion in the space group symmetry from the symmetric $Ia\bar{3}d$ to the non-centrosymmetric $I\bar{4}3d$ space group. This symmetry distortion, together with the presence of a broad vibration band above 3500 cm^{-1}, indicated the existence of protons inside the garnet structure. This protonation of the garnet material due to Li^+/H^+ exchange could be responsible for the expanded cell parameter and lower thermal stability of the material.

In-situ NPD measurements were performed and showed that the pre-calcinated gel consisted in a mixture of Li_2CO_3 and nanocrystalline $La_2Zr_2O_7$. The *in-situ* experiment revealed that calcination of the material under a vacuum environment protects the sol-gel synthesised LLZO from decomposition at temperatures up to 1000 ^oC, avoiding reaction with CO_2 and oxygen. Rietveld refinements of the NPD data for the material revealed a Li deficiency compared to the solid-state material, which was attributed to the possible protonation of the sol-gel synthesised material during the synthesis.

The macroscopic transport properties of the materials analysed by variable temperature EIS revealed a lower ionic conductivity and higher activation energy for the sol-gel material compared to the high temperature solid-state synthesised LLZO garnet. μ^+SR analyses showed that the microscopic diffusion properties of the materials remained similar to the high temperature analogue material, with the diffusion coefficient experiencing a small decrease possibly due to the lower number of Li^+ in the 96h positions and possible presence of protons in these octahedral positions. The energy requirements for the hopping remained invariable suggesting that diffusion pathway remained unaltered. These observations indicated that the difference observed in the macroscopic measurements may be due of a combination of lower concentration of Li^+ carriers with H^+ hindering the long-range diffusion together with lower sintering temperature/small particle size affecting the total ionic conductivity, thus the higher activation energy.

References

[1] C. A. Geiger, E. Alekseev, B. Lazic, M. Fisch, T. Armbruster, R. Langner, M. Fechtelkord, N. Kim, T. Pettke and W. Weppner, *Inorg. Chem.*, 2011, **50**, 1089–1097.

[2] E. Rangasamy, J. Wolfenstine and J. Sakamoto, *Solid State Ionics*, 2012, **206**, 28 – 32.

[3] I. Kokal, M. Somer, P. H. L. Notten and H. T. Hintzen, *Solid State Ionics*, 2011, **185**, 42–46.

[4] N. F. Uvarov, *Composite Solid Electrolytes*, Wiley-VCH Verlag GmbH and Co. KGaA, 2011, pp. 31–71.

[5] M. Matsui, K. Takahashi, K. Sakamoto, A. Hirano, Y. Takeda, O. Yamamoto and N. Imanishi, *Dalton Trans.*, 2014, **43**, 1019–1024.

[6] S. Toda, K. Ishiguro, Y. Shimonishi, A. Hirano, Y. Takeda, O. Yamamoto and N. Imanishi, *Solid State Ionics*, 2013, **233**, 102 – 106.

[7] Y. Wang and W. Lai, *J. Power Sources*, 2015, **275**, 612 – 620.

[8] G. Larraz, A. Orera and M. L. Sanjuan, *J. Mater. Chem. A*, 2013, **1**, 11419–11428.

[9] H. Xie, Y. Li and J. B. Goodenough, *Mater. Res. Bull.*, 2012, **47**, 1229 – 1232.

[10] A. E. Danks, S. R. Hall and Z. Schnepp, *Mater. Horiz.*, 2016, **3**, 91–112.

[11] S. A. Yoon, N. R. Oh, A. R. Yoo, H. G. Lee and H. C. Lee, *J. Korean Ceram. Soc.*, 2017, **54**, 278–284.

[12] C. Ma, E. Rangasamy, C. Liang, J. Sakamoto, K. L. More and M. Chi, *Angew. Chem. Int. Ed.*, 2015, **54**, 129–133.

[13] L. Truong and V. Thangadurai, *Inorg. Chem.*, 2012, **51**, 1222–1224.

[14] V. Thangadurai, S. Narayanan and D. Pinzaru, *Chem. Soc. Rev.*, 2014, **43**, 4714–4727.

[15] C. Galven, G. Corbel, F. Le Berre and M.-P. Crosnier-Lopez, *Inorg. Chem.*, 2016, **55**, 12872–12880.

[16] C. Galven, J. Dittmer, E. Suard, F. Le Berre and M.-P. Crosnier-Lopez, *Chem. Mater.*, 2012, **24**, 3335–3345.

[17] C. Galven, J.-L. Fourquet, E. Suard, M.-P. Crosnier-Lopez and F. Le Berre, *Dalton Trans.*, 2010, **39**, 4191–4197.

[18] C. Galven, E. Suard, D. Mounier, M.-P. Crosnier-Lopez and F. Le Berre, *J. Mater. Res.*, 2013, **28**, 2147–2153.

[19] A. Boulant, J. F. Bardeau, A. Jouanneaux, J. Emery, J.-Y. Buzare and O. Bohnke, *Dalton Trans.*, 2010, **39**, 3968–3975.

[20] T. W. S. Yip and E. J. Cussen, *Inorg. Chem.*, 2013, **52**, 6985–6993.

[21] G. Larraz, *Estudio de electrolitos solidos para baterias de litio basadas en $Li_7La_3Zr_2O_{12}$ and $LiZr_2(PO_4)_3$*, Universidad de Zaragoza, 2016.

[22] W. Xia, B. Xu, H. Duan, X. Tang, Y. Guo, H. Kang, H. Li and H. Liu, *J. Am. Ceram. Soc.*, 2017, **100**, 2832–2839.

[23] A. Orera, G. Larraz, J. A. Rodríguez-Velamazán, J. Campo and M. L. Sanjuán, *Inorg. Chem.*, 2016, **55**, 1324–1332.

[24] L. Cheng, E. J. Crumlin, W. Chen, R. Qiao, H. Hou, S. Franz Lux, V. Zorba, R. Russo, R. Kostecki, Z. Liu, K. Persson, W. Yang, J. Cabana, T. Richardson, G. Chen and M. Doeff, *Phys. Chem. Chem. Phys.*, 2014, **16**, 18294–18300.

[25] G. Larraz, A. Orera, J. Sanz, I. Sobrados, V. Diez-Gomez and M. L. Sanjuan, *J. Mater. Chem. A*, 2015, **3**, 5683–5691.

[26] M. L. Sanjuan, A. Orera, I. Sobrados, A. F. Fuentes and J. Sanz, *J. Mater. Chem. A*, 2018, **6**, 2708–2720.

[27] M. Bahout, S. S. Pramana, J. M. Hanlon, V. Dorcet, R. I. Smith, S. Paofai and S. J. Skinner, *J. Mater. Chem. A*, 2015, **3**, 15420–15431.

[28] M. Amores, T. E. Ashton, P. J. Baker, E. J. Cussen and S. A. Corr, *J. Mater. Chem. A*, 2016, **4**, 1729–1736.

[29] C. Liu, K. Rui, C. Shen, M. E. Badding, G. Zhang and Z. Wen, *J. Power Sources*, 2015, **282**, 286 – 293.

[30] D. Wang, G. Zhong, W. K. Pang, Z. Guo, Y. Li, M. J. McDonald, R. Fu, J.-X. Mi and Y. Yang, *Chem. Mater.*, 2015, **27**, 6650–6659.

[31] Z. F. Yow, Y. L. Oh, W. Gu, R. P. Rao and S. Adams, *Solid State Ionics*, 2016, **292**, 122 – 129.

[32] T. Thompson, A. Sharafi, M. D. Johannes, A. Huq, J. L. Allen, J. Wolfenstine and J. Sakamoto, *Adv. Energy Mater.*, 2015, **5**, 1500096.

[33] R. Murugan, V. Thangadurai and W. Weppner, *J. Electrochem. Soc.*, 2008, **155**, A90–A101.

[34] A. Sharafi, E. Kazyak, A. L. Davis, S. Yu, T. Thompson, D. J. Siegel, N. P. Dasgupta and J. Sakamoto, *Chem. Mater.*, 2017, **29**, 7961–7968.

[35] P. J. Baker, I. Franke, F. L. Pratt, T. Lancaster, D. Prabhakaran, W. Hayes and S. J. Blundell, *Phys. Rev. B*, 2011, **84**, 174403.

[36] M. Månsson and J. Sugiyama, *Phys. Scr.*, 2013, **88**, 068509.

[37] Y. Zhang, F. Chen, J. Li, L. Zhang, J. Gu, D. Zhang, K. Saito, Q. Guo, P. Luo and S. Dong, *Electrochim. Acta*, 2018, **261**, 137 – 142.

[38] M. Park, X. Zhang, M. Chung, G. B. Less and A. M. Sastry, *J. Power Sources*, 2010, **195**, 7904 – 7929.

Chapter 6: Synthesis and ionic conductivity studies of In-and Y-doped $Li_6Hf_2O_7$ as solid-state electrolytes

In previous chapters, the synthesis of Li-rich garnet materials by different methodologies have been explored together with the advanced characterisation of their structure and ionic transport properties. Despite the promising microscopic transport properties of the these materials,[1–4] their implementation in commercial Li batteries is still hampered by the high electrode-garnet interfacial resistance and its complicated microstructure optimisation, where high temperatures are usually needed to achieve sufficient macroscopic conduction.

As previously introduced, there are other candidate systems as solid-state electrolytes for Li batteries,[5] such as the air stable NASICON-like Li*MM'*$(PO_4)_3$ structures,[6] $La_{2/3}Li_{1/3}TiO_3$ oxide perovskites,[7,8] and the most recent thio-LISICON $Li_{10}GeP_2S_{12}$ materials with conductivities topping the $10^{-}2$ S cm^{-1},[9–11] matching those of liquid electrolytes. However, despite achieving ionic conductivities comparable with those of liquid electrolytes, these also present some drawbacks such as instability at low voltages or large grain-boundary resistances,[12–15] that have hampered their full implementation, similarly as in the case of the garnet family. Thus, the search for new candidate materials remains a challenge for the realisation of next generation of Li-ion batteries.

From the different unexplored materials that could allow lithium to diffuse on their structure, the $Li_6Hf_2O_7$ material was selected here to explore due to the high number of lithium-ions per formula unit which could enhance diffusion when ionic transport is facilitated through a cooperative mechanism.[16] In addition, the existence of possible pathways on the crystal structure for Li^+ diffusion and the presence of redox-stable Hf^{4+} ions to maintain the crystal structure as Li^+ ions hop also anticipate good properties of the $Li_6Hf_2O_7$ material as solid-state electrolyte.

Ionic conductors with full occupancy of the atomic positions are known to have lower transport properties if vacancies or interstitial ions are not introduced within the structure, as discussed in the Introduction. The use of non-stoichiometry in $Li_6Hf_2O_7$ could increase the transport properties of the material, as demonstrated for $Li_6Zr_2O_7$.[17,18] Thus, the introduction of interstitial Li^+ ions in the $Li_6Hf_2O_7$ structure by selective aliovalent doping could reasonably be expected to increase the Li^+ ionic conductivity of the material.

For these reasons, in this chapter fast microwave-assisted solid-state synthesis of In- and Y-doped $Li_6Hf_2O_7$ materials was developed. The crystal structure of the materials was analysed by PXRD measurements and the solubility limits of the dopants determined from these. The microstructure of the powdered and pelletised materials was analysed by SEM. For the study of the ionic conductivity properties of the resultant materials, variable

temperature AC EIS measurement were performed.

6.1 Synthesis and structural characterisation

The In- and Y-doped $Li_6Hf_2O_7$ materials with nominal compositions $Li_{6+x}Hf_{2-x}In_xO_7$ ($0 \leq x \leq 0.20$) and $Li_{6+x}Hf_{2-x}Y_xO_7$ ($0 \leq x \leq 0.15$) were synthesised by the same microwave-assisted solid-state route employed in Chapters 3 and 4 for the syntheses of the LBLTO and LLZO garnet materials.[3] The use of microwave radiation in these solid-state synthesises demonstrated to be an energy efficient synthetic route which enabled the use of lower temperatures and shorter times compared with conventional solid-state synthetic routes.[19] The synthesis of these In- and Y-doped $Li_6Hf_2O_7$ materials was facilitated by the presence of starting materials, such as the LiOH precursor,[20] that strongly couples with microwaves and with materials with high dielectric constants such as the HfO_2 that can effectively absorb microwave radiations at high temperatures, in a similar way to the ZrO_2 precursor.[21–23]

The undoped $Li_6Hf_2O_7$ and doped compounds up to x = 0.05 were obtained as single phase samples at 850 ^oC. This required only four hours for the synthesis compared with "several days" required by conventional methods previously reported.[24]

The structure of the $Li_6Hf_2O_7$, shown in Figure 6.1, contains Li^+ ions in 5-fold oxygen coordination in a square pyramid geometry and Hf^{4+} ions octahedrally coordinated by oxide anions. The Li^+ ions form pair of chains through the crystal framework, which suggests that at least one dimension diffusion could be possible. This monoclinic phase can be considered as an anion-deficient NaCl rock salt structure with Li^+ and Hf^{4+} ions on the Na^+ positions and the oxide occupying $^7/_8$ of the anion positions.[24,25] The presence of these vacant positions and the availability of interstitial positions in the structure suggested it should be possible to tailor the lithium stoichiometry in order to modify the ionic conductivity of the material.

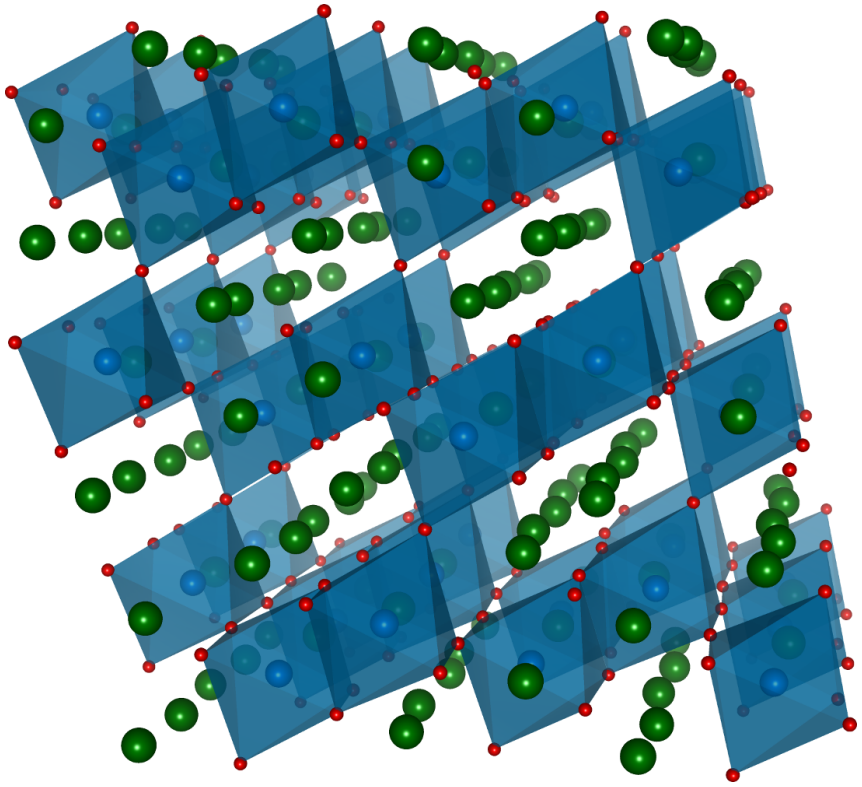

Figure 6.1: Crystal structure of the $Li_6Hf_2O_7$ material with *C*2/*c* space group symmetry. Li^+ ions are shown in green; O^{2-} anions are shown in red and Hf^{4+} are shown in blue with their octahedral coordination environment explicitly shown.

Rietveld refinement of the PXRD data for the undoped $Li_6Hf_2O_7$ material were performed to obtain the lattice parameters, profile coefficients and to asses the purity of the parent compound. The refinements showed that this fast microwave-assisted approach gave a good agreement between the experimental data and a calculated model for the $Li_6Zr_2O_7$ material with *C*2/*c* monoclinic space group (Fig. 6.2). The cell parameters obtained from the Rietveld refinements resulted in a = 10.4157(2) Å, b = 5.9678(1) Å and c = 10.1589 (2) Å with a β angle of 100.385(1)° leading to a cell volume of 621.13(2) $Å^3$ for the undoped material.

Due to the dominance of the diffraction profile by the Hf^{4+} cations and the low symmetry of the structure, the atomic coordinates and anion occupancies were fixed at the published values (Table 10.1 in the Appendix). In addition, the minimal scattering from Li^+ meant it was not possible to identify the location of the possible additional Li^+ in the structure for the doped materials.

In order to induce Li^+ non-stoichiometry in the material, the substitution of Hf^{4+} cations with M^{3+} ions was undertaken, with the anticipation that crystal electrical neutrality would be maintained by the incorporation of additional Li^+ ions into the structure. Of the various trivalent cations in the periodic table, In^{3+} and Y^{3+} were the most suitable ions to dope the $Li_6Hf_2O_7$ material due their relatively close ionic size to Hf^{4+} (In^{3+} = 0.79 Å, Y^{3+} = 0.90 Å and Hf^{4+} = 0.71 Å),[26] together with the redox stability of these ions required for any

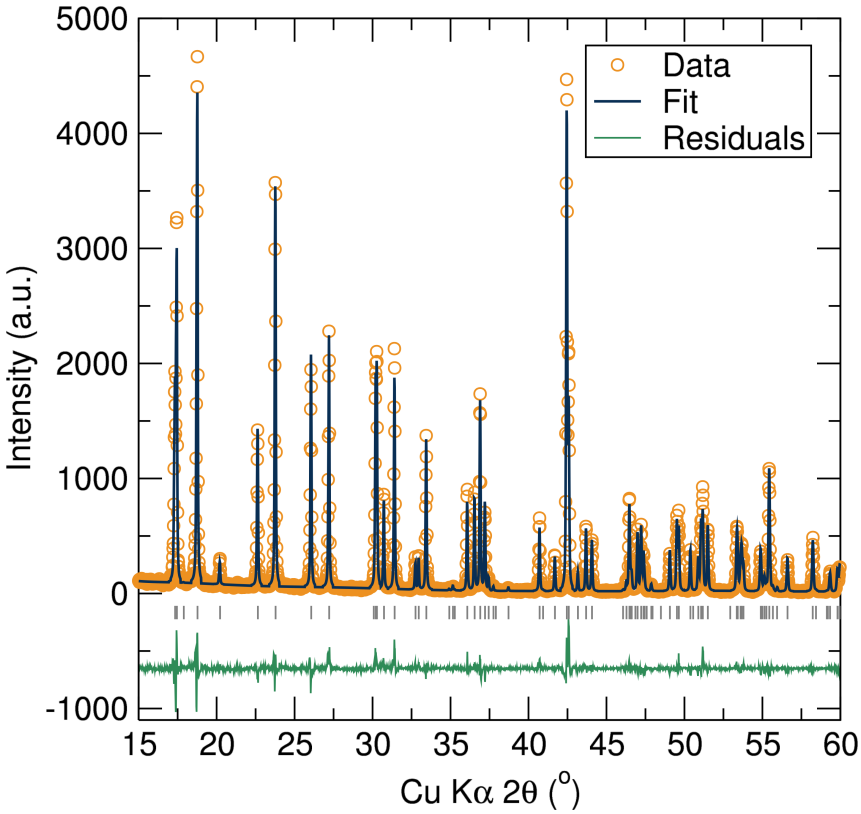

Figure 6.2: Rietveld refinement against PXRD data collected from the undoped $Li_6Hf_2O_7$ material. The monoclinic structure gives a good agreement with the data. R_{wp} = 12.75% and R_p = 9.41%.

solid-state electrolyte for lithium-ion battery applications.

It has to be noted that aliovalent doping on the Hf^{4+} cations position with M^{5+} dopants was also attempted in order to study the opposite strategy for Li-non-stoichiometry, ie. vacancy formation. Doping with 0.1 mol per formula unit, $Li_{5.9}Hf_{1.9}M_{0.1}O_7$ with Ta^{5+} or Sb^{5+} as M^{5+}, was performed with the same synthetic conditions as for the In^{3+} and Y^{3+} dopings. PXRD data of the Ta- and Sb-doped $Li_6Hf_2O_7$ compositions (Fig. 6.3) revealed the formation of secondary phases, such as Li_2HfO_3, $LiSbO_3$ and $Li_8Ta_2O_9$, among others. The reason behind this may be related to the smaller M^{5+} dopant cation sizes (Ta^{5+} = 0.64 Å and Sb^{5+} = 0.61 Å) which may not be tolerated by this crystal structure. It could also be due to a higher thermodynamic stability of the secondary phases. Applying higher reaction temperatures did not remove the secondary phases, nor did longer heating times.

For the highest dopant concentrations up to $Li_{6.15}Hf_{1.85}In_{0.15}O_7$ and $Li_{6.10}Hf_{1.90}Y_{0.10}O_7$ an additional heating of 4 hours at 850 °C was required in order to achieve phase purity. The solubility limit for the In^{3+} doping was then identified at concentrations higher than z = 0.15, when the secondary phase $LiInO_2$ started to appear and further heat treatments led to decomposition of the targeted material. In the case of the Y^{3+} doping, the solubility limit is reached just above x = 0.10, with the appearance of additional peaks. These peaks could not be indexed by a reduction in space group symmetry and did not arise

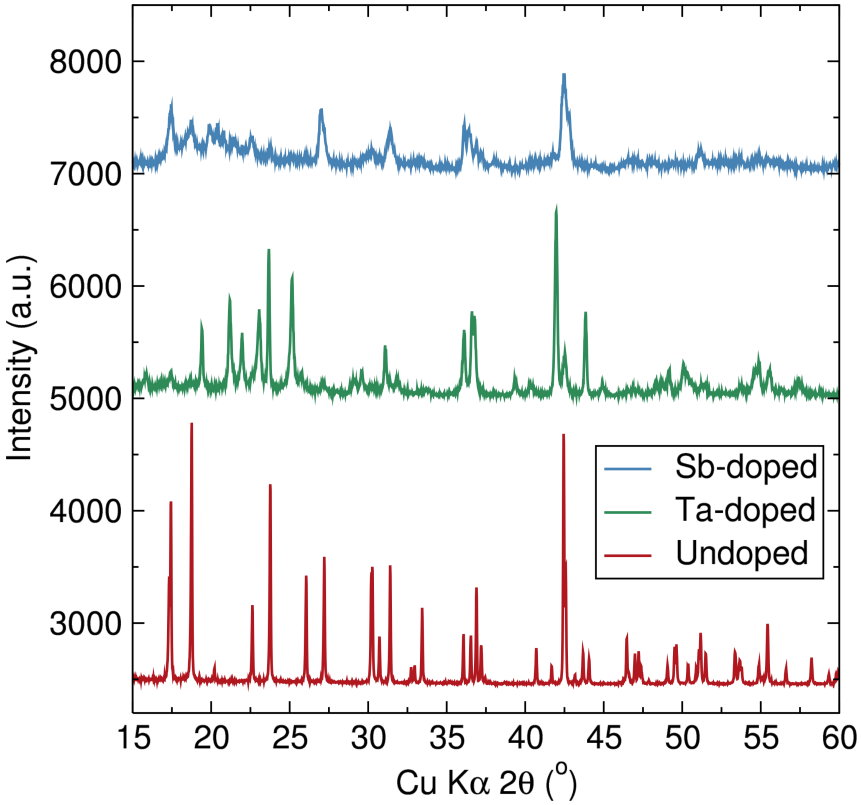

Figure 6.3: PXRD patterns collected for the $Li_{5.9}Hf_{1.9}M_{0.1}O_7$ (M = Ta^{5+}, Sb^{5+}) compositions. The clear presence of secondary phases indicated the unsuccessful synthesis of single phase M^{5+}-doped $Li_6Hf_2O_7$ materials.

from any of the starting materials or obvious binary or ternary oxides that may result in this system. The lower solubility of the Y^{3+} cation in the structure could be presumably due to the larger deviation from the cation size of Y^{3+} compared to Hf^{4+} (0.90 vs 0.79 Å, respectively).

Inspection of the diffraction patterns shown in Figure 6.4 showed no gross changes in the diffraction profiles suggesting the structure was largely retained. The clearest indication of effective Hf^{4+} substitution in the structure was observed as the relative intensities of the Bragg reflections at $2\theta \approx$ 17.45 and 18.85 °, corresponding to the (200) and ($\bar{1}11$) Bragg reflections, respectively, which followed an inverse trend as dopant concentration increased. This could be related to the different scattering strength of the Y^{3+} and In^{3+} ions compare to Hf^{4+} ions. In the case of the Y^{3+} doping, this effect was also evident as the increasing intensity of the ($\bar{2}23$) Bragg reflections, *ca.* $\approx$ 42.5 °, as the Y^{3+} doping concentration increases.

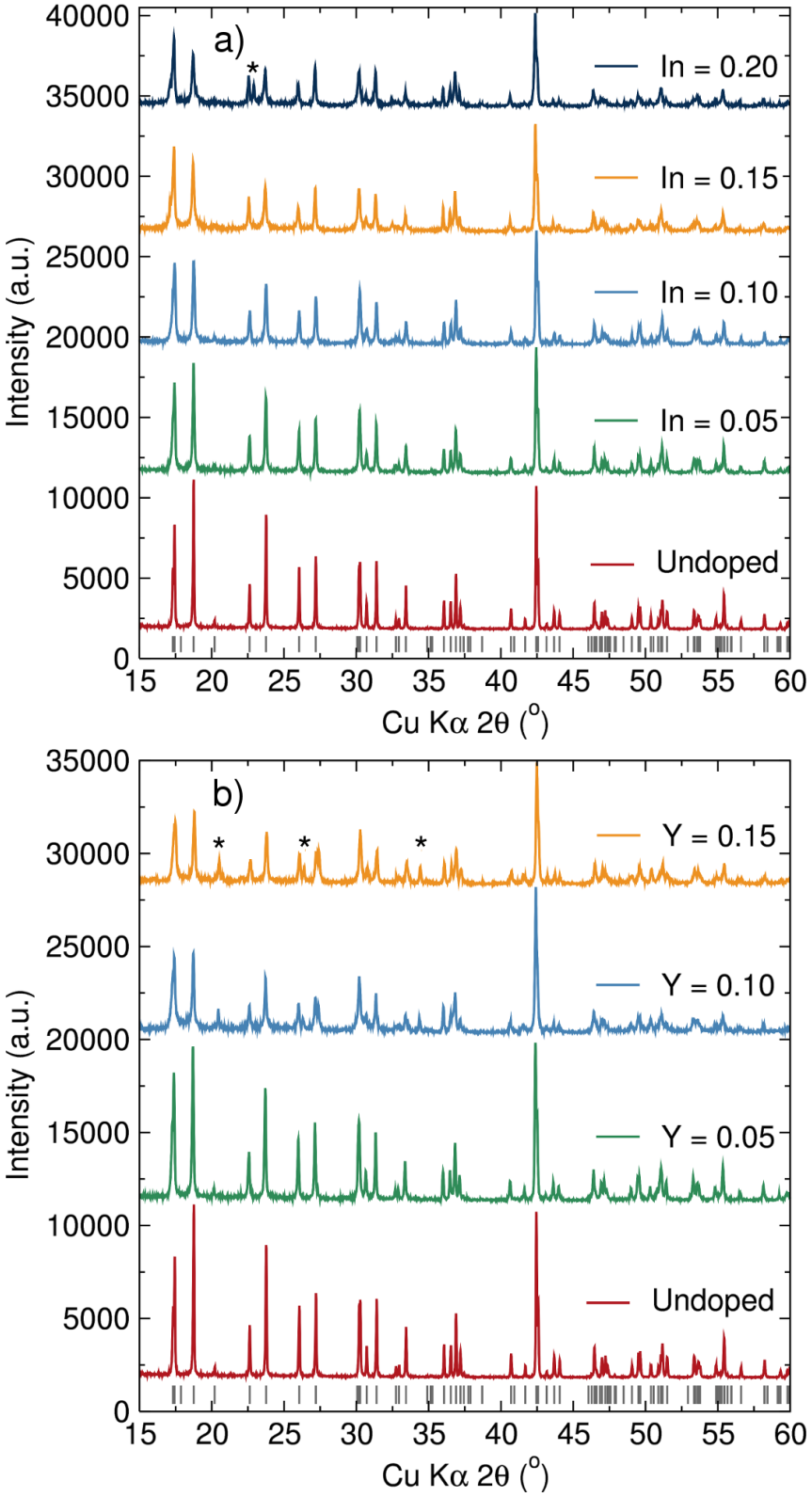

Figure 6.4: PXRD patterns collected from the (a) $Li_{6+x}Hf_{2-x}In_xO_7$ and (b) $Li_{6+x}Hf_{2-x}Y_xO_7$. The peaks arising from impurity phases at the highest dopant levels are indicated.

Due to the negligible X-ray scattering arising from Li^+ in the presence of the dominant scatterer Hf^{4+}, these data gave no insights into the placement of the additional lithium in the structure. It was assumed that Li^+ existed at interstitial positions, where computational

studies on the analogue $Li_6Zr_2O_7$ found to be energetically stable for Li^+ ions to reside.[18]

In addition, the quality of the laboratory PXRD data did not provide enough intensity and resolution to allow for a full refinement of the atomic parameters. Therefore, the changes in the unit cell were tracked by Le Bail analyses for these doped materials. An example of Bragg peak reflection positions for the calculated cell parameters matching the experimental PXRD peaks is shown in Figure 6.5.

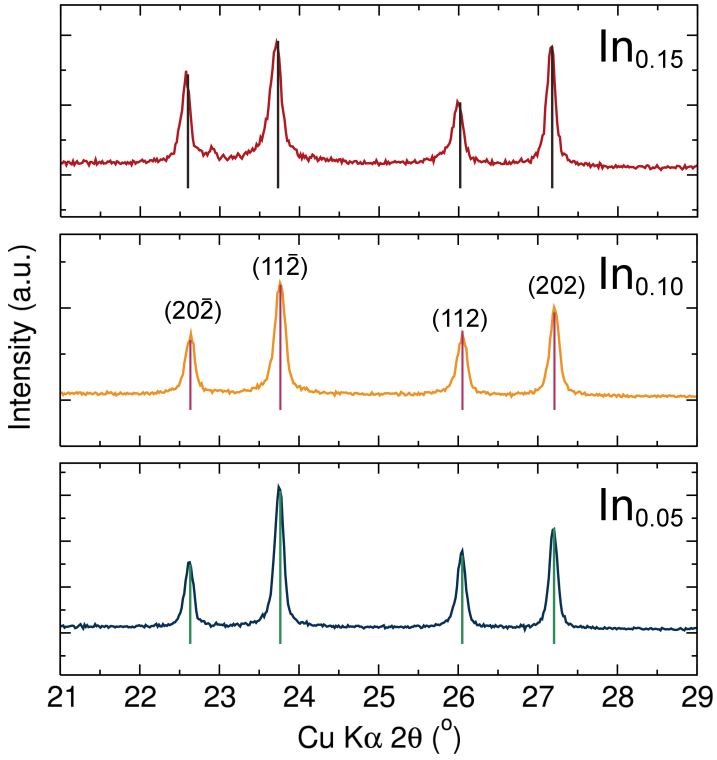

Figure 6.5: PXRD data of the In-doped $Li_{6+x}Hf_{2-x}In_xO_7$ materials and the calculated Bragg peak positions (vertical lines) from Le Bail analyses.

There were no dramatic changes or trends observed in the structure derived from these Le Bail analyses (Table 6.1), with the most significant change being a decrease in the monoclinic distortion with Y^{3+} doping as observed in the β lattice parameter shown in Figure 6.6. In the case of the In^{3+} doping, there were no significant changes in the structure. Again, these results can be rationalised after consideration of the ionic radii of In^{3+} and Hf^{4+}, and the relative doping concentrations.

Table 6.1: Cell parameters details obtained from Le Bail analyses of the PXRD data for the $Li_{6+x}Hf_{2-x}In_xO_7$ and $Li_{6+x}Hf_{2-x}Y_xO_7$ materials.

	Undoped	$In_{0.05}$	$In_{0.10}$	$In_{0.15}$	$Y_{0.05}$	$Y_{0.10}$
a (Å)	10.4157(2)	10.4119(4)	10.4084(5)	10.418(1)	10.4123(3)	10.421(1)
b (Å)	5.9678(1)	5.9677(2)	5.9668(3)	5.9719(6)	5.9681(2)	5.9776(7)
c (Å)	10.1589(2)	10.1570(4)	10.1534(5)	10.1632(9)	10.1598(3)	10.169(1)
β(°)	100.385(1)	100.378(2)	100.381(3)	100.396(5)	100.370(2)	100.333(6)
V ($Å^3$)	621.13(2)	620.77(6)	620.24(7)	621.9(1)	621.03(4)	623.2(2)

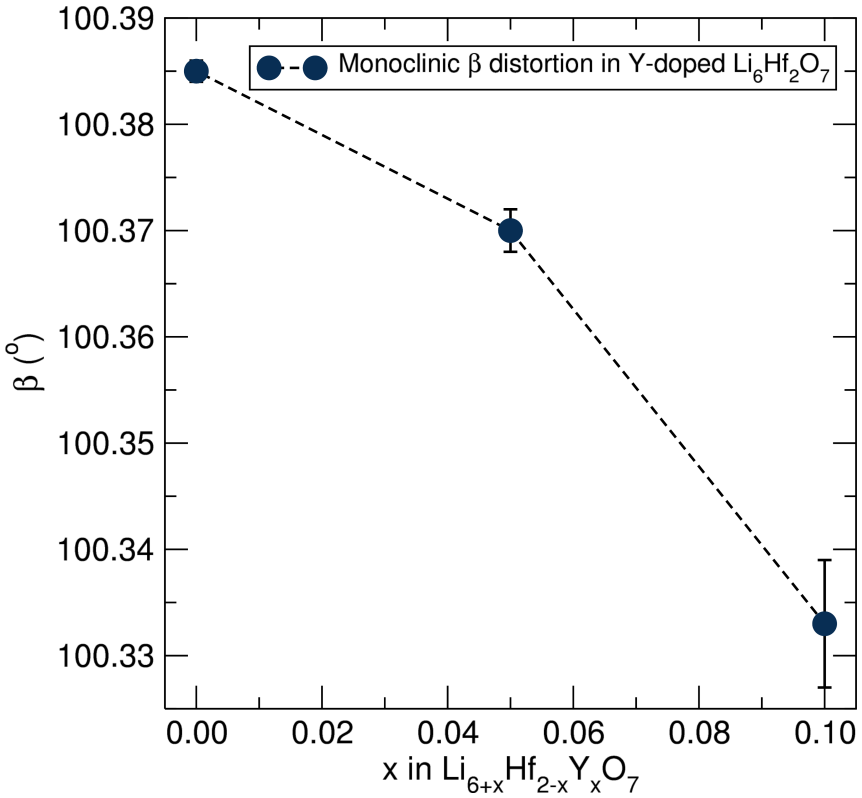

Figure 6.6: Monoclinic distortion (β-angle) variation following the substitution of Hf^{4+} ions with Y^{3+}. A progressive decrease is observed due to the bigger size of the Y^{3+}ions compared to Hf^{4+}.

In order to study the compositions, EDX analyses of the highest doped $Li_6Hf_2O_7$ compounds, $Li_{6.15}Hf_{1.85}In_{0.15}O_7$ and $Li_{6.10}Hf_{1.90}Y_{0.10}O_7$, were performed. The relative atomic concentration ratios had a value of In:Hf = 0.09 and Y:Hf = 0.05, which were in good agreement with the theoretical values of 0.08 and 0.05 for the targeted stoichiometries.

The microstructure of the as-synthesised $Li_6Hf_2O_7$ was analysed by SEM. The powdered sample showed agglomerates of microparticles between 10 and 50 microns with irregular morphology as shown in Figure 6.7a. In addition, a fractured pellet for the $Li_{6.15}Hf_{1.85}In_{0.15}O_7$ material was also analysed (Figure 6.7b). The micrograph revealed large grains with relatively good connectivity between them. The density of the sintered pellet for this material was $\sim$ 78% of the theoretical density. Further sintering at higher

temperatures to achieve higher relative densities resulted in partial decomposition of the material, which could be possibly attributed to lithium evaporation.

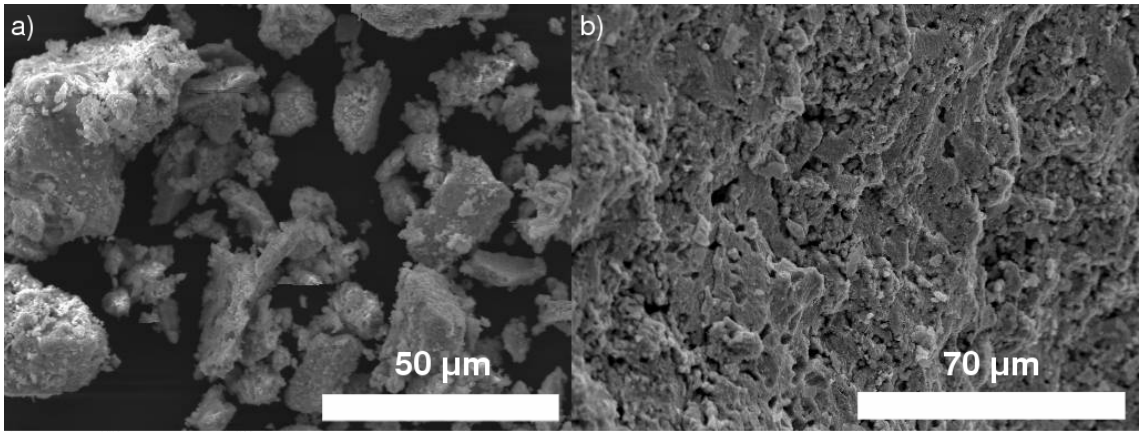

Figure 6.7: SEM image of (a) the as-synthesised $Li_6Hf_2O_7$ and (b) the pelleted $Li_{6.15}Hf_{1.85}In_{0.15}O_7$ material prepared for EIS analyses.

An elemental compositional map was also generated from a cracked pellet of the material that presented the highest conductivity, $Li_{6.10}Hf_{1.90}Y_{0.10}O_7$ (Fig. 6.8). Evaluation of this compositional map indicated a uniform distribution of Hf, Y and O across the pellet without any apparent segregation or inhomogeneity.

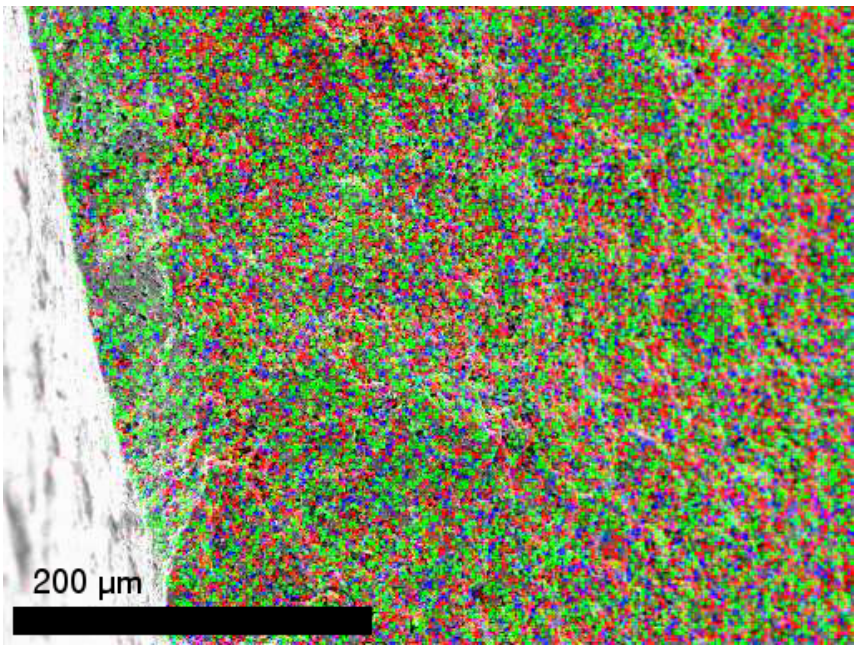

Figure 6.8: Elemental map of the Hf, Y and O distributions on a fractured pellet of $Li_{6.10}Hf_{1.90}Y_{0.10}O_7$ for impedance analysis. This is generated from EDX measurements and false coloured to indicate the contributions from Hf (green), Y (blue) and O (red).

6.2 Ionic conductivity behaviour

The ionic transport properties of the undoped and doped materials were analysed using AC EIS analysis. A typical Nyquist plot for the undoped material at 174 °C is shown in Figure 6.9a. Data at room temperature were not reliable enough.

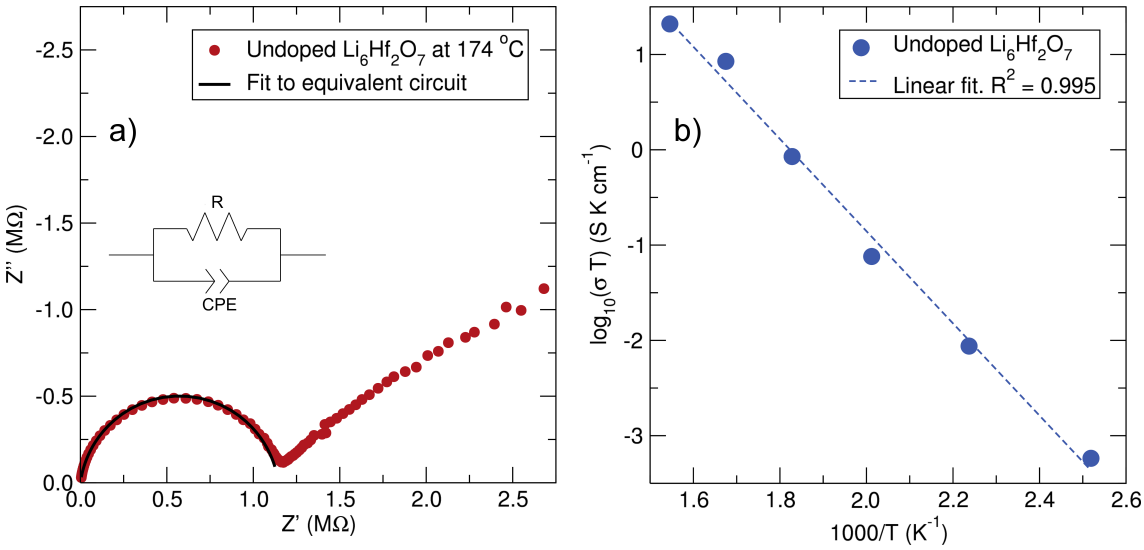

Figure 6.9: (a) Nyquist plot of the impedance data for $Li_6Hf_2O_7$ at 174 °C and the fit to the electrical circuit of a parallel resistor (R) with a constant phase element (CPE). (b) Arrhenius plot of the conductivity measured over the 124 to 424 °C temperature range.

Similarly as in the lithium garnets studied in previous chapters, a clear semicircle was observed at higher frequencies due to the resistance of the materials toward ionic conductivity. The linear lower frequency response is typical of the blocking of Li^+ due to the use of platinum electrodes, indicating the ionic nature of the impedance. To obtain the value for the resistance of the material, the Nyquist plot data were fitted using an equivalent circuit of a resistor, due to the resistance to ionic conduction, with a parallel constant phase element to account for the double layer polarisation effect. For the undoped material, the capacitance resulting from the fit was on the order of 10^{-12} F, indicating that the observed resistance is mainly due to intra-grain conductivity.[27]

The calculated ionic conductivity value from Pouillet's law (Equation 3.1) was 1.95×10^{-5} S cm^{-1} at 174 °C. The conductivity of the undoped $Li_6Hf_2O_7$ material at this temperature was already competitive with that reported for the undoped $Li_6Zr_2O_7$ at 300 °C on the order of 10^{-6} to 10^{-5} S cm^{-1}.[17,18] Since Hf^{4+} and Zr^{4+} have similar ionic sizes, and the structures of both materials have similar sizes, with <1% volume contraction for the $Li_6Hf_2O_7$ material, the differences could not be ascribed to changes in the crystal structure, it is more likely those differences arise due to microsctructural differences. Since there was more than one different variable parameter in these experiments – synthetic conditions, density and set-up employed on the measurements, among others – a direct comparison between these values is difficult to arrive at and potentially inconclusive. A

detailed study between both isostructural families of materials would be required in order to have a better understanding regarding the role of the Hf^{4+} and Zr^{4+} atoms in the ionic conductivity of these materials.

To obtain further insights into the ionic conduction in the undoped material, the activation energy was determined by variable temperature conductivity measurements. An arrhenius fit of the data is shown in Figure 6.9b. The calculated activation energy for ionic diffusion in $Li_6Hf_2O_7$ was 0.97(4) eV, which lies between the values reported by Goodenough and co-workers[18] of 0.84 eV and the 1.25 eV value obtained by Rao *et al.* for the isostructural $Li_6Zr_2O_7$.[17] Again, due to the different variables between the works, it is not possible to drawn a specific reasoning behind these differences in activation energies.

Similar measurements were performed on doped compositions with highest purity [$0 \leq x(In) \leq 0.15$ and $0 \leq x(Y) \leq 0.10$]. When the In^{3+} cations are introduced within the $Li_6Zr_2O_7$ material, the ionic conduction at 174°C was progressively enhanced (Fig. 6.10a). The conductivity was increased by one order of magnitude at 174 °C for the x(In) = 0.15 composition. The activation energy for ionic conductivity was also experienced a 28% decrease compared to the undoped parent material. For all compositions studied, the evolution of ionic conductivity with temperature agreed accurately with an Arrhenius behaviour as shown in Figure 6.10b.

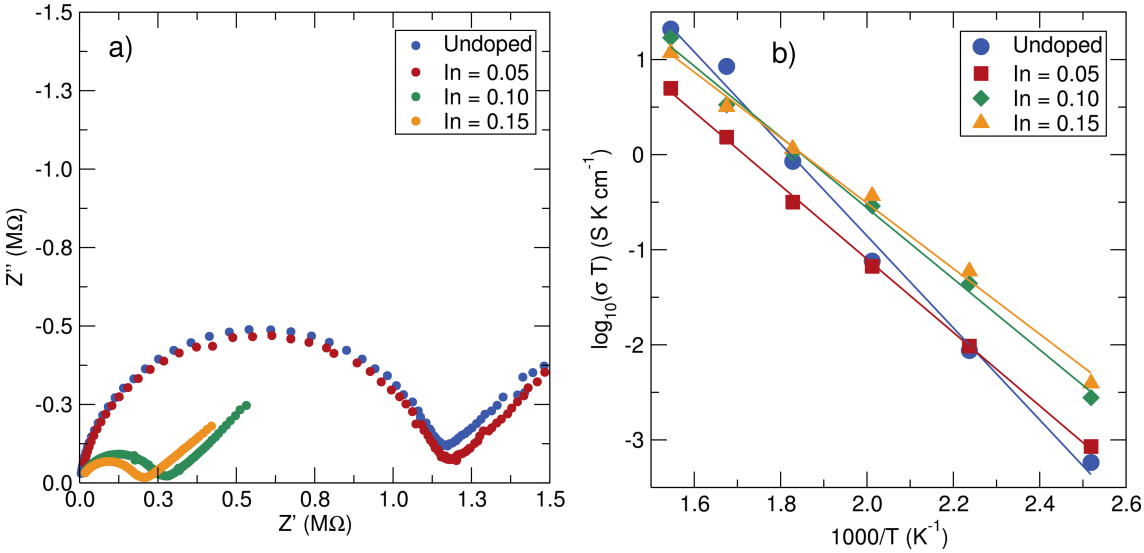

Figure 6.10: Nyquist plot of the impedance spectra of the In-doped family at 174°C (a) and Arrhenius plot of the conductivity measured over the 124 to 424 °C temperature range (b).

In the case of the Y-doped materials, the introduction of Y^{3+} also increased the ionic conductivity proportionally to Y^{3+} doping stoichiometry as shown in Figure 6.11a, resulting again in an order of magnitude higher for the x = 0.10 composition at 174 °C. Due to the increased ionic conductivity, for the Y-doped material, reliable data could be also acquired at room temperature. The activation energy was also significantly enhanced by this Y^{3+} doping, reaching a value as low as 0.42(3) eV for the x(Y) = 0.10 composition

as shown in Figure 6.11b. The transport properties of all of the studied compositions are collected in Table 6.2 and Figure 6.12.

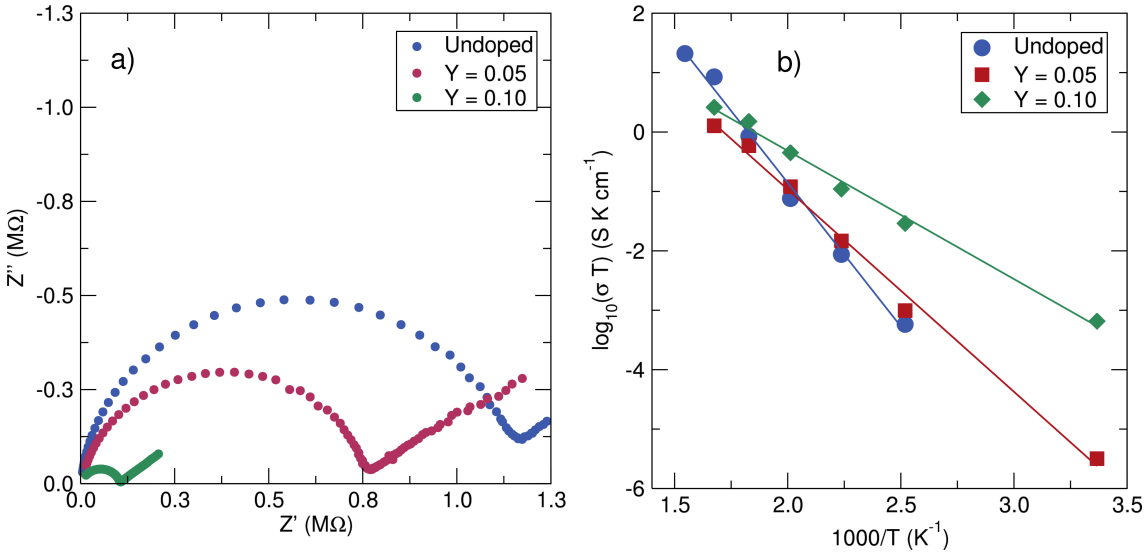

Figure 6.11: Nyquist plot of (a) the impedance of the $Li_{6+x}Hf_{2-x}Y_xO_7$ compounds at 174ºC and (b) the values of conductivity derived in the range $20 \leq T\ /\ ^{\circ}C \leq 424$.

Table 6.2: Ionic conductivity and activation energy data for the In- and Y-doped $Li_{6+x}Hf_{2-x}In_xO_7$ and $Li_{6+x}Hf_{2-x}Y_xO_7$ materials.

Compound	Ionic Conductivity at 174 °C (S cm^{-1})	Activation Energy (eV)
$Li_{6.00}Hf_{2.00}O_7$	1.95×10^{-5}	0.97(4)
$Li_{6.05}Hf_{1.95}In_{0.05}O_7$	2.17×10^{-5}	0.77(1)
$Li_{6.10}Hf_{1.90}In_{0.10}O_7$	9.88×10^{-5}	0.74(3)
$Li_{6.15}Hf_{1.85}In_{0.15}O_7$	1.33×10^{-4}	0.68(3)
$Li_{6.05}Hf_{1.95}Y_{0.05}O_7$	3.28×10^{-5}	0.68(2)
$Li_{6.10}Hf_{1.90}Y_{0.10}O_7$	2.46×10^{-4}	0.42(3)

Due to the absence of structural information on the location of the additional Li^+ inserted into the material, it was only possible to speculate on the origin of these enhanced ionic conductivity of the doped materials. If interstitial Li^+ was introduced, then a step change in activation energy would be expected due to the introduction of a new pathway for Li^+ migration. The more gradual trend observed in these analyses suggested that increasing concentrations of the dopants may be causing incremental increases in electrostatic repulsion and destabilising Li^+ and so reducing the barrier to ion hopping, as consequence of the Li^+ excess introduced into the structure. To further study the transport properties of the materials, the relationship of the conductivity with the frequency was also analysed (Fig. 6.13). This conductivity-frequency relationship displayed two clear behaviours as the frequency was varied. At low to intermediate frequencies, the

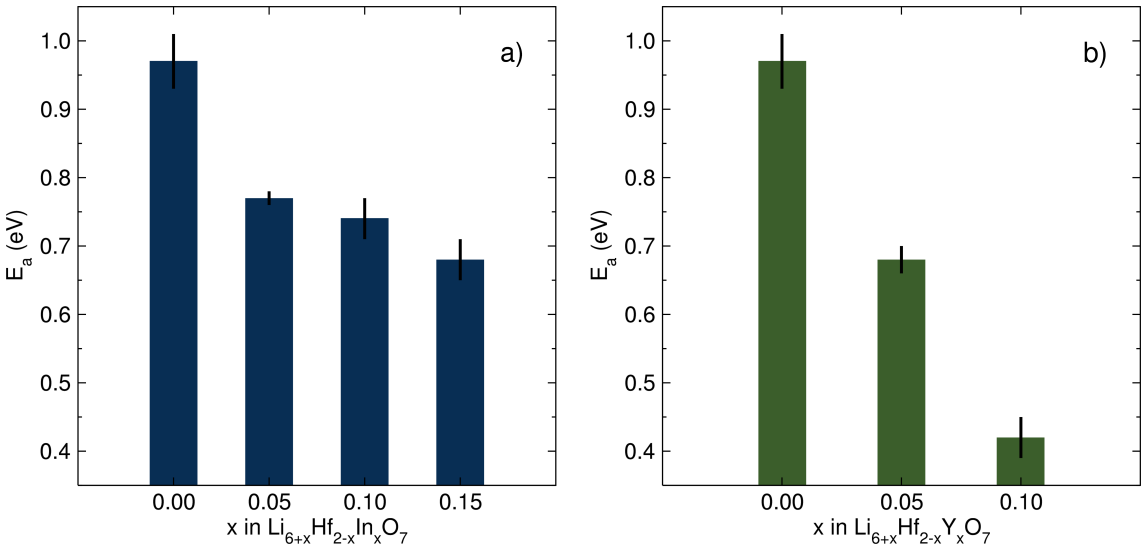

Figure 6.12: Activation energy for ionic diffusion as calculated from Arrhenius fitting for the different levels of In (a) and Y doping (b) of the $Li_7Hf_6O_7$ material. A clear decrease is observed with increasing amount of dopant.

conductivity was approximately constant due to the dominance of the jump relaxation of Li ions by dc conductivity, leading to a plateau-like region on the graph. This region presented a slight curvature at very low frequencies due to the polarisation arising from the increasing resistance to lithium diffusion at the Li-blocking Pt electrodes. The second region at higher frequencies indicated a rapid increase in charge transport that can be attributed to the forward and backward movements of the Li^+ under the influence of the rapid ac field.[28–30]

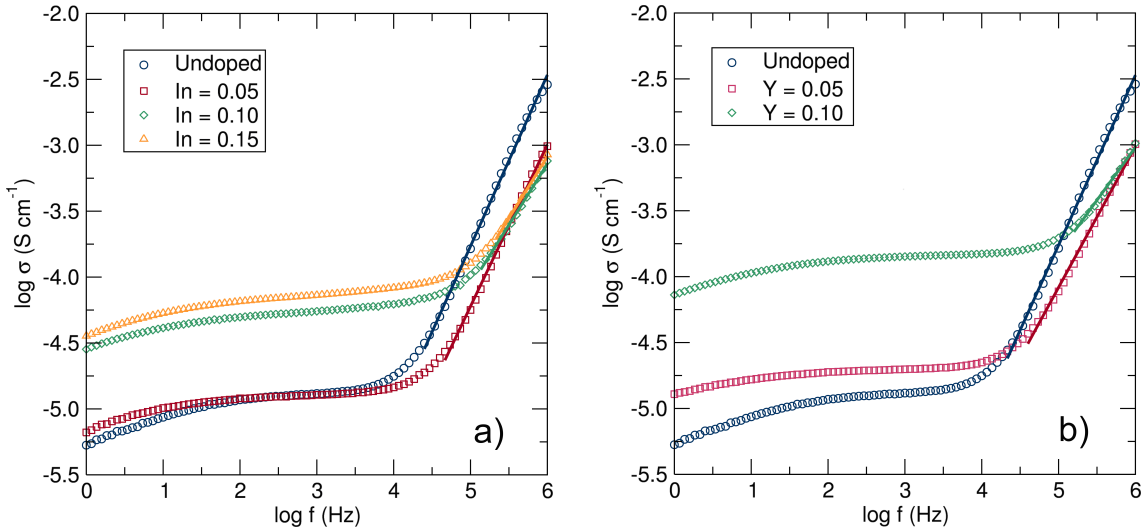

Figure 6.13: Ionic conductivity of the (a) In- and (b) Y-doped $Li_6Hf_2O_7$ materials as a function of the frequency measured for the different amounts of dopant. Fits to the frequency dependent range data are indicated by a solid line of the same colour as the fitted data set.

This behaviour was in agreement with the Jonscher universal power law[31] (Eq. 6.1)

where σ_{dc} corresponds to the plateau region and f^n corresponds to the linear region multiplied by a proportionality constant A:

$$\sigma(f) = \sigma_{dc} + Af^n \tag{6.1}$$

The value for the dc conductivity in the plateau region is increased as the doping concentration increases, indicating the positive impact on the ionic conductivity of the dopant ions. The frequency exponent *n* was then calculated from linear fits of the frequency dependent range. The variation of the *n* exponent with respect to the doping (Table 6.3) was clear, where a decrease in the *n* exponent with increasing dopant was observed. This indicates a lower contribution of the forward-backward jumps in favour of macroscopic ionic diffusion. These values for the *n* exponent were close to unity, similar to the values reported for other crystalline Li^+ ion conductor materials, such as the Li-NASICON structures.[32]

Table 6.3: Values of the frequency exponent *n* for the $Li_{6+x}Hf_{2-x}In_xO_7$ and $Li_{6+x}Hf_{2-x}Y_xO_7$ materials.

Compound	*n* exponent value
$Li_{6.00}Hf_{2.00}O_7$	1.29(1)
$Li_{6.05}Hf_{1.95}In_{0.05}O_7$	1.23(1)
$Li_{6.10}Hf_{1.90}In_{0.10}O_7$	0.93(2)
$Li_{6.15}Hf_{1.85}In_{0.15}O_7$	0.94(1)
$Li_{6.05}Hf_{1.95}Y_{0.05}O_7$	1.07(2)
$Li_{6.10}Hf_{1.90}Y_{0.10}O_7$	0.80(2)

6.3 Conclusions

In this chapter, the successful synthesis and characterisation of the $Li_6Hf_2O_7$ material has been demonstrated. The aliovalent doping of the material using Y^{3+} and In^{3+} was employed as a strategy to increase the number of lithium per formula unit, improving the ionic conductivity of the material. PXRD was used to follow the dopant insertion within the crystal structure, identifying upper solubility limits of x = 0.15 for $Li_{6+x}Hf_{2-x}In_xO_7$ and x = 0.10 for $Li_{6+x}Hf_{2-x}Y_xO_7$. The ionic conductivity of the undoped and doped materials was analysed by AC EIS, revealing an enhancement of the transport properties. The ionic conduction was increased from 1.95×10^{-5} S cm^{-2} to 1.33×10^{-4} S cm^{-2} at 174 °C for the highest In^{3+} doping. The enhancement was greater for the Y = 0.10 doped material, reaching a value of 2.46×10^{-4} S cm^{-2}. The activation energy for ionic diffusion in the materials showed a decrease from 0.97(4) eV for the undoped material to 0.68(3) eV for the 0.15 In-doped material and to a value of 0.42(3) eV for the 0.10 Y-doped compound. These low activation energy values compare favourably to other promising solid-state

electrolyte materials.[33] The results in this chapter have also demonstrated the potential of disorder in relatively simple crystal structures to generate new materials for solid-state electrolytes applications.

References

[1] R. Inada, S. Yasuda, M. Tojo, K. Tsuritani, T. Tojo and Y. Sakurai, *Front. Energy Res.*, 2016, **4**, 28.

[2] V. Thangadurai, S. Narayanan and D. Pinzaru, *Chem. Soc. Rev.*, 2014, **43**, 4714–4727.

[3] M. Amores, T. E. Ashton, P. J. Baker, E. J. Cussen and S. A. Corr, *J. Mater. Chem.A*, 2016, **4**, 1729–1736.

[4] C. Bernuy-Lopez, W. Manalastas, J. M. Lopez del Amo, A. Aguadero, F. Aguesse and J. A. Kilner, *Chem. Mater.*, 2014, **26**, 3610–3617.

[5] P. Knauth, *Solid State Ionics*, 2009, **180**, 911–916.

[6] N. Anantharamulu, K. Koteswara Rao, G. Rambabu, B. Vijaya Kumar, V. Radha and M. Vithal, *J. Mater. Sci.*, 2011, **46**, 2821–2837.

[7] X. Lin, H. Wang, H. Du, X. Xiong, B. Qu, Z. Guo and D. Chu, *ACS Appl. Mater. Interfaces*, 2016, **8**, 1486–92.

[8] C. Ma, Y. Q. Cheng, K. Chen, J. C. Li, B. G. Sumpter, C. W. Nan, K. L. More, N. J. Dudney and M. F. Chi, *Adv. Energy Mater.*, 2016, **6**, 1600053.

[9] N. Kamaya, K. Homma, Y. Yamakawa, M. Hirayama, R. Kanno, M. Yonemura, T. Kamiyama, Y. Kato, S. Hama, K. Kawamoto and A. Mitsui, *Nat. Mater.*, 2011, **10**, 682–686.

[10] R. Kanno, T. Hata, Y. Kawamoto and M. Irie, *Solid State Ionics*, 2000, **130**, 97–104.

[11] Y. Kato, S. Hori, T. Saito, K. Suzuki, M. Hirayama, A. Mitsui, M. Yonemura, H. Iba and R. Kanno, *Nat. Energy*, 2016, **1**, 16030.

[12] W. D. Richards, L. J. Miara, Y. Wang, J. C. Kim and G. Ceder, *Chem. Mater.*, 2016, **28**, 266–273.

[13] S. Wenzel, S. Randau, T. Leichtweiss, D. A. Weber, J. Sann, W. G. Zeier and J. Janek, *Chem. Mater.*, 2016, **28**, 2400–2407.

[14] Y. S. Jung, D. Y. Oh, Y. J. Nam and K. H. Park, *Isr. J. Chem.*, 2015, **55**, 472–485.

[15] A. C. Luntz, J. Voss and K. Reuter, *J. Phys. Chem. Lett.*, 2015, **6**, 4599–4604.

[16] M. Salanne, D. Marrocchelli and G. W. Watson, *J. Phys. Chem. C*, 2012, **116**, 18618–18625.

[17] R. P. Rao, M. V. Reddy, S. Adams and B. V. R. Chowdari, *Mater. Sci. Eng., B*, 2012, **177**, 100–105.

[18] Y. Liao, P. Singh, K.-S. Park, W. Li and J. B. Goodenough, *Electrochim. Acta*, 2013, **102**, 446–450.

[19] H. J. Kitchen, S. R. Vallance, J. L. Kennedy, N. Tapia-Ruiz, L. Carassiti, A. Harrison, A. G. Whittaker, T. D. Drysdale, S. W. Kingman and D. H. Gregory, *Chem. Rev.*, 2014, **114**, 1170–1206.

[20] W. Hennig, W. Voss, J. Dubowik, J. Piche, R. Griffiths, R. Kovar and H. Kua, *Novel microwave susceptor composition and method for making same*, 1991, https://www.google.com/patents/WO1991015094A1?cl=en, WO Patent App. PCT/US1991/001,782.

[21] J. Robertson, *Eur. Phys. J. Appl. Phys.*, 2004, **28**, 265–291.

[22] J. Lasri, P. D. Ramesh and L. Schächter, *J. Am. Ceram. Soc.*, 2000, **83**, 1465–1468.

[23] J. De Roo, K. De Keukeleere, J. Feys, P. Lommens, Z. Hens and I. Van Driessche, *J. Nanopart. Res.*, 2013, **15**, 1–11.

[24] R. Czekalla and W. Jeitschko, *Z. Anorg. Allg. Chem.*, 1993, **619**, 2038–2042.

[25] I. Abrahams, P. Lightfoot and P. G. Bruce, *J. Solid State Chem.*, 1993, **104**, 397–403.

[26] R. Shannon, *Acta Crystallogr.*, 1976, **A32**, 751–767.

[27] J. T. S. Irvine, D. C. Sinclair and A. R. West, *Adv. Mater.*, 1990, **2**, 132–138.

[28] K. Funke, *Solid State Ionics*, 1997, **94**, 27–33.

[29] J. C. Dyre, *J. Appl. Phys.*, 1988, **64**, 2456–2468.

[30] K. Funke, *Prog. Solid State Ch.*, 1993, **22**, 111–195.

[31] A. K. Jonscher, *Cah. Rev. The.*, 1977, **267**, 673–679.

[32] C. J. Leo, G. V. Subba Rao and B. V. R. Chowdari, *J. Mater. Chem.*, 2002, **12**, 1848–1853.

[33] J. C. Bachman, S. Muy, A. Grimaud, H. H. Chang, N. Pour, S. F. Lux, O. Paschos, F. Maglia, S. Lupart, P. Lamp, L. Giordano and Y. Shao-Horn, *Chem. Rev.*, 2016, **116**, 140–62.

Chapter 7: $Li_{1.5}La_{1.5}MO_6$ (M = W^{6+}, Te^{6+}) Li-rich double perovskites as versatile new materials for all-solid-state Li batteries

Following the journey to discover new materials with battery applications started on the previous chapter, in this chapter a new family of Li-rich double perovskites as versatile materials $Li_{1.5}La_{1.5}MO_6$ for Li batteries has been explored. In this chapter the isostructural $Li_{1.5}La_{1.5}WO_6$ (LLWO) as a low voltage anode material and the $Li_{1.5}La_{1.5}TeO_6$ (LLTeO) as solid-electrolyte material for Li batteries are presented.

In parallel to the research presented in this chapter, Rosseinsky and co-workers reported one of the member of this novel family of lithium-rich double perovskites, the LLWO material.[1] The motivation of Rosseinsky and co-workers to obtain the LLWO material was determined by the replacement of the Ti^{4+} ions in the $Li_{3x}La_{0.66-x}TiO_3$ with more stable W^{6+} d^0 ions, in the search for a more stable solid state electrolyte at low potentials.[1] In the case of the study in this thesis, the driving force for the development of the LLWO composition was based on the synthesis of a novel $Li_3La_3W_2O_{12}$ garnet in analogy to the $Li_3Nd_3W_2O_{12}$ material reported by Goodenough and co-workers.[2]

In this chapter, the synthesis of these novel lithium-rich double perovskites $Li_{1.5}La_{1.5}MO_6$ has been performed by microwave-assisted solid-state chemistry. The crystal structure has been analysed by PXRD and NPD diffraction methods, Raman and XAS spectroscopies, confirming the monoclinic $P2_1/n$ symmetry and the presence of Li^+ in both A- and B-sites, with La^{3+} deficiency on the A-sites. The electrochemical performance of the materials has been analysed by CV and galvanostatic cycling. Ionic conductivity studies have been performed by EIS and μ^+SR, as well as investigating the stability against Li metal electrode. Preliminary studies on a hybrid cell formed by the LLWO and LLTeO double perovskite have also been carried out.

7.1 Synthesis and crystal structure characterisation

The synthesis of these novel lithium-rich double perovskites $Li_{1.5}La_{1.5}MO_6$ (M = W^{6+}, Te^{6+}) was carried out by the same energy efficient microwave-assisted solid-state approach, used in previous chapters of this thesis. A first heat treatment at 750 ^{o}C for six hours was employed to allow precursor decomposition, followed by a calcination step at 950 ^{o}C for another six hours to obtain the double perovskite phase. A final calcination step at 1000 ^{o}C for an hour was carried out in order to remove any unreacted products to obtain phase pure material. Different Li:La:W ratios were tested in order to unveil the correct stoichiometry leading to phase pure material (Fig. 7.1), as at that point the work by Santibáñez-Mendieta *et al.* was unpublished.[1]

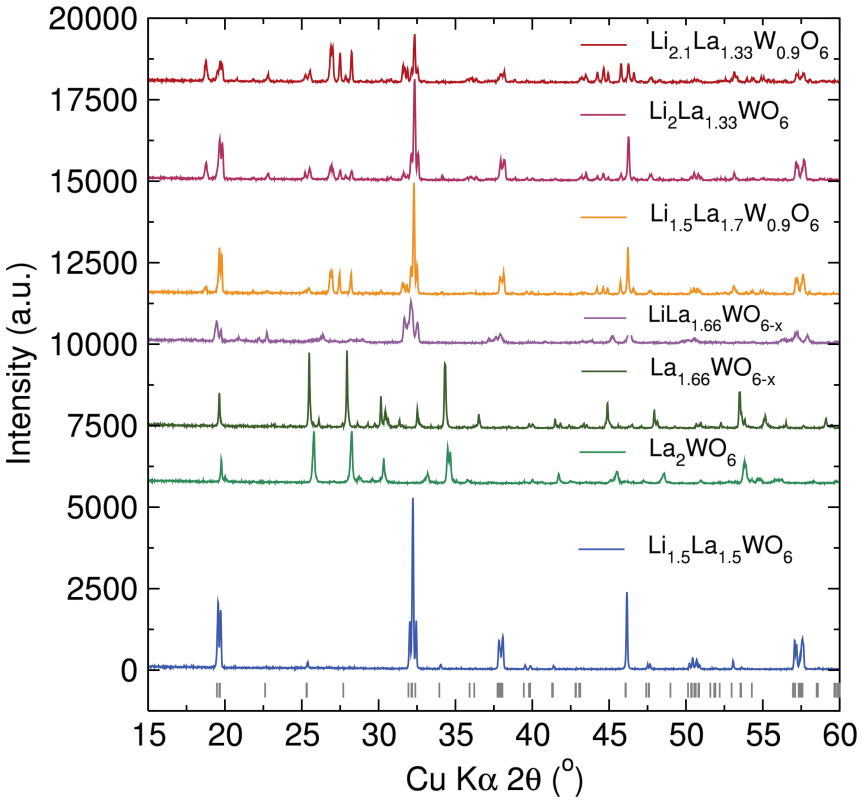

Figure 7.1: PXRD patterns of the different $Li_aLa_bW_cO_{6-x}$ compositions prepared to analyse the phase purity of the final calcined material (solid lines). Bragg reflections calculated for the $P2_1/n$ monoclinic double perovskite are indicated by the vertical grey tick marks.

It can be observed that only the $Li_{1.5}La_{1.5}WO_6$ stoichiometry led to phase pure materials, with the recognisable Bragg peak reflections arising from a double perovskite structure, as indicated by the bottom tick marks. From the stoichiometry employed, it was possible to ascertain a 25% vacancy on the La^{3+} occupying A-sites, with B-sites fully occupied by one mol of Li^+ and another mol of W^{6+} cations. This leaves an excess of 0.5 mols of Li^+ to be distributed across the double perovskite framework.

Rietveld refinements of PXRD data confirmed the crystal symmetry belongs to the monoclinic $P2_1/n$ space group (Fig. 7.2a). Subsequent substitution of the W^{6+} cations (0.60 Å) by similar sized[3] Te^{6+} (0.56 Å) also led to formation of the double perovskite structure with similar structural arrangements, *i.e.* $P2_1/n$ monoclinic space group presenting A-site La^{3+} vacancies and additional Li^+ beyond the full occupancy of B-sites. This monoclinic distortion from the prototype cubic perovskite structure found in these novel double perovskites is due to the small size of the La^{3+} ions compared by the A-site void left by the Li^+ and W^{6+}/Te^{6+} octahedral network.[4]

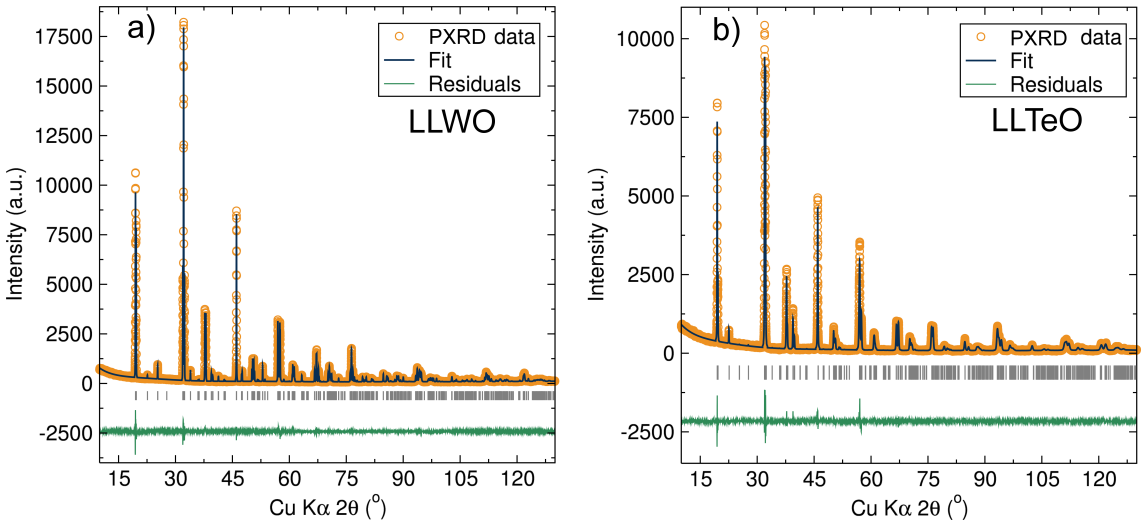

Figure 7.2: Rietveld refinements to PXRD for the $Li_{1.5}La_{1.5}WO_6$ (a) and $Li_{1.5}La_{1.5}TeO_6$ (b) double perovskites. Fits were in excellent agreement to the monoclinic space group $P2_1/n$, with cell parameters from (a) a = 5.53868(3) Å, b= 5.61487(3) Å, c = 7.9016(4) Å, β= 90.107(1)° and V = 245.376(3) Å^3 (R_{wp} = 0.0844 and R_p = 0.0618, χ^2 = 1.768) and (b) a = 5.5750(2) Å, b = 5.6124(2) Å, c = 7.9109(4) Å, β= 90.568(2)° and V = 247.517(6) Å^3 (R_{wp} = 0.0955, R_p = 0.0729 and and χ^2 = 2.262).

This discrepancy between the void left by the W^{6+}/Te^{6+} and Li^+ octahedra framework and the size of the La^{3+} can be quantified by the Goldschmidt tolerance factor (f),[5] which for a double perovskite with A-site mixed ions A'$_{2-x}$A"$_x$B'B"O_6 can be calculated through Equation 7.1 where r_X represents the atomic radius of the X ion. This tolerance factor has a value of 0.85 for the LLWO perovskite and 0.86 for the LLTeO analogue. These tolerance factors fall within lower limit of tolerance factors reported for double perovskites of $\sim$ 0.85, all belonging to the monoclinic $P2_1/n$ symmetry.[4]

$$f = \frac{(1-\frac{x}{2})r_{A'} + \frac{x}{2}r_{A''} + r_O}{\sqrt{2}(\frac{r_{B'}}{2} + \frac{r_{B''}}{2} + r_O)} \tag{7.1}$$

These structural arrangements in these Li-rich materials differ from other lithium-containing double perovskites, La_2LiMO_6,[6] where Li^+ is solely occupying the B-site and the A-sites are full occupied by the La^{3+} ions. From consideration of the crystal chemistry, one may predict that this additional 0.5 Li^+ could be located at the La^{3+} vacant A-sites, as in the case of the $Li_{3x}La_{0.66-x}TiO_3$ superionic Li^+ conducting materials.[7] In order to confirm this peculiar crystallographic arrangement and to obtain a more precise structural model, NPD analyses were carried out at GEM and Polaris instruments in ISIS for the LLWO and LLTeO materials. The negative scattering length of the ^{7}Li nucleus can provide sufficient contrast as to be able to locate the additional 0.5 Li^+ within the perovskite framework.

The acquired NPD data were refined (Fig. 7.3) to the $P2_1/n$ crystal model refined from the PXRD data, where the La^{3+} occupied A-sites presented a $\sim$25% vacancy. The

additional unlocated Li^+ by PXRD were placed into different positions close to the A-site until a stable refinement was achieved. These additional Li^+ were found to be displaced from the La^{3+} position towards the base of a trigonal pyramid, presumably to satisfy the smaller charge and size of the Li^+ compared to the La^{3+}, inducing a lower coordination number for these A-site located Li^+. While in the case of the LLWO compound it was possible to leave all atomic fraction and thermal energy parameters free to refine, in the case of the LLTeO the Li^+ ion atomic fraction on the A-sites must be fixed at 0.25. A slightly higher thermal factor for the Li^+ on the A-sites compared to the Li^+ in the B-sites [0.239(2) $Å^2$ vs 0.005(1) $Å^2$ respectively] was found in the LLWO material. This indicates a possible dynamical disorder at the A-site position which may enable its use as battery material, allowing Li^+ to flow through the perovskite structure. The refined LLWO crystal

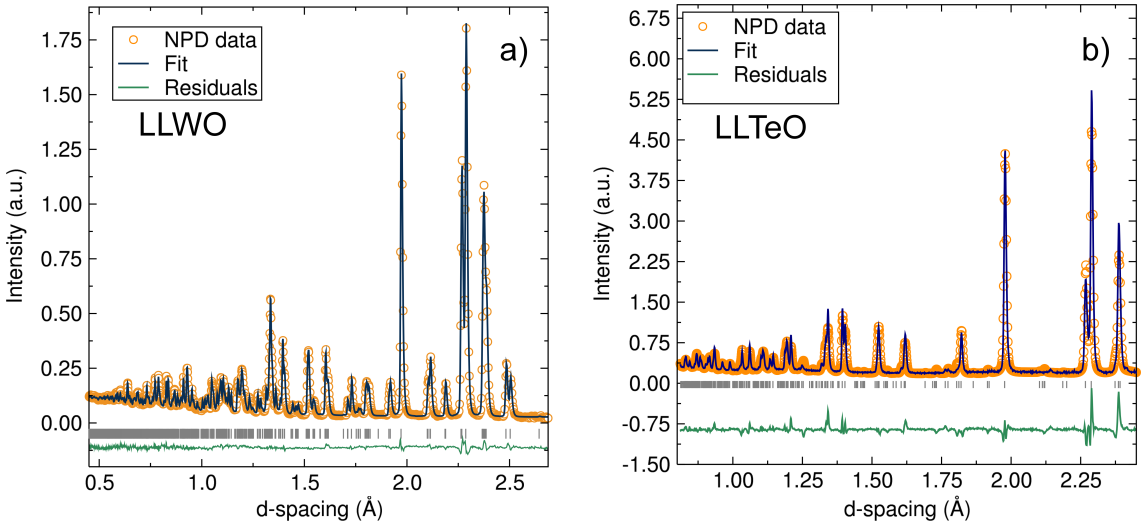

Figure 7.3: Rietveld refinements to NPD for the $Li_{1.5}La_{1.5}WO_6$ (a) and $Li_{1.5}La_{1.5}TeO_6$ (b) double perovskites. Fits were in good agreement to the monoclinic space group $P2_1/n$, with cell parameters from (a) a = 5.53537(6) Å, b = 5.61275(5) Å, c = 7.88629(9) Å, β= 90.105(1)° and V = 245.016 $Å^3$ (R_{wp} = 0.0468, R_p = 0.0543, χ^2 = 3.363) and (b) a = 5.5738(2) Å, b = 5.6120(2) Å, c = 7.9046(3) Å, β= 90.562(2)° and V = 247.24(1) $Å^3$ (R_{wp} = 0.0664, R_p = 0.0528, χ^2 = 8.432).

Table 7.1: Refined atomic parameters for NPD data for the $Li_{1.5}La_{1.5}WO_6$ perovskite fit to the monoclinic $P2_1/n$ space group.

Atom	Site	Frac.	x	y	z	Uiso (100/$Å^2$)
La1	4e	0.717(6)	0.0082(3)	0.9613(2)	0.7488(2)	0.44(4)
Li1	2d	0.99(3)	1/2	0	0	0.5(1)
Li2	4e	0.20(1)	0.501(5)	0.355(5)	0.224(5)	2.3(2)
O1	4e	1.00(1)	0.2780(4)	0.6947(5)	0.9579(4)	1.20(9)
O2	4e	0.99(1)	0.1923(4)	0.2210(5)	0.9574(4)	1.11(9)
O3	4e	1.00(1)	0.9168(4)	0.5150(3)	0.7634(4)	1.35(8)
W1	2c	0.971(9)	1/2	0	1/2	1.09(6)

structure is in good agreement with that reported from Rosseinsky's group.[1] Details of the Rietveld co-refinement to NPD and PXRD for the LLWO material are included in Table 7.1. Details of the Rietveld refinements of the LLTeO material can be found in Table 10.3 in the Appendix.

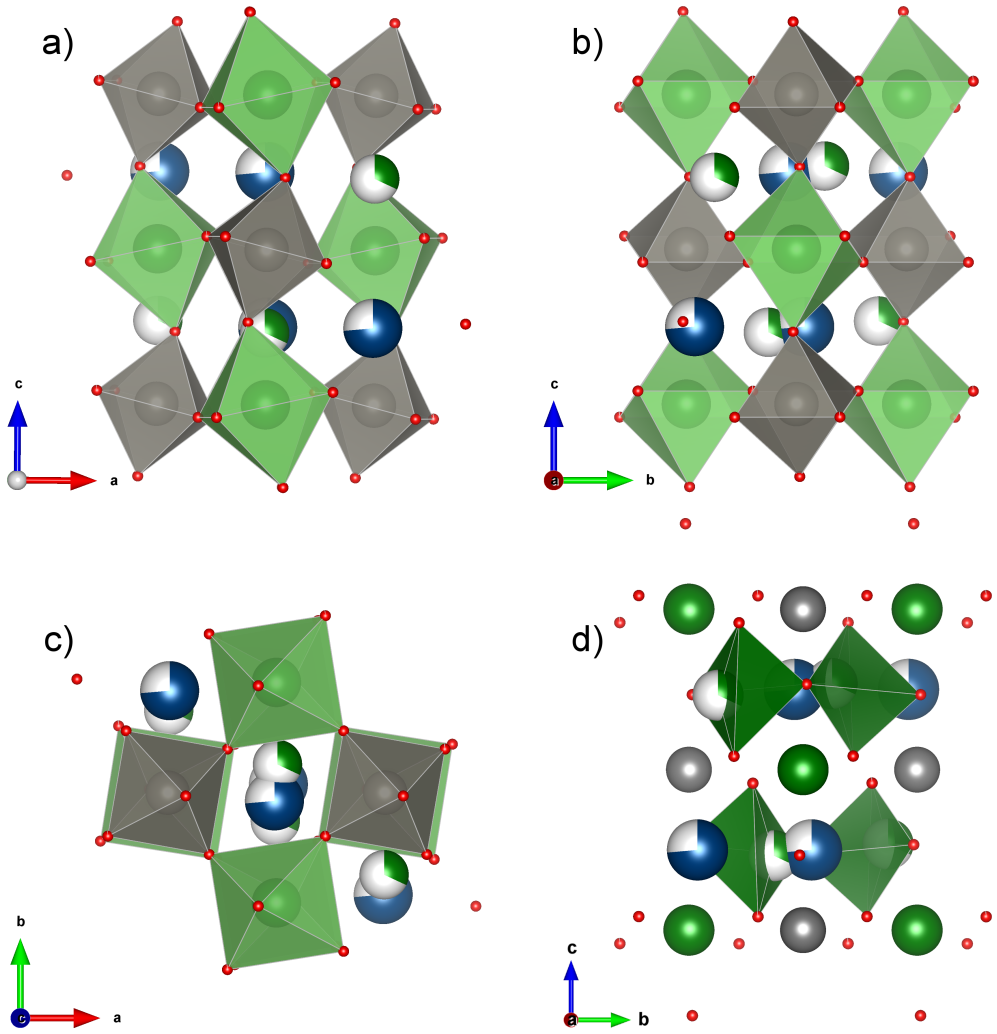

Figure 7.4: (a,b,c) Crystallographic representations of the $Li_{1.5}La_{1.5}WO_6$ structure with monoclinic symmetry $P2_1/n$ where grey spheres in the octahedra represent W^{6+} ions, dark blue spheres represent 8-fold coordinate La^{3+} ions, green spheres are Li^+, with green octahedra representing Li^+ occupying perovskite B sites, and oxygen anions are shown in red. (d) Crystal structure for LL*M*O where the coordination polyhedra for off-centred Li^+ on the A site has been explicitly represented in darker green. (b) and (d) show same projections but highlight the differing Li^+ coordination sites.

The crystal structure for these novel LL*M*O Li-rich double perovskites is presented in Figure 7.4. Figures 7.4 a, b and c show the unit cell of the double perovskite with $P2_1/n$ monoclinic symmetry, where the tilting of the Li^+ and M^{6+} octahedra is clearly observed. This octahedral tilting is out-phase along the a and b direction and in-phase along the c axis, leading to an $a^-a^-b^+$ configuration in Glazer notation.[8] These octahedral tilts can be calculated from the Li-O-M angle, yielding a value of in 13.4º for the LLWO material

and 10.8º for LLTeO. The tilting on the LLWO is similar to that reported by the Rosseinsky group[1] and the lower tilting angle in the LLTeO analogue is expected as the smaller size of the Te^{6+} ions allows for a smaller A-site cavity for the La^{3+} ions. On Figure 7.4d, the coordination geometry of the Li^+ on the A-site is explicitly shown. The Li^+ is located on the base of a trigonal pyramid, displaced from the centre of the A-site position.

It should be noted that for the LLTeO material, the model obtained for the LLWO material resulted in intensity mismatch in various Bragg peaks. These mismatches were found to have origin on the oxide sub-lattice. Specifically, it was found that the oxygen positions are split into two to give a total of six crystallographically-independent oxide anions with distances of $\sim$ 0.7 Å between neighbouring oxide anions in the split sites (Fig. 7.5). These observations, however, will require further advanced characterisation such as modelling of neutron total scattering data to confirm and detail the observed oxygen disorder, which falls beyond the scope of this chapter.

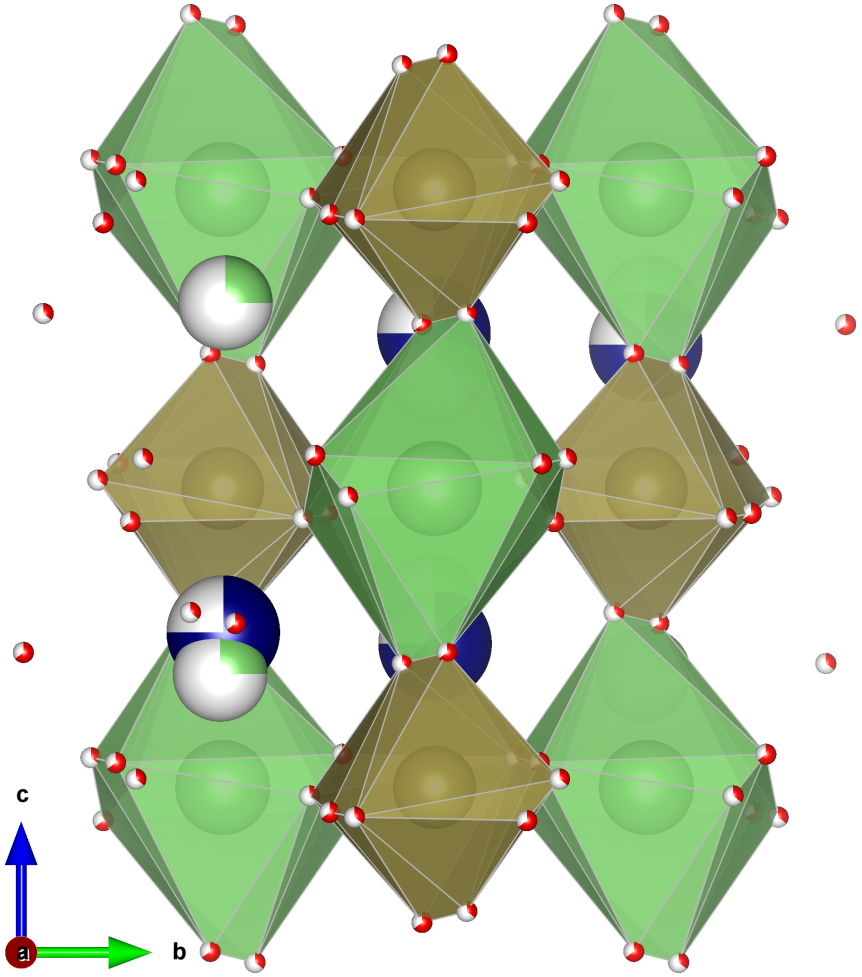

Figure 7.5: Crystallographic representations of the $Li_{1.5}La_{1.5}TeO_6$ structure with monoclinic symmetry $P2_1/n$ where brown spheres in the octahedra represent Te^{6+} ions, dark blue spheres represent 8-fold coordinate La^{3+} ions, green spheres are Li^+, with green octahedra representing Li^+ occupying perovskite B sites, and oxygen anions are shown in red.

In addition to the LLWO and LLTeO materials, the mixed-metal $Li_{1.5}La_{1.5}W_{0.5}Te_{0.5}O_6$

(LLWTeO) material was also prepared. The PXRD of the as-synthesised material confirmed the formation of the solid-solution compound between both parent compounds. Rietveld refinement of the PXRD data for this mixed metal LLWTeO compound is shown in Figure 7.6. As expected, A-site vacancies were detected for the La^{3+} ($\sim$ 21%), which was presumed to be filled by the additional Li^{+}, following the parent compound trend and as the phase pure employed stoichiometry suggests. W^{6+} and Te^{6+} are distributed in a disordered manner throughout the B-sites without any indication from PXRD of cation ordering. The refined cell volume resulted in a value of 246.7 $Å^3$, which lies in between the values obtained for the LLTeO (247.2 $Å^3$) and LLWO (245.0 $Å^3$) solid-solution extremes, which further confirmed the solid-solution formation. The full Rietveld refined parameters are reported in Table 10.2 in the Appendix.

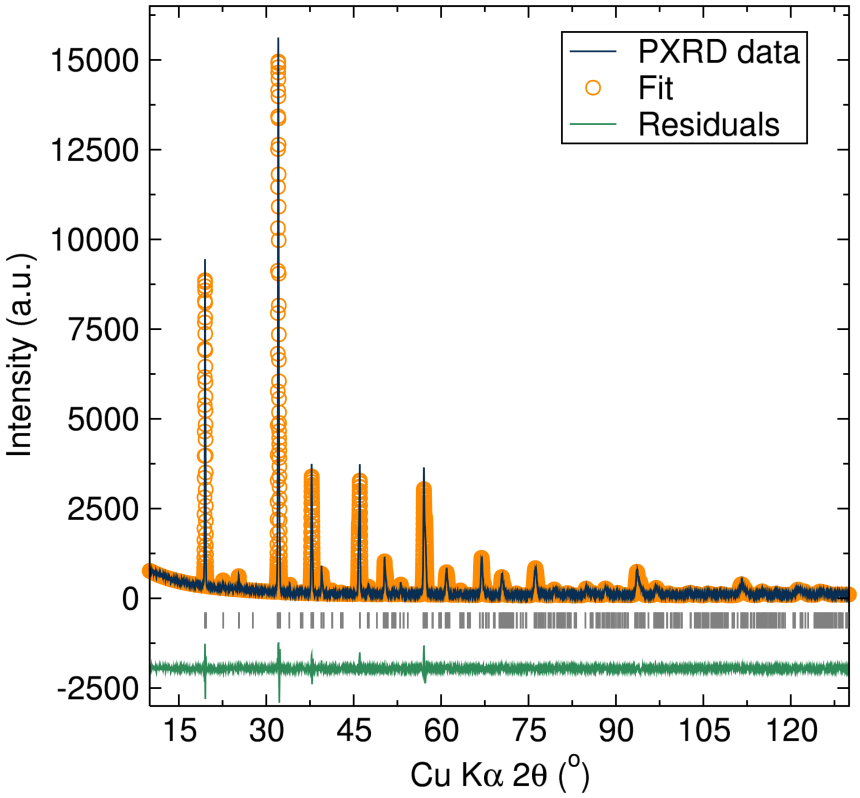

Figure 7.6: Rietveld refinements to PXRD data for the $Li_{1.5}La_{1.5}W_{0.5}Te_{0.5}O_6$ compound. Fits were in excellent agreement to the monoclinic space group $P2_1/n$ with the following cell parameters: a = 5.56418(9) Å, b = 5.5976(5) Å, c = 7.9209(1) Å, β= 90.161(2)° and V = 246.704(9) $Å^3$. R_{wp} = 0.0914, R_p = 0.0679, R_{F^2} = 0.0724 and χ^2 = 2.346.

The stoichiometry arising from Rietveld refinements of PXRD and NPD for the LLWO and LLTeO parent compounds were found to be $Li_{1.39(5)}La_{1.43(1)}W_{0.971(9)}O_{6.00(6)}$ and $Li_{1.39(5)}La_{1.43(1)}Te_{0.971(9)}O_{6.00(6)}$, very close to the targeted stoichiometries. In order to further confirm the stoichiometry, ICP-MS and EDX analyses were performed. ICP-MS yielded a Li:La atomic ratio of 1.03:6(4), 1.075(3) and 1.075(1) for the LLWO, LLWTeO and LLTeO respectively, and EDX showed La:W:Te atomic ratios of 1.51:1, 1.52:0.49:0.5

and 1.5:1 (Table 7.2). All of these results are in good agreement with the target stoichiometries.

Table 7.2: Atomic percentages of La, Te and W determined from by EDX measurements with a 20 kV electron beam on the as-synthesised powders. The atomic ratio has been normalised using W atomic percentage as reference for $Li_{1.5}La_{1.5}WO_6$ and $Li_{1.5}La_{1.5}W_{0.5}Te_{0.5}O_6$, and Te atomic percentage for the $Li_{1.5}La_{1.5}TeO_6$ material.

Material	La (atomic %)	Te (atomic %)	W (atomic %)	La:W:Te ratio
LLWO	60.0(7)	N/A	40.0(7)	1.5:1
LLWTeO	60.6(6)	19.5(1)	19.9(5)	1.52:0.49:0.5
LLTeO	60.2(4)	39.8(4)	N/A	1.51:1

Raman analyses were also performed in order to further confirm the $P2_1/n$ symmetry of the three double perovskites prepared here. $P2_1/n$ double perovskites have an irreducible representation $\Gamma = \nu_1(A_g + B_g) + \nu_2(2A_g + 2B_g) + \nu_5(3A_g + 3B_g) + T(3A_g + 3B_g) + L(3A_g + 3B_g)$ for the Raman active modes,[9] where ν, T and L represent the vibrational, translational and librational modes respectively. All of these modes are present in the LL*M*O materials (Fig. 7.7). Vibrational modes are related to the *M*-O stretching modes, the translational modes are related to lattice vibrations and the librational modes are due to the rotations of the MO_6 octahedra. The most intense mode is the vibrational mode

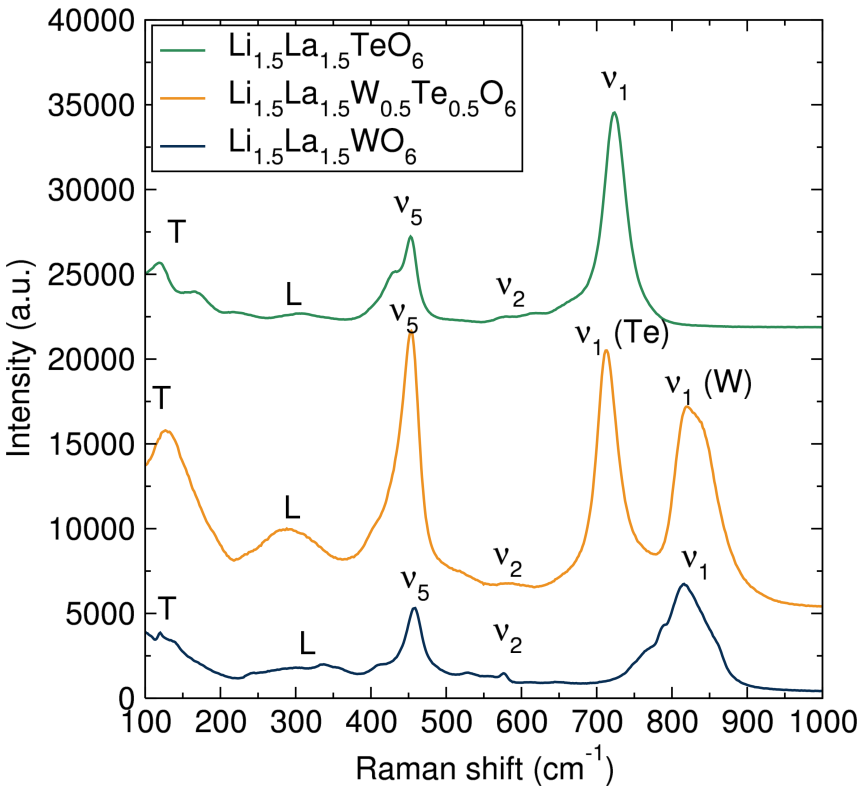

Figure 7.7: Raman spectra of the three $Li_{1.5}La_{1.5}MO_6$ double perovskites under the excitation of a λ = 532 nm Argon-ion laser.

ν_1 representing the Li-O-W/Te symmetric stretching motion. This ν_1 band is found at a Raman shift *ca.* 815 cm^{-1} for the LLWO double perovskite and at a lower Raman shift of *ca.* 723 cm^{-1} for the LLTeO analogue. The lower Raman shift of the Li-O-Te symmetric stretching mode can be related to the higher Li-O-*M* distance on the LLTeO material (3.96 Å) compared to the LLWO analogue (3.94 Å). Both ν_1 contributions are presented in the mixed metal compound, indicating again the formation of the solid-solution, making possible to discern the discrete contributions of both Li-O-*M* distances. This is more difficult to assess by diffraction techniques due to the static disorder of the W and Te atoms in the average crystal structure. Similar Raman bands were found in other tellurium and tungsten containing double perovskites, such as Ca_2MgTeO_6 [10] and A_2MWO_6. [9]

The local structure of the LLWO material was studied by EXAFS from XAS data on the W L_{III}-edge collected in the B18 beamline at Diamond Light Source for the LLWO material. Fits to the EXAFS data arising from the different W-O and W-La multiple/single scattering paths of the produced photoelectrons revealed a good agreement between the local coordination of W^{6+} cations and the perovskite structure (Fig. 7.8). The average W-O bond length calculated from the EXAFS was found to be 1.87 Å (Table 7.3), close to the 1.90 Å value obtained from average structure refined from NPD data. EXAFS analyses also revealed a W-La distance of 3.35 Å which is also close to the distance obtained from NPD (3.37 Å), indicating the absence of large distortions from the average to the local structure.

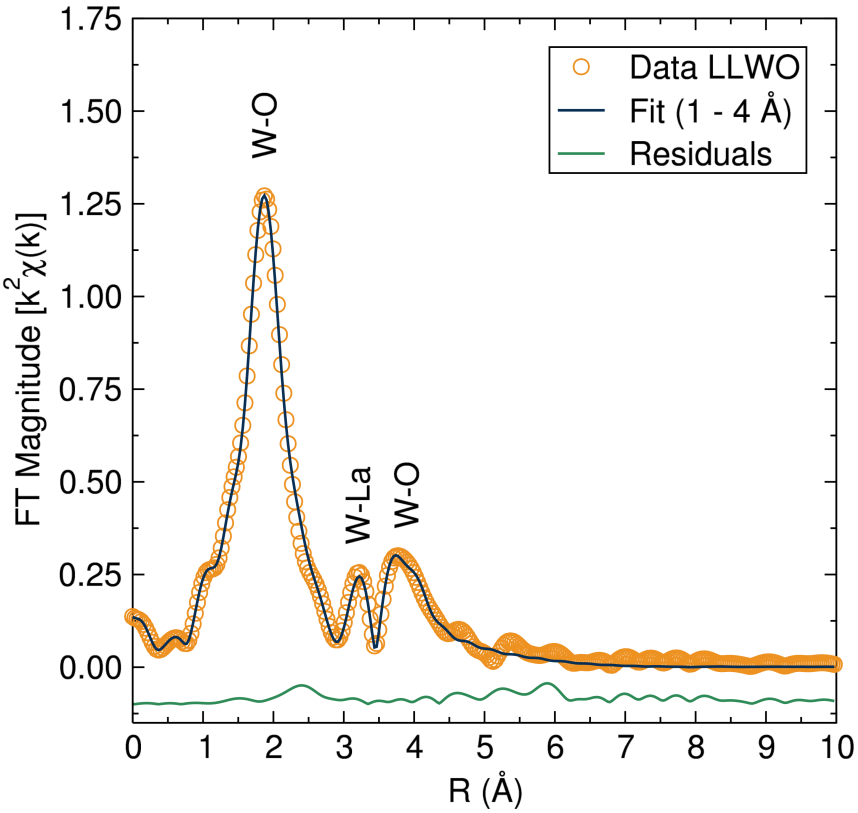

Figure 7.8: Real part of the Fourier transform for the EXAFS data measured on the L_{III} W-edge for the $Li_{1.5}La_{1.5}WO_6$ material. The fit was performed on the 1-4 Å windows corresponding using data from 4.0 to 13.3 $Å^{-1}$ in reciprocal space (k). The first peak corresponding to the W first shell is the W-O single scattering path at a effective distance of 1.87 Å in good agreement with the NPD data. The second peak correspond to the W-La single scattering at an effective distance of 3.35 Å and a third double-peak at *c.a.* 3.5 to 3.9 Å has been fitted to the contribution of the W-La single scattering of the second shell and the O-W-O forward path through the W absorber. The final fitting R-factor was 0.0016. The data have been represented phase-corrected using the W-O first shell.

Table 7.3: Effective distances fitted for the main path contributing to the EXAFS spectra measured on the W L_{III}-edge of the $Li_{1.5}La_{1.5}WO_6$ double perovskite.

Atomic Pair	r(EXAFS) (Å)	r (NPD) (Å)
W-O	1.872(5)	1.901(3)
W-La	3.35(1)	3.368(3)
O-W-O	3.76(2)	3.801(6)

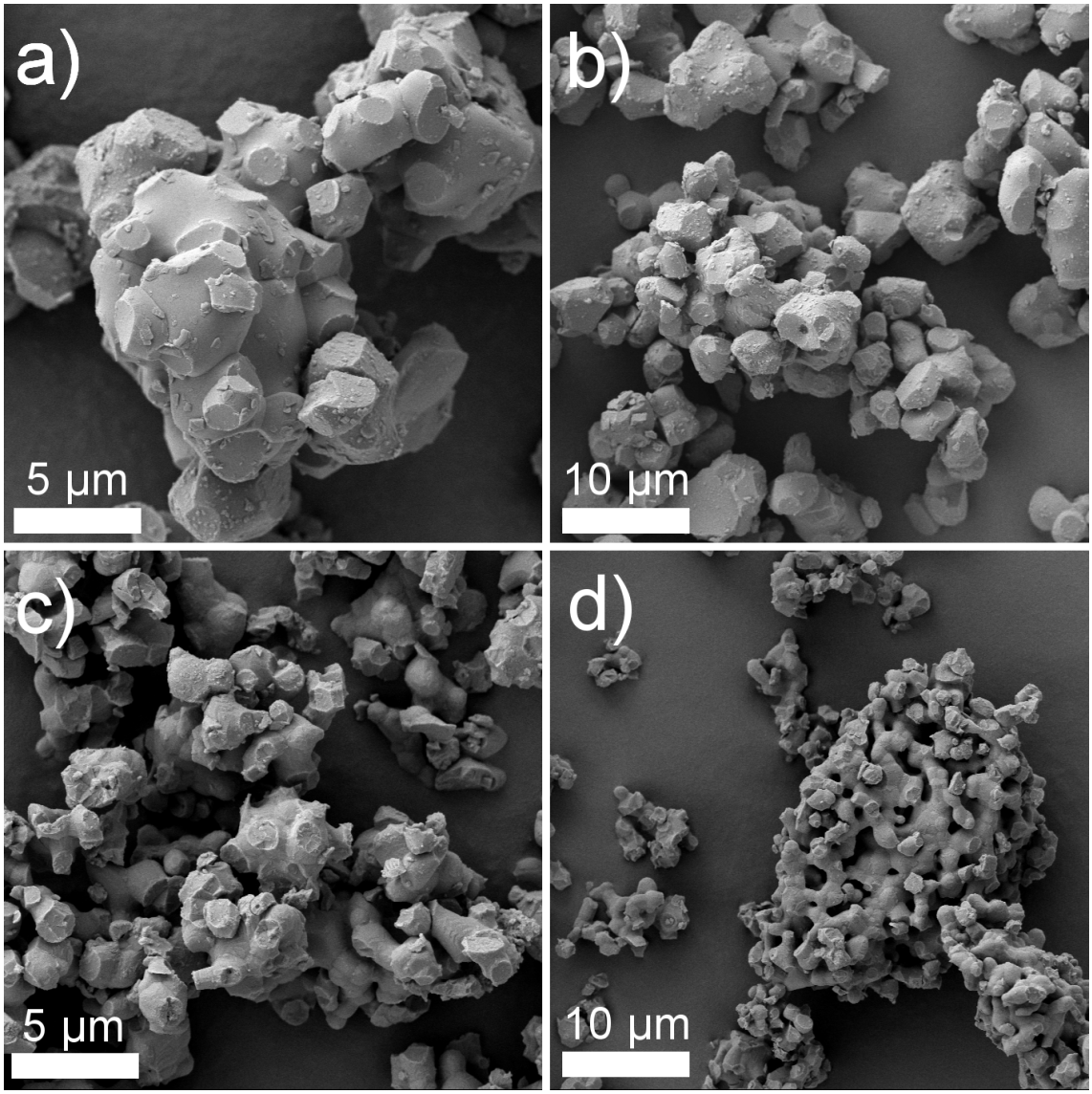

Figure 7.9: SEM images of the $Li_{1.5}La_{1.5}WO_6$ (a,b) and $Li_{1.5}La_{1.5}TeO_6$ (c,d) Li-rich double perovskite materials at 10 kX and 5 kX magnifications.

SEM analyses were performed on the LLWO and LLTeO materials to analyse their microstructure (Fig. 7.9). The SEM micrographs show primary particles with a size ranging from $\sim$ 2 to 10 µm in the case of the LLWO material, and a smaller particle size for the LLTeO compound of $\sim$ 1 to 5 µm. The particles had irregular shapes with clear faceted surfaces produced by breakage of the inter-particle joints of the sintered powders after mortar-grounding.

7.2 Electrochemical characterisation

7.2.1 Electrochemical properties of the LLWO material as anode electrode

In the case of the LLWO material, the presence of W^{6+} ions and the robust perovskite framework suggested the possible applicability of this material as an insertion electrode

material, due to the available redox couple(s) of tungsten, similar to the $Li_3Nd_3W_2O_{12}$ garnet material.[2]

In order to determine any redox activity of the LLWO double perovskite, CV analyses were performed in the voltage range of 0.01 to 2.8 V against Li metal as the counter and reference electrode, at a scan rate of 0.1 mV s^{-1}. The upper voltage window from 2.8 to 4.5 V was also explored without any redox activity attributable to tungsten (Fig. 10.1, Appendix). The LLWO material displayed two strong redox couples as observed in Figure 7.10a. The first voltage redox couple occurs at $\sim$ 0.7 V in the reduction regime and at $\sim$ 1 V in the oxidation regime. The second redox process takes place at lower potentials; below 0.2 V in the reduction regime, which is masked by the large peak near 0 V corresponding to the irreversible lithium insertion into the carbon black additive employed, and near 0.3 V for the oxidation process. In the first CV cycle, a broad peak in the reduction regime is observed due to the formation of a solid-electrolyte interphase (SEI) as consequence of the partial decomposition of the liquid electrolyte ($LiPF_6$ in EC:DMC) at low voltages.[11] The isostructural LLTeO analogue, on the contrary, did not show any redox couple over the same potential range (Fig. 7.10b) apart from that arising from carbon black and SEI formation (Fig. 10.2, Appendix). The electrochemical performance of LLWO was then further investigated by galvanostatic cycling in order to assess its lithium (de)insertion capabilities (Fig. 7.11). Figure 7.11a shows the cycling profiles for the three double perovskite compounds prepared in this chapter, where the first cycle for each material has been omitted due to the large SEI contribution to the capacity, masking the perovskite contributions. In the case of LLWO, a specific capacity of close to 150 mAh g^{-1} is achieved in the second discharge which decreases to 125 mAh g^{-1} in the following two cycles. The shape of the cycling profile shows a clear flat plateau at 0.3 V and a

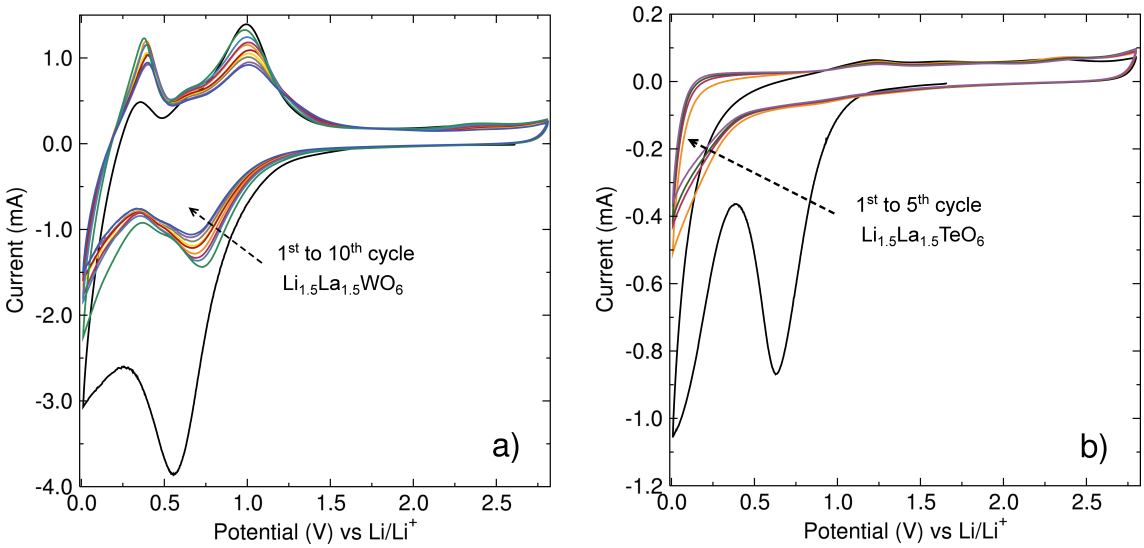

Figure 7.10: CV data for (a) $Li_{1.5}La_{1.5}WO_6$ and (b) $Li_{1.5}La_{1.5}TeO_6$ double perovskites mixed with 5% carbon black and 5% PTFE binder between 0.01 V and 2.8 V *vs* Li. The scan rate was fixed at 0.1 mV s^{-1} for both measurements.

pseudo-plateau in the 0.75 - 1.25 V range during charging, which matches well with the redox potentials observed in CV analyses. On the discharge cycle, a pseudo-plateau is observed between 1.0 - 0.5 V and an almost flat plateau at $\sim$ 0.25 V, again in good agreement with the CV data. In order to establish the net capacity arising from the tungsten ions in the double perovskite and separate it from the contributions of carbon black and electrolyte decomposition, identical half cells using the LLTeO and LLWTeO compounds were subjected to galvanostatic cycling (Fig. 7.11a). Lack of a clear plateau in the LLTeO material and a drop in capacity to just above 25 mAh g^{-1} indicates that any insertion taking place at low voltage is with the 5% carbon black additive added to the electrode mixture.[12] In the case of the mixed-metal LLWTeO material, the capacity falls to a value slightly below half that between the LLTeO and LLWO parent compounds. This may be due to the lower accessibility for Li^+ to the active tungsten ions by the presence of inactive Te^{6+} in the same crystallographic sites. By subtracting the capacity from the LLTeO compound from that observed for the LLWO analogue, a net capacity of $\sim$ 100 mAh g^{-1} can be attributed to the redox activity of the tungsten ions. Taking into account the molecular mass of the LLWO perovskite material (498.6 g mol^{-1}), this capacity corresponds to $\sim$ 2 e^- transfer per formula unit of double perovskite (theoretical capacity of 53.75 mAh g^{-1} per electron transferred).

A longer cycling study up to 20 cycles was carried out to investigate the reversibility of the capacity for the LLWO material (Fig. 7.11b). An irreversible initial capacity above 300 mAh g^{-1} is observed in the first discharge cycle due to the contribution of SEI formation. In subsequent cycles, a moderate reversibility close to 150 mAh g^{-1} drops down to 75 mAh g^{-1} by the end of 20 cycles. This capacity drop may be influenced by degradation

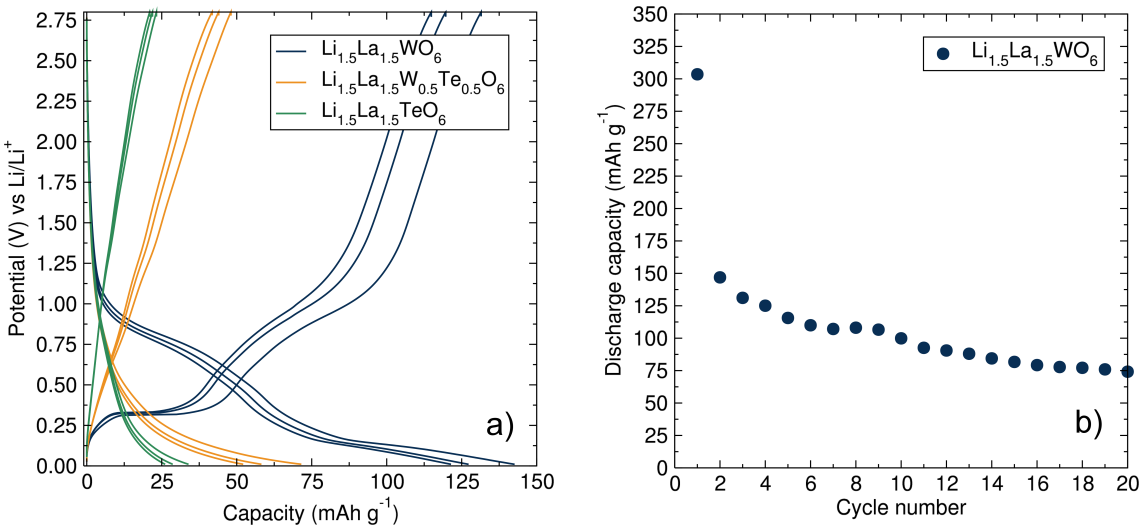

Figure 7.11: (a) Galvanostatic cycling of $Li_{1.5}La_{1.5}MO_6$ double perovskites mixed with 5% carbon black and 5% PTFE binder, between 0.01 and 2.8 V *vs* Li at a current of 36 mA g^{-1}. (b) Discharge capacity fading test for $Li_{1.5}La_{1.5}WO_6$ material at 36 mA g^{-1} over 20 cycles. The high first discharge is due to the irreversible formation of the SEI layer.

of the liquid electrolyte at low voltages and irreversible Li^+ intercalation into the carbon black additive.[13] The cycling rate employed was fixed to at 36 mA g^{-1}, which was slow enough to characterise the features observed from CV analyses.

The specific capacity of LLWO on the first cycle (>100 mAh g^{-1} at 0.75/0.01 V) is lower compared to insertion oxide materials such as the $Li_4Ti_5O_{12}$ spinel (175 mAh g^{-1}, 1.55 V)[14] and similar to the above mentioned $Li_3Nd_3W_2O_{12}$ garnet material (125 mAh g^{-1} with redox couples at 0.76/0.34 V)[2]. On the other hand, the low voltage observed for the redox processes of LLWO would increase the energy density of a battery by producing a higher voltage when used as an anode in a hypothetical full cell.

The rate capability of the LLWO material was also studied by analysing the evolution of the discharge capacity material when cycled at different rates (Fig. 7.12). It is clear that increasing rates negatively affects the battery capacity, where a low capacity below 25 mAh g^{-1} is observed at a cycling rate above 0.3 A g^{-1}. The capacity is then recovered when decreasing the cycling rate back to the initial rate (36 mA g^{-1}). The capacity at 36 mA g^{-1} seems to follow the same trend as if it were not cycled at higher rates, as indicated by the dotted line. The capacity in this case remained above 85 mAh g^{-1} after 40 cycles. The poor rate capability of the material may be due to difficult Li^+ conduction through the LLWO perovskite framework, as this could be hampered by the presence of La^{3+} on the Li^+ diffusion pathways. The sample was also carbon coated to analyse if the electronic conduction was the limiting factor. The rate capability barely improved as shown in Figure 10.3 in the Appendix section, suggesting that the electronic conductivity of the material may not be the limiting factor.

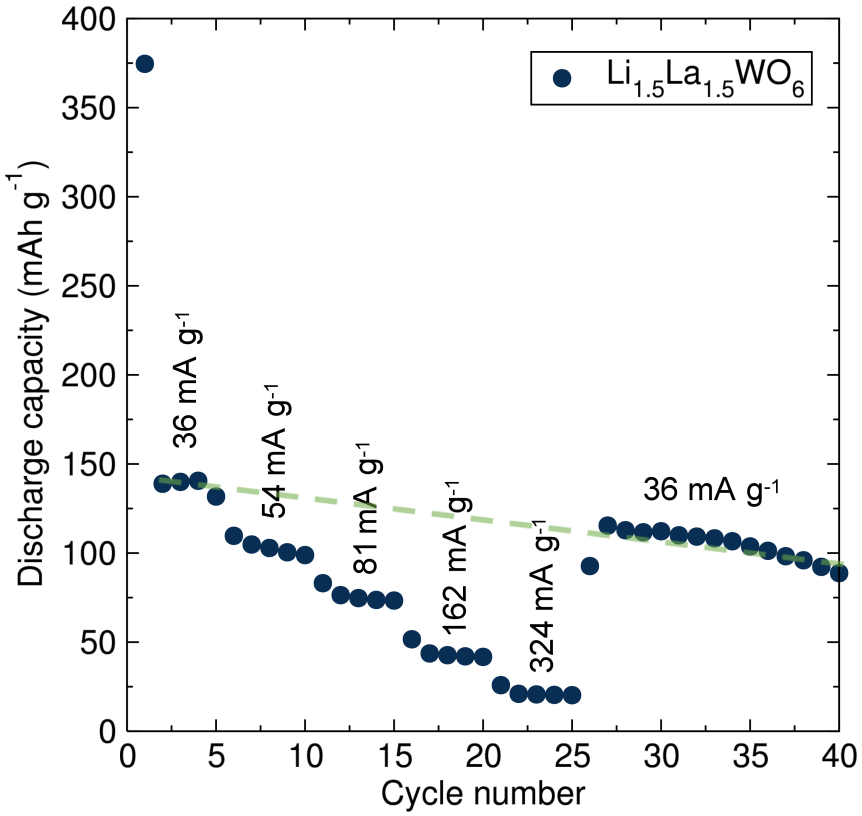

Figure 7.12: Rate capability of the $Li_{1.5}La_{1.5}WO_6$ material mixed with a 5% of carbon black and 5% of PTFE as a binder between 0.01 and 2.8 V at different cycling rates between 36 and 324 mA g^{-1}.

7.2.2 Insights into the electrochemical mechanism of LLWO cycling

After demonstrating the effective redox properties of the LLWO material as an anode material for a Li-ion battery, the next steps focused in the study of the mechanism behind its redox activity upon lithiation. The first approach was to study the PXRDs of the LLWO materials pre- and post-cycling which are shown in Figure 7.13. The *ex-situ* PXRD of the fully discharged LLWO revealed that the perovskite structure is retained upon lithiation with a small displacement of the diffraction pattern towards higher d-space values which is then reversed when charging back the material to 2.8 V. This observation indicates intercalation as the main mechanism for the observed electrochemical activity of the LLWO material, as no other phases could be observed on the cycled PXRD patterns, which should be apparent where conversion processes occur.[15] The calculated volume for the LLWO materials was 245.016(3) $Å^3$ before cycling and 245.50(2) $Å^3$ post-lithiation, indicating a low volume expansion of only 0.2%. This is in contrast to conversion electrodes which suffer from large volume expansion,[15] and similar to other intercalation electrodes such as the above mentioned zero-strain $Li_4Ti_5O_{12}$ titanate[14] or the $LiFe_{0.8}Mn_{0.2}SO_4F$ cathode material which shows a volume change of 0.6 % between the lithiated and delithiated phases.[16,17] Commercialised $LiFePO_4$ cathode materials for example experience a larger volume change of 6.6%.[18] Broadening of the Bragg reflections is also observed

upon lithiation, which may indicate some degree of amorphisation upon cycling, or some small variations of the LLWO structure as a consequence of cycling. Unfortunately the resolution of the laboratory PXRD was insufficient to clearly discern any additional sub-phases.

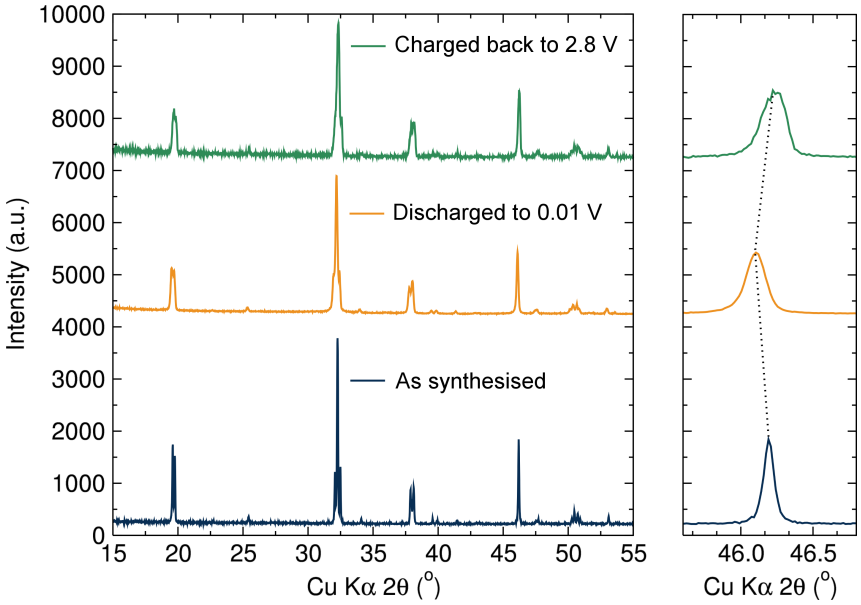

Figure 7.13: *Ex-situ* XRD patterns of the $Li_{1.5}La_{1.5}WO_6$ material as-synthesised, after fully electrochemical lithiation and after subsequent de-lithiation (20 cycles) (green line). Magnification of the (220) Bragg peak evidences the reversible insertion and de-insertion of Li-ions to and from the structure. The calculated volume expansion upon full lithiation is 0.2%.

In order to confirm and quantitatively assess the contribution of unpair electrons as consequence of cycling which may arise from oxidation changes in tungsten (W^{+6} reduction to W^{5+}/W^{4+}), SQUID measurements were carried out on a fully discharged sample and a sample charged back to 0.4 V. From these SQUID measurements, it is possible to see changes related the oxidation state of tungsten. For the material discharged to 0.01 V, strong magnetic coupling is observed which indicates reduction to W^{5+} of *ca.* 0.8 mols per formula unit of LLWO perovskite material obtained from fitting the inverse susceptibility to the Curie-Weiss law (Figure 7.14a) where a Curie Constant, C = 0.254(8) cm^3 K mol^{-1} and a Weiss Constant, Θ = -120(10) K were obtained. A deviation from linearity is observed at low temperatures indicating to an antiferomagnetc behaviour similar to other double perovskites, such as the Ba_2YMoO_6.[19] W^{4+} was expected at this voltage if only intercalation processes are to account for the observed capacity. However, relaxation processes cannot be ruled out which occur after the material is removed from the battery cell which might lead to re-oxidation to W^{5+}, or conversion processes leading to diamagnetic species. This observations open up the possibility that not all the reduction occurs as intercalation within the perovskite phase and that conversion processes not observable by lab PXRD during cycling may be occurring which give rise to diamagnetic species that have no measurable contribution to the magnetometry data. The magnetic

data for the material charged back to 0.4 V, *i.e.* cycled beyond the first oxidation process, revealed a change in the magnetism of the cycled material with a large reduction of the paramagnetic moment. This indicates almost complete re-oxidation to W^{6+}, which confirms the oxidation state change on the tungsten upon lithium intercalation on the studied redox couple.

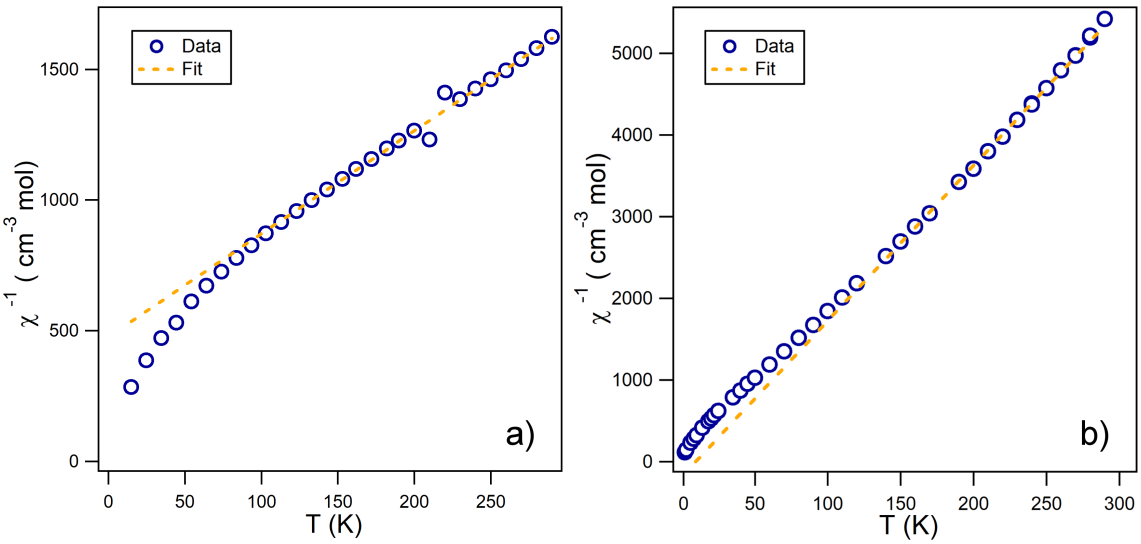

Figure 7.14: *Ex-situ* squid measurements on fully reduced $Li_{1.5}La_{1.5}WO_6$ material to 0.01 V (a) and half oxidised charged back to 0.4 V (b). The fit of the data to the Curie-Weiss law was performed between 150 and 290 K, observing a paramagnetic behaviour of *ca.* 0.8 e^- per formula unit of perovskite material (a) and diamagnetic behaviour (b).

DFT calculations were also performed by our collaborators at Loughborough University, Dr. Stephen Yeandel at Dr. Pooja Panchmatia's research group, in order to analyse the possible Li^+ insertion mechanism in the LLWO material. Their calculated structures for the unlithiated and lithiated LLWO materials are shown in Figure 7.15. It can be observed that the structure barely varies when adding the first Li^+ mol but becomes heavily distorted when adding an additional 0.5 Li^+ mols. These calculations suggest that it could be possible that only one mol of Li^+ per formula unit of LLWO material can be inserted that allows retention of the perovskite framework, again suggesting the possibility of additional contributing processes for the observed battery capacity.

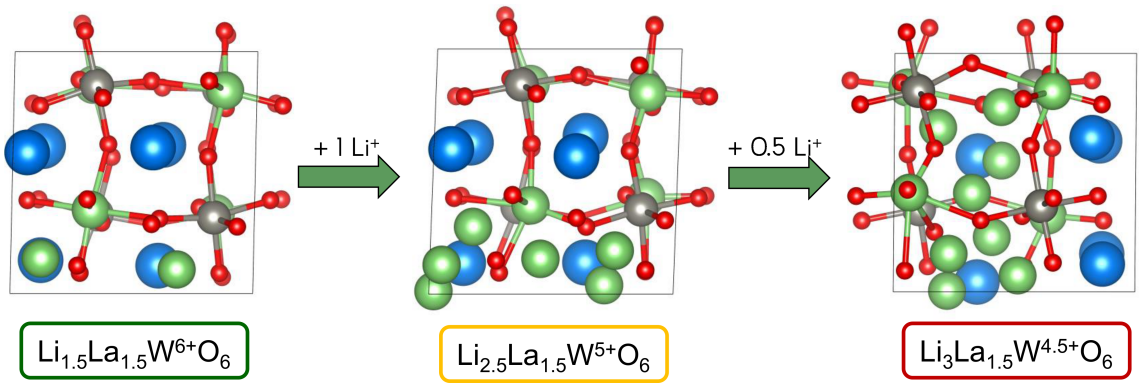

Figure 7.15: DFT calculated structures of the as-prepared $Li_{1.5}La_{1.5}WO_6$ material (a), lithiated with 1 mol of Li^+ (b) and further lithiated with additional 0.5 Li^+ mols. Li^+ is indicated in green, La^{3+} in blue, W^{n+} in grey and O^{2-} in red.

Ex-situ PXRD data of the cycled mixed metal LLWTeO compound was also obtained to further examine the source of additional capacity (Fig. 7.16). During cycling of the mixed metal LLWTeO compound (Fig. 7.11a), there is a clear loss in definition of the plateaus from the low voltage redox couple present in the LLWO analogue, which can be attributed to the insertion mechanism. The *ex-situ* PXRD of the discharged LLWTeO material revealed a large extend of degradation of the double perovskite phase, indicating this composition could be undergoing a conversion process. This could be also indicated

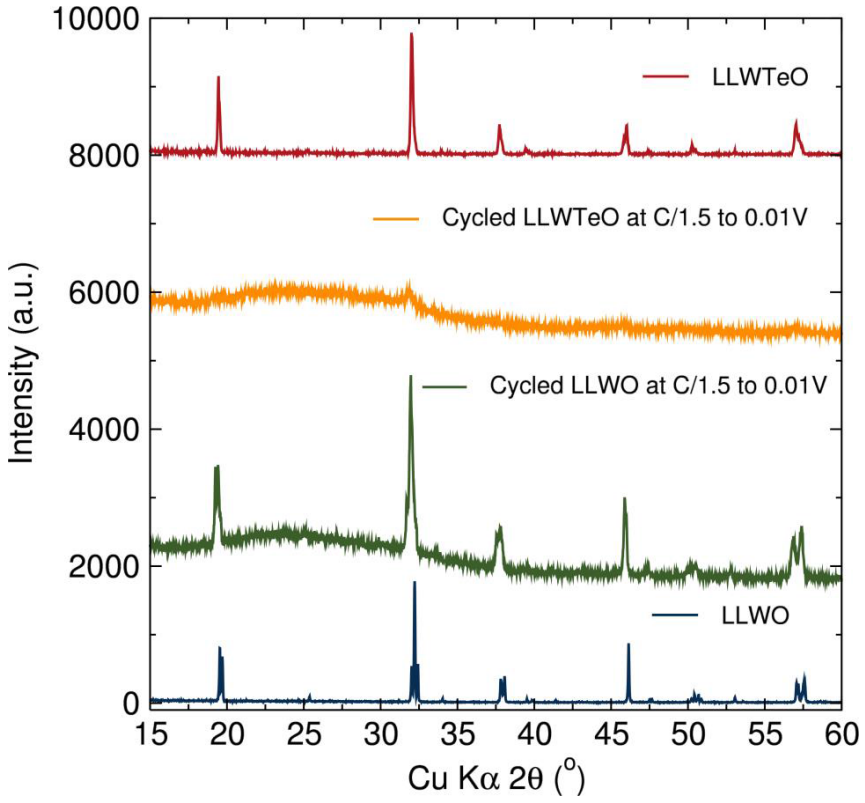

Figure 7.16: *Ex-situ* PXRD of the $Li_{1.5}La_{1.5}WO_6$ and $Li_{1.5}La_{1.5}W_{0.5}Te_{0.5}O_6$ materials as-synthesised and after full reduction to 0.01 V.

by the greater polarisation during cycling (Fig. 7.11), more frequent in conversion electrodes.[20] These observations reinforce the idea that the flat plateaus at low voltage redox processes observed on the LLWO material could be related to intercalation processes, while the higher voltage redox couple may be due to conversion processes, as this occurs mostly on the LLWTeO material and partially in the LLWO material. The CV also points to a lower reversibility of the higher voltage redox couple (around 1 V) (Fig. 7.10a), again more common in conversion processes.[21] However, it should be noted there are no Bragg peaks arising from conversion products such as Li_2O or W metal, thought we cannot rule out these as small amorphous particles which may contribute to the background.

From these observations across multiple analyses, it could be hypothesised that the overall mechanism may consist of a partial conversion process at the higher voltage redox couple, paired with intercalation processes at low voltages (Fig. 7.17). In the conversion process (W^{6+} to W^0) *ca.* 0.2 mols of LLWO material could transform into elemental tungsten species providing 1.2 e^-. During the intercalation processes at low voltages, the remaining 0.8 mol of LLWO material could undergo intercalation processes (W^{6+} to W^{5+}) providing the additional 0.8 e^- to account for the 2 e^- transfer observed on the galvanostatic cycling. This hypothesised mechanism is summarised in Fig. 7.17. A similar combined mechanism has been found in the $LiVO_3$ vanadate which displays intercalation and conversion processes below the 2 V window.[22]

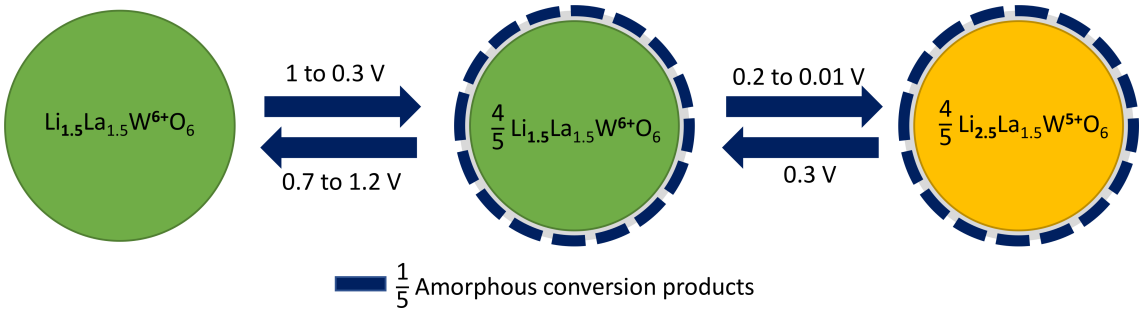

Figure 7.17: Proposed mechanism for the electrochemical reduction of the $Li_{1.5}La_{1.5}WO_6$ material with Li.

7.2.3 $Li_{1.5}La_{1.5}TeO_6$ as solid electrolyte

The LLTeO material did not show any redox activity from the CV analyses performed in half cells with liquid electrolyte, which suggests a possible application of this material as a solid-state electrolyte. EIS, CV and polarisation tests were carried out at 80 °C in (a)symmetric solid-state cells to assess the Li^+ diffusion and redox behaviour. The use of 80 °C as temperature for the measurements allowed a better contact between the LLTeO material and the Li metal electrode and enhance Li^+ mobility.

The full redox stability range of the LLTeO material was analysed by CV measurement of an asymmetric LLTeO cell using Li metal as a reference electrode and plasma deposited gold as a counter-electrode (Fig. 7.18). The CV measurement at 80 °C shows

the ability of the LLTeO material to plate and strip Li, as denoted by the strong oxidation and reduction peaks around 0 V. In the first CV cycle, it is also possible to observe several peaks on the reduction sweep, indicating the possible formation of an interfacial layer. This interfacial layer could resulted from the formation of LiO_2 from unreacted LiOH on the LLTeO surface.[23] Subsequent cycles demonstrate the stabilisation of this interfacial layer with no further reaction of the material. The LLTeO material displays stable cyclability of the material up to $\sim$ 5 V. This is in good agreement with the literature, where Te-containing oxides are known for their good redox stability.[24–28]

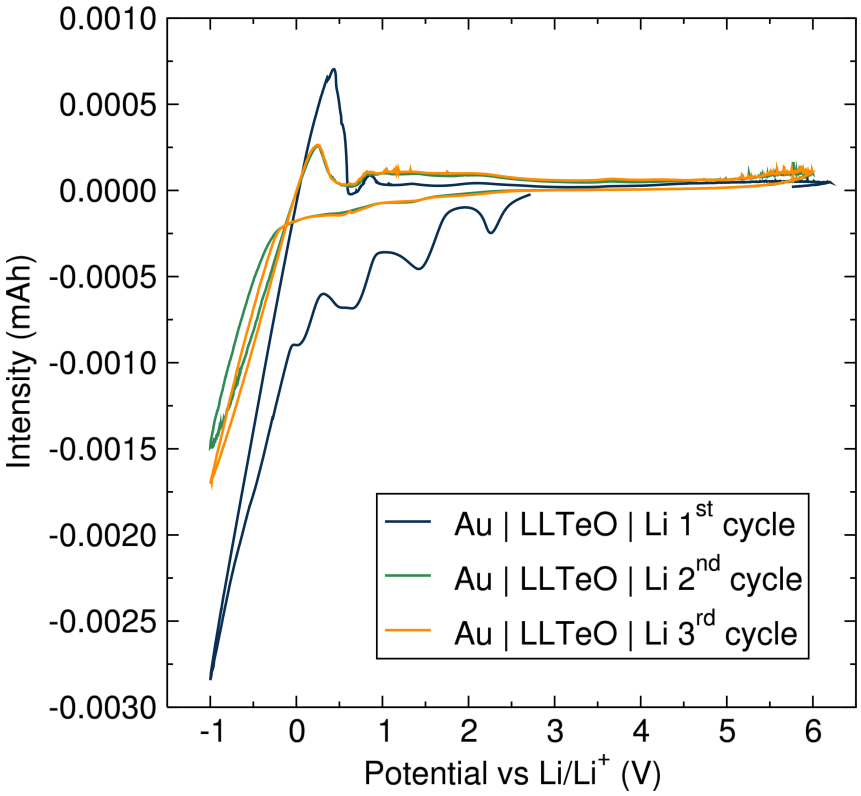

Figure 7.18: CV measurements on an asymmetric Li|$Li_{1.5}La_{1.5}TeO_6$|Au solid-state cell at 80 °C constant temperature.

The good stability against Li metal of the LLTeO material was further confirmed by polarisability tests (Fig. 7.19a), demonstrating the long term cycling stability of the material. The polarisability test shows the good plating/stripping of Li upon several cycles, indicating the good compatibility between the Li metal and the LLTeO material, with the absence of any short-circuit due to dendrite growth from the conditions and time window studied. The voltage response was above 4 V, which is quite large for the low currents applied (<10 μA cm^{-2}). This may be related to the high resistance of the LLTeO material, compared with other solid electrolytes, such as the LLZO garnet where currents up to 0.5 mA cm^2 can be applied with voltage responses below 0.5 V.[29]

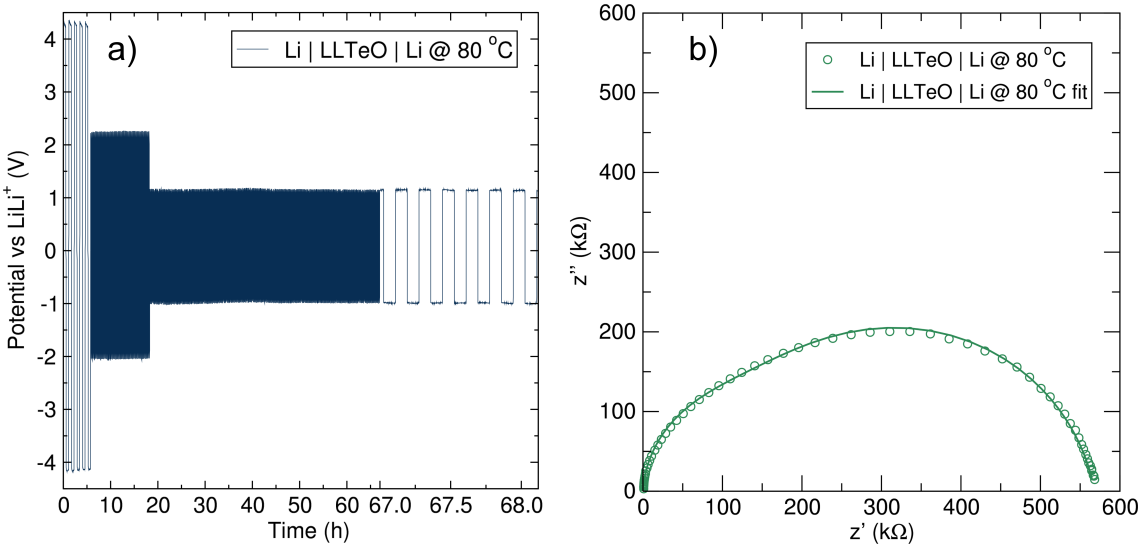

Figure 7.19: (a) Polarisation tests of the Li|$Li_{1.5}La_{1.5}TeO_6$|Li symmetric solid-state cell. The applied current density was 10, 5 and 2.5 μA cm^2 pulses with a duration of 30, 5 and 5 mins at a fixed temperature of 80 °C. (b) EIS measurement on the 1 MHz - 1 Hz frequency range at 80 °C of a Li|$Li_{1.5}La_{1.5}TeO_6$|Li symmetric cell. Experimental data is represented in open circle and the fit to an equivalent electrical circuit composed of R1/Q1 + R2/Q2 is represented by the solid line.

To analyse the resistance of the symmetric cell, EIS of the LLTeO material with Li electrodes was performed at 80 °C (Fig. 7.19b). The Nyquist plot shows that Li^+ conduction is responsible for the ionic transport in the double perovskite as the low frequency tail observed when using blocking Pt electrodes (Fig. 7.20b, next subsection) transforms into a semicircle, indicative of the resistance of Li^+ transport between the LLTeO material surface and the Li-conducting electrodes.

7.2.4 Ionic conductivity studies

In order to analyse the bulk and local ionic conductivity properties of the LLWO anode material and LLTeO solid electrolyte material, EIS and μ^+SR analyses were performed.

The macroscopic ionic conduction was analysed for the LLWO and LLTeO materials by means of EIS. The Nyquist plots of the EIS data at 124 °C are shown in Figure 7.20 where a semircicle due to ionic resistance across the pelletised material and a tail corresponding to the Warburg resistance due to the blocking Pt electrodes are observed. The calculated ionic conductivities from fits to the Nyquist plots to a R/Q circuit and Pouillet's law (Equation 3.1) had values of 1.1×10^{-5} and 5.8×10^{-5} S cm^{-1} at 124 °C respectively for the LLWO and LLTeO materials. The value for the LLWO material is slightly higher than that reported in Rosseinsky's work of $\sim 10^{-6}$ S cm^{-1} at 150 °C,[1] which may be ascribed at the different sintering conditions and synthetic methodology employed which may affect the EIS measurements, as described in the garnet chapters. Compared to similar oxides of alike Li^+ concentrations per formula unit, such as the $Li_3Ln_3Te_2O_{12}$ (Ln = Gd, Er, Tb, Lu) garnets materials with conductivities in the range of 10^{-6} to 10^{-8} S

cm^{-1} at 450 °C,[30] the double perovskites have a better performance which may be due to the presence of Li^+ in two positions while the Li_3 garnets possess Li^+ solely in tetrahedral positions. The conductivities reported for both double perovskite materials here are still far from the $Li_{3x}La_{0.66-x}TiO_3$ perovskite with conductivities in the mS cm^{-1} range at room temperature.[7] This difference may be originated by the different distribution of Li^+ and La^{3+} cations on the A-site. While in the $Li_{3x}La_{0.66-x}TiO_3$ perovskite both cations are ordered in alternative layers facilitating ionic conduction in the Li^+-rich layers, in the double perovskites presented here the cations are disordered on the A-sites, resulting in hampered Li^+ diffusion between A-sites by the presence of immobile neighbouring La^{3+} in adjacent A-sites.

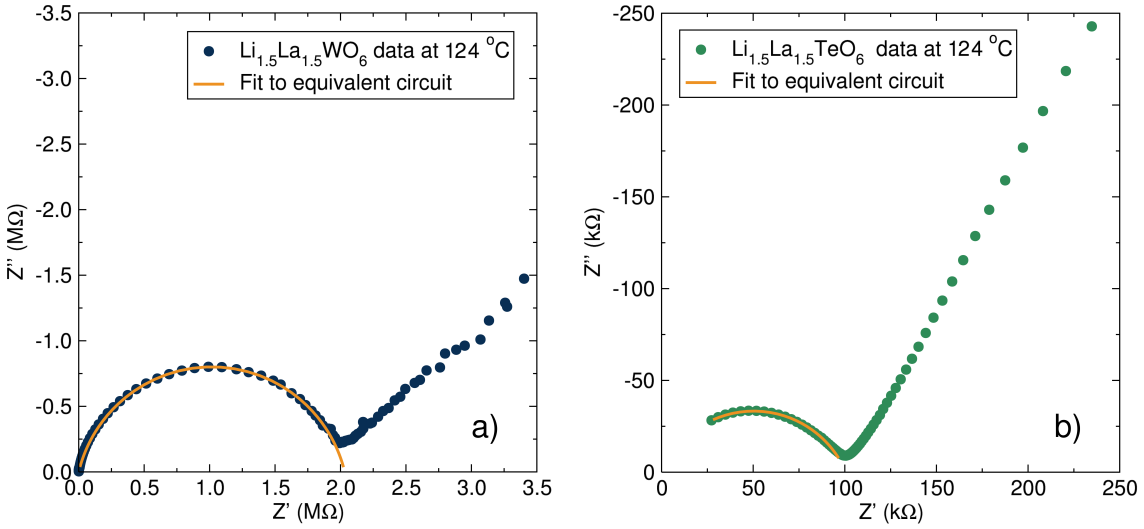

Figure 7.20: Nyquist plot of the impedance data and fit to an equivalent electric circuit of a resistance with a parallel capacitance for the $Li_{1.5}La_{1.5}WO_6$ (a) and $Li_{1.5}La_{1.5}TeO_6$ (b) materials at 124 °C.

Arrhenius plots of the temperature evolution of the ionic conductivity were also carried out in order to evaluate the activation energy for Li^+ conduction (Fig. 7.21). Linear fits to the Arrhenius plots revealed activation energies of 0.59(3) and 0.68(2) eV for the LLWO and LLTeO materials, respectively.

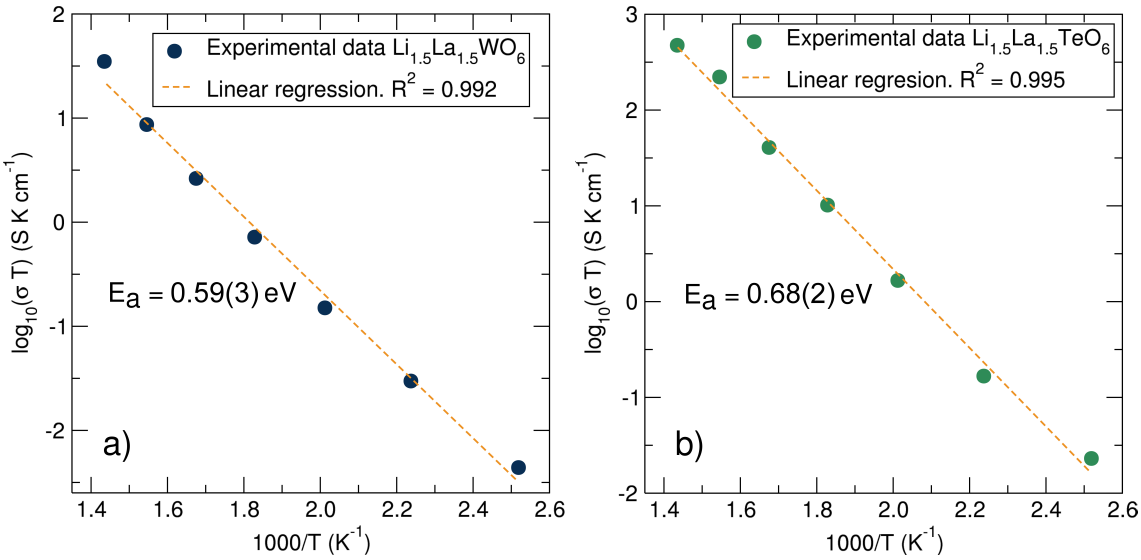

Figure 7.21: Arrhenius plots of the macroscopic ionic transport properties measured by EIS the $Li_{1.5}La_{1.5}WO_6$ (a) and $Li_{1.5}La_{1.5}TeO_6$ (b) compounds.

The activation energy for the LLWO material is very similar (within standard deviation) to that reported by Rosseinsky and co-workers of 0.50(5) eV.[1] Comparing to the $Li_3Ln_3Te_2O_{12}$ garnet materials with activation energies ranging from 0.77 to 1.21 eV,[30] the activations energies found for the LL*M*O double perovskites are lower, which again may be due to the presence of Li^+ in two positions, enabling more lithium pathways for diffusion. In the case of the $Li_{3x}La_{0.66-x}TiO_3$ perovskite which also contains Li^+ on the A-sites, the activation energy goes down to 0.15 eV,[7] indicating again its better performance. The slightly lower macroscopic activation energy for ionic conduction in the LLWO double perovskite is consistent with the larger particle size observed in the SEM measurements which results in smaller grain boundary resistance contributions to the EIS data.

In order to analyse the microscopic Li^+ diffusion in the LLWO and LLTeO materials, μ^+SR analyses were carried out at different temperatures in a similar manner to previous chapters for the garnet materials. Fits of the position decay asymmetry are shown in Figure 7.22. The positron decay asymmetry data follows a moderate decay at short times followed by a slower decay at longer times. This is in good agreement with with the profiles exhibited by the garnet materials with any paramagnetic ions present and with active nuclear spins,[31,32] which in the case of the LL*M*O materials are the ^{139}La, ^{125}Te and ^{183}W and ^{7}Li nuclei.

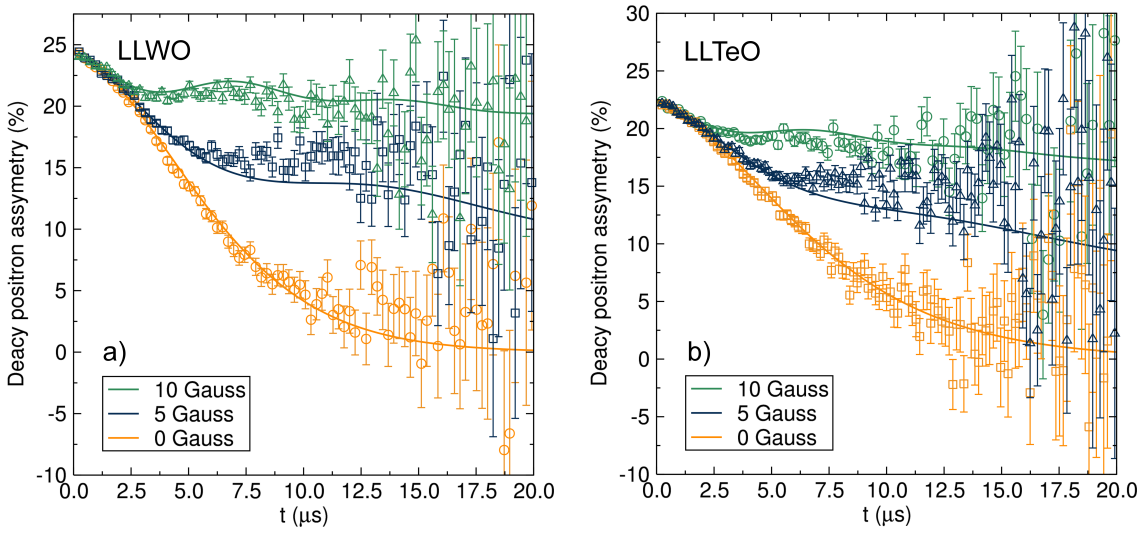

Figure 7.22: Decay positron asymmetry temporal evolution measured from the μ^+SR experiments for the $Li_{1.5}La_{1.5}WO_6$ (a) and $Li_{1.5}La_{1.5}TeO_6$ (b) at room temperature with the fits to the Keren function indicated by a solid line

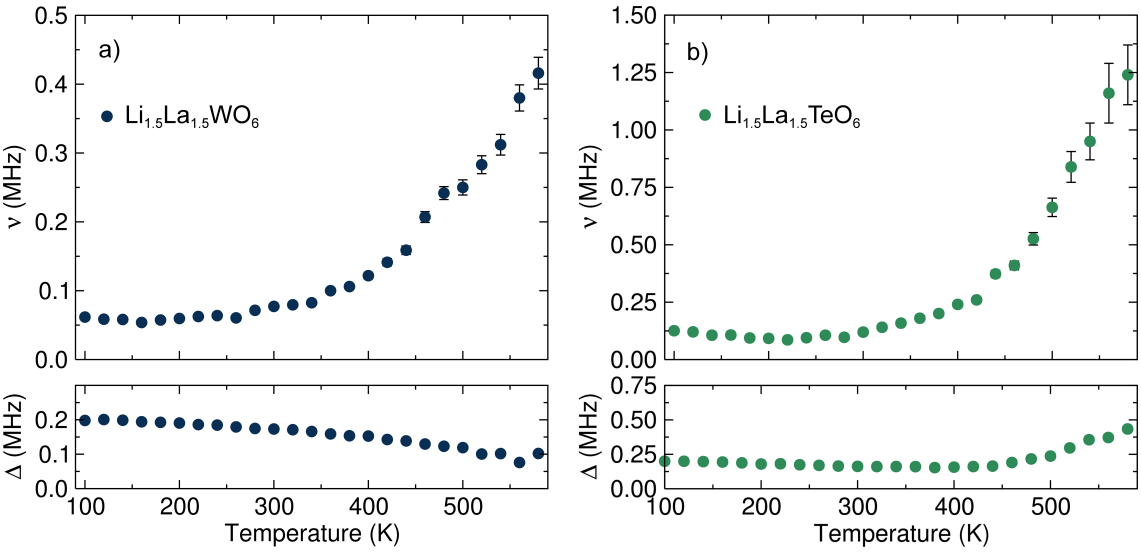

Figure 7.23: Temperature dependence of ν and Δ values obtained for the fits to the Keren function for the $Li_{1.5}La_{1.5}WO_6$ (a) and $Li_{1.5}La_{1.5}TeO_6$ (b) materials measured from 100 K to 600 K.

Fits to the Keren function (Equation 2.9)[33] (Fig. 7.22) allowed calculation of evolution of the ν and Δ parameters at different temperatures, which are shown in Figure 7.23. The muon fluctuation rate, ν, shows a plateau region at low temperatures followed by an exponential increase at higher temperatures due to the thermally activated motion of Li^+. In the case of the Δ , this experiences a smooth decrease from 0.2 to $\sim$ 0.1 MHz for the LLWO material, in a similar manner to the garnet materials, due to the progressive motion of the Li^+ nuclei. In the case of the LLTeO material, the Δ parameter displays a plateau region up to 450 K, when an increase is observed up to $\sim$ 0.4 MHz at high temperatures. The reasons behind this increase are unclear at the moment, but it may be

related to oxygen disorder glimpsed on the NPD data which could results in further oxide sub-lattice rearrangements at higher temperatures[34] which could displace the muon's position within the perovskite frameworks, hence varying the Δ value.

In order to calculate the Li^+ diffusion coefficient (Equation 3.3) for both materials, the structural data obtained from the NPD experiments in conjunction with a model for Li^+ diffusion from the A sites to the two neighbouring B sites and from the B sites to the four neighbouring A sites (Fig. 7.24) were employed. This model is a simplified version of the diffusion model calculated by DFT for the LLWO material by Rosseinsky and co-workers where Li-ions move from A to B sites through an intricate pathway composed by multiple individual hops.[1] The two different Li_A-Li_B distances employed in the calculation were 2.66 and 3.61 Å for the LLWO and 2.95 and 3.38 Å for the LLTeO material.

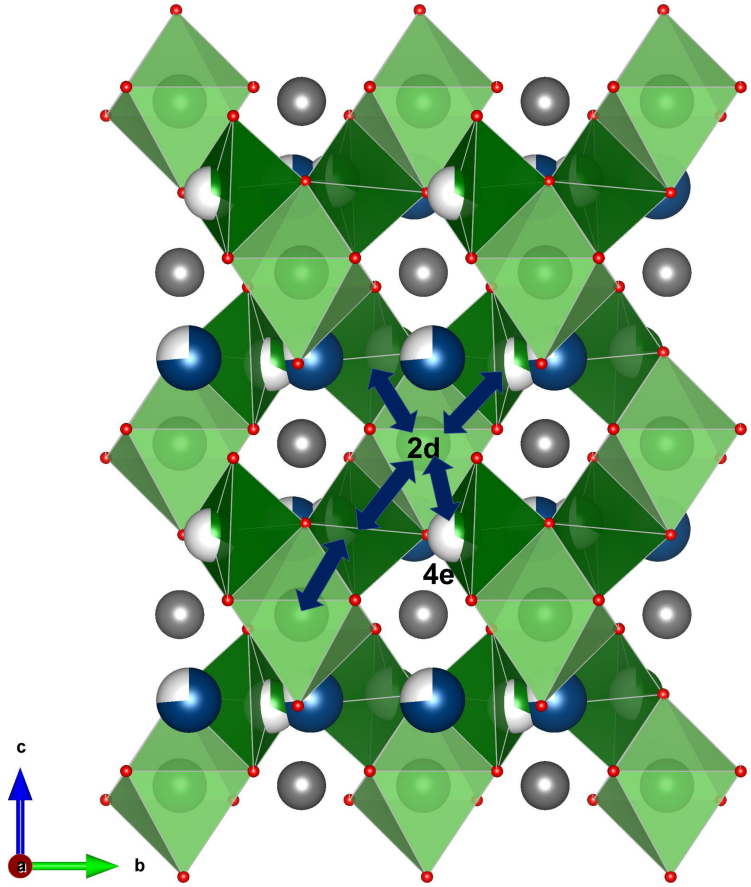

Figure 7.24: Representation of the $Li_{1.5}La_{1.5}WO_6$ crystal structure where the proposed Li_A-Li_B hopping pathways are explicitly displayed by the blue arrows. Li^+ are represented in green and with their coordination environments represented, La^{3+} in blue, W^{6+} in grey and oxygen anions represented in red.

The calculated room temperature Li^+ diffusion coefficients have a value of 6.6×10^{-12} $cm^2\ s^{-1}$ and 1.8×10^{-11} $cm^2\ s^{-1}$ respectively for the LLWO and LLTeO materials. These lithium diffusion coefficients are similar to those found for other fast ion conductors materials in similar μ^+SR measurements such as the above mentioned LLZO garnet material (4.62×10^{-11} $cm^2\ s^{-1}$),[32] the $Li_4Ti_5O_{12}$ anode material (3.2×10^{-11} $cm^2\ s^{-1}$)[35] or the

high energy NMC cathode (3.5×10^{-12} cm^2 s^{-1})[36].

Arrhenius plots of the conductivities are shown in Figure 7.25. The calculated activation energies values obtained from the Arrhenius fits were 0.136(5) eV for the LLWO compound and 0.196(8) eV for LLTeO analogous perovskite. These values are lower than that observed by EIS, likely due to the absence of a grain boundary resistance contribution in these local analyses and/or to the contribution of low energy localised hops which don't contribute to the long range diffusion and hence are virtually "invisible" to activation energy analysis for ionic conductivity calculated from EIS. These differences between microscopic and long-range transport can also be related to the blocking of long range Li^+ diffusion by the La^{3+} ions on the A-sites. These observation suggest that further development on these new class of Li-rich double perovskites could see improvements in conductivities from La^{3+} substitution with a more favourable cation.

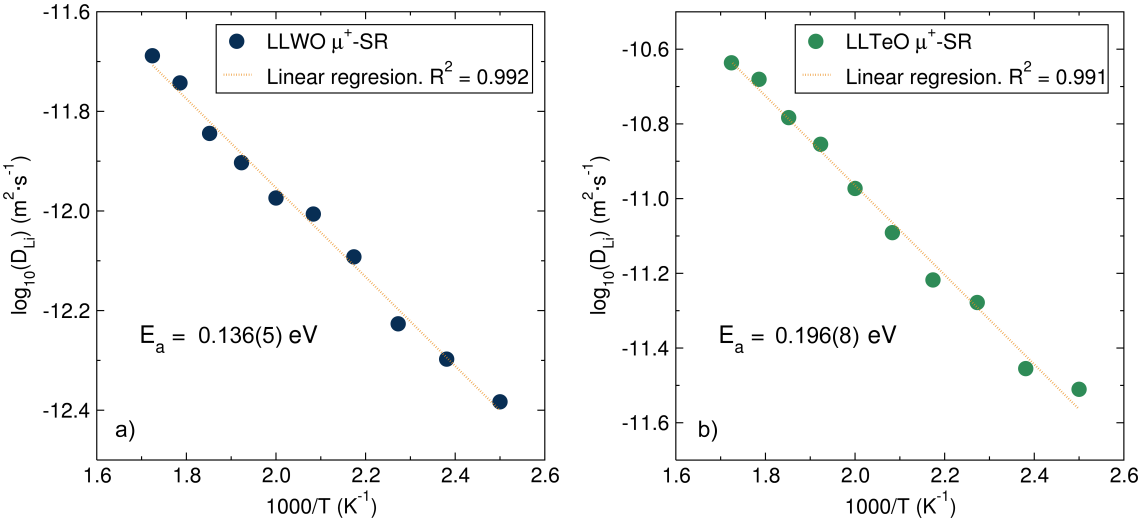

Figure 7.25: Arrhenius plots of the microscopic ionic transport properties measured by μ^+SR the $Li_{1.5}La_{1.5}WO_6$ (a) and $Li_{1.5}La_{1.5}TeO_6$ (b) compounds.

In addition, the DFT calculations and NMR studies on the LLWO compound by Rosseinsky and co-workers revealed individual hoping steps for Li^+ diffusion with energies in the range of 0.1-0.2 eV, which are in good agreement with the microscopic lithium activation energies found in the μ^+SR experiments in this chapter.[1]

7.2.5 Pseudo solid-state half-cell using LLTeO hybrid electrolyte and LLWO electrode materials

Mismatch between electrodes and solid electrolytes and poor interfacial conductivities remain bottlenecks the realisation of all solid-state batteries. Intriguingly, this work has provided an electrode (LLWO) and a solid electrolyte (LLTeO) of the same crystal structure.

To investigate whether this crystal chemistry similarity across battery components can facilitate Li^+ transport, an hybrid electrolyte Li half-cell formed by LLWO:CB:PTFE

composite active material and the hybrid electrolyte formulation LLTeO:LiTFSI:Py_{14}TFSI (80:1:19 $\%_{wt}$) was tested in order to assess the compatibility of both materials (LLTeO and LLWO) and as a proof of concept. The presence of the Py_{14}TFSI ionic liquid allowed a better contact between the LLWO and LLTeO material as well as lowering the resistance of Li^+ diffusion through the LLTeO solid-electrolyte.

CV analyses at 80 ºC (Fig. 7.26a) revealed a redox response of the LLWO material similar to the observed in a conventional liquid cell, arising from the presence of redox active tungsten centres toward the electrochemical electron transfer. The intense reduction peak at $\sim$ 0.63 V could be indicative of the irreversible formation of SEI at the carbon black surface, similar to that on the liquid cell.[11]

Preliminary studies on the galvanostatic cycling of this hybrid electrolyte cell at a 12 mAh g^{-1} rate at 80 ºC (Fig. 7.26b) showed a much lower performance of the system compared to the liquid system, with a small of capacity between 20 to 25 mAh g^{-1} on the 5 cycles tested. This may be due to the higher ionic resistance of the LLTeO material compared to the liquid electrolyte, hampering the lithium insertion on the LLWO side. On the other side, the cycling profile does retain the features observed in the liquid electrolyte cell (pseudo plateaus at similar voltages, see orange box in Fig. 7.26b), indicating the positive insertion of Li^+ into the LLWO material and diffusion through the LLTeO material. These preliminary results suggest a good compatibility between both isostructural electrode and solid electrolyte double perovskites and encourage the further development of this system, looking for example for double perovskites with a redox couple in the high

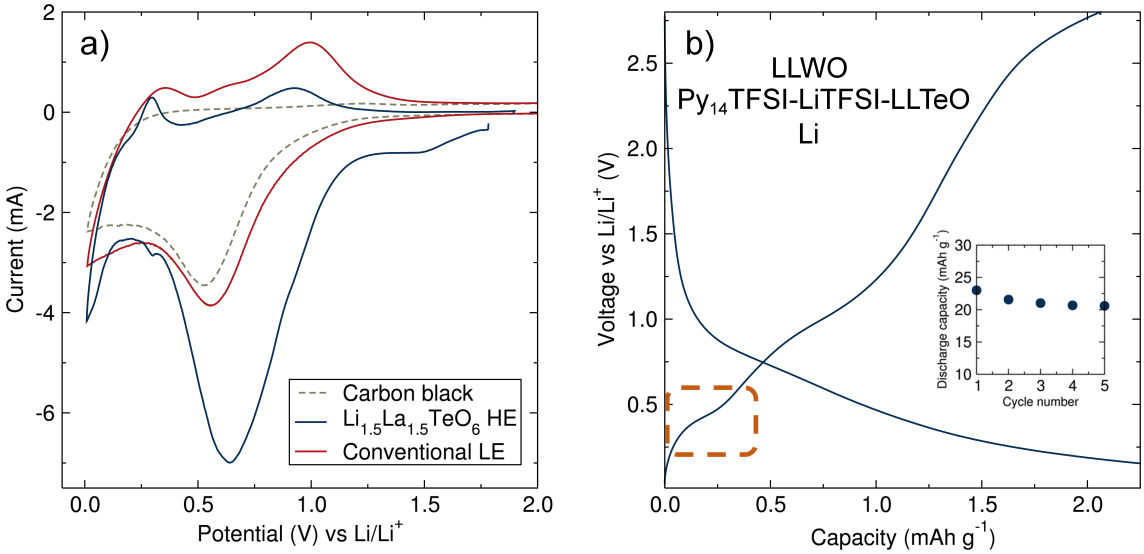

Figure 7.26: (a) CV of a Li half-cell form by $Li_{1.5}La_{1.5}WO_6$:CB:PTFE (90:5:5 $\%_{wt}$) as active material and a $Li_{1.5}La_{1.5}TeO_6$:LiTFSI:Py_{14}TFSI (80:1:19 $\%_{wt}$) hybrid electrolyte was tested against Li metal at 0.05 mV s^{-1} in the voltage range 0.01 V - 1.90 V at 80 ºC. CVs of carbon black and $Li_{1.5}La_{1.5}WO_6$ perovskite materials on conventional liquid electrolyte cells have been included and normalised for clarity. (b) Amplification of the one galvanostatic cycle of the hybrid electrolyte cell at 80 ºC at a rate of 12 mAh g^{-1} and the discharge capacity for the 5 first cycles (inset).

voltage region to persuade an all-solid-state double perovskite Li battery.

7.3 Conclusions

In this chapter, the synthesis and characterisation of a novel family of Li-rich double perovskites $Li_{1.5}La_{1.5}MO_6$ (M = W^{6+}, Te^{6+}) have been presented. The crystal structure of these novel compounds has been resolved by PXRD and NPD diffraction techniques in conjunction with Raman and XAS spectroscopies, revealing a monoclinic $P2_1/n$ symmetry with Li^+ occupying both the B-sites and the vacant A-sites left by the La^{3+}. For the LLTeO material, a disorder on the oxygen positions was also observed by NPD.

Electrochemical testing of the LLMO materials revealed a redox activity of the LLWO material at low voltage upon lithium insertion (<1 V), and good redox stability of the LLTeO material at low and high voltages. The LLWO material was further tested as an anode material by galvanostatic analyses which demonstrated a capacity above 100 mAh g^{-1}. The rate capability of the material on the other side was poor at high cycling rates, which may be due to constrained Li^+ diffusion within the perovskite framework.

The mechanism for Li^+ insertion within the LLWO perovskite framework was studied by PXRD, magnetometry and DFT calculations. From these analyses, it was confirmed that oxidation changes in tungsten are involved in the observed capacity and that intercalation could be the main mechanism without discarding some contribution from conversion processes.

The LLTeO material was further tested as solid-state electrolyte, allowing plating and stripping of Li metal electrodes with a good stability against lithium metal as demonstrated in the polarisation tests.

The ionic diffusion properties of the LLWO and LLTeO materials were investigated by EIS and μ^+SR. The EIS experiments showed ionic conductivities in the order of 10^{-5} S cm^{-1} at 124 °C and modest activation energies of 0.59(3) and 0.68(2) eV. In the case of the μ^+SR experiments, microscopic diffusion coefficients in the order 10^{-11}–10^{-12} cm^2 s^{-1} were calculated, similar to those founds for the garnets electrolytes. Small energy barriers for microscopic lithium diffusion below 0.2 eV were found, indicating that further optimisation to enhance the macroscopic conduction properties of these novel Li-rich double perovskites is possible. Stoichiometry and state-of-the-art micro-structure engineering have allowed the garnet materials to reach extraordinary Li^+ conduction properties with ionic conduction in the mS cm^{-1} range and activation energies as low as 0.2 eV as in the case of the LLZO garnet.[37] It can be foreseen that these novel Li-rich double perovskites could also experience similar development if further research is carried out, for example by trying to increase the Li^+ concentration per formula unit.

To conclude this chapter, preliminary tests on a pseudo solid-state cell composed of Li metal and LLWO as electrodes, and a mixture of LLTeO, LiTFSI and Py_{14}TFSI ionic liquid as hybrid electrolyte, demonstrated the retention of the LLWO redox properties which

may indicate good compatibility between both LLWO and LLTeO isostructural materials.

References

[1] A. B. Santibáñez Mendieta, C. Didier, K. K. Inglis, A. J. Corkett, M. J. Pitcher, M. Zanella, J. F. Shin, L. M. Daniels, A. Rakhmatullin, M. Li, M. S. Dyer, J. B. Claridge, F. Blanc and M. J. Rosseinsky, *Chem. Mater.*, 2016, **28**, 7833–7851.

[2] R. Satish, V. Aravindan, W. C. Ling, J. B. Goodenough and S. Madhavi, *Adv. Energy Mater.*, 2014, **4**, 1301715.

[3] R. D. Shannon, *Acta Crystallogr. A*, 1976, **32**, 751–767.

[4] S. Vasala and M. Karppinen, *Prog. Solid State Chem.*, 2015, **43**, 1 – 36.

[5] V. M. Goldschmidt, *Naturwissenschaften*, 1926, **14**, 477–485.

[6] K. Hayashi, H. Noguchi and M. Ishii, *Mater. Res. Bull.*, 1986, **21**, 401 – 406.

[7] S. Stramare, V. Thangadurai and W. Weppner, *Chem. Mater.*, 2003, **15**, 3974–3990.

[8] A. M. Glazer, *Acta Crystallogr. B*, 1972, **28**, 3384–3392.

[9] R. L. Andrews, A. M. Heyns and P. M. Woodward, *Dalton Trans.*, 2015, **44**, 10700–10707.

[10] A. Dias, G. Subodh, M. T. Sebastian, M. M. Lage and R. L. Moreira, *Chem. Mater.*, 2008, **20**, 4347–4355.

[11] J. Vetter, P. Novák, M. Wagner, C. Veit, K.-C. Möller, J. Besenhard, M. Winter, M. Wohlfahrt-Mehrens, C. Vogler and A. Hammouche, *J. Power Sources*, 2005, **147**, 269 – 281.

[12] K. A. See, M. A. Lumley, G. D. Stucky, C. P. Grey and R. Seshadri, *J. Electrochem. Soc.*, 2017, **164**, A327–A333.

[13] S. Flandrois and B. Simon, *Carbon*, 1999, **37**, 165 – 180.

[14] T.-F. Yi, S.-Y. Yang and Y. Xie, *J. Mater. Chem. A*, 2015, **3**, 5750–5777.

[15] S. Goriparti, E. Miele, F. D. Angelis, E. D. Fabrizio, R. P. Zaccaria and C. Capiglia, *J. Power Sources*, 2014, **257**, 421 – 443.

[16] R. Tripathi, G. Popov, B. L. Ellis, A. Huq and L. F. Nazar, *Energy Environ. Sci.*, 2012, **5**, 6238–6246.

[17] P. Barpanda, M. Ati, B. C. Melot, G. Rousse, J.-N. Chotard, M.-L. Doublet, M. T. Sougrati, S. Corr, J.-C. Jumas and J.-M. Tarascon, *Nat. Mater.*, 2011, **10**, 772.

[18] G. X. Wang, S. Bewlay, S. A. Needham, H. K. Liu, R. S. Liu, V. A. Drozd, J.-F. Lee and J. M. Chen, *J. Electrochem. Soc.*, 2006, **153**, A25–A31.

[19] E. J. Cussen, D. R. Lynham and J. Rogers, *Chem. Mater.*, 2006, **18**, 2855–2866.

[20] A. Grimaud, *Nat. Energy*, 2017, **2**, 17003.

[21] Y.-M. Chiang, *Science*, 2010, **330**, 1485–1486.

[22] J. B. Lee, J. Moon, O. B. Chae, J. G. Lee, J. H. Ryu, M. Cho, K. Cho and S. M. Oh, *Chem. Mater.*, 2016, **28**, 5314–5320.

[23] M. Moshkovich, Y. Gofer and D. Aurbach, *J. Electrochem. Soc.*, 2001, **148**, E155–E167.

[24] A. Gupta, C. B. Mullins and J. B. Goodenough, *J. Power Sources*, 2013, **243**, 817 – 821.

[25] M. Sathiya, K. Ramesha, G. Rousse, D. Foix, D. Gonbeau, K. Guruprakash, A. S. Prakash, M. L. Doublet and J.-M. Tarascon, *Chem. Commun.*, 2013, **49**, 11376–11378.

[26] Z. Yang, Y. Jiang, L. Deng, T. Wang, S. Chen and Y. Huang, *J. Power Sources*, 2017, **360**, 319 – 323.

[27] E. A. Zvereva, V. B. Nalbandyan, M. A. Evstigneeva, H.-J. Koo, M.-H. Whangbo, A. V. Ushakov, B. S. Medvedev, L. I. Medvedeva, N. A. Gridina, G. E. Yalovega, A. V. Churikov, A. N. Vasiliev and B. Büchner, *J. Solid State Chem.*, 2015, **225**, 89 – 96.

[28] Y. Li, Z. Deng, J. Peng, E. Chen, Y. Yu, X. Li, J. Luo, Y. Huang, J. Zhu, C. Fang, Q. Li, J. Han and Y. Huang, *Chem. Eur. J.*, 2018, **24**, 1057–1061.

[29] K. K. Fu, Y. Gong, J. Dai, A. Gong, X. Han, Y. Yao, C. Wang, Y. Wang, Y. Chen, C. Yan, Y. Li, E. D. Wachsman and L. Hu, *Proc. Natl. Acad. Sci. U.S.A*, 2016, **113**, 7094–7099.

[30] E. J. Cussen, T. W. Yip, G. O'Neill and M. P. O'Callaghan, *J. Solid State Chem.*, 2011, **184**, 470 – 475.

[31] H. Nozaki, M. Harada, S. Ohta, I. Watanabe, Y. Miyake, Y. Ikedo, N. H. Jalarvo, E. Mamontov and J. Sugiyama, *Solid State Ionics*, 2014, **262**, 585 – 588.

[32] M. Amores, T. E. Ashton, P. J. Baker, E. J. Cussen and S. A. Corr, *J. Mater. Chem. A*, 2016, **4**, 1729–1736.

[33] A. Keren, *Phys. Rev. B*, 1994, **50**, 10039–10042.

[34] T. Vogt and W. W. Schmahl, *Europhys. Lett.*, 1993, **24**, 281.

[35] J. Sugiyama, H. Nozaki, I. Umegaki, K. Mukai, K. Miwa, S. Shiraki, T. Hitosugi, A. Suter, T. Prokscha, Z. Salman, J. S. Lord and M. Månsson, *Phys. Rev. B*, 2015, **92**, 014417.

[36] M. Månsson, H. Nozaki, J. M. Wikberg, K. Prša, Y. Sassa, M. Dahbi, K. Kamazawa, K. Sedlak, I. Watanabe and J. Sugiyama, *J. Phys. Conf. Ser.*, 2014, **551**, 012037.

[37] V. Thangadurai, S. Narayanan and D. Pinzaru, *Chem. Soc. Rev.*, 2014, **43**, 4714–4727.

Chapter 8: $Na_{1.5}La_{1.5}TeO_6$: Na^+ conduction in a novel Na-rich double perovskite

The primary focus of this thesis has been the synthesis and advanced characterisation of Li-rich complex oxides for their application in Li batteries. This last results chapter, however, will explore a novel $Na_{1.5}La_{1.5}TeO_6$ Na-rich double perovskite as a candidate solid-electrolyte for Na batteries, extending the reach of the work in this thesis beyond-lithium battery chemistry.

Chapter 7 introduced a new family of Li-rich double perovskites, $Li_{1.5}La_{1.5}MO_6$, with applications as electrode and electrolyte materials for Li batteries. The natural research flow was to investigate the possibility of Li^+ replacement by other cations in order to expand the application range of these novel double-perovskites. In this manner, a Na^+ version of the $Li_{1.5}La_{1.5}TeO_6$ solid-state electrolyte, $Na_{1.5}La_{1.5}TeO_6$, was successfully synthesised.

Na batteries represent a cheap alternative to Li batteries, due to lower price of sodium while offering a similar redox couple potential – *ca.* 0.3 V lower for Na/Na^+ compared to Li/Li^+. The larger size and weight of Na^+ promotes the application of Na batteries primarily for medium to large-scale stationary energy storage. The use of solid-state electrolytes in Na batteries could increase the safety and energy density of the battery, provide longer cyclability and enable the use of versatile geometries.[1,2] Thus, the discovery and development of Na^+ solid-state electrolytes is an expanding research area at present.

From the different Na^+ solid-state electrolyte systems already existing, Na^+ conductivity at room temperatures range from values near 10^{-10} S cm^{-1} for the $Na(B/Al)H_4$ complex hydrides to 10^{-3} S cm^{-1} for the most recent Na-containing chalcogenide materials.[1–3] Other systems completing this list include the NASICON phosphate materials, the classic β″-Al_2O_3 and the more recent layered P2-type $Na_2M_2TeO_6$ materials.[1,4] The electrolyte choice needs to fit to the specific application, operating temperature and the electrode materials employed. For example, β″-Al_2O_3 degrades in ambient moisture[5] and presence of the β' phase decreases the conductivity considerably.[6] Na-containing sulphide materials could present superionic conductivities at room temperatures, but they suffer from poor electrochemical stability and reaction with Na metal.[7] Thus, further development of Na^+ solid-state electrolytes is necessary in order to develop new systems that could fulfil the gaps between the present systems.

This chapter presents the synthesis of the $Na_{1.5}La_{1.5}TeO_6$ double perovskite performed by microwave-assisted solid-state chemistry. The crystal structure and stoichiometry of the material was analysed by PXRD, and *in-situ* variable temperature PXRD analyses were carried out to study the temperature stability and phase behaviour of the material. The macroscopic electrochemical properties of this novel Na-rich double perovskite were studied by variable temperature AC EIS and its stability against Na metal was also

tested on a symmetrical cell by analysing the voltage response to constant current measurements. To conclude, the local Na^+ diffusion properties of the material were analysed by μ^+SR measurements and compared to those of the analogous Li-rich double perovskite.

8.1 Synthesis, crystal structure and thermal phase evolution studies

Following the synthesis of the novel $Li_{1.5}La_{1.5}TeO_6$ Li-rich double perovskite solid-electrolyte in the previous Chapter, the Na-rich $Na_{1.5}La_{1.5}TeO_6$ double perovskite was prepared by replacing the Li^+ by Na^+ in both A- and B-sites within the perovskite structure. This was performed easily by replacing the source of Li^+ in the precursor mixture, $LiOH\cdot H_2O$, with NaOH as Na^+ source for the formation of the $Na_{1.5}La_{1.5}TeO_6$ material.

The synthesis was performed following the same heat treatments as for the $Li_{1.5}La_{1.5}MO_6$ materials, *i.e.* 6 hours at 700 ^oC to decompose the precursors followed of two additional heatings at 950 ^oC to form the perovskite structure and 1000 ^oC to obtain phase pure material. The synthesis was carried out in the same hybrid microwave furnace, where the advantageous microwave heating enhanced by the hydroxide and oxides precursors could be exploited.

Inspection of the PXRD of the material after the last heat treatment confirmed that the use of stoichiometric amounts of the starting materials to form $Na_{1.5}La_{1.5}TeO_6$ led to phase pure perovskite structure (Figure 8.1). This was the first indication that the formation of this unusual A-site deficient double perovskite with an alkali-metal, in this case Na^+, in both A and B sites was successfully achieved.

To confirm the synthesised material was indeed a novel Na-rich $Na_{1.5}La_{1.5}TeO_6$ double perovskite, Rietveld refinements of overnight laboratory PXRD data were performed (Fig. 8.1).

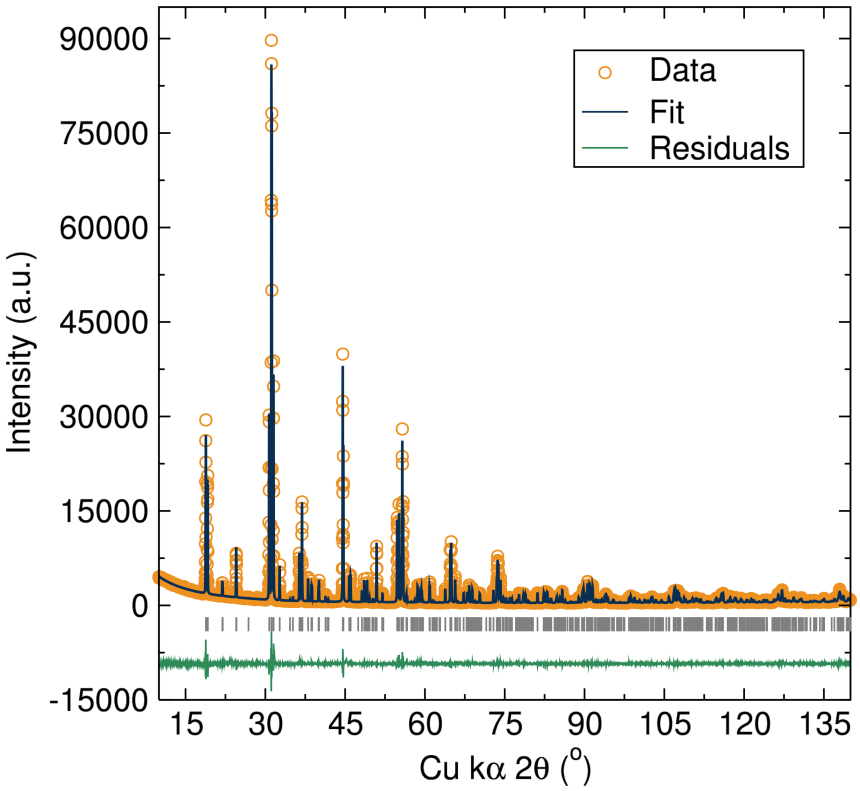

Figure 8.1: Rietveld refinements of XRD data for the $Na_{1.5}La_{1.5}TeO_6$ double perovskite to the the $P2_1/n$ monoclinic space group. Bragg peaks positions for the monoclinic $P2_1/n$ structure are indicated by vertical grey tick marks. Fit in good agreement to monoclinic space group $P2_1/n$, with cell parameters a = 5.69186(2) Å, b= 5.83933(2) Å, c = 8.13119(3) Å, β = 90.186(1)° and V = 270.253(1) Å^3. R_{wp} = 0.0743, R_{exp} = 0.0530 and χ^2 = 7.051.

The refinements confirmed that the synthesised material was a novel monoclinic double perovskite. The PXRD data were successfully refined and ascribed to the $P2_1/n$ space group. Refinement of the sites fraction occupancies (Table 8.1) revealed the presence of ∼ 25% vacancies on the La^{3+} occupying the A-site, mimicking the related Li-rich double perovskites.[8] Na^+ and Te^{6+} cations were placed on the B-sites in a rock salt-type ordered fashion, with the thermal parameters refined leading to reasonable values of 0.16(2) and 2.4(2) 100/A^2 respectively. The remaining 0.5 mol Na^+ was added into the vacant A-sites unoccupied by the La^{3+}. The occupancy fraction of these Na^+ in the A-site was 0.239(2), which falls within the standard deviation in the number of remaining unallocated Na^+ and available vacancies (∼0.25) in the A-site. The stoichiometry from Rietveld refinement was found to be $Na_{1.48(1)}La_{1.534(4)}TeO_6$, which was further confirmed by EDX analyses, where an atomic ratio of $Na_{1.52(8)}La_{1.48(4)}Te_{1.00(4)}$ was found, in good agreement with PXRD and the target stoichiometry.

Table 8.1: Refined parameters of the PXRD data of the $Na_{1.5}La_{1.5}TeO_6$ double perovskite to the $P2_1/n$ monoclinic space group.

Atom	Site	Frac.	x	y	z	Uiso (100/Å^2)
La1	4e	0.767(2)	0.0118(2)	0.9552(1)	0.7486(1)	0.91(2)
Na1	2d	1.00(1)	1/2	0	0	2.4(2)
Na2	4e	0.239(2)	0.0118(2)	0.9552(1)	0.7486(1)	2.4(2)
O1	4e	1	0.279(1)	0.692(1)	0.9559(9)	1.5(2)
O2	4e	1	0.168(1)	0.216(1)	0.9441(9)	1.4(2)
O3	4e	1	0.910(1)	0.534(1)	0.7719(8)	1.3(2)
Te1	2c	1	1/2	0	1/2	0.16(2)

Refinements of the thermal parameters showed that the Na^+ ions displayed the highest values, which indicated the possible mobility of these ions within the perovskite framework. Oxygen anions also showed high thermal parameters which may indicate they could be also mobile at high temperatures, as observed in other double perovskites systems used in fuel cells or Na-O_2 batteries,[9–11] which could broad the potential applicability range of these novel materials to other energy conversion/storage purposes.

The final refined structure is shown in Figure 8.2. The distinct Na_BO_6 and TeO_6 octahedral tilts and rotations due to the discrepancies in ionic size between the A and B cations can be observed. Specifically the calculated tolerance factor has a value of 0.83, which forces the perovskite framework to distort from the ideal cubic structure by a $a^-a^-b^+$ tilting. The calculated Glazer tilt for the Na_B-O-Te was 152.9^o leading to a tilt of 13.9^o, higher than that found for the $Li_{1.5}La_{1.5}TeO_6$ (10.8^o). The higher octahedra tilting in the Na^+ material can be related to the higher octahedral size of Na^+ compared to Li^+ (1.02 vs 0.74 Å)[12]. This results in a higher A-site size for the relatively small La^{3+} cations, inducing further tilting of the B-site octahedra.

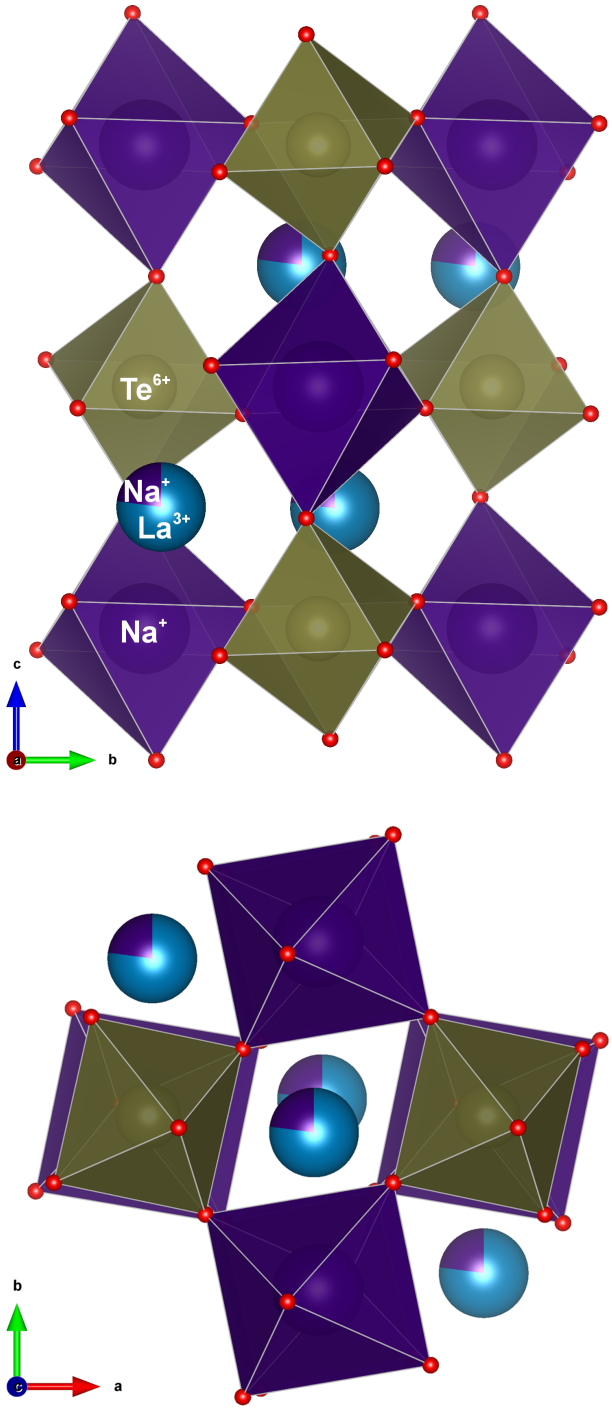

Figure 8.2: Crystallographic representations of the $Na_{1.5}La_{1.5}TeO_6$ structure with monoclinic symmetry $P2_1/n$ where brown spheres in their octahedron represent Te^{6+} ions, blue spheres represent 8-fold coordinated La^{3+} ions, purple spheres are the Na^+ ions, with their octahedral shown for the Na^+ occupying perovskite B positions, and the oxygen anions are represented in red.

It should be noted that the syntheses of the W^{6+} and W^{6+}/Te^{6+} mixed metal solid solutions analogous to the Li^+ system were also attempted (Fig. 8.3). The resulting materials, however, did not form phase pure double perovskite structures.

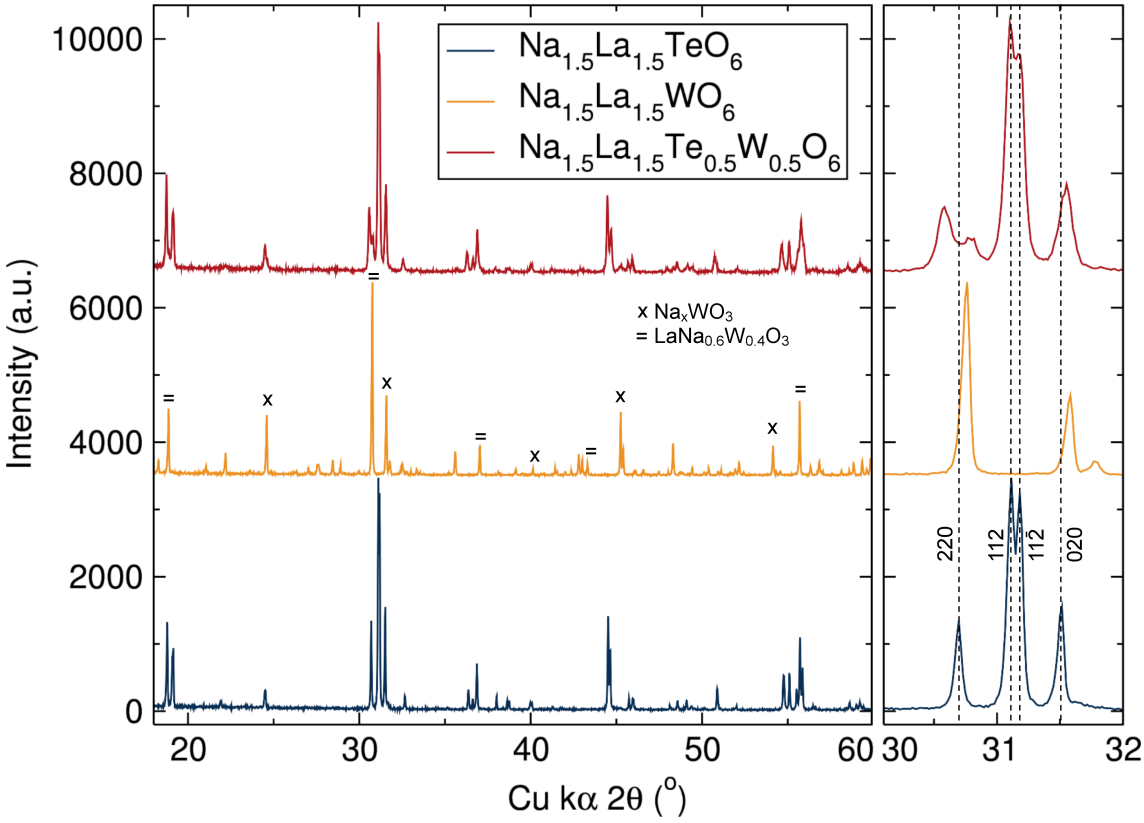

Figure 8.3: PXRD patterns of the parent $Na_{1.5}La_{1.5}TeO_6$ material, and the $Na_{1.5}La_{1.5}WO_6$ and $Na_{1.5}La_{1.5}W_{0.5}Te_{0.5}O_6$ attempted compositions. Inset: amplification of diffraction pattern area where the presence of the secondary $LaNa_{0.6}W_{0.4}O_3$ orthorhombic perovskite impurity in the $Na_{1.5}La_{1.5}W_{0.5}Te_{0.5}O_6$ composition is more evident with the (200), (112), (11$\bar{2}$) and (020) double perovskite Bragg reflections also marked by the dotted lines.

In the case of the $Na_{1.5}La_{1.5}WO_6$ attempted stoichiometry, a mixture of other perovskites appeared, mainly composed of the Na_xWO_3 perovskite and a $LaNa_{0.6}W_{0.4}O_3$ orthorhombic perovskite.[13,14] For the $Na_{1.5}La_{1.5}Te_{0.5}W_{0.5}O_6$ proposed composition, a phase segregation seemed to occur, leading to partial formation of the $Na_{1.5}La_{1.5}TeO_6$ material and the $LaNa_{0.6}W_{0.4}O_3$ perovskite. The reason behind the insolubility of W^{6+} cations on the Na-rich double perovskite system is unclear at the moment, but it could related to a higher thermodynamic stability of the secondary phases. The relative displacement between the (200), (112), (11$\bar{2}$) and (020) Bragg reflections respect to the parent $Na_{1.5}La_{1.5}TeO_6$ compound (inset Fig. 8.3) indicated small structural changes which may be produced as some W^{6+} could be entering the double perovskite structure. The tolerance factor of the $Na_{1.5}La_{1.5}TeO_6$ material, 0.83, is very low with the majority of double perovskites having values above 0.85.[15] Introduction of W^{6+} within the double perovskite framework would decrease the tolerance factor further to 0.82. This tolerance factor could be below the stability limit of the perovskite framework and be a possible explanation of the unsuccessful formation of the $Na_{1.5}La_{1.5}WO_6$ material. Since it was clear that a solid solution of W^{6+} into the $Na_{1.5}La_{1.5}TeO_6$ double perovskite system was not possible to

achieve by the synthetic methodology employed, further structural analyses on this W-doped $Na_{1.5}La_{1.5}TeO_6$ material were discarded. Total Te^{6+}– W^{6+} replacement would be necessary for a plausible applicability of this material as possible anode material with sufficient specific capacity.

A comparison between the lattice parameters of the $Na_{1.5}La_{1.5}TeO_6$ and $Li_{1.5}La_{1.5}TeO_6$ materials is presented in Table 8.2. An expansion of 9.3% in volume of the unit cell is evidenced when replacing the Li^+ by the larger Na^+ ions. This expansion was nearly isotropic with the three parameters expanding between 2% and 4%. In addition, the monoclinic distortion, β angle, is reduced in the case of the Na-containing double perovskite, most likely as a consequence of the closer cationic size between the Na^+ in A- and B-sites with the La^{3+} in the A-sites.

Table 8.2: Unit cell parameters obtained from Rietveld refinements for the Na- and Li-rich $M_{1.5}La_{1.5}TeO_6$ double perovskites and the relative expansion as Li^+ is replaced by Na^+.

	$Na_{1.5}La_{1.5}TeO_6$	$Li_{1.5}La_{1.5}TeO_6$	Expansion (%)
a (Å)	5.69186(2)	5.5738(2)	2.1
b (Å)	5.83934(2)	5.6120(2)	4.0
c (Å)	8.13121(3)	7.9046(3)	2.9
Volume (Å^3)	270.253(1)	247.24(1)	9.3
β(º)	90.1859(3)	90.562(2)	-

In order to further analyse the crystal structure of this new $Na_{1.5}La_{1.5}TeO_6$ double perovskite, Raman measurements were carried out to analyse the local framework features (Fig. 8.4).

The Raman spectrum of the $Na_{1.5}La_{1.5}TeO_6$ double perovskite presents bands that could be assigned to a monoclinic $P2_1/n$ space group with an irreducible representation $\Gamma = \nu_1(A_g + B_g) + \nu_2(2A_g + 2B_g) + \nu_5(3A_g + 3B_g) + T(3A_g + 3B_g) + L(3A_g + 3B_g)$ for the Raman active modes, as introduced in Chapter 7. Vibrational modes (ν) are related to internal M-O stretching and bending modes, the translational modes (T) arise from translations of the A cations and the librational modes (L) are due to the asymmetric MO_6 octahedral rotation. Translational modes appear at low Raman shift, around 100 to 200 cm^{-1} close to the elastic peak and the librational modes appear at higher Raman shift between 200 and 400 cm^{-1}. The vibrational mode ν_1 represents the most intense peak of the spectra at *ca.* 710 cm^{-1} for the Na-rich double perovskite and at a higher Raman shift of *c.a.* 723 cm^{-1} for the Li^+ analogue. This difference in Raman shift is due to the shorter Te-O bond in the Li-double perovskite ($\sim$ 1.90 Å), which increases as the volume of the unit cell expands with the introduction of Na^+ ($\sim$ 1.96 Å). No other peaks above the plotted region were observed, indicating the absence of carbonate or hydroxide moieties that could arise from secondary phases, typically invisible to laboratory PXRD.

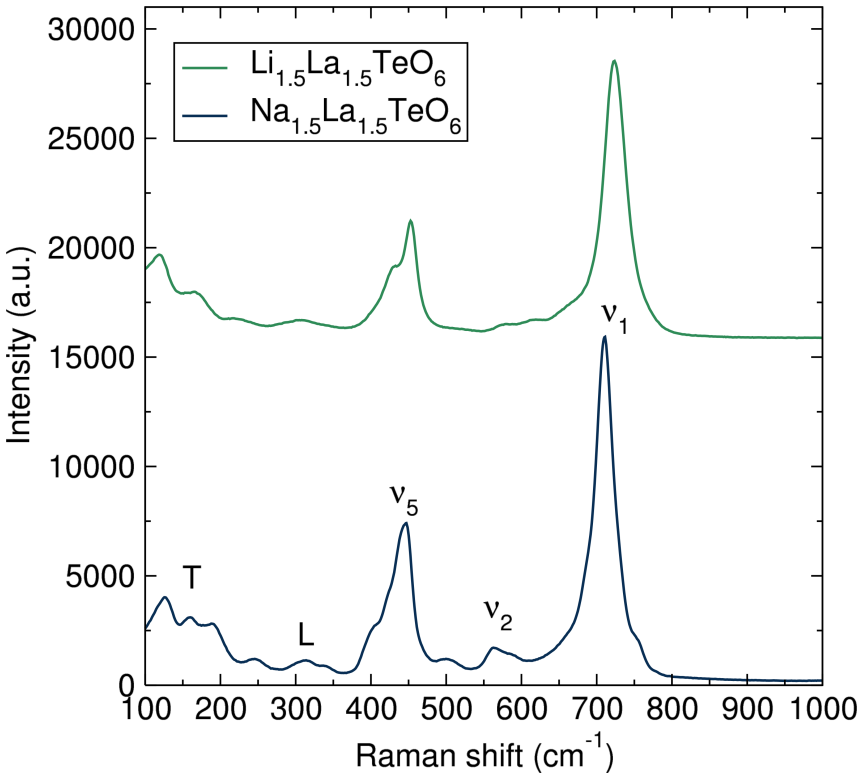

Figure 8.4: Raman spectra of the Na- and Li-rich $M_{1.5}La_{1.5}TeO_6$ double perovskites under excitation of an Argon-ion laser with a wavelength λ = 532 nm.

In order to study the phase stability of the $Na_{1.5}La_{1.5}TeO_6$ material for high temperature applications, *in-situ* variable temperature PXRD measurements were performed. Figure 8.5 shows the PXRDs of the $Na_{1.5}La_{1.5}TeO_6$ material collected at different temperatures (a) and three different zoomed areas where specific Bragg reflections evolution (b, c and d) can be followed. In plot (a) the temperature stability of the Na-rich double perovskite material is observed, where there were no growth of any additional secondary phases indicating the stability of the material post-synthesis up to 800^{o}C. The anisotropic expansion of the cell can be identified by the displacements of the (200) and (020) reflections, in plot (b). The merging of the (220) reflection with the (004) (plot c) and the (22$\bar{4}$) with the (224) Bragg reflection above 500 ^{o}C (plot d) indicates an increase in the crystal symmetry of the double-perovskite material at high temperatures.

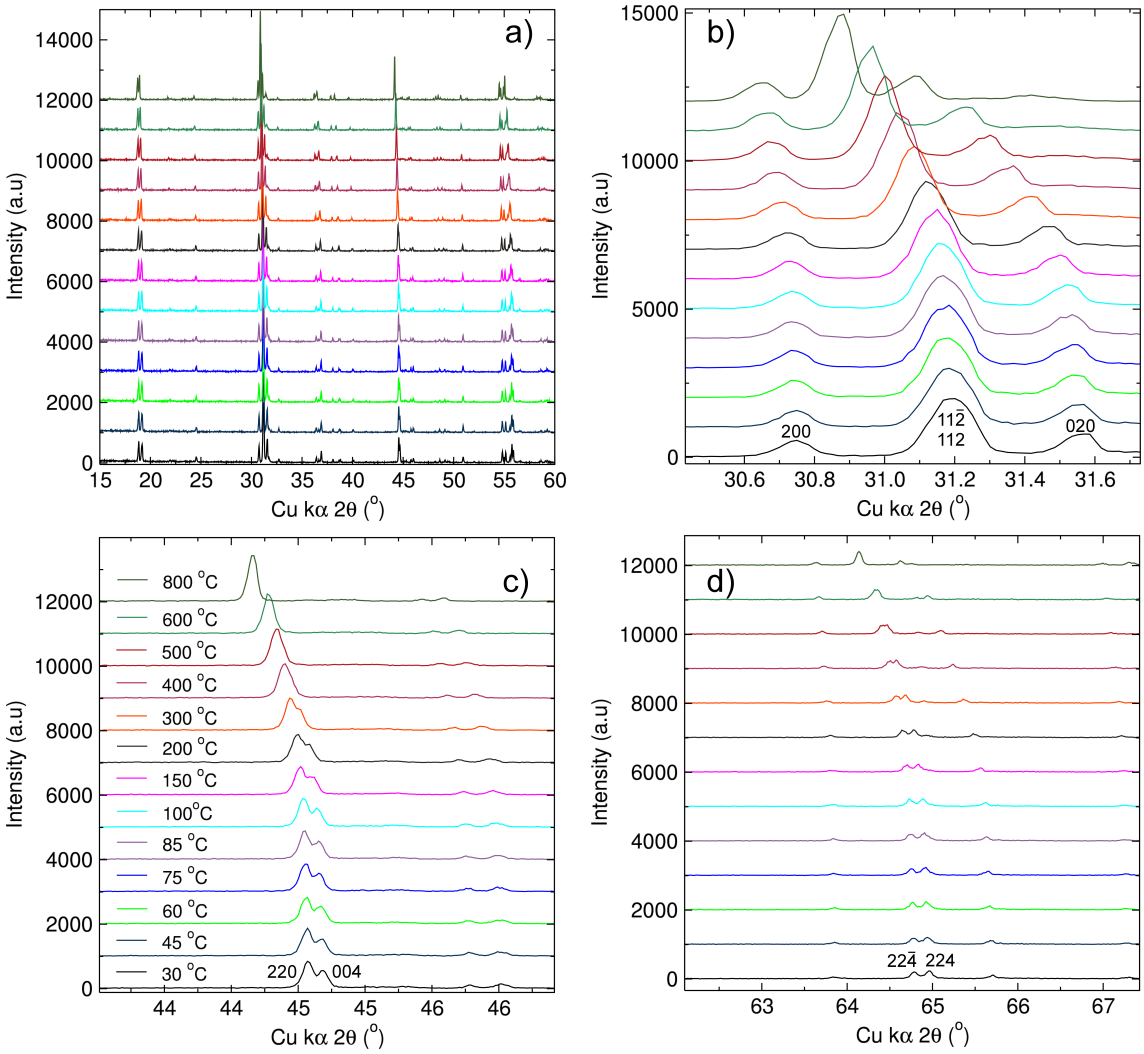

Figure 8.5: *In-situ* PXRD data acquired for the $Na_{1.5}La_{1.5}TeO_6$ at different temperatures (a) and different amplifications of certain 2θ ranges for a clearer vision of Bragg reflections displacements and mergers upon heating (b,c and d).

Refinements of the cell parameters at 30, 200, 400, 600 and 800 ºC allows quantification of the unit cell expansion and monoclinic distortion of the $Na_{1.5}La_{1.5}TeO_6$ material upon heating (Fig. 8.6). Cell parameter changes and anisotropic expansion were followed up to 800 ºC (Fig. 8.6b), with the a and c parameters experiencing expansions above 1% and the b parameter experiencing expansion <0.5%. The total volume expansion reached the 3% at 800 ºC. In the case of the monoclinic distortion, this is observed to reduce close to an orthogonal value, indicating a possible transformation to a higher crystal symmetry, most likely to an orthorhombic space group.

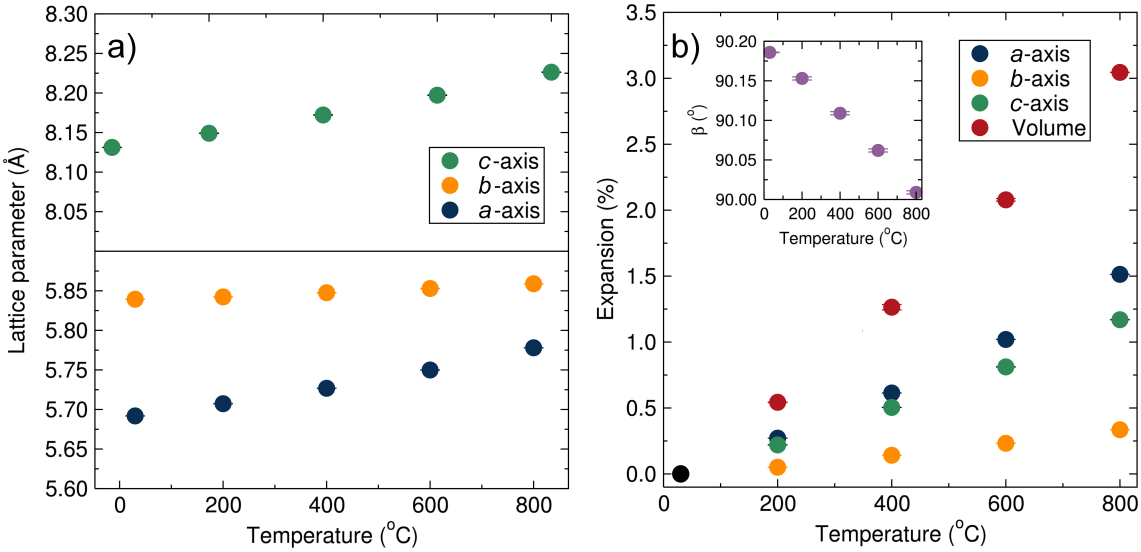

Figure 8.6: Lattice parameters expansions and β monoclinic distortion (inset) evolution of the cell parameters for the $Na_{1.5}La_{1.5}TeO_6$ material as calculated from refinements of the PXRD data at different temperatures.

The trends observed for the cell parameters (Fig. 8.6a) anticipate a further transformation to a tetragonal symmetry as the *a* and *b* cell parameters could merge upon further heating. Specifically, from the thermal expansion coefficient of the *a* and *b* axes [$a(T) = 1.1 \times 10^{-4}T + 5.6857$ Å and $b(T) = 2.6 \times 10^{-5}T + 5.8378$ Å], the transition temperature to a tetragonal phase was calculated to be 1783 °C. This indicated that if the thermal expansion of the *a* and *b* parameters would continue linearly above 800 °C and the material was stable, the *a* and *b* parameters would merge, driving a transformation of the perovskite symmetry to tetragonal. This is based on the assumption that the β angle remains orthogonal. Otherwise, the change would be likely to produce a monoclinic *C*2/*m* phase if the β angle would continue decreasing. Similar transitions have been observed for the $La_{0.33}TaO_3$ perovskites with transitions from monoclinic to tetragonal symmetry occurring at elevated temperatures,[16,17] or the second predicted scenario with transitions from monoclinic to a different monoclinic space group.[18]

The microstructure of the material was analysed by SEM (Fig. 8.7). The mortar-ground powdered material formed micro-size agglomerates >10 µm of $Na_{1.5}La_{1.5}TeO_6$ particles. The $Na_{1.5}La_{1.5}TeO_6$ isolated particles had sizes ranging from 1 to 5 µm approximately, with irregular, faceted morphologies.

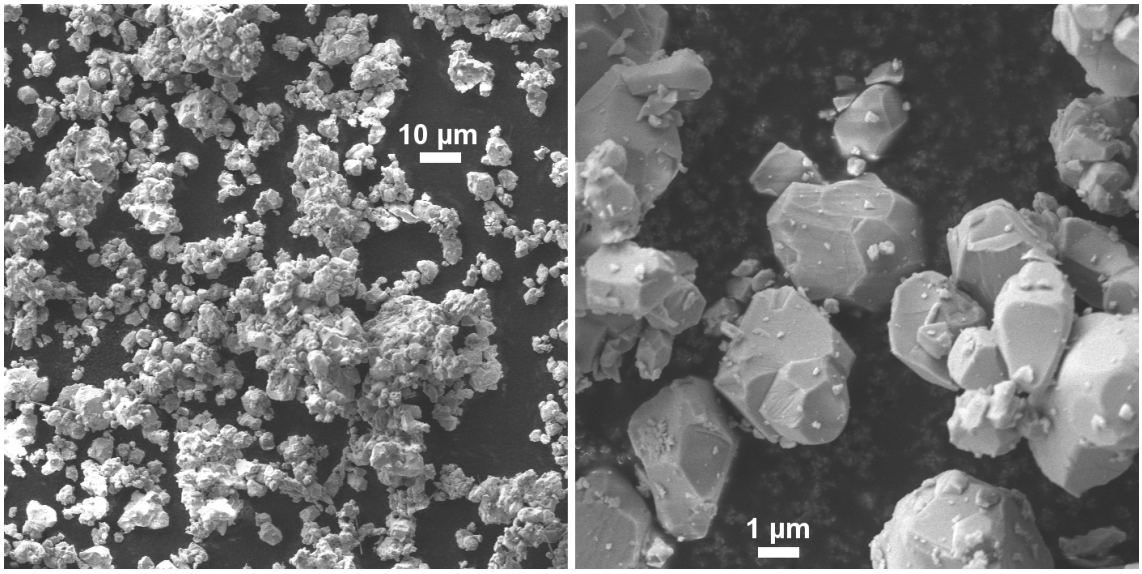

Figure 8.7: High resolution SEM images of the $Na_{1.5}La_{1.5}TeO_6$ Na-rich double perovskite material at two different magnifications.

8.2 Macroscopic electrochemical properties

The presence of Na^+ ions in both A- and B-sites suggested the possibility of Na^+ conductivity in this novel Na-rich double perovskite, similarly as its Li^+ sister. In order to study the ionic conductivity of the $Na_{1.5}La_{1.5}TeO_6$ material, AC EIS measurements were carried out. The Nyquist plots of the impedance data at different temperatures for the $Na_{1.5}La_{1.5}TeO_6$ material are shown in Figure 8.8a. Two main components are observed in the Nyquist plots. The first consists of a semicircle at high frequencies, due to the resistance towards ionic diffusion, and a second contribution is apparent as a linear tail at low frequencies resulting from the sodium-blocking gold electrodes used for the measurements.[19] The presence of the low frequencies tail confirmed the predominantly ionic-conduction contribution to the impedance of the material. In order to obtain the resistance from the EIS data, the Nyquist plots were fitted to an equivalent circuit composed of an electrical resistance with a parallel constant phase element and a Warburg resistance.

The room temperature ionic conductivity of the sample was calculated (Table 8.3) by means of Pouillet's law (Equation 3.1) and found to be 5.39×10^{-8} S cm^{-1}. This value is approximately one order of magnitude lower than that obtained for the $Li_{1.5}La_{1.5}TeO_6$ material (9.28×10^{-7} S cm^{-1}). This difference may be ascribed to the higher mass and cationic radius of the Na^+ ions, slightly hindering its long range conduction through the $Na_{1.5}La_{1.5}TeO_6$ material. Since the ionic conductivity extracted from the EIS measurements has contributions from the pellet microstructure and set-up employed, a certain explanation for this difference is difficult to draw from isolated EIS analyses. Attempts to reproduce the same set up and temperature range used for the $Li_{1.5}La_{1.5}TeO_6$ were unsuccessful due to the odd behaviour of the $Na_{1.5}La_{1.5}TeO_6$ material when using Pt

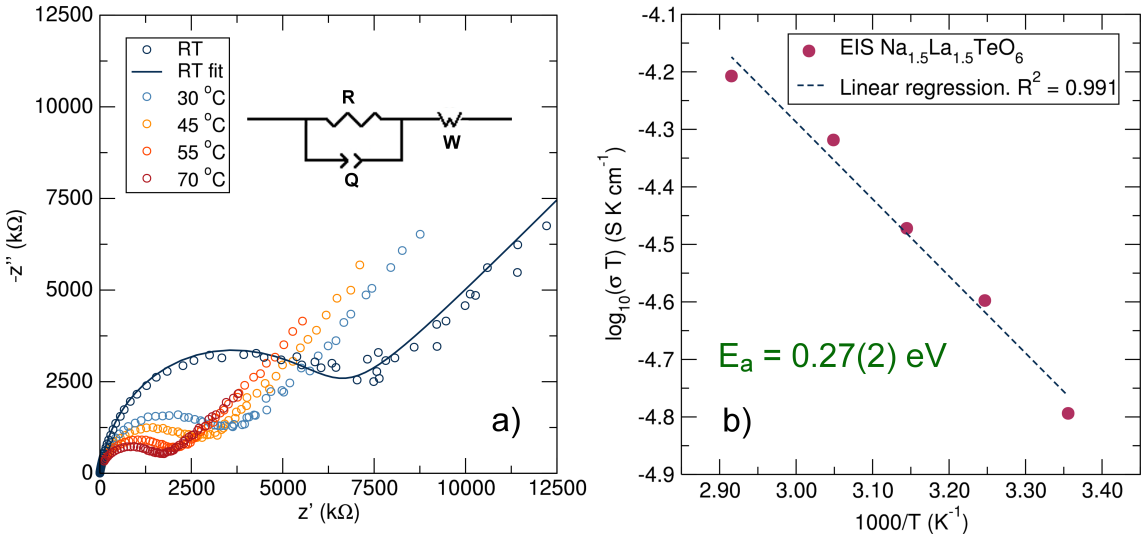

Figure 8.8: (a) Nyquist plot of the EIS data for the $Na_{1.5}La_{1.5}TeO_6$ material double perovskite at different temperatures and a representative fit to the equivalent electrical circuit. (b) Arrhenius plot of the ionic conductivity for the $Na_{1.5}La_{1.5}TeO_6$ material. The calculated activation energy is 0.27(2) eV.

electrodes in air, where a decrease in the conductivity with increasing temperature were observed. Further studies to investigate possible reaction with different atmospheres will be performed soon after completion of this thesis to investigate this observed phenomenon.

Table 8.3: Ionic conductivity values obtained from AC EIS measurements at different temperatures for the $Na_{1.5}La_{1.5}TeO_6$ double perovskite material.

Temperature (K)	Total conductivity (S cm^{-1})
298	5.2×10^{-8}
308	8.2×10^{-8}
318	1.1×10^{-7}
328	1.5×10^{-7}
343	1.8×10^{-7}

Comparing with current benchmark sodium electrolytes, the conductivity value obtained for this $Na_{1.5}La_{1.5}TeO_6$ double perovskite material is up to five orders of magnitude lower.[1,2] However, the improvement that other sodium ionic conductors systems have experienced gives a ray of light that further improvements are also possible for the $Na_{1.5}La_{1.5}TeO_6$ material. For example, in the case of the phosphate NASICON materials, early 2000 reports showed room temperature conductivities of *ca.* 10^{-8} S cm^{-1} which have increased up to 10^{-3} S cm^{-1} in recent years by different stoichiometry and structure tailoring strategies.[20–24] In the case of the P2-type $Na_2M_2TeO_6$ tellurate oxide materials, the original work reported conductivities of 10^{-6} S cm^{-1} which have been optimised to

reach also the mS cm^{-1} range.[4,25] In addition, the use of polymer-inorganic composites to form hybrid materials has also been employed with the NASICON materials in order to increase their macroscopic conductivity for use in final batteries.[26,27]

The activation energy required for ionic conduction in the material was calculated from an Arrhenius plot of the obtained ionic conduction values, resulting in 0.27(2) eV (Fig. 8.8). This value is significantly lower compared to that obtained for the $Li_{1.5}La_{1.5}TeO_6$ material of 0.68(2) eV. This lower energetic requirement for the ionic diffusion found in the $Na_{1.5}La_{1.5}TeO_6$ material could be related to the high relative density of the sintered material which results in lower inter-grain energy requirement for Na^+ to diffusion between sintered particles. As it has been explained in previous chapters, the microstructure of the material has dramatic effects on the macroscopic conduction properties of the materials, as measured by AC EIS. The relative density of the sintered $Na_{1.5}La_{1.5}TeO_6$ pellet was near 97% of the theoretical density, which could decrease the contribution from inter-grain resistance. A photograph showing the increased densification of the $Na_{1.5}La_{1.5}TeO_6$ material compared to the Li^+ analogue is presented in Figure 8.9 where a clear reduction in the pellet diameter is observed for the Na^+ material.

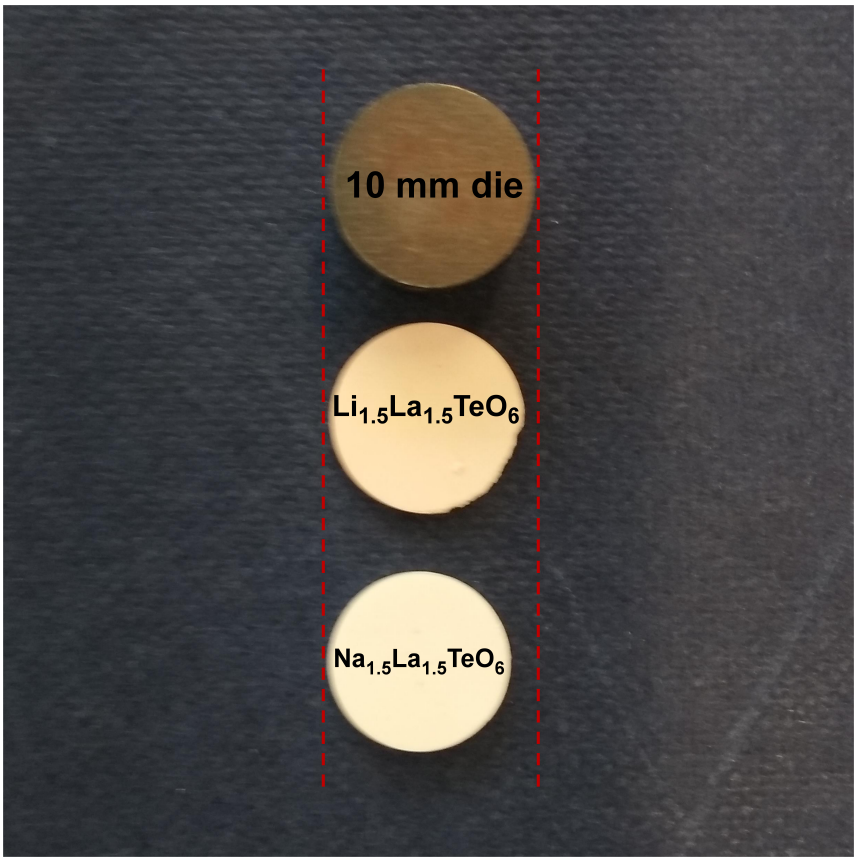

Figure 8.9: Photograph of the as-sintering pellets of for the Li-rich and Na-rich $M_{1.5}La_{1.5}TeO_6$ double perovskites. A 10 mm pellet die used to form the green body for sintering is added as a reference. A clear shrinkage from the 10 mm diameter is observed for the Na-containing double perovskite.

The macroscopic activation energy found for this novel Na-rich double perovskite is similar to current benchmark systems with low activation energy values from EIS measurements approaching the 0.2 eV barrier,[1,2,28] as in the case of the Na_3PSe_4 material displaying an activation energy of 0.21 eV.[29]

As the material showed it could conduct sodium through its double perovskite framework, the following step was to study the electrochemical stability against sodium metal. Figure 8.10a shows the plot of a constant current experiment, in which a constant current was applied to a symmetric cell of the $Na_{1.5}La_{1.5}TeO_6$ material sandwiched between two sodium metal electrodes at 80 °C. This temperature was selected to enhance the conductivity of the material, increase the contact between the double perovskite material and the sodium metal electrodes, and unveil any possible side reaction between the materials.

The response to two applied small constant currents of ± 2 and ± 5 nA cm^{-2}, was a high voltage polarisation up to 10 V, when the experiment was then terminated for safety reasons. This behaviour differs completely from that observed for the $Li_{1.5}La_{1.5}TeO_6$ material with Li metal electrodes, where a robust constant voltage response over time was found.

In addition, an increase in the voltage response to constant current of the $Na_{1.5}La_{1.5}TeO_6$ material over time was observed. This may be due to an increase on the resistance in the cell, likely to be caused from reaction at the interface of the double perovskite with the more reactive sodium metal, compared to lithium at that temperature, which did not stabilise over time or cycling.[30–32] Similar reactivity between Na metal and solid electrolytes has been observed in the Na_3PS_4 system where protection with β-Al_2O_3

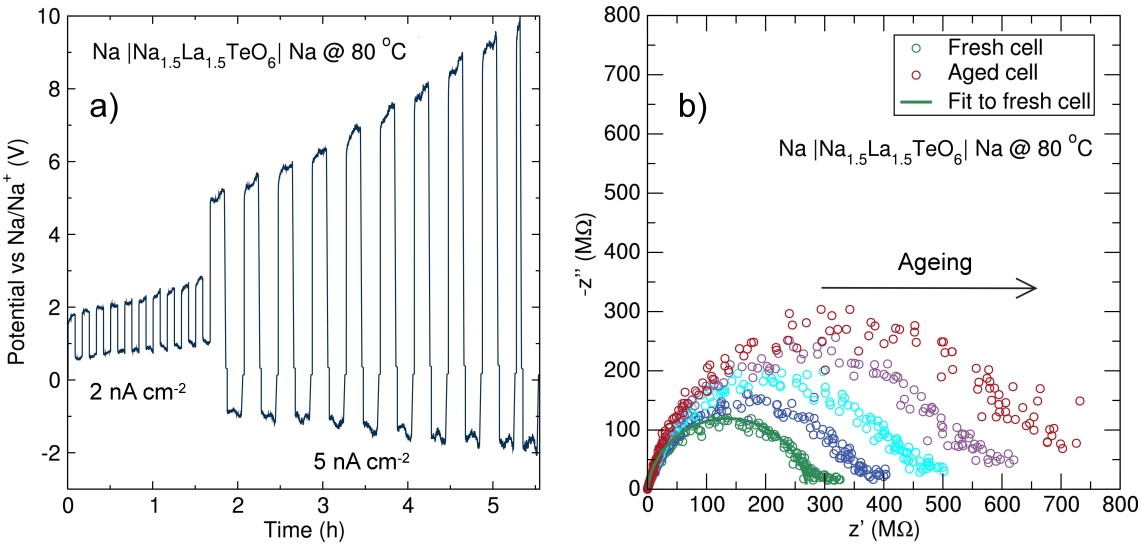

Figure 8.10: (a) Constant current voltage response tests of the symmetric $Na_{1.5}La_{1.5}TeO_6$ cell with sodium metal electrodes. The applied current density was 2 nA cm^{-2} and 5 nA cm^{-2} at a fixed temperature of 80 °C. (b) Nyquist plots of the EIS data for the symmetric $Na_{1.5}La_{1.5}TeO_6$ cell at 80 °C over time. Experimental data is represented in open circle and the fit to an R/Q equivalent electrical circuit is represented by the solid line.

was used mitigate it,[33] the superionic conductor $Na_{10.8}Sn_{1.9}PS_{11.8}$,[7] and more in general in Na-containing sulfide materials.[34]

Figure 8.10b shows the Nyquist plots of AC EIS measurements on this symmetric cell at 80 ^oC, confirming the increase in the cell resistance over time. These Nyquist plots of the symmetric cell revealed the lack of a linear tail due Warburg resistance, confirming the ionic character of the conductivity in the $Na_{1.5}La_{1.5}TeO_6$ material, most likely to be ascribed to Na^+ conduction at these low temperatures. The ionic conductivity obtained from fit to the Nyquist plot had a value of 1.1×10^{-9} S cm^{-1}, clearly decreased from intrinsic value of the $Na_{1.5}La_{1.5}TeO_6$, which may due to the presence of extra resistance at the sodium metal inter-phase.

These findings indicate further processing is necessary in order to apply this $Na_{1.5}La_{1.5}TeO_6$ perovskite as a solid-electrolyte in Na-metal batteries at this temperature. The use of protecting layers[1,33,35] have proven to mitigate these reactions, so it is reasonable to conclude that similar approaches and knowledge transfer from state-of-art protection in Li-metal anodes could decrease these reactions observed in this $Na_{1.5}La_{1.5}TeO_6$ Na-rich double perovskite material.[36–38]

8.3 Local Na^+ conduction studies by μ^+SR

In order to analyse the local Na^+ diffusion properties, μ^+SR measurements were performed at the EMU instrument at the ISIS Neutron and Muon Source. Similarly as in the case of lithium battery materials, the use of μ^+SR as a local probe to study Na^+ diffusion in battery materials has growth in parallel with the increasing interest in Na-batteries by the energy storage research community. The natural abundance of 1/2 spin ^{23}Na isotope is 100%, making Na^+ an ideal candidate to be studied by μ^+SR.

The temporal evolution of the decay positron asymmetry for the $Na_{1.5}La_{1.5}TeO_6$ material at three different longitudinal magnetic fields is shown in Figure 8.11. At short times the decay positron asymmetry followed a moderate decay, while at longer times the asymmetry decrease followed a slower trend, as expected for this Na-rich double perovskite with no paramagnetic ions in its structure and active nuclear spins (^{23}Na, ^{139}La and ^{125}Te) that can interact with the muon's spin.

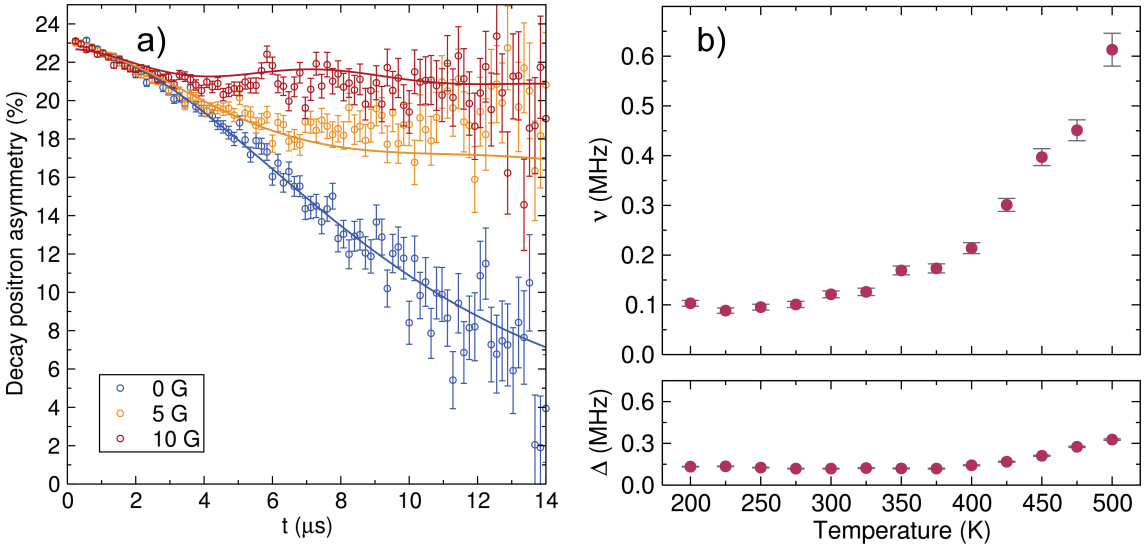

Figure 8.11: (a) μ^+SR raw data collected at room temperature at zero field and applied longitudinal magnetic fields of 5 G and 10 G, fits (solid lines) using the Keren function for the $Na_{1.5}La_{1.5}TeO_6$ double perovskite. (b) Temperature dependence of ν and Δ values obtained for the fits to the Keren function for the $Na_{1.5}La_{1.5}TeO_6$ material measured from 200 K to 500 K.

The decay positron asymmetry data for the $Na_{1.5}La_{1.5}TeO_6$ material were then fit to the Keren function (Equation 2.9) for each temperature at three longitudinal applied magnetic fields (0, 5 and 10 G) parallel to the initial muon spin polarisation and are shown in Figure 8.11a. The calculated ν and Δ values from these fits are plotted in Figure 8.11b as a function of temperature.

The temperature evolution of the muon's spin fluctuation rate (ν) follows a plateau from 200 K to $\sim$ 300 K, experiencing an exponential increase above these temperatures. This is indicative of the thermally activated diffusion of the Na^+ ions in the double perovskite structure above this temperature (*ca.* 300 K). Similar thermal activation temperatures around room temperature have been found in other Na-containing systems such as the layered $Na_{0.5}CoO_2$.[39] In the case of the field width distribution (Δ), the parameter tends to a constant value of 0.15 MHz at low to medium temperatures, with a small increase towards $\sim$ 0.3 MHz at high temperatures. This slightly increase of the Δ parameter near 500 K could be related to possible small structural rearrangements, as suggested in the previous section such as oxygen displacements near the muon implanting positions.[40] This behaviour matches the analogous $Li_{1.5}La_{1.5}TeO_6$ material where oxygen disorder was detected from NPD analyses. The value for this Δ parameter is similar to the obtained for the $Li_{1.5}La_{1.5}MO_6$ ($\sim$ 0.2 MHz) material as both materials share a very similar crystal framework. The most important fact to note is the absence of a drastic decrease in Δ, which would have indicated muon self-diffusion in the material.

Since a detailed model of the Na^+ diffusion pathways for this novel Na-rich double perovskite is still not available, a simplified model similar to the one used in Chapter 7 for the $Li_{1.5}La_{1.5}MO_6$ materials, and based on the calculations reported by Rosseinsky

and co-workers for the $Li_{1.5}La_{1.5}WO_6$ perovskite,[8] was employed. The model is shown in Figure 8.12 where Na^+ diffuses from the A sites to the two neighbouring B sites and from the B sites to the four neighbouring A sites. Additionally, a conservative 0.01 vacancy fraction in the Na positions was introduced in both A and B sites to allow diffusion. From this preliminary model, and introducing the two different Na_A-Na_B distances of 3.33 and 3.46 Å, a Na^+ diffusion coefficient at room temperature of 4.2×10^{-12} cm^2 s^{-1} was obtained from Equation 3.3. This value is slightly lower than that observed in the Li-containing double perovskite analogue 1.8×10^{-11} cm^2 s^{-1} which may be ascribed again to the higher mass and cationic size of Na^+. This diffusion coefficient is similar to the one reported for the Na_xCoO_2 layered cathode material, indicating the possibility of good compatibility in terms of Na^+ diffusion between both materials.[41–43]

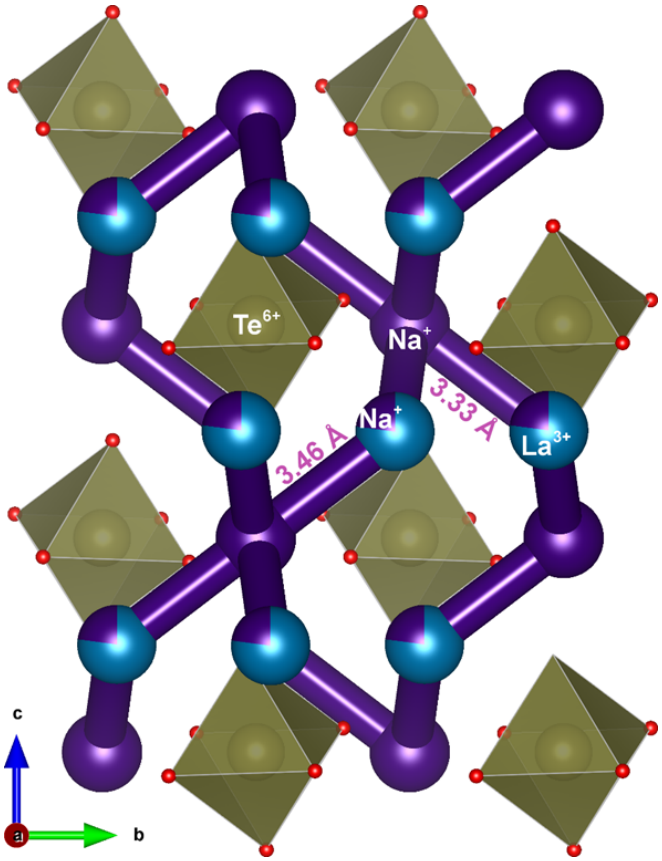

Figure 8.12: Representation of the $Na_{1.5}La_{1.5}TeO_6$ crystal structure where the proposed Na_A-Na_B hopping pathways are explicitly displayed in purple. Na^+ ions are represented in purple, La^{3+} in blue and Te^{6+} in brown with their coordination octahedron displayed also in brown with oxygen anions represented in red.

The microscopic diffusion of the $Na_{1.5}La_{1.5}TeO_6$ material is in line with other Na^+ ionic conductors such as the $Na_xWO_2Cl_2$ tungsten bronze with a Na^+ diffusion coefficient of 10^{-13} cm^2 s^{-1},[44] or the Na_3PS_4 material with a value in the 10^{-12} cm^2 s^{-1}.[45]

The activation energy required for Na^+ diffusion was then calculated from an Arrhenius plot of the Na^+ diffusion coefficients (Figure 8.13) and was found to be 0.163(9) eV. This

value is similar to the 0.196(8) eV found for the Li^+ analogue double perovskite, with a small decrease. Despite the heavy and higher size properties of sodium ions, the larger cell volume of the Na^+ system could enable reduction in the energetic requirement for sodium to diffusion from one position to the other. Similar decreases when replacing Li^+ by Na^+ has been observed in β-Al_2O_3 [46,47] and $Na_{10}GeP_2S_{12}$ sulfide materials.[28]

This low activation energy is similar to related oxide materials, such as the Ga-doped $Na_2Zn_2TeO_6$ with an activation energy of 0.12eV as obtained from NMR measurements,[25] or β'-alumina single crystals with activations energies in the 0.12 - 0.16 eV range.[48]

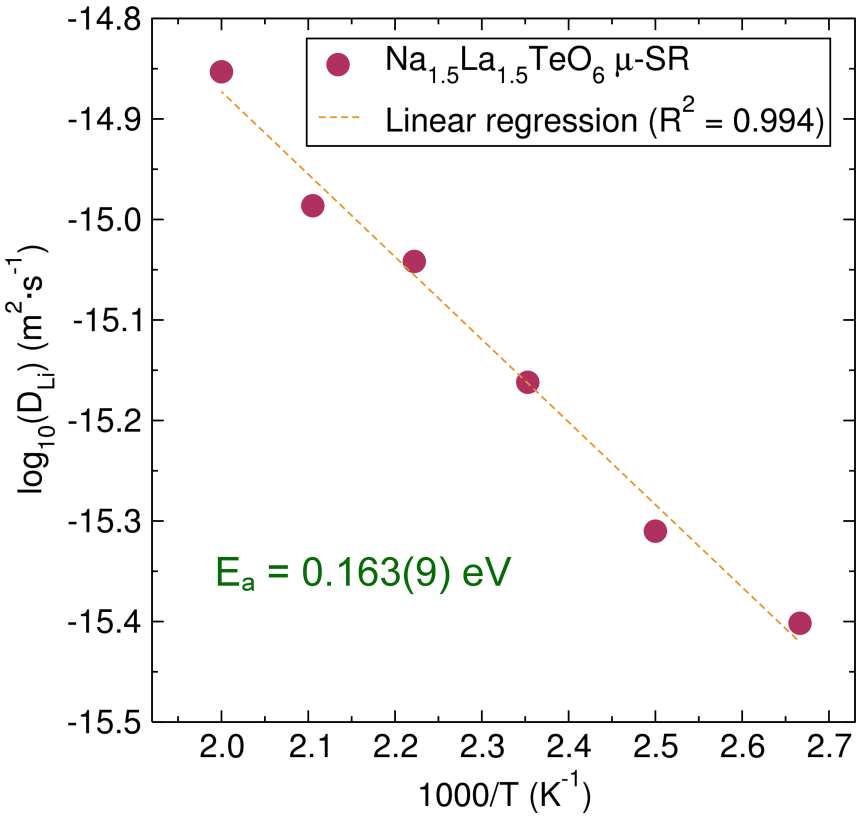

Figure 8.13: Arrhenius plot of the diffusion coefficient calculated from μ^+SR for the $Na_{1.5}La_{1.5}TeO_6$ Na-rich double perovskite. The calculated activation energy is 0.163(9) eV.

In addition, the difference in activation energy between μ^+SR and EIS values, $\sim$ 0.1 eV, is considerably smaller than the observed for the Li-containing garnet and double perovskites studied in previous chapters, >0.3 eV. This small difference between the macroscopic (EIS) and local (μ^+SR) probes could have its origin in the better sintering observed for this Na-system, which reduce the grain boundary contribution to the energy requirement for macroscopic conduction.

These promising microscopic transport properties displayed by this new Na-rich double perovskite indicates that if further improvement to the macroscopic conductivity is performed to match the microscopic diffusion properties, this $Na_{1.5}La_{1.5}TeO_6$ material could be a good candidate as a solid electrolyte for the next generation of Na batteries.

8.4 Conclusions

In this chapter, the synthesis of a new Na-rich double perovskite, $Na_{1.5}La_{1.5}TeO_6$, has been prepared by microwave-assisted solid-state chemistry. The crystal structure and stoichiometry were analysed by PXRD and EDX data, confirming the formation of the P21/n double perovskite with the $Na_{1.5}La_{1.5}TeO_6$ target stoichiometry. The temperature behaviour of the material upon heating has been studied by *in-situ* variable temperature PXRD measurements, where the material retained the perovskite structure up to 800 ^oC, with an increase in the crystal symmetry to an almost orthorhombic symmetry at the highest temperature.

The macroscopic conductivity of the material was analysed by AC EIS measurements which revealed ionic conductivity at room temperature on the order of 10^{-8} S cm^{-1} with a low activation energy of 0.27(2) eV. Impedance measurements and constant current experiments at 80 ^oC of a Na metal symmetric cell of the Na-rich double perovskite revealed increasing resistance over time as a consequence of reaction between the $Na_{1.5}La_{1.5}TeO_6$ material and Na metal at that temperature.

μ^+SR measurements were carried out in order to study the local Na^+ diffusion properties of the $Na_{1.5}La_{1.5}TeO_6$ material. These analyses showed a diffusion coefficient for microscopic diffusion of Na^+ at room temperature in the order of 10^{-12} cm^2 s^{-1}, similar to other solid electrolytes, and a very low activation energy of 0.163(9) eV indicating promising potential transport properties for this material if further developments are performed to optimise the macroscopic transport to its full potential.

References

[1] J.-J. Kim, K. Yoon, I. Park and K. Kang, *Small Methods*, 2017, **1**, 1700219.

[2] H. Che, S. Chen, Y. Xie, H. Wang, K. Amine, X.-Z. Liao and Z.-F. Ma, *Energy Environ. Sci.*, 2017, **10**, 1075–1101.

[3] K. B. Hueso, M. Armand and T. Rojo, *Energy Environ. Sci.*, 2013, **6**, 734–749.

[4] M. A. Evstigneeva, V. B. Nalbandyan, A. A. Petrenko, B. S. Medvedev and A. A. Kataev, *Chem. Mater.*, 2011, **23**, 1174–1181.

[5] F. G. Will, *J. Electrochem. Soc.*, 1976, **123**, 834–836.

[6] S.-T. Lee, D.-H. Lee, S.-M. Lee, S.-S. Han, S.-H. Lee and S.-K. Lim, *B. Mater. Sci.*, 2016, **39**, 729–735.

[7] Z. Yu, S.-L. Shang, Y. Gao, D. Wang, X. Li, Z.-K. Liu and D. Wang, *Nano Energy*, 2018, **47**, 325–330.

[8] A. B. Santibáñez Mendieta, C. Didier, K. K. Inglis, A. J. Corkett, M. J. Pitcher, M. Zanella, J. F. Shin, L. M. Daniels, A. Rakhmatullin, M. Li, M. S. Dyer, J. B. Claridge, F. Blanc and M. J. Rosseinsky, *Chem. Mater.*, 2016, **28**, 7833–7851.

[9] Y.-H. Huang, R. I. Dass, Z.-L. Xing and J. B. Goodenough, *Science*, 2006, **312**, 254–257.

[10] Y. Zhu, Z.-G. Chen, W. Zhou, S. Jiang, J. Zou and Z. Shao, *ChemSusChem*, 2013, **6**, 2249–2254.

[11] N. Bonanos, K. Knight and B. Ellis, *Solid State Ionics*, 1995, **79**, 161 – 170.

[12] R. Shannon, *Acta Crystallogr.*, 1976, **A32**, 751–767.

[13] I. Alvarez, J. Martinez, M. Veiga and C. Pico, *J. Solid State Chem.*, 1996, **125**, 47 – 53.

[14] C. N. W. Darlington, J. A. Hriljac and K. S. Knight, *Acta Crystallogr. B*, 2003, **59**, 584–587.

[15] S. Vasala and M. Karppinen, *Prog. Solid State Ch.*, 2015, **43**, 1 – 36.

[16] Q. Zhou, P. J. Saines, N. Sharma, J. Ting, B. J. Kennedy, Z. Zhang, R. L. Withers and K. S. Wallwork, *Chem. Mater.*, 2008, **20**, 6666–6676.

[17] A. N. Salak, O. Prokhnenko and V. M. Ferreira, *J. Phys.: Condens. Matter*, 2008, **20**, 085210.

[18] Q. Zhou, B. J. Kennedy, C. J. Howard, M. M. Elcombe and A. J. Studer, *Chem. Mater.*, 2005, **17**, 5357–5365.

[19] J. T. S. Irvine, D. C. Sinclair and A. R. West, *Adv. Mater.*, 1990, **2**, 132–138.

[20] F. E. Mouahid, M. Bettach, M. Zahir, P. Maldonado-Manso, S. Bruque, E. R. Losilla and M. A. G. Aranda, *J. Mater. Chem.*, 2000, **10**, 2748–2757.

[21] N. Anantharamulu, K. Koteswara Rao, G. Rambabu, B. Vijaya Kumar, V. Radha and M. Vithal, *J. Mater. Sci.*, 2011, **46**, 2821–2837.

[22] H. Park, K. Jung, M. Nezafati, C.-S. Kim and B. Kang, *ACS Appl. Mater. Interfaces*, 2016, **8**, 27814–27824.

[23] S. Song, H. M. Duong, A. M. Korsunsky, N. Hu and L. Lu, *Sci. Rep.*, 2016, **6**, 32330.

[24] P. Colomban, *Solid State Ionics*, 1986, **21**, 97 – 115.

[25] Y. Li, Z. Deng, J. Peng, E. Chen, Y. Yu, X. Li, J. Luo, Y. Huang, J. Zhu, C. Fang, Q. Li, J. Han and Y. Huang, *Chem. Eur. J.*, 2018, **24**, 1057–1061.

[26] J.-K. Kim, Y. J. Lim, H. Kim, G.-B. Cho and Y. Kim, *Energy Environ. Sci.*, 2015, **8**, 3589–3596.

[27] Z. Zhang, Q. Zhang, C. Ren, F. Luo, Q. Ma, Y.-S. Hu, Z. Zhou, H. Li, X. Huang and L. Chen, *J. Mater. Chem. A*, 2016, **4**, 15823–15828.

[28] V. S. Kandagal, M. D. Bharadwaj and U. V. Waghmare, *J. Mater. Chem. A*, 2015, **3**, 12992–12999.

[29] L. Zhang, K. Yang, J. Mi, L. Lu, L. Zhao, L. Wang, Y. Li and H. Zeng, *Adv. Energy Mater.*, 2015, **5**, 1501294.

[30] D. I. Iermakova, R. Dugas, M. R. Palacín and A. Ponrouch, *J. Electrochem. Soc.*, 2015, **162**, A7060–A7066.

[31] X. Bi, X. Ren, Z. Huang, M. Yu, E. Kreidler and Y. Wu, *Chem. Commun.*, 2015, **51**, 7665–7668.

[32] P. M. Bayley, N. M. Trease and C. P. Grey, *J. Am. Chem. Soc.*, 2016, **138**, 1955–1961.

[33] S. Wenzel, T. Leichtweiss, D. A. Weber, J. Sann, W. G. Zeier and J. Janek, *ACS Appl. Mater. Interfaces*, 2016, **8**, 28216–28224.

[34] Y. Tian, T. Shi, W. D. Richards, J. Li, J. C. Kim, S.-H. Bo and G. Ceder, *Energy Environ. Sci.*, 2017, **10**, 1150–1166.

[35] D. Zhang, B. Li, S. Wang and S. Yang, *ACS Appl. Mater. Interfaces*, 2017, **9**, 40265–40272.

[36] Y. Liu and Y. Cui, *Joule*, 2017, **1**, 649 – 650.

[37] C. Yang, K. Fu, Y. Zhang, E. Hitz and L. Hu, *Adv. Mater.*, 2017, **29**, 1701169.

[38] X.-B. Cheng, R. Zhang, C.-Z. Zhao and Q. Zhang, *Chem. Rev.*, 2017, **117**, 10403–10473.

[39] M. Weller, A. Sacchetti, H. R. Ott, K. Mattenberger and B. Batlogg, *Phys. Rev. Lett.*, 2009, **102**, 056401.

[40] R. C. Williams, F. Xiao, I. O. Thomas, S. J. Clark, T. Lancaster, G. A. Cornish, S. J. Blundell, W. Hayes, A. K. Paul, C. Felser and M. Jansen, *J. Phys.: Condens. Matter*, 2016, **28**, 076001.

[41] A. Mendiboure, C. Delmas and P. Hagenmuller, *J. Solid State Chem.*, 1985, **57**, 323 – 331.

[42] A. Bhide and K. Hariharan, *Solid State Ionics*, 2011, **192**, 360 – 363.

[43] M. Månsson and J. Sugiyama, *Phys. Scr.*, 2013, **88**, 068509.

[44] P. G. Bruce, J. Nowiński and V. C. Gibson, *Solid State Ionics*, 1992, **50**, 41 – 45.

[45] Z. Zhu, I.-H. Chu, Z. Deng and S. P. Ong, *Chem. Mater.*, 2015, **27**, 8318–8325.

[46] J. Kummer, *Prog. Solid State Ch.*, 1972, **7**, 141 – 175.

[47] S. C. Jung, H.-J. Kim, J. W. Choi and Y.-K. Han, *Nano Lett.*, 2014, **14**, 6559–6563.

[48] Z. Yang, J. Zhang, M. C. W. Kintner-Meyer, X. Lu, D. Choi, J. P. Lemmon and J. Liu, *Chem. Rev.*, 2011, **111**, 3577–3613.

Chapter 9: Conclusions and further work

9.1 Summary of conclusions

In this thesis, a number of Li-rich complex oxides materials have been prepared by a microwave-assisted solid-state synthetic route and their properties explored by a range of diffraction, spectroscopic, electrochemical and synchrotron-based techniques.

The Zn^{2+}, Ga^{3+}, and Al^{3+} aliovalent doping in LBLTO garnet material has been demonstrated by PXRD where a lattice parameter decrease has been observed due to the smaller size of the dopants compared to Li^{+}. The dopant position within the garnet structure has been studied by XANES suggesting that Zn could be residing mainly in the tetrahedral sites while Ga could be distributed between the tetrahedral and octahedral Li^{+} sites. The transport properties of the material have been probed by EIS and μ^{+}SR techniques, where it has been found that only in the case of low concentrations of Al^{3+} enhancement in the macroscopic transport properties of the LBLTO material can be observed, demonstrating that the macrostructure and stoichiometry could be further optimised.

By introducing microwave radiation during the synthesis of the Al- and Ga-doped LLZO garnet it was possible to stabilise the cubic phase at temperatures below 1000 ^{o}C after 6 hours reaction time. The purity quality of the materials have been proven by PXRD and NPD, and the possible location of the Ga^{3+} in the tetrahedral and octahedral Li^{+} sites analysed. As a consequence of the milder synthetic conditions. a large intergrain resistance was detected by EIS due to smaller grains and lower pellet density. Local Li^{+} dynamics have demonstrated the low barrier to Li^{+} diffusion of 0.19(1) eV and a Li^{+} diffusion coefficient *ca.* 10^{-11} cm^2 s^{-1}, similar to current state-of-art cathode materials.

The Al-doped LLZO cubic garnet can be also synthesised at 700 ^{o}C for 2 hours by sol-gel chemistry. This low temperature stabilisation could be a consequence of Li^{+}/H^{+} exchange occurring during the synthesis, as demonstrated by PXRD, Raman and *in-situ* NPD, where an expanded cell parameter, high temperature decomposition and lithium deficiency results from this exchange. The macroscopic transport properties experience a detrimental change due to the small particle size with an increase in the macroscopic activation energy of $\sim$ 0.3 eV. The activation energy for local diffusion, however, remains constant compared to the solid-state synthesised material suggesting the main conduction mechanism is retained.

It has also been demonstrated that introduction of Li-excess in the $Li_6Hf_2O_7$ solid-electrolyte by Y^{3+} and In^{3+} aliovalent doping can enhance the transport properties of the material, with activation energies decreasing from 0.97(4) to 0.42(3) eV and increases of up to one order of magnitude in the ionic conductivity.

A novel family of alkali metal-rich double perovskites [$A_{1.5}La_{1.5}MO_6$ (A = Li^{+}, Na^{+} and M = W^{6+}, Te^{6+})] has been prepared and characterised. The structure presented

the alkali metal-ion in both the A- and B-sites with La^{3+} occupying partially the A-sites, as proved by PXRD, NPD and EXAFS studies. The materials present alkali metal ionic conductivity, with low activation energies for their conduction. While the $Li_{1.5}La_{1.5}WO_6$ presented promising properties as a low voltage (<1 V) combined insertion/conversion anode as analysed by electrochemical, DFT and magnetic characterisations, the Te^{6+} counterpart have shown promise as solid-state electrolyte for Li and Na batteries with microscopic activation energies below 0.2 eV.

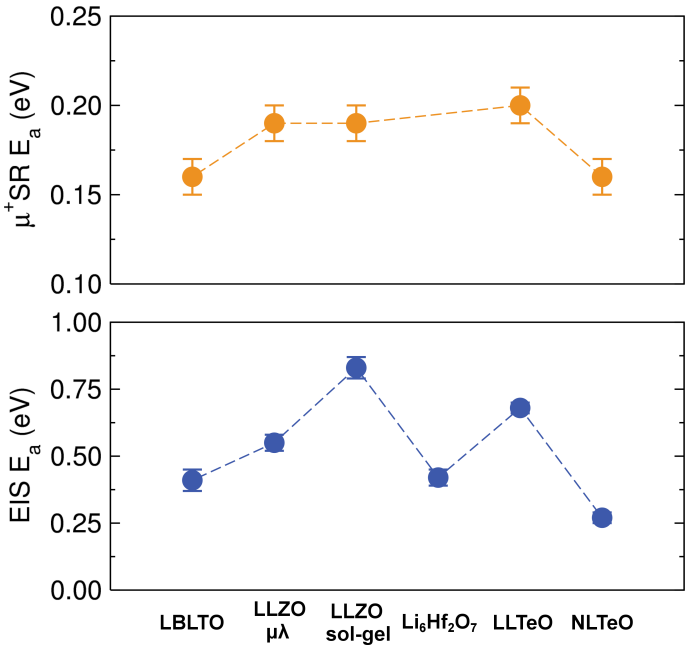

Figure 9.1: Activation energies obtained from EIS and μ^+SR techniques for the solid electrolytes systems studied in this thesis. The y-axes scale have been adapted in both graphs for a clearer vision of the energy trends within each technique.

A summary of the macroscopic and microscopic activation energies for ionic conduction obtained by EIS and μ^+SR is shown in Figure 9.1. A similar trend is observed from both techniques, where higher differences can be observed in the case of the EIS data as the microstructure of the materials plays an important role. In the case of the μ^+SR data, similar values in the range of 0.15 - 0.20 eV were obtained, suggesting these materials are promising candidates as solid electrolytes upon further optimisation of their macroscopic properties.

In summary, the work carried out in this thesis has provided an improved route for the solid state synthesis of the Li-rich complex oxides using microwave radiation, insights into their properties at the macro and local scale and has produced novel materials with battery applications.

9.2 Further work

The research presented in this thesis have opened new lines of investigation by the insights provided by the local diffusion properties of the materials and the discovery of novel materials for battery applications. Some of the possible further studies arising from this thesis are presented in this section.

From the lithium-rich garnet materials, analyses of the PDF data for the LBLTO material are ongoing, which could provide insights into the local distribution of Li^+. Fits of neutron total scattering data obtained prior this thesis for the conventional $Li_3Nd_3W_2O_{12}$ garnet materials have shown a lack of disorder in the structure (Fig. 9.2). The same analyses on the LBLTO material show a discrepancy between the local and average structure as a result of disorder in the Li^+ ionic network. Studies employing a big box modelling approach with RMCProfile are forthcoming.

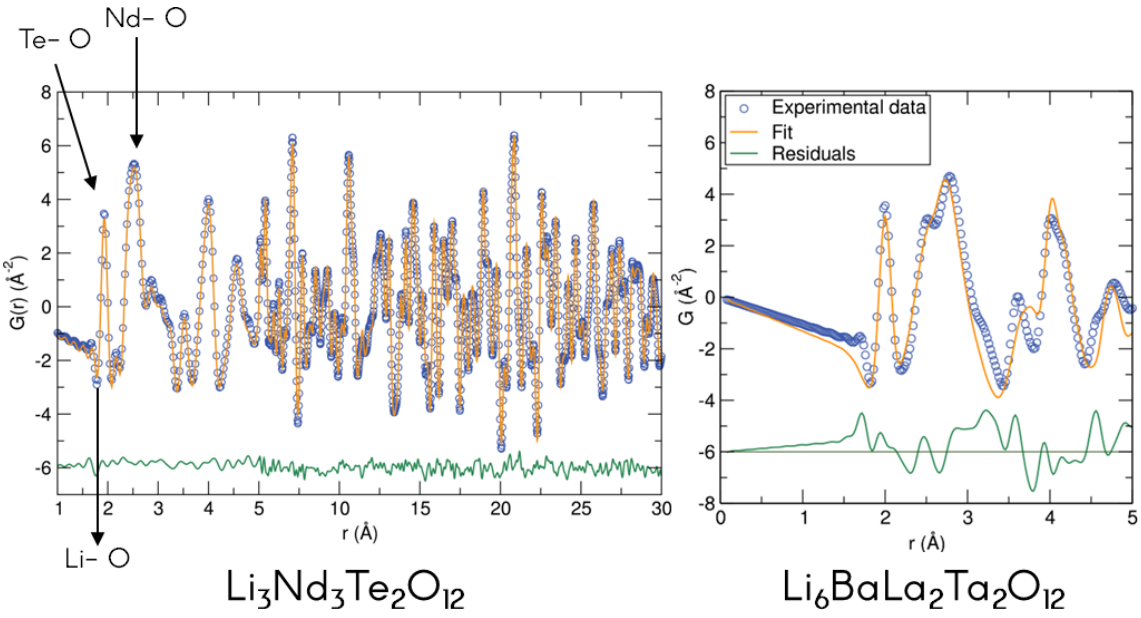

Figure 9.2: PDF data for the $Li_3Nd_3W_2O_{12}$ and $Li_6BaLa_2Ta_2O_{12}$ garnets materials analysed with PDFgui software.

It will be vital to optimise the macrostructural properties of the microwave prepared LLZO materials in order to maximise the transport properties of these materials. This may be achieved by employing hot-pressing post-sintering treatments or by the introduction of sintering aids that could enhance the sintering during the microwave processing.

The insights gained here of the sol-gel synthesised LLZO material has stressed the need for continued work on this synthetic pathway and to the develop new protocols to avoid protonation of the material, by using aprotic polar solvents such as acetonitrile, for example, together with the evaluation of the thermal stability and the transport properties of the resulting materials.

Also of interest would be to study the lithium excess in the doped $Li_6Hf_2O_7$ in detail

by low temperature NPD in heavily doped compositions in order to analyse the location of the excess lithium within the structure. μ^+SR analyses would be also interesting to perform to analyse the maximum potential of these materials by identifying their local transport properties.

Regarding the novel alkali metal double perovskites, a vast number of future research lines are in hand, with some of them already in progress. In the case of the LLWO material, sol-gel chemistry has been successfully carried out (Fig. 9.3) in the hope of obtaining smaller particle sizes which could result in a higher rate capability by increasing the surface of the particles, promoting quicker Li^+ diffusion to the electrolyte.

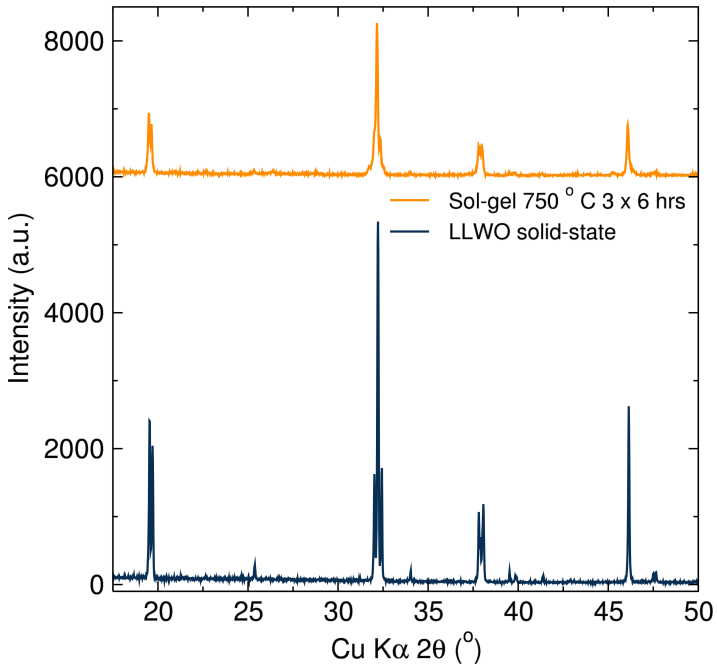

Figure 9.3: PXRDs of the solid-state and sol-gel synthesised LLWO materials.

For both Li-rich double perovskite materials, neutron total scattering measurements have been carried out at different temperatures (Fig. 9.4) to model the possible Li^+ disordering within the perovskite framework, especially for the A-sites cations.

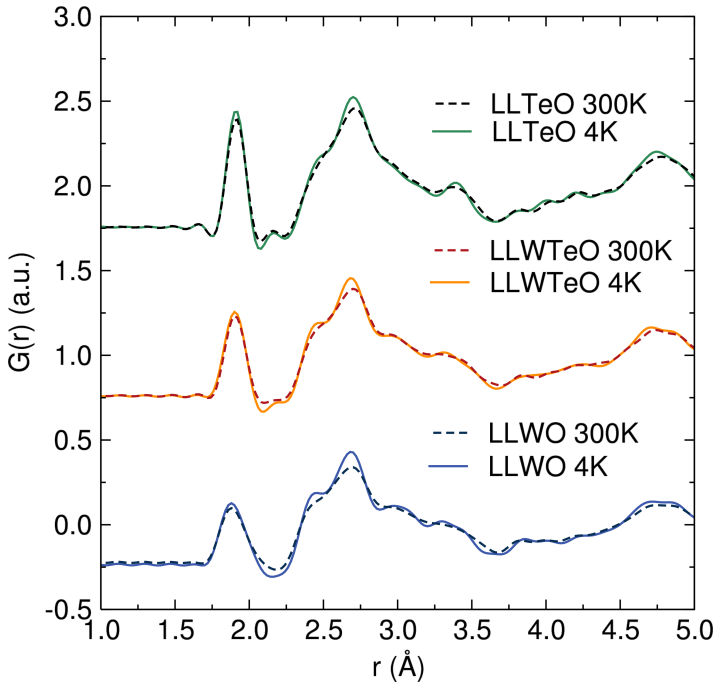

Figure 9.4: PDF for the three Li-rich double perovskite materials presented in Chapter 7 normalised from neutron total scattering data collected on Polaris instrument at ISIS.

Further analyses of the cycled LLWO material in order to unveil the precise mechanism under lithium reaction are under way, for which total scattering data and XPS measurements could help to unveil the presence of amorphous conversion materials and probe the various oxidation states present.

For the Te^{6+} containing double perovskites, stoichiometry tailoring to increase the alkali metal content could also be carried out to increase the transport properties of these materials. In the case of the Na-rich analogue, premature decomposition at mild temperatures upon contact with Na metal electrodes has been noted which will require analysis of the decomposition products by TEM or/and XPS for example, and the development of mediating thin film materials, for example, to avoid the observed increasing resistance over time.

These are just a few ideas that can be developed following the results shown in this thesis. However, different eyes can see different landscapes, therefore the dissemination of these results could benefit the entire energy storage research community.

Appendix

Table 10.1: Atomic parameters for the $Li_6Hf_2O_7$ crystal structure.

Atom	Site	Frac.	x	y	z	Uiso ($Å^2$)
Hf1	8f	1	0.18321	0.12251	0.36484	0.01
Li1	8f	1	0.2927	0.1286	0.1075	0.02
Li2	8f	1	0.4341	0.403	0.398	0.02
Li3	8f	1	0.0622	0.354	0.0833	0.01
O1	4e	1	0	0.155921	0.25	0.02
O2	8f	1	0.121558	0.356451	0.504722	0.02
O3	8f	1	0.38413	0.349815	0.023592	0.02
O4	8f	1	0.252479	0.404488	0.253037	0.02

Table 10.2: Extracted atomic parameters from Rietveld refinement of the $Li_{1.5}La_{1.5}W_{0.5}Te_{0.5}O_6$ PXRD data.

Atom	Site	Frac.	x	y	z	Uiso ($100/Å^2$)
La1	4e	0.788(2)	0.0056(5)	0.9706(2)	0.7479(2)	1.75(3)
Li1	2d	1	1/2	0	0	0.5
O1	4e	1	0.274(2)	0.700(2)	0.964(2)	0.7(1)
O2	4e	1	0.234(2)	0.233(2)	0.955(2)	0.7(1)
O3	4e	1	0.889(2)	0.513(1)	0.751(1)	0.7(1)
W1	2c	0.5	1/2	0	1/2	2.02(3)
Te1	2c	0.5	1/2	0	1/2	0.09(2)

Table 10.3: Extracted atomic parameters from Rietveld refinement of the $Li_{1.5}La_{1.5}TeO_6$ NPD data.

Atom	Site	Frac.	x	y	z	Uiso (100/Å^2)
La1	4e	0.75	0.01134(25)	0.9987(6)	0.74037(18)	0.0086(3)
Li1	4e	0.25	-0.048(6)	0.006(8)	0.8111(35)	0.0039(13)
Li2	2d	1	1/2	0	0	0.0039(13)
O1	4e	0.356	0.2268(11)	0.7947(14)	1.0141(11)	0.0021(5)
O2	4e	0.356	0.3522(12)	0.3112(12)	0.9501(8)	0.0021(5)
O3	4e	0.356	0.9762(11)	0.5762(15)	0.7929(8)	0.0021(5)
Te1	2c	1.002(3)	1/2	0	1/2	0.0057(3)
O1spl	4e	0.644	0.2669(6)	0.7178(7)	0.9443(6)	0.0021(5)
O2spl	4e	0.644	0.2378(6)	0.2528(8)	0.9584(6)	0.0021(5)
O3spl	4e	0.644	0.9396(7)	0.4705(10)	0.7742(4)	0.0021(5)

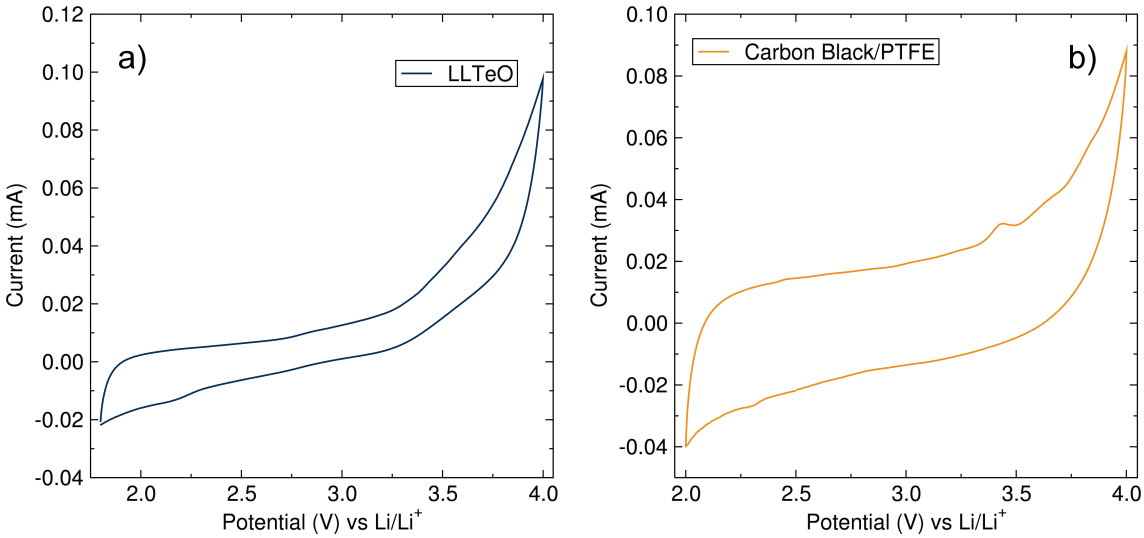

Figure 10.1: CV data of the $Li_{1.5}La_{1.5}TeO_6$ double perovskite material mixed with 5% of carbon black and 5% of PTFE as a binder (a) and 50% of carbon black and 50% of PTFE (b). The scan rate was fixed at 0.1 mV s^{-1}.

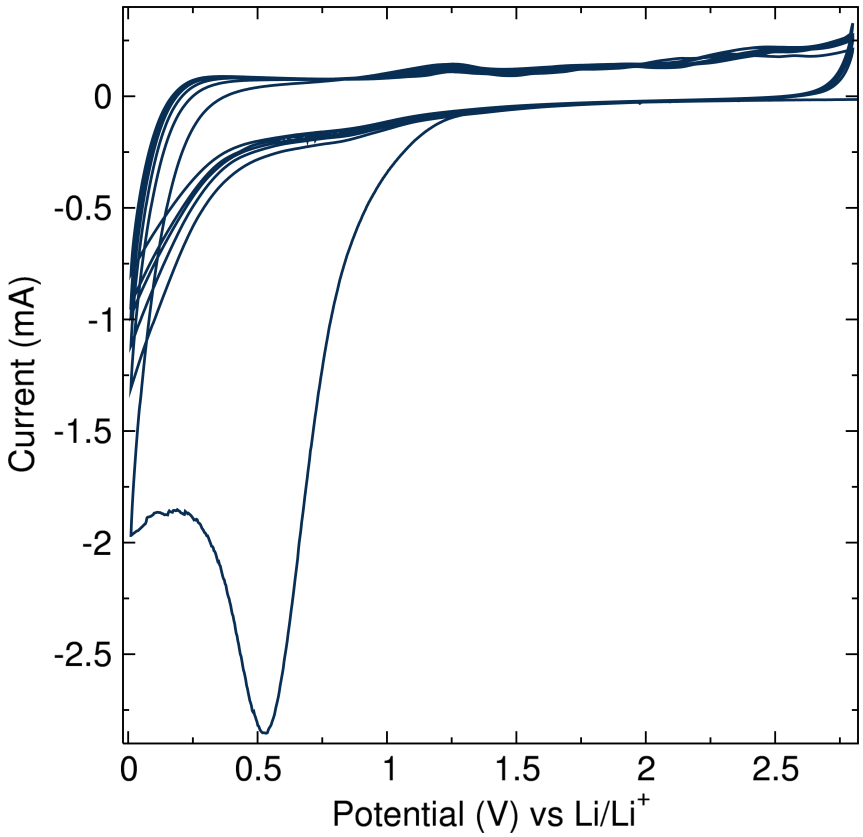

Figure 10.2: CV of 50% of carbon black and 50% of PTFE (b). The scan rate was fixed at 0.1 mV s^{-1}.

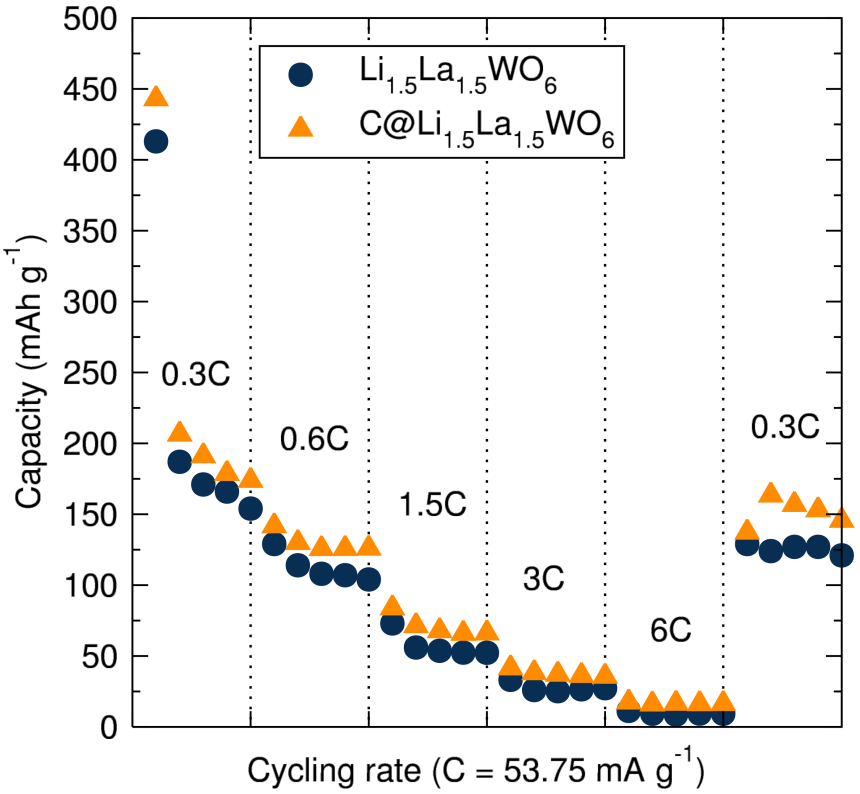

Figure 10.3: Rate performance of $Li_{1.5}La_{1.5}WO_6$ (blue circles) and 6% carbon coated from sucrose $Li_{1.5}La_{1.5}WO_6$ (orange triangles) materials mixed with a 5% of carbon black and 5% of PTFE as a binder between 0.01 and 2.8 V at different C rates. C = 53.75 mA g^{-1}.